

Multiscale Design, Fabrication, and Mechanical Analysis of Structural Hierarchies in Functional Materials

Thesis by
Seola Lee

In Partial Fulfillment of the Requirements for the
Degree of
Doctor of Philosophy

The logo for the California Institute of Technology (Caltech), featuring the word "Caltech" in a bold, orange, sans-serif font.

CALIFORNIA INSTITUTE OF TECHNOLOGY
Pasadena, California

2025
Defended March 24th, 2025

© 2025

Seola Lee

ORCID: 0000-0002-4538-0890

All rights reserved.

ACKNOWLEDGEMENTS

My journey at Caltech has been one of the most challenging yet rewarding chapters of my life. I am deeply grateful for the extraordinary people and institutional support that have shaped my graduate studies over the years.

First and foremost, my heartfelt gratitude goes to my advisor, Professor Julia R. Greer, for her unwavering support, patient guidance, and steadfast belief in me. Julia's passion for science and her open-minded approach have empowered me to explore new ideas, helping me grow as an independent researcher. As both an advisor and mentor, she has been a constant source of encouragement, particularly in moments of self-doubt. Her confidence in me has been truly inspiring, pushing me to embrace challenges, take initiative, and become a better colleague, researcher, and leader. I am profoundly grateful for her trust, wisdom, and invaluable insights.

I extend my sincere appreciation to my thesis committee members, Professor Zhen-Gang Wang, Professor Guruswami Ravichandran, and Professor Chiara Daraio, for their invaluable guidance and mentorship throughout my PhD. Zhen-Gang's rigorous approach to science has reinforced the importance of fundamentals in my work, and his insightful feedback—both academically and beyond—has profoundly shaped my growth as a scholar. Ravi, thank you for serving as the chair of my thesis committee and for your steadfast support. Your wise advice has guided me through the challenges of my PhD journey and helped me navigate my career path with confidence. Chiara, I am deeply grateful not only for your role on my committee but also for your continuous mentorship during my internship at Meta and beyond. Thank you for the instrumental guidance in broadening my research perspective and shaping my approach to scientific inquiry.

None of this work would have been possible without my exceptional collaborators and my incredible Greer Group colleagues. To my dear MPEC team—Pierre Walker, Seneca Velling, Dr. Amy Chen, Cyrus Fiori, Professor Vatsa Gandhi, and Zane Taylor—thank you for the countless late-night experiments, thought-provoking discussions, and shared excitement for our projects. To the Scalability team—Professor Matias Kagias and Dr. Andrew Friedman—our relentless efforts and constructive collaborations have been some of my most cherished research experiences. Also, to all my other collaborators, Dr. Israel Kellestein, Zixiao Liu, Dr. Gunho Kim, and Dr. Suyeong Jin, thank you so much. I am also deeply grateful to my former mentors,

Dr. Amy Chen, Dr. Widiyanto Moestopo, Professor Rebecca Gallivan, Professor Max Saccone, Dr. Fernando Villafuerte, and Dr. Jane Zhang, for their invaluable guidance and encouragement. To my wonderful colleagues, Dr. Yuchun Sun, Dr. Weiting Deng, Kevin Nakahara, Wenxin Zhang, Thomas Tran, Sammy Shaker, Wen Chen, and Yingjin Wang, and all Greer group colleagues, your camaraderie and support have made this journey even more meaningful.

Beyond the lab, my Caltech experience has been shaped by the unwavering support of my friends. I am especially grateful to Caltech's Korean community, K-tennis, all my Korean friends and Team DFA—your friendship, laughter, and encouragement have been an anchor throughout this journey. I look forward to celebrating our continued successes together.

Finally, my deepest love and gratitude go to my family. Junho, my partner in life, you have been my rock through every triumph and challenge. Thank you for standing beside me with unwavering love and support—I cannot wait to embark on our next adventure together. To my parents, Hosuk and Junghee, and my twin brother, Jinwoo, your unconditional love and belief in me have been the foundation of everything I have achieved. I am forever grateful for your sacrifices, encouragement, and endless support.

To all those who have supported, inspired, and believed in me—thank you from the bottom of my heart.

ABSTRACT

Hierarchical structuring has emerged as a powerful strategy in functional material design to enhance mechanical performance and impart functional properties across multiple scales. In architected materials, leveraging tessellated multiscale geometrical features enables unconventional properties such as ultra-low density and high energy absorption. Similarly, in functional polymers, rational design of molecular chemistries and polymer microstructures allows for tunable mechanical properties and stimuli-responsive behaviors. However, a substantial knowledge gap persists in understanding how multiscale interactions connect to determine the macroscale performance of these materials. This gap arises from challenges in scalable fabrication, multiscale characterization, and limited mechanistic insight from theory and simulations. To address these challenges, this thesis presents a comprehensive approach that integrates scalable fabrication, multiscale characterization, and theoretical modeling to develop hierarchical materials with tunable functionalities. Specifically, we (1) demonstrate scalable fabrication of hierarchical materials using additive manufacturing, (2) investigate the bulk mechanical responses by tuning the smallest level in hierarchical design, and (3) perform multiscale studies to bridge the gap between unit-level interactions and macroscale performance.

In the first study, we explore the role of structural hierarchies in architected polymeric materials for enhanced energy dissipation. Using metasurface-based holographic lithography, we fabricate nano-architected polymeric sheets and demonstrate how geometrical parameters for unit cell design such as relative density and beam aspect ratio influence stiffness, energy dissipation, and deformation modes. These findings highlight the significance of hierarchical structuring in enhancing mechanical performance and establish design principles for scalable manufacturing. In the second study, we focus on dynamic polymers and examine how dynamic crosslinking at the molecular level influences macroscale material responses. A single-step stereolithography approach is developed to tune molecular-level controls in the material. Through multiscale modeling and experimental characterizations, we reveal how dynamic bonding mechanisms govern stiffness, stretchability, and fracture energy. The results underscore the significance of multiscale interactions in tuning mechanical behavior and suggest a pathway for designing materials with programmable responses. In the final study, we build on these insights by integrating molecular-level controls with nonlinear structural responses such as buckling and

shape transformations. The central premise is that molecular interactions dictate local responsiveness, while structural geometries can amplify or suppress these responses through localized deformation or stress redistribution. As a demonstration, we explore how tailored viscoelasticity and controlled instabilities can determine the buckling mode of a structural beam. This synergistic interplay highlights the potential of the materials requiring programmed reconfigurability, shape morphing, and stimuli-responsive properties.

The findings presented in this thesis offer a robust framework for bridging molecular-level design with macro-scale performance through scalable fabrication and characterization strategies. By expanding the design space of material-level behavior, this work lays the groundwork for developing next-generation materials with enhanced functionality, adaptability, and intelligence for applications such as soft robotics, healthcare, and sustainable materials.

PUBLISHED CONTENTS AND CONTRIBUTIONS

Chapter 2 has been adapted from:

1. M. Kagias[†], S. Lee[†], A.C. Friedman[†], T. Zhang, D. Veysset, A. Faraon & J.R. Greer*. “Metasurface-Enabled Holographic Lithography for Impact-Absorbing Nanoarchitected Sheets”. *Advanced Materials* **35**, 2209153 (2023). DOI: [10.1002/adma.202209153](https://doi.org/10.1002/adma.202209153)

Contributions: S.L. designed the experiments, performed experimental characterizations, analyzed the results, and wrote the manuscript.

Chapter 3 and 4 have been adapted from:

2. S. Lee^{*†}, P. Walker[†], S. Velling, A. Chen, Z. Taylor, C. Fiori, V. Gandhi, Z-G. Wang & J.R. Greer. “Molecular Control via Dynamic Bonding Enables Material Responsiveness in Additively Manufactured Metallo-Polyelectrolytes”. *Nature Communications* **15**, 6850 (2024). DOI: [10.1038/s41467-024-50860-6](https://doi.org/10.1038/s41467-024-50860-6)

Contributions: S.L. conceived and designed the project, fabricated samples, performed experimental characterization, analyzed the results, and wrote the manuscript.

3. S. Lee, Z. Liu, K. Funk, X. He & J.R. Greer. "Cation-Induced Pattern Transformation of Additively Manufactured Polyelectrolytes". *In Preparation*.

Contributions: S.L. conceived and designed the project, fabricated samples, performed experimental characterization, analyzed the results, and wrote the manuscript.

[†] equal contribution

* corresponding author

TABLE OF CONTENTS

Acknowledgements	iii
Abstract	v
Published Contents and Contributions	vii
Table of Contents	viii
List of Illustrations	xi
List of Tables	xxviii
Chapter I: Introduction	1
1.1 The Concept of Structural Hierarchies in Material Design	1
1.2 Hierarchy in Structure Design: Architected Materials	2
1.2.1 Fabrication Techniques	3
1.2.2 Material Properties	4
1.3 Hierarchy in Material Design: Polymer Structures	5
1.3.1 Design Strategies and Fabrication Techniques	6
1.3.2 Material Functionality	9
1.4 Challenges in Hierarchical Material Design	10
1.5 Chapter Outlines	12
Chapter II: Large Scale, Nano-Architected Polymers	15
2.1 Chapter Summary	15
2.2 Introduction	16
2.3 Scalable Fabrication: Metasurface-based Holographic Lithography	17
2.4 Microstructural Characterization	20
2.5 Quasi-static Characterization	21
2.5.1 Ex-situ Nanomechanical Indentation	21
2.5.2 Mechanical Response of Architected Materials	21
2.5.3 In-Plane Inhomogeneity Across the Large-scale Sheet	23
2.6 Effects of Structural Designs: Relative Density and Beam Aspect Ratio	26
2.6.1 Two-Photon Polymerization for Variations in Unit Cell Design	26
2.6.2 In-situ Nanomechanical Compression	28
2.6.3 Mechanical Response of Architected Materials	28
2.7 Dynamic Characterization	35
2.7.1 Laser Induced Particle Impact Testing	35
2.7.2 Energy Absorption and Impact Response	35
2.8 Conclusion	42
Chapter III: Multiscale Interactions in Metal-Coordinated Dynamic Polymer	44
3.1 Chapter Summary	44
3.2 Introduction	45
3.3 Additive Manufacturing of MPEC Gels via Stereolithography	46
3.4 Material Characterization for AM-Fabricated MPEC Gels	49
3.5 Molecular-Level Controls: Binding and Coordination	56

3.5.1	Metal Valency	56
3.5.2	Polyanion Charge Density	59
3.6	Multiscale Interactions	61
3.6.1	Chain Relaxations	62
3.6.2	Chain Configurations	66
3.6.3	Network Topology	68
3.6.4	Phase Behavior	70
3.6.5	Multiscale Study Summary	73
3.7	Macroscale Mechanical Behavior	74
3.7.1	Uniaxial Tensile Testing	74
3.7.2	Fracture Toughness	79
3.8	Additional Molecular-Level Controls: Solvent and Metal Identity	87
3.8.1	Solvent Effects	87
3.8.2	Metal Identity Effects	90
3.9	Conclusion	95
Chapter IV: Bridging Molecular-to-Mechanics: Molecular Control for Global Material Response		96
4.1	Chapter Summary	96
4.2	Introduction	97
4.3	Mechanical Stimuli: Controllable Deformation of Bilayer Structure	97
4.3.1	Strain-rate Dependent Buckling	99
4.3.2	Relaxation Dependent Curling	102
4.4	Solvent Stimuli: Swelling-induced Shape Transformation	106
4.4.1	Charge Density, Metal Valency Dependent Swelling	107
4.4.2	Qualitative Bi-material Shape Transformation	110
4.4.3	Large Deformation Coupled With Molecular Interactions	112
4.4.4	Outlook for Complex Shape Transformation	120
4.5	Beyond Mechanics: Towards Multifunctionality	121
4.5.1	Dissolution and Reprocessing	121
4.5.2	Shape Memory Effects	126
4.6	Conclusion	127
Chapter V: Summary and Outlook		129
5.1	Summary	129
5.2	Outlook	130
Bibliography		133
Appendix A: Fabrication Optimization for Scalable Holographic Lithography		148
A.1	Scanning Step Size Optimization for Holographic Lithography	148
A.2	Diffraction efficiency measurements and mask uniformity	149
Appendix B: Experimental Characterization for Multivalent ions and Polyelectrolyte system		150
B.1	Vibrational Spectroscopy for Metal-Carboxylate Coordination	150
B.2	Effects of Entanglement in AM-Fabricate MPEC Gels	151
B.3	Experimental Tracking in the Constructed MPEC Phase Diagrams	151
Appendix C: Theoretical Framework for Multivalent Ions and Polyelectrolyte System		156

C.1 Modified Henderson–Hasselbach Equation	156
C.2 Mean-field Theory of Multivalent Ions and Polyelectrolyte Systems .	160

LIST OF ILLUSTRATIONS

<i>Number</i>	<i>Page</i>
1.1 Structural hierarchies in architected materials.	2
1.2 Hierarchical organizations in dynamic polymers.	5
2.1 Metasurface based holographic lithography. a , Schematic representation of the lithographic setup. The scanning trajectory of a laser beam is highlighted by the dashed blue line. b , The metasurface is placed directly on top of the sample substrate covered with SU8 photoresist. The metamask diffracts the incoming laser beam and creates a near field 3D intensity distribution within the photoresist. c , The fabricated metamask (scale bar 5 mm). Insets represent a top-view helium ion microscope (HIM) image of the utilised metamask (scale bar 450 nm) and a zoomed-in tilted HIM image of the outlined region (scale bar 100 nm). d , Near field 3D intensity modulation generated by the fabricated metamask design, color represents light intensity normalized by the maximum intensity.	18
2.2 Morphology and pattern fidelity. a , A top view photo of the fabricated sample. White square in the middle corresponds to the patterned area, whose appearance is opaque (scale bar 1 cm). b , Scanning electron microscopy (SEM) image showing a typical cross section of the fabricated material. A clear pattern transfer is observed throughout the entire sample thickness (scale bar 25 μm). The inset shows the beam arrangement within a single layer (scale bar 1 μm). c , A zoomed-in SEM image of the cross section showing the generated beam structure and difference in diameter d . The blue area in (ii) corresponds to the adhesion layer (scale bar 1 μm).	20

2.3	Quasi-static nanoindentation characterization. a , Schematic representation of Nanoindenter setup. b , Representative load-displacement response of the nanoarchitected material during compressive indentation with a 100 μm -diameter flat punch at a strain rate of $\dot{\epsilon} \sim 10^{-4} \text{ s}^{-1}$. The dashed lines represent the slopes of the initial elastic loading, plateau-like response, and the upper 30% of the unloading data segment. The arrows in the plateau region depict a series of displacement bursts that correspond to the collapse of individual structural layers and crack formation. c , SEM image of the representative indentation mark after the nanomechanical experiment, with the intended cross-sectional plane denoted by the red-dashed line (tilt 30°). d , SEM image of a cross-section through a 12 μm -deep and 100 μm -wide residual impression of the indentation mark.	22
2.4	Spatial Mapping of Stiffness Across Macroscale Architected SU8 Sheet. a , Indentation mapping of the 25 \times 25 indents conducted on the nano-architected SU8 sheet. An array of dots represents individual indents located on a 820 μm in X 840 μm in Y Cartesian grid across the sheet (scale bar 6 mm). b , Distribution of experimentally measured elastic modulus with an average of 0.96 GPa and a standard deviation of 0.52 GPa. c , Spatial mapping of in-plane modulus across the sheet (scale bar 6 mm).	23
2.5	Stiffness Variations Correlation to Metamask Inhomogeneity. a , Spatial mapping of in-plane modulus across the sheet (left) and the corresponding metamask diffraction efficiency map over the same area (scale bar 6 mm). b , SEM images of the samples at two distinct locations, A and B. c , The effects of laser power on the constituent material properties. Stiffness was measured from the unpatterned, monolithic SU8 crosslinked with a different laser power attainable in the actual patterning process.	25
2.6	Simulated diffraction efficiencies for varying nano-pillar width.	26

2.7	Two Photon Lithography for SU8 Photoresist. a , Schematic representation of the 2PP lithographic setup featuring the galvo scanning mode and oil immersion configuration. b , The effect of variations in scan speed (SS) and laser power (LP) on the SU-8 photoresist. Lower SS combined with high LP resulted in overexposure and, in some cases, explosive delamination due to excessive heat generation. c , The effect of variations in slicing and hatching distances on 2PP voxel conditions. Larger slicing and hatching distances reduced the printing time but compromised structural integrity and weakened the interfaces between subcomponents within the design.	27
2.8	Variations in Relative Density ($\bar{\rho}$) for Small Lattice SU8. a , CAD models of unit cells illustrating different morphologies with varying relative densities. b , SEM images of 3-by-3 SU8 lattices fabricated using 2PP lithography, showing variations in relative density across different samples.	29
2.9	Quasi-static compression results for nanoarchitected SU8 with different relative densities ($\bar{\rho}$). a , Stress vs. strain curves measured during compression. b , Zoomed-in stress vs. strain curves comparing elastic modulus and yield strength. c , Effective elastic modulus vs. relative density. d , Effective yield strength vs. relative density.	30
2.10	Deformation and Energy absorption of nanoarchiated SU8 with different relative density ($\bar{\rho}$). a , Post-mortem SEM images of deformed samples. Scale bar 30 μm b , Calculated absorbed energy (J/m^3) and c , specific absorbed energy (J/kg^3) for the samples with different $\bar{\rho}$	31
2.11	Variations in Beam Aspect Ratio (p_z/D) for Small Lattice SU8. a , The geometrical parameters, the lateral (p_x) and longitudinal (p_z) periodicity with beam diameter (D), define the aspect ratio of the nanoarchitected SU8. b , Theoretically attainable aspect ratio of the fabricated SU8 lattice by adjusting the lateral periodicity of metasurface (p_x) for the developed holographic setup ($\lambda = 532\text{nm}$, $n = 1.6$). The longitudinal periodicity (p_z) is a direct result of the Talbot effect. The maximum shrinkage during the post-processing can be up to 60% of the as-printed structures. c , SEM images of 3-by-3 or 3-by-2 SU8 lattices with $\bar{\rho} = 0.4$ fabricated using 2PP lithography, showing variations in beam aspect ratio across different samples.	32

2.12	Quasi-static compression results for nanoarchitected SU8 with different beam aspect ratios (p_z/D). a , Stress vs. strain curves during compression. b , Zoomed-in stress vs. strain curves for elastic modulus and yield strength comparison. c , Effective elastic modulus vs. beam aspect ratio (p_z/D). d , Effective yield strength vs. beam aspect ratio (p_z/D).	33
2.13	Effects of beam aspect ratio on material deformation mode. a , Post-mortem SEM images of a deformed large-scale nanoarchitected SU8 sheet fabricated via holographic lithography. Scale bar: 30 μm . b , Post-mortem SEM images of 2PP-fabricated nanoarchitected SU8 samples with varying beam aspect ratios (p_z/D).	34
2.14	Analysis of micro-ballistic experiments on nano-architected SU8 sheet. a , Dissipated and rebound energetics versus impact energetics. A linear fit of the dissipated energy is presented with a green dashed line. As a function of impact energy, four deformation regimes were exhibited: (i) elastic rebound, (ii) shallow and (iii) deep crater formation to (iv) particle capture. b , Corresponding post-impact micrograph of each regime. (scale bar 5 μm).	37
2.15	Crater morphology and cross-sectional micrographs. a , Shallow crater formed after an impact with $v_o = 345 \text{ m s}^{-1}$. b , Deep crater formed with impact velocity $v_o = 600 \text{ m s}^{-1}$ (scale bar 5 μm)	38
2.16	Specific dissipation energy of nano-architected SU8 sheet. W_d^* of nano-architected SU8 thin sheet compared with other bulk and nanomaterials [5, 26–37].	39
2.17	Contribution of crater kinetic energy and delocalization energy during dissipation process. a , Decomposition of W_d^* into two terms, $W_{delocalization}^*$ and $W_{craterKE}^*$. b , Percentile of dissipation contribution from each factor.	41
3.1	Additive manufacturing of MPEC using stereolithography. a , Schematic representation of Liquid Crystal Display (LCD) Stereolithography set-up. A layer-by-layer printing is processed to produce solidified parts. b , Resin formulation for one-pot synthesis of MPEC. c , Free-radical photopolymerization reaction is initiated by projecting UV light into a liquid photoresin in the bath. The polymerized chains undergo in-situ coordination with multivalent metal ions.	46

3.2	Additive manufactured MPEC gels. a, Optical images of synthesized photo resins (without tartrazine to show coordination color) and 3D-printed lattices (with tartrazine) with different metal ions. Scale bar 15 mm. b, Magnified images of 3D-printed octet lattices, showing multiple unit cells. Scale bar 2 mm.	48
3.3	Metal-carboxylate coordination bond for AM-fabricated MPECs. a, FTIR spectra exhibits signatures of both carboxyl and carboxylate functional groups, with the later being associated with bidentate chelation of Na^+ , Ca^{2+} , and Al^{3+} . b, Visual representative of structural models of coordination for Na^+ , Ca^{2+} , and Al^{3+}	50
3.4	Thermogravimetric analysis of MPEC gels for contents quantification. a, Weight loss profiles of MPEC gels with different metal ions. During thermal ramp, the gels undergo dehydration-desolvation-decarboxylation-and-polymer thermal degradation. b, Weight loss profiles of MPEC gels for each metal ion with different pH: (i) pure PAA without any metal crosslinkers, (ii) Na^+ -MPEC, (iii) Ca^+ -MPEC, and (iv) Al^+ -MPEC. c, Dash lines are theoretical metal binding ratio based on the resin formulation. The makers are measured metal binding ratio as inferred from TGA using residual oxide weights.	51
3.5	X-Ray Fluorescence (XRF) mapping of AM-fabricated MPECs. a, Na^+ MPEC, b, Ca^{2+} MPEC, and c, Al^{3+} with sodium counterion from buffer. From top to bottom in each pane shows samples fabricated in most acidic to most alkaline conditions. Outset shows large area map of XRF relative to total sample width. Spot size for all XRF maps is $20 \mu\text{m} \times 20 \mu\text{m}$	54
3.6	Thermodynamic equilibrium of AM-fabricated MPECs. a, Mass tracking of MPEC-gels over fabrication stages, confirming mass equilibration. b, Reproducible thermal cycles over 25°C to 60°C c, Reproducible thermo-mechanical behaviors of re-equilibrated gels at $T > T_g$ (i) Mass tracking of Ca^{2+} (green) and Al^{3+} -MPEC gels (yellow) to ensure constant solvent content between tests. (ii) Temperature profile applied during the test, using four different equilibration temperatures to probe the rheological behavior of (iii) Ca^{2+} (green) and (iv) Al^{3+} -MPEC gels.	55

3.7	Binding energy of multivalent metal ions. Binding energy vs. metal-carboxylate separation of multivalent metal ions printable with the developed fabrication method. Dashed curves represent theoretical metal cation-PAA dipole interactions. The inset highlights how the different charges of metal cations lead to distinct coordination numbers around the metal center.	57
3.8	Experimentally measured activation energy of metal. a, A schematic of bond dissociation activation energy measured from rheological data. b, Measured rheological data for Al^{3+} -MPEC via time-temperature superposition. The data indicates that clear.	58
3.9	Infrared spectrum of poly(acrylic acid) under variable pH from most acidic (pH \approx 0.9) to most alkaline (pH \approx 3.25) in region of signature bands for the carboxyl and asymmetric carboxylate stretches. pH control of (de)protonation of the polyacid is clearly observed in the infrared spectrum via the disappearance of the monomeric R-COOH shoulder and emergence of the R-COO ⁻ asymmetric mode as pH increases.	60
3.10	Modified Henderson equation for polyanion charge density estimation. a, Henderson Hasselbach equation estimate charge density w.r.t. the pH values. b, pH versus charge sparsity of polyanion chains, with varying cation valency of fixed concentration (0.02 mol%). Strong association of multivalent metal cations pushes the equilibrium forwards below the Henderson–Hasselbach theory in the range of pH of interest.	61
3.11	Multiscale-span hierarchical organization of polymer structures.	62
3.12	Chain relaxation and plateau modulus. a, Thermomechanical analysis of MPEC gels (storage modulus vs. temperature) showing distinct phase transitions of MPECs during a temperature ramp at $\sim 5^\circ\text{C min}^{-1}$. b, Zoomed-in thermogram of the leathery-to-rubbery transition in the temperature range of 80°C to 200°C , highlighting differences in relaxation behavior. c, Influence of pH and metal ion valency on the plateau modulus of MPECs in the rubbery state. Plateau modulus values were extracted from Figure 3.12b and compared with analytically estimated plateau modulus.	64

- 3.13 **MD simulated ion-pair and polymer chain relaxations.** **a**, Schematic representation of ion-pair relaxation. **b**, Schematic representation of polymer relaxation. Autocorrelation functions of the **c**, ion-pair and **d**, polymer end-to-end vector for MPECs with different ion valencies at low charge sparsity. Effects of high pH to the autocorrelation functions of the **e**, ion-pair and **f**, polymer end-to-end vector for MPECs with different ion valencies (solid lines correspond to the low pH and dashed ones correspond to high pH). 65
- 3.14 **Chain configurations.** **a**, Different possible configurations for intra- and inter-crosslinks. Different colors represent different chains. **b**, Theoretically- (lines) and computationally- (markers with 95% confidence interval) predicted fraction of inter-crosslinked ions for divalent (green) and trivalent (yellow) systems at different charge sparsity. Dotted line corresponds to the sparsity where the metal ions perfectly neutralize the polyanion. **c**, Schematic representation of the effects of metal ion valency and charges sparsity on the distribution of intra- vs. interchain crosslinks. 67
- 3.15 **Polymer network.** **a**, MD simulation set-up for cluster analysis. **b**, Violin plot of simulated cluster distribution across different metal valencies and charge sparsity. The wider distributions represent greater fluctuations in cluster formation. **c**, Representative MD snapshots illustrating the percolation of polymer chains under different valency conditions. The same color represents polymer chains that are interconnected. 68
- 3.16 **Small-angle X-ray Scattering for cluster size estimation.** **a**, Simulated X-ray scattering signatures for mono-, di-, and trivalent gels. **b**, Experimentally measured SAXS spectrum for Na^+ , Ca^{2+} , and Al^{3+} -MPEC gels. 69
- 3.17 **Charge-density-dependent opacity and microstructure in MPECs.** **a**, Optical images of as-printed MPECs at different pH values, showing increased opacity at higher pH. **b**, Equilibrated MPECs after air drying. **c**, SEM micrographs capturing the transition from uniform microstructures at low pH to phase-separated morphologies at high pH. Regardless of the cation types, all MPECs exhibit similar responses. Ca^{2+} -MPECs were shown as a representative. 70

3.18	Mean-field representation of MPEC phase behavior. The excluded-volume, electrostatic, and metal-polyelectrolyte association interactions determine the overall phase behavior. Different species are represented: polymer chains (colored), charged polyelectrolyte sites (red), metal crosslinkers (yellow), polyelectrolyte counterions (light blue), and metal co-ions (brown).	71
3.19	Phase diagram of MPEC systems. a, Comparison of divalent (left) and trivalent (right) metal ions, showing that trivalent gels develop a ‘notch’ feature at low concentrations, indicating gel-gel phase separation. b, Influence of charge sparsity (pH) on phase stability. Through-the-height contour plot demonstrate an expanded two-phase region at higher charge density (higher pH).	72
3.20	Optical images of different phases in MPEC. Optical images of gels at each phase from Figure 3.19a. Scale bar 20 mm.	72
3.21	Confocal microscope images for phase separation observation Confocal microscopy (LSM 800, Zeiss) conducted on pH-controlled MPEC samples. It shows poly(acrylic acid) autofluorescence (purple) at 640 nm whereas negative void space corresponds to fluid filled regions. All samples are imaged across $800 \mu\text{m}$ by $800 \mu\text{m}$ at the depth of $50 \pm 25 \mu\text{m}$. Higher pH of the gels demonstrating severe phase separation of fluid filled regions from polymeric region for similar molecular weight network. Scale bar for all images $150 \mu\text{m}$	74
3.22	Summary of multiscale studies. The mechanistic correlation between molecular parameters (metal valency and polyanion charge sparsity) and macroscale gel properties. Stronger metal association leads to slow relaxation and coalescent polymer networks, while weaker association promotes faster relaxation and segregated networks. The intermediate regime exhibits a mixed behavior.	75
3.23	The dependence of bulk tensile response to weakly associated bonds. The mechanical response under load is dominated by: the initial structural topology of the network at low strain regime and the dynamics of bond relaxation at higher strain which determines the tensile failure mode. Reprinted by permission from [102]. Copyright ©2016, American Chemical Society.	76

- 3.24 **Uniaxial tensile response of bulk MPEC gels with different metal valency.** **a**, Optical image of uniaxial tensile test for Ca^{2+} -MPEC gels. **b**, Experimental stress–strain data of gels crosslinked with each metal crosslinks versus with MBAA under uniaxial tensile loading. **c**, Mooney-Rivlin representation of the stress-strain curves. **d**, MD simulation snapshots of divalent(top) and trivalent (bottom) gels under uniaxial loading. **e**, MD simulation stress-strain data for different metal valency under uniaxial loading. **f**, The change in fraction of inter-crosslinked divalent and trivalent ions during elastic deformations obtained using MD simulations. 78
- 3.25 **Uniaxial tensile response of bulk MPEC gels with different polyanion charge sparcity.** **a**, Experimental stress—strain data as a function of pH, which shows degradation in mechanical performance in increasingly alkaline environments. **b**, MD simulation stress-strain data for different pH gels under uniaxial loading. **c**, The change in fraction of inter-crosslinked for high pH gels during elastic deformations obtained using MD simulations. 79
- 3.26 **Design principles for fracture toughness in soft gels.** The total fracture toughness of the tough hydrogel, Γ is contributed from the intrinsic fracture energy, Γ_o from fracturing a layer of polymer chains and the mechanical dissipation in the process zone around the crack tip, Γ_D . Reprinted by permission from [104]. Copyright ©2021, American Chemical Society. 81
- 3.27 **Fracture test set-up and DIC analysis.** **a**, Experimental setup for tension testing using the MTS load frame. A series of flashlights are used to sufficiently and uniformly illuminate the sample for image capture using the high-resolution camera and DIC analysis. **b**, Overview of the DIC analysis with the region of interest (ROI), dimensions of the samples, cross-head width for calibration, and labeled subsets. **c**, Comparison of ε_{yy} calculated from actuator displacement data and averaged DIC data within the orange circle as a function of time for an un-notched sample undergoing uniaxial tension. Additionally, the strain field at $t = 150\text{s}$ is shown to demonstrate the uniform distribution of ε_{yy} indicating no slip occurred. 83

- 3.28 **Stress-strain curves for un-notched and notched MPEC for fracture experiment.** Un-notched and notched samples were stretched uniaxially at a strain rate of $\dot{\epsilon} \approx 0.02 \text{ s}^{-1}$ 84
- 3.29 **Fracture energy of MPEC gels.** **a**, Sample dimensions of un-notched and notched samples for pure shear test. **b**, Fracture energy, Γ measured using the initial gauge length (H_o , the un-notched sample stress-strain curve, and critical strain, λ_{crit} as per [108]. Box plots for Γ and λ_{crit} for crack initiation for **c**, charge-sparse MPEC and **d**, charge-dense MPEC. 85
- 3.30 **Crack propagation behavior of MPEC gels.** **a**, High-resolution images of MPEC gels at crack initiation and crack propagation. Scale bar 20 mm.**b**, the corresponding spatial mapping of ϵ_{yy} from DIC analysis, applied with a subset size of $15 \times 15 \text{ px}^2$, a step size of 1, and a strain filtering radius of 15 px [107]. Scale bar 20 mm. **c**, Crack tip velocity during the propagation. 87
- 3.31 **Effects of solvent content in MPEC gels.** Different amount of water included in trivalent (left) and divalent (right) MPEC gels by equilibrating the gels in high-humidity environment (RH~80%). **a**, TGA analysis confirms that the gels contain different amount of water contents. **b**, Stress-strain curves obtained for different water contents on. The respective young's moduli, area enclosed by the loading-unloading curve (hysteresis) and energy dissipation percent (hysteresis normalized by the total energy induced from the applied loading) of each gel have been given in the tables above. 89
- 3.32 **Stress-strain curves obtained for different co-solvent contents.** For **a**, the trivalent and **b**, the divalent MPEC gels. The respective storage moduli and standard deviations of each gel have been given in the tables above. The same protocol was used to print and perform the experiments on the gels as described in the main text. 90

3.33	MD simulations of MPEC gels with varying applied pressure. a, Stress-strain curves from uniaxial stretching. b, Cluster size distribution under different system pressure. c, Ion-pair relaxation and d, end-to-end vector relaxation. Solid curves correspond to pressures of $0.001\epsilon/\sigma^3$ and dashed curves correspond to pressures of $0.005\epsilon/\sigma^3$. The color scheme used in this figure follow the scheme used in the main text (blue: monovalent, green: divalent and yellow: trivalent ions).	91
3.34	Stress-strain curves obtained for different divalent metal ions (Ca^{2+}, Zn^{2+} and Ni^{2+}) at varying pH. (a,: low, b,: medium, c,: high). The respective young's moduli and standard deviations of each gel have been given in the tables above. The same protocol was used to print and perform the experiments on the gels as described in the main text.	92
3.35	Stress-strain curves obtained for different trivalent metal ions (Al^{3+}, Ga^{3+}, Fe^{3+} and Cr^{3+}). The respective young's moduli and standard deviations of each gel have been given in the table on the right. The same protocol was used to print and perform the experiments on the gels as described in the main text.	92
3.36	MD simulations of MPEC gels with varying ion diameters. a, Stress-strain curves from uniaxial stretching. b, Cluster size distribution over different ion diameters. c, Ion-pair relaxation and d, end-to-end vector relaxation. Solid curves correspond to diameters of 0.5σ and dashed curves correspond to diameters of σ . The color scheme used in this figure follow the scheme used in the main text (blue: monovalent, green: divalent and yellow: trivalent ions).	94
4.1	Vat polymerization set-up for bimaterial/composite structure of MPECs.	98
4.2	Controllable buckling mode under compressive stress.	99
4.3	Stress relaxation of selected MPECs and Prony series fitting. a, Fitting of experimental data of relaxation modulus for Al^{3+} at high pH (yellow) and Ni^{2+} at low pH (green). A four-term Prony series (n=4) was selected for fitting based on the residual norm analysis (inset). b, The Prony parameters determined for each material.	101

4.4	Strain-rate-dependent buckling direction control in MPEC bilayer beams. a , Calculated critical buckling strain as a function of strain rate for the fabricated MPEC bilayer beam. b , Experimental validation demonstrating controlled buckling direction under different strain rates. Scale bar 4 mm.	103
4.5	Controllable curling curvature induced by tensile stress in MPEC bilayer strips.	103
4.6	Distinct recovery strain of selected MPEC gels. a , Schematic representation of the bilayer strip. b , Representative strain and stress profiles, with colored annotations indicating material-dependent properties. Measured plastic strain evolution for c , Al ³⁺ -MPEC and d , Ni ²⁺ -MPEC over recovery time (t_{recovery}) after being stretched by $\lambda = 1.4$ for various hold times (t_{hold}). e , Induced mismatch strain resulting from differences in relaxation rate and degree between the two material systems.	104
4.7	Relaxation-dependent curling curvature from stretch-release shape change. a , Calculated curvature (markers) for the constructed MPEC bilayer strip at $t_{\text{recovery}} = 100\text{s}$. A line curve is included as a visual guide. b , Experimental verification of curling curvature variation depending on t_{hold} . The measured curvatures (stars) are plotted in Figure 4.7a. Scale bar 4 mm.	106
4.8	Fabrication processes for swellable MPECs.	107
4.9	Confocal microscope image of printed blank PAA gel with different pH. Increased phase separation is observed in high pH gels. . . .	108
4.10	Swelling ratio of low vs. high pH PAA gels in a water-acetone mixture. The gel pH modulates solvent interaction, influencing swelling behavior.	109
4.11	Swelling ratio of low vs. high pH PAA gels in Na⁺, Ni²⁺, and Al³⁺ solutions. Salt concentrations were varied in a , a 70% water - 30% acetone mixture and b , a 30% water - 70% acetone mixture to analyze metal valency effects.	109
4.12	Metal-valency selective bending direction. Swelling-induced deformation of a bilayer beam composed of Na ⁺ -MPEC with low pH (left) and high pH (right). Scale bar 30 mm.	111

4.13	In-plane bimaterial design for cooperative buckling. Spatially controlled swelling patterns induce out-of-plane buckling. Scale bar 15 mm.	111
4.14	Poroelastic relaxation via indentation. a , Experimental indentation setup for submerged swollen gels. b , A cylindrical indenter (radius = 1.5 mm) applies a fixed displacement $\delta=0.3$ mm, inducing solvent migration within the gel. c , Measured force relaxation over time for a low-pH PAA gel in water.	117
4.15	Comparison of experimental and theoretical swelling of PAA gels in Na⁺ solution. The developed model effectively captures the swelling behavior of low-pH (left panel) and high-pH (right panel) gels immersed in Na ⁺ solutions, demonstrating the experimentally observed insensitivity of low-pH gels and the swelling-to-shrinkage transition in high-pH gels.	118
4.16	Geometrically confined shape transformation. a , The swelling-induced buckling instability mechanism, where interconnected and geometrically confined pores exert compressive forces on neighboring domains, triggering coordinated structural rotation. b , Experimental observations of shape-transformed hydrogels as a function of swelling degree (Reproduced from [127] with permission from the Royal Society of Chemistry). c , Simulated MPEC shape transformation as a function of sodium ion concentration, demonstrating continuous shape evolution rather than discrete transitions.	119
4.17	Gel dissolution of MPECs with varied metal ions. a , The swelling and dissolution progress of MCPs crosslinked with different metal species were monitored. b , Optical images of the remaining MPEC gels extracted from the supernatant liquid during the dissolution time (DT).	122
4.18	Gel dissolution of MPECs with varied charge sparsity. a , The swelling and dissolution progress of MCPs crosslinked with Ca ²⁺ and Al ³⁺ at different pH (solid: low pH, dashed: high pH) were monitored. b , Optical images of the remaining MPEC gels extracted from the supernatant liquid during the dissolution time (DT).	123

- 4.19 **Guided dissolution pathway for Al³⁺-MPEC. a, b**, Dissolution path of printed Al³⁺-MPECs with varied crosslinking densities upon submersion in water. The yellow markers represent the initial phase states of the printed gels, while the blue markers indicate the subsequent phases achieved during dissolution. The inset shows images of printed Al³⁺-MPECs with different crosslinking densities. Scale bar 10 mm. **c, d**, Modified dissolution pathway by introducing pre-polymerized poly(acrylic acid) solutions in water to navigate controlled phase transitions. This adjustment enables more homogeneous dissolution while preventing excessive swelling. Scale bar 10 mm. 124
- 4.20 **Reprocessibility of 3D-printed MPECs.** The dynamic nature of metal-coordination bonds enables complete dissolution and reprocessing of MPECs. AM-fabrication MPEC gels with various metal cations were dissolved in water and recast into different shapes. Scale bar 10 mm. 126
- 4.21 **Controlled shape recovery in MPECs. a**, Heating-induced shape memory behavior of a flower-shaped MPEC gel. **b**, Influence of metal valency on shape recovery rates. Scale bars 20 mm. 127
- A.1 **Scanning step size optimization for holographic lithography. a**, Recorded beam profile/ Scale bar 1 mm. **b**, Uniformity factor for various beam step sizes. The insets show the resulting intensity distributions at step sizes 0.1 mm, 0.4 mm, and 1 mm respectively. Scale bar 4 mm. 148
- A.2 **Metamask diffraction efficiency measurement. a**, Photograph of measurement setup. **b**, Raw power data for the first and zeroth diffraction orders. **c**, Reconstructed images of the two measured orders. Scale bar 1 cm. **d**, Computed diffraction efficiency map. Scale bar 1 cm. 149

- B.1 Quantum DFT simulated infrared spectra of acetate (RCOO^-) complexation of Na^+ , Ca^{2+} , and Al^{3+} in vacuo and with explicit coordinating aqua (H_2O) ligands.** Simulations demonstrate agreement with asymmetric and symmetric stretching modes of carboxylates seen experimentally. Representative structural models of coordination generated by simulation show a clear bidentate chelation coordinating environment in vacuo, while increasing explicit water in the ligand field appears to introduce some monodentate chelation to otherwise predominantly bidentate metal cation chelation, in agreement with experimental conclusions. 150
- B.2 Different monomer concentrations were used to fabricate Na^+ -MPEC gels with different polymerization degree.** The measured pH for each photoresin was included. Images of as-printed gels with the corresponding conditions. 151
- B.3 Quasi-static tensile test for the fabricated Na^+ -MPEC gels.** All gels were post-processed to the same conditions described in the main text. **a**, all samples, **b**, zoomed-in axes for samples with lower concentration to show stress-strain curve shape change, and **c**, summary of the measured young's modulus. 152
- B.4 Experimental plan for exploring different phase regions on the constructed phase diagram for Ca^{2+} (left) and Al^{3+} -MPEC (right).** The star marker represents an arbitrarily chosen starting gel condition. Different phases were observed depending on the solution type and concentration, aligning with the behavior predicted from the phase diagram. 152

- B.5 Experimental validation of the phase diagram for Al^{3+} -MPEC.** To explore different phase regions on the diagram, equilibrated Al-gels with different density (400:1, 200:1, 50:1, 20:1 for AA:Metal ratio) were immersed in various solutions, including water, calcium nitrate solutions with different concentrations, and polyacrylic acid solutions with different concentrations, until equilibrium was reached. Different phases were observed depending on the solution type and concentration. aligning with the behavior predicted from the phase diagram. Gels become opaque in two-phase region whereas remain transparent in the single-phase region. (i) Equilibrated gels after post-processing; (ii) and (iii) immersed in 3 ml and 6 ml of 1M $\text{Al}(\text{NO}_3)_3$ solution; (iv) and (v) immersed in 4 ml and 8 ml of water; (vi) and (vii) immersed in 3 ml, 6 ml of 8M PAA solution ($M_w \sim 5$ kDa). Scale bar for all images 10 mm. 153
- B.6 Additional experimental validation of the constructed phase diagram for Al^{3+} -MPEC.** (i) Equilibrated gels after post-processing; (ii), (iii), (iv) immersed in 3 ml of 1.5M, 1.75M and 2M $\text{Al}(\text{NO}_3)_3$ solution; (v) and (vi) immersed in 4 ml and 8 ml of 4M PAA solution ($M_w \sim 5$ kDa). Scale bar for all images 10 mm. 154
- B.7 Experimental validation of the phase diagram for Ca^{2+} -MPEC.** To explore different phase regions on the diagram, equilibrated Ca-gels with different density (400:1, 200:1, 50:1, 20:1 for AA:Metal ratio) were immersed in various solutions, including water, calcium nitrate solutions with different concentrations, and polyacrylic acid solutions with different concentrations, until equilibrium was reached. Different phases were observed depending on the solution type and concentration. aligning with the behavior predicted from the phase diagram. Gels become opaque in two-phase region whereas remain transparent in the single-phase region. (i) As-printed gels; (ii) Equilibrated gels after post-processing; (iii) and (iv) immersed in 3 ml and 6ml of 1.5M $\text{Ca}(\text{NO}_3)_2$ solution; (v) immersed in water; (vi), (vii) and (viii) immersed in 3 ml, 6 ml, 8 ml of 8M PAA solution ($M_w \sim 5$ kDa). Scale bar for all images 10 mm. 155

C.1	Visual representation of the possible associations of a weak polyelectrolyte in the presence of multivalent cations. Association constants are denoted by K_i and the fraction of polymers existing in state i are denoted by f_i	156
C.2	Theoretically estimated charge sparsity of a polyelectrolyte chain at a , different divalent metal concentrations and b , different valency metals at the same concentration, $f_m = 0.01$	159
C.3	Visual representation of the proposed theory. Colors have been used to distinguish between chains. Charged sites on the polymer backbone have been highlighted in red. The metal crosslinker, polyelectrolyte counter-ion and metal co-ion have been highlighted in yellow, light blue and brown, respectively.	161
C.4	Summary of the impact of each term in the proposed theory. The dielectric medium is represented with a change in the background color. Color scheme is identical to that in Figure C.3.	165
C.5	Visual representation of different possible chain configurations. for intra- (a-c) and inter- (d-f) crosslinks. Different colors represent different chains.	167

LIST OF TABLES

<i>Number</i>	<i>Page</i>
2.1 References for Other Micro-LIPIT/Macro spherical projectile ballistic experiments on other materials	40
3.1 MPEC photoresin composition	47
3.2 LCD printing and post-processing parameters.	49
3.3 Quantified water contents in MPEC gels from TGA analysis. Using inflection points in derivative data, regions of loosely bound water evaporation and tightly bound water was determined. The cumulative total of these values is reported as the total water content (wt%).	52
3.4 XRF Counts in constant volume mapping volume across cation and pH ranges tested. Counts are reported for identical area (3.5 mm × 3.5 mm), sample thickness (2.5 mm), resolution (20 μm), and dwell time (40 ms/px) under 50kV, 600 μA conditions.	54
3.5 pH measurement of photoresin.	60
4.1 Estimated fixed charge density (f) for modeling in MPEC gels.	116
4.2 Estimated polymer chain density (N) from indentation experiments.	118

Chapter 1

INTRODUCTION

1.1 The Concept of Structural Hierarchies in Material Design

Materials are at the core of nearly every engineering application, fundamentally determining the functionality, efficiency, and performance of systems ranging from consumables and textiles to electronics, architecture, and biomedical devices. As the demands on materials grow, there is an increasing push to expand their capabilities, making them smarter, more adaptable, and capable of extreme mechanical properties. Achieving this requires materials to not only exhibit basic properties such as elasticity, plasticity, and stability but also advanced functionalities like self-healing, stimuli responsiveness, and high energy dissipation.

One promising strategy to meet these evolving demands is hierarchical structuring, the design of materials with multiscale architectures that span from a unit-level to continuum macro-scale levels. By organizing material structures hierarchically, it becomes possible to in functional material design to enhance mechanical performance and impart functional properties across multiple scales. This strategy is indeed drawing the inspiration from natural systems, where hierarchical structuring is a fundamental design principle. For instance, in plants tissue, the arrangement of cellulose fibrils, cell walls, and stacked layers enables a balance of stiffness, toughness, and anisotropic properties. Similarly, in biological systems, the hierarchical organization of DNA sequences defines protein structures, which in turn govern the functional behaviors of cells. These examples highlight how nature leverages multiscale hierarchical configurations to achieve exceptional mechanical properties and adaptability.

Inspired by these natural systems, material scientists, chemists, and engineers are increasingly adopting hierarchical structuring principles to expand the design space of engineered materials. The integration of hierarchical designs not only enhances mechanical resilience and energy dissipation but also opens pathways for designing smart materials capable of self-regulation and adaptive responses to external stimuli. Among the diverse strategies for enhancing material performance, two approaches stand out for their effectiveness in leveraging multiscale architectures: (1) structural hierarchies in architected materials and (2) hierarchical organizations in dynamic

polymers. These strategies have been instrumental in expanding the design space of materials, enabling a range of advanced functionalities from energy absorption to stimuli responsiveness.

In the next section, we delve into the efforts of two approach and how each explore how hierarchical structuring has been utilized to expand the design space and enhance the functional capabilities of modern materials.

1.2 Hierarchy in Structure Design: Architected Materials

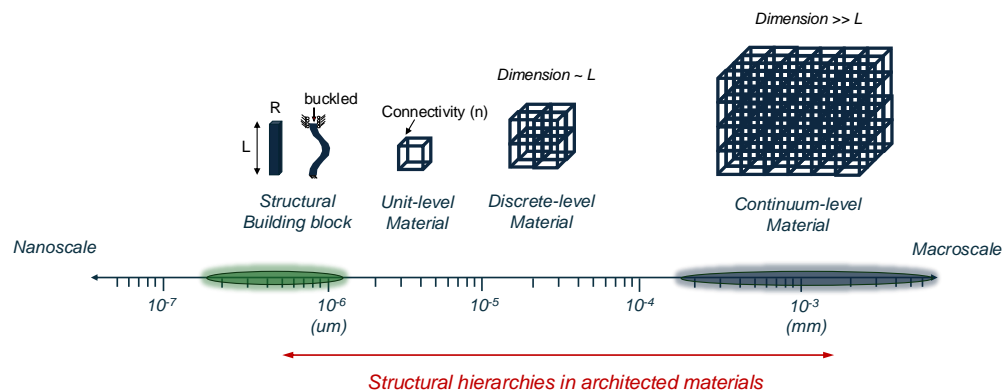


Figure 1.1: **Structural hierarchies in architected materials.**

Hierarchical structuring in architected materials enables precise control over mechanical behavior, unlocking properties that surpass those of conventional bulk materials. By leveraging multiscale geometrical features and arrangement, shown in Figure 1.1, architected materials can be tailored for ultra-low density, high energy absorption, damage tolerance, and enhanced mechanical resilience. These materials often mimic nature’s structural hierarchies—similar to how plant cell walls are architected to achieve a balance of stiffness, toughness, and anisotropy.

At the core of architected materials is the strategic design of unit cells, which determines global material properties. The hierarchical arrangement of multi-scale structural constituents, such as beam-based lattices, shell-based structures, and origami/kirigami patterns, enables tunable mechanical responses and multifunctionality. These unit cells can be engineered for periodic, stochastic, or functionally graded designs, allowing fine-tuned control over energy dissipation, impact mitigation, and reusability.

Recent advances in additive manufacturing (AM) have revolutionized the fabrication of architected materials, enabling the realization of nano-, micro-, and macroscale

hierarchical structures with unprecedented precision. The following sections discuss the fabrication techniques and mechanical properties that define these materials.

1.2.1 Fabrication Techniques

The fabrication of architected materials has significantly progressed with the advent of advanced additive manufacturing and nanofabrication techniques. These developments have enabled the creation of high-resolution structures, even at the submicron scale, expanding the design space and geometrical controllability in the architected materials.

Submicron- and Micro-Fabrication Techniques

Two-photon lithography (TPL) is widely regarded as the gold standard for fabricating nano-architected materials with submicron resolution and high pattern fidelity [1]. This maskless 3D printing technique uses a tightly focused laser beam to polymerize photosensitive resins at the voxel level, enabling the fabrication of intricate 3D lattices. TPL has been successfully used to produce high-strength nanolattices with ultralow densities, demonstrating enhanced mechanical properties [2]. However, a significant limitation of TPL lies in its serial processing nature, which results in prohibitively slow fabrication rates, making large-scale production inefficient.

For a microscale resolution, projection-based microstereolithography provides an alternative [3]. Unlike TPL's voxel-by-voxel approach, this method combines light scanning with focused image projection, enabling the fabrication of microscale lattices with feature sizes on the order of tens of microns while significantly improving fabrication speed compared to serial TPL processes.

Macro-Fabrication Techniques

Well-established additive manufacturing techniques are primarily used for macroscale architected materials, enabling the fabrication of large-volume hierarchical structures with a balance of precision and scalability. The most commonly used methods include:

- Vat Photopolymerization (VP): Techniques such as stereolithography (SLA) and digital light processing (DLP) selectively cure a liquid photosensitive resin using light exposure [4]. These methods enable the fabrication of large

sample volumes (10–100 cm³) with feature resolutions in the range of 1–10s of microns.

- **Material Extrusion:** This category includes fused deposition modeling (FDM) and direct ink writing (DIW), where materials such as thermoplastics or shear-thinning inks are extruded through a nozzle to define the printed structure. These methods offer a broad selection of printable materials but are generally limited by resolution ($\geq 100 \mu\text{m}$) due to the extrusion process [4].
- **Powder Bed Fusion (PBF):** Commonly used for metallic structures, PBF techniques such as selective laser sintering (SLS) and laser melting (SLM) achieve high-resolution lattice architectures with feature sizes down to 100s of microns over tens of millimeters [5, 6].

These fabrication approaches enable the design and realization of hierarchical structures at the macro-scale, providing an optimal balance between feature resolution and manufacturability.

1.2.2 Material Properties

By designing unit-cell geometries with precise control, it has been demonstrated to achieve desired material properties such as enhanced damage-tolerance [2], reusable energy absorption [7], and stimulus responsivity [8]. For example, nanolattices with ultra-low relative densities of 5% exploit nanoscale-induced material size effects to derive higher strengths and stiffnesses compared with their constituent material, while others can suppress brittle failure in architected materials composed of intrinsically brittle materials [9, 10]. Optimizing lattice architecture by, for example, beam- versus plate-based patterns and periodic versus stochastic geometries, enables approaching the theoretical mechanical parameter limits in engineered materials [11]. Beyond these advantageous quasi-static mechanical properties, Portela *et al.* demonstrated that nano-architected pyrolytic carbon with a relative density of 23% (i.e. 77 % porosity) can combine material-level size effects and structure-level densification mechanisms in cellular solids to mitigate impact of 14 μm -diameter projectiles traveling from 50 to 1000 m s⁻¹ with a 70% higher specific energy dissipation compared to Kevlar [12]. These hierarchical designs allow for a balance of strength and lightweight properties, making them ideal for protective systems and aerospace applications. Architected materials can also be designed for reconfigurability and stimuli-responsive behaviors. By integrating stimuli-responsive polymers

into lattice structures, researchers have demonstrated reconfigurable metamaterials capable of self-healing, shape memory, and adaptable stiffness.

1.3 Hierarchy in Material Design: Polymer Structures

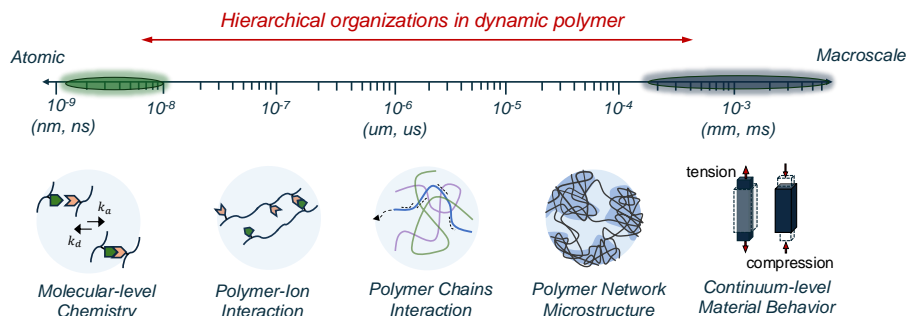


Figure 1.2: **Hierarchical organizations in dynamic polymers.**

Dynamic polymers represent a diverse and highly tunable class of materials whose properties arise from hierarchical structuring across multiple length scales, from molecular interactions to continuum-scale material responses. The ability to tailor polymer structures at different scales has led to significant advancements in mechanical tunability, environmental adaptability, and stimuli-responsive functionalities. Many biological materials, such as collagen, silk, and DNA, exemplify how molecular-scale interactions propagate to mesoscale and macroscale architectures, dictating mechanical robustness, elasticity, and self-repair capabilities. Inspired by these natural systems, synthetic polymers have been designed to incorporate hierarchical interactions to achieve desired performance characteristics.

A central approach in dynamic polymer material design is introducing dynamic bonding mechanisms, such as metal-ligand coordination, reversible covalent bonds, and hydrogen bonding, and leveraging molecular-scale interactions to program macroscale behavior such as stimuli-responsive and tunable mechanical behavior. For example, tuning the cross-linking dynamics or densities with the metal-ligand bond tunes the stiffness an order of magnitude difference [13].

To fully exploit these design principles, it is essential to understand how hierarchical configurations of dynamic polymers evolve across multiple scales. As illustrated in Figure 1.2, hierarchical organizations in dynamic polymers can be classified into four key levels:

- Molecular-level interactions – Governing bonding dynamics (e.g., metal-

ligand coordination, hydrogen bonding, ionic interactions).

- Polymer chain architectures – Dictating entanglement, crosslinking density, and segmental mobility.
- Polymer network structures – Determining viscoelasticity, fracture resistance, and processability.
- Continuum material behaviors – Governing macroscale mechanical properties such as toughness, elasticity, and responsiveness.

Since materials performances are inherently dictated by molecular structure and morphology, a deep understanding of multiscale configurations is essential. Similar to how DNA sequences encode protein structure and function, the composition and architecture of polymers dictate their bulk behavior. The following sections review some of fabrication and characterization techniques which exploiting different level design in hierarchical polymer structuring in dynamic bonds to designing mechanical properties and functional performance.

1.3.1 Design Strategies and Fabrication Techniques

Designing hierarchical polymer structures requires precise control over both temporal and spatial dimensions, which dictate material behavior and responsiveness. This control is achieved through bond kinetics, which modulate relaxation dynamics over time, and polymer morphology, which governs macroscopic properties such as stiffness, toughness, and adaptability.

Temporal control via bond kinetics

Dynamic polymer networks achieve tunable mechanical responses through reversible crosslinks that continuously associate and dissociate. By tailoring bond kinetics, these materials can transition from a soft, viscous polymer melt to a stiff, elastic solid, offering a wide range of mechanical tunability and advanced functionalities such as self-healing, shape memory, and stimuli-responsiveness.

Dynamic bonds can be broadly categorized into noncovalent interactions and dynamic covalent interactions [14]. Dynamic noncovalent interactions such as hydrogen bonding, $\pi - \pi$ stacking, host-guest interactions, ionic interactions, and metal coordination create transient, rapidly exchanging crosslinks that enable energy dissipation and adaptive mechanics [15–17]. In contrast, dynamic covalent bonds,

such as Diels–Alder reactions, thiol–Michael reactions, and boronic ester bonds, offer greater stability while retaining reversibility, allowing materials to undergo controlled reconfiguration over longer timescales [18–20]. These bonds rearrange via dissociative pathways (where bonds fully break before reforming) or associative pathways (where bond exchange occurs continuously). While distinct in mechanism, both pathways have been shown to follow similar Arrhenius-type scaling, indicating a common kinetic framework that governs their exchange dynamics [21].

The key determinant of polymer behavior is bond lifetime, which dictates network rearrangement and macroscale mechanical responses. Short-lived bonds facilitate rapid stress relaxation and viscoelasticity, while longer-lived bonds maintain structural integrity, leading to stiffer, load-bearing materials [22]. The tunability of bond association and dissociation rates enables materials to transition between these states. Achieving optimal performance requires balancing bond reversibility and stability. Strategies such as electronic and steric effects, solvent interactions, help fine-tune equilibrium constant (K_{eq}), association rate (K_a), and dissociation rate (K_d), all of which govern network morphologies and material response [23–25].

Spatial control via polymer morphologies

While bond kinetics regulate time-dependent behavior, polymer morphology plays a crucial role in defining network integrity, phase behavior, and mechanical performance. Combining network topology with dynamic bonding mechanisms allows materials to retain reversibility while significantly enhancing stability and mechanical robustness. Some of effective approaches to improve mechanical robustness in dynamic polymer systems:

Hybrid networks: Double-network (DN) hydrogels incorporate two interpenetrating polymer networks with distinct mechanical roles. A covalently crosslinked primary network provides mechanical stability and load-bearing strength, while a secondary dynamic network incorporates reversible crosslinks that break and reform under stress, dissipating energy and enhancing resilience. This interplay allows DN gels to achieve high fracture toughness and fatigue resistance, as observed in stretchable hydrogels that combine rigid, sacrificial domains with soft, extensible regions [26]. Beyond dual-network strategies, orthogonal dynamic bonding—where distinct dynamic bonds with different strengths operate independently—enables energy dissipation without significant hysteresis. Incorporating both strong covalent bonds and weaker metal-coordination bonds leads to materials with enhanced fracture en-

ergy and mechanical durability, exhibiting superior fatigue resistance under repeated loading [27].

Polymer chain architecture: Structuring entanglements allows better transmission of tension along polymer chains and across the network, improving toughness and elasticity [28]. Creating spatially varying crosslinking densities produces regions of differential extensibility and localized stiffness, enabling materials to exhibit adaptive strain localization and tunable failure modes. Beyond linear polymers, brush-like architectures, which expand polymer chain diameters and reduce entanglement density while maintaining extensibility, provide an effective strategy to decouple stiffness and stretchability. These topological optimizations enable networks to be designed with independently tunable elastic moduli and extensibility [29].

Microphase separation: Beyond molecular and chain-level configurations, microstructural heterogeneities provide an additional mechanism to program functionally graded mechanical properties in dynamic polymers. For example, incorporating block copolymers with dynamic bonds allow microphase separation enables materials to achieve tunable morphologies in response to different stimuli [30]. Beyond molecular and chain-level configurations, microstructural heterogeneities provide an additional mechanism to program functionally graded mechanical properties in dynamic polymers [31]. Even the dynamic bond immisibility at different temperature was used as a mechanism for phase separation that enables instant stiffening upon temperature applied [32].

Fabrication techniques

Fabricating hierarchical dynamic polymer networks involves a range of techniques, from traditional bulk processing to advanced additive manufacturing, each offering distinct advantages in spatial control, network formation, and scalability.

Layer-by-layer deposition (LBL): LBL is a widely used bottom-up technique for assembling hierarchical polymer structures particularly using charge interactions, with precise nanoscale control. In this approach, alternating layers of oppositely charged polymer solutions are sequentially deposited, allowing tunable crosslinking density, film thickness, and molecular orientation [33, 34]. Each deposition cycle results in a nanometer-thick layer, and the process can be repeated to construct multilayered polymer networks. This method is particularly advantageous for fabricating dynamic polymer thin films, biointerfaces, and stimuli-responsive coatings

[35]. However, LBL can be time-consuming due to the need for multiple dipping cycles and is generally limited in achieving bulk mechanical control.

Molding and injection techniques: It is widely adopted method for producing bulk hydrogels and elastomers with controlled network formation. In these processes, pre-synthesized polymers are cast into molds or injected into predefined cavities, where they undergo crosslinking via thermal, UV, or chemical curing [36–39]. This approach allows large-scale material production with controlled macroscopic shapes and bulk composition. However, conventional molding techniques often result in uniform crosslinking throughout the polymer matrix, limiting the ability to introduce spatial heterogeneities or graded architectures. Additionally, while effective for scalable production, these methods lack the precision necessary for engineering microscale and nanoscale features.

Additive Manufacturing: Recent advances in additive manufacturing have transformed the fabrication of dynamic polymers by enabling direct spatial control over structure, composition, and crosslinking density. Among AM techniques, projection-based stereolithography (SLA, DLP) and extrusion-based direct ink writing (DIW) are particularly effective for dynamic polymer fabrication. SLA and DLP leverage UV/visible-light photopolymerization to pattern polymer networks with exceptional precision, enabling hierarchical structuring down to the micron scale. These techniques allow for intricate spatial control of crosslinking density and polymer heterogeneity, though they require specialized photoinitiators and monomers with high UV sensitivity [40–42]. In contrast, DIW enables multi-material printing by extruding highly viscous polymer inks, which are subsequently crosslinked via ionic interactions, thermal curing, or UV exposure [43–45]. This method offers superior versatility for printing complex dynamic polymer architectures, including heterogeneous networks and functional gradients. However, precise rheological tuning is required to ensure consistent extrusion and prevent clogging, while structural stability must be maintained post-printing to prevent collapse.

1.3.2 Material Functionality

By leveraging spatiotemporal control through bond kinetics and polymer architecture, dynamic polymers have been tailored for specialized functionalities, including tunable mechanical properties, extreme toughness, efficient energy dissipation, stimuli responsiveness, and self-healing. Dynamic bonding strategies enable materials to transition from soft and stretchable to highly stiff and impact-resistant. The incor-

poration of multiple dynamic metal-ligand bonds allows broad damping over large frequency domains due to sequential polymer relaxation mechanisms [46]. When combined with highly entangled polymer networks, these materials achieve exceptional fracture resistance, where dynamic bonds serve as primary energy dissipation mechanisms.

Beyond mechanical performance, tunable metal-ligand coordination provides a mechanism for stimuli-responsive behavior. By selecting specific metal-ligand pairs, materials can be designed to exhibit tunable stiffness, self-healing, volumetric changes, and even optical shifts in response to environmental triggers such as pH, temperature, or mechanical stress. These adaptable properties have been harnessed in various applications, including soft robotics [13, 47–49], sensors [50, 51], and smart coatings [52–54], where reconfigurable material behavior is essential [43, 55, 56].

The reversible nature of these bonds also enables self-healing capabilities[57, 58], allowing materials to autonomously repair damage and extend their functional lifespan. Similar mechanisms facilitate adaptive adhesion, where materials reversibly adhere or detach in response to external stimuli by dynamically forming and breaking physical bonds [59, 60]. This versatility in bonding kinetics and polymer structuring establishes dynamic polymers as a powerful platform for engineering multifunctional, adaptive materials [61].

1.4 Challenges in Hierarchical Material Design

Despite significant advancements in both architected materials and dynamic polymers, several key challenges remain in realizing their full potential for scalable fabrication, multiscale characterization, and predictive modeling. These challenges must be addressed to enable more precise material control, reliable manufacturing, and systematic integration of hierarchical designs for enhanced performance.

Challenges in Scalable Fabrication

A major barrier to widespread implementation of hierarchical materials is scalable and high-resolution fabrication. While additive manufacturing (AM) has revolutionized material design by enabling complex geometries and fine structural control, existing techniques face a fundamental trade-off between resolution, printing speed, and sample volume.

- For architected materials, large-area, high-resolution fabrication techniques

are essential to transition nano-architected materials from lab-scale prototypes to functional macrostructures with tunable mechanical properties. While light-based lithography has demonstrated scalability, further developments are needed to enhance pattern fidelity, resolution, and process efficiency for manufacturing large-scale nano-architected materials.

- For dynamic polymers, a reliable and scalable synthesis platform is critical to precisely tune molecular interactions and crosslinking dynamics. Current fabrication methods for dynamic polymers often rely on multi-step fabrication or batch-based solution synthesis, which lacks spatial control over network structures. Developing photo-controlled polymerization or direct-write AM approaches would enable more localized, tunable, and high-throughput fabrication of hierarchical dynamic polymers.

Challenges in Multiscale Characterizations

A persistent knowledge gap exists in understanding how multiscale interactions, ranging from molecular dynamics to continuum material behavior, govern macroscale performance. Capturing material responses across multiple length scales presents fundamental challenges:

- Architected materials require characterization techniques that correlate unit-cell deformations and material-level responses across different scales. While in situ nanomechanics and high-speed imaging have provided insights into mechanical response and structural failure mechanisms, integrating these methods into a unified multiscale characterization framework remains a challenge.
- Dynamic polymers introduce characterization complexity due to multiscale, highly-coupled interactions among design parameters. Characterizing their bond dynamics, microstructure morphologies, phase transitions, and mechanical evolution across different time and length scales requires an integrated approach combining rheology, molecular spectroscopy, and in situ imaging techniques. No single experimental technique can fully capture the broad span of hierarchical interactions, necessitating hybrid methodologies that integrate experimental characterization across multiple scales.

Challenges in Predictive Design & Modeling

The lack of predictive modeling frameworks capable of bridging hierarchical interactions across orders of magnitude hinders the rational design of hierarchical

materials.

- For architected materials, existing models often treat structures as continuum approximations, which may not accurately capture local deformations, instabilities, and failure mechanisms in nano-architected materials. Advanced finite element models (FEM) and data-driven approaches, such as machine learning-assisted structure-property predictions, are needed to optimize architected material designs for energy dissipation, resilience, and impact resistance.
- For dynamic polymers, traditional viscoelastic models fail to incorporate bond-exchange dynamics, molecular relaxation, and network reconfiguration under external stimuli. Developing multiscale computational models—such as coarse-grained molecular dynamics (MD) simulations coupled with continuum mechanics models—would enable predictive design of tunable polymer networks with programmable mechanical and functional properties.

To address these challenges, a comprehensive approach that integrates scalable fabrication, multiscale characterization, and modeling should be developed to effectively design hierarchical materials with tunable functionalities.

1.5 Chapter Outlines

This thesis addresses some of the multiscale challenges in hierarchical material design (Section 1.4). The work explores how hierarchical structuring, spanning molecular interactions to macro-scale architectures, can be leveraged to achieve tunable and enhanced material properties. By integrating novel fabrication and characterization techniques, we investigate how structural hierarchies—ranging from molecular interactions to macro-scale architectures—can be strategically employed to achieve enhanced and tunable material properties. The subsequent chapters systematically investigate these themes, providing experimental findings and analytical insights based on scalable fabrication techniques and multiscale material characterization.

Chapter 2 focuses on the creation of structural hierarchies within architected materials through the use of two-photon lithography and holographic lithography. These methods enable precise control over unit cell length scales and allow for the tessellation of these units into macroscale domains. The chapter presents a comprehensive study on how geometrical parameters, such as relative density and beam

aspect ratio, influence stiffness, energy absorption, and failure mechanisms. By employing metamask-based holographic lithography, we demonstrate the ability to fabricate nano-architected sheets with high specific energy dissipation and impact resistance, highlighting the role of hierarchical structuring in enhancing mechanical performance. The findings in this chapter provide critical insights into the design principles required for scalable manufacturing of functional architected materials.

Chapter 3 investigates the role of dynamic crosslinkers in shaping the mechanical properties of constituent polymers through a hierarchical organization spanning molecular, nano, micro, and macro levels. By examining multiscale interactions and their propagation across these levels, this chapter reveals how molecular-level dynamics significantly influence macroscale material responses. The study employs a combination of experimental techniques and multiscale modeling to elucidate the coupling mechanisms between dynamic bonding and material stiffness, energy dissipation, and deformation modes. The results underscore the importance of hierarchical structuring in tuning mechanical responses and offer a framework for designing responsive materials that leverage multiscale phenomena for enhanced functional performance.

Building on the insights from Chapter 3, Chapter 4 explores how the multiscale knowledge of hierarchical interactions can be leveraged to design functional materials with tailored properties. This chapter presents strategies for manipulating material functionality at the global scale by controlling molecular interactions and microstructural arrangements. Key case studies include the design of materials with programmable buckling deformation, stimuli-responsive shape transformation, and guided dissolution. By integrating experimental findings with theoretical modeling, we demonstrate how multiscale design principles can be systematically applied to optimize material performance for specific functionalities. The chapter concludes by highlighting the potential of hierarchical structuring in advancing the field of additively manufactured functional materials.

Finally, Chapter 5 offers a concise summary of the findings presented in this thesis, emphasizing the role of hierarchical structuring in expanding the design space and controlling mechanical responses in nano-architected and dynamic polymer-based materials. The chapter also outlines future research directions focusing on the additive manufacturing of functional soft materials, the challenges of scalable fabrication, and the potential for multiscale modeling to further refine the design of hierarchical materials. I hope the insights gained from this thesis contribute to pave

the way for the development of advanced materials with enhanced functionality and adaptability.

LARGE SCALE, NANO-ARCHITECTED POLYMERS

This chapter has been adapted from:

M. Kagias[†], S. Lee[†], A.C. Friedman[†], T. Zhang, D. Veysset, A. Faraon & J.R. Greer*. “Metasurface-Enabled Holographic Lithography for Impact-Absorbing Nanoarchitected Sheets”. *Advanced Materials* **35**, 2209153 (2023). DOI: [10.1002/adma.202209153](https://doi.org/10.1002/adma.202209153)

Contributions: S.L. designed the experiments, performed experimental characterizations, analyzed the results, and wrote the manuscript.

2.1 Chapter Summary

This chapter explores the role of structural hierarchies in enhancing the mechanical performance of architected materials—a class of metamaterials that leverage tessellated multiscale geometrical features to achieve unconventional properties such as ultra-low density and high energy absorption. In particular, we focus on nanoarchitected polymeric materials that exploit size-dependent mechanical effects at the unit cell level and extend these effects into complex structural designs over macroscale domains.

A significant challenge in realizing the potential of these materials lies in the development of scalable fabrication techniques capable of producing sub-micron resolution features over large areas. To address this limitation, we developed a holographic lithography-based fabrication technique utilizing laser exposure of phase metasurface masks to pattern negative-tone photoresists. This approach enables the production of nanoarchitected sheets with thicknesses of 30 to 40 μm , lateral dimensions of $2.1 \times 2.4 \text{ cm}^2$, and an intricate 3D brick-and-mortar-like lattice structure with strut widths of 500 nm and overall porosity ranging from 50% to 70%.

Nanoindentation arrays across the entire sample reveal that the in-plane elastic modulus varies between 300 MPa and 4 GPa, with post-elastic deformation initiating

through mechanisms such as individual nano-strut buckling, layer densification, shear band formation along perturbation perimeters, and tensile cracking. Further analysis of geometrical parameters highlights the relative ratio and relative density as critical factors in determining overall material stiffness and deformation behavior.

To assess energy dissipation capabilities, we performed laser-induced particle impact tests (LIPIT), which revealed a specific inelastic energy dissipation of 0.51-2.61 MJ kg⁻¹. These values are comparable to high-impact energy-absorbing materials such as Kevlar/polyvinyl butyral (PVB) composites, polystyrene, and pyrolyzed carbon nanolattices with 23% relative density.

These results underline the potential of holographic lithography as a scalable platform for fabricating nano-architected materials with impact-resistant capabilities, while preserving the multiscale correlations between unit cell design and bulk material properties. By demonstrating how structural hierarchies can control mechanical properties across different length scales, this chapter establishes a foundation for exploring hierarchical structuring as a key design principle in the development of functional materials.

2.2 Introduction

Holographic lithography has been demonstrated as a viable platform for rapid and scalable manufacturing of nano-architected materials [1–4]. This technique fundamentally relies on the interference of light to generate three-dimensional patterns, which are subsequently imprinted into a photosensitive polymer. The interference patterns can be either achieved by multiple independent light beams or by the use of a diffractive mask that splits a single incoming beam into multiple diffracted orders that interfere coherently. Several approaches to holographic lithography have been explored for fabricating nano-architected structural materials. For instance, Bagal *et al.* employed 3D colloidal nano-lithography[5] to produce 1 μm thick nano-structured metal oxide films [6] with the out-of-plane elastic moduli of 1.19 GPa and specific energy dissipation of 0.32 MJ kg⁻¹, defined as energy dissipated per unit mass. This approach utilized a single layer of colloidal nanoparticles as a phase shifting photolithographic mask. This allows for cost-effective and scalable fabrication of nanoarchitected sheets. However, the fidelity of the achievable patterns was significantly constrained by the use of spherical nanoparticles. Another noteworthy example is the work of Bae *et al.* who utilized a binary phase-modulating photomask to fabricate 4 \times 4 in² regions with 600 nm periodic patterns in 10 μm thick negative

tone photoresist through a single laser exposure [7]. Despite its effectiveness, a major limitation of binary phase masks is the limited control over the generated pattern morphology, stemming from their inherently low diffraction efficiencies. In contrast, Kamali *et al.* demonstrated through numerical simulations that optical metasurfaces—or metamasks, as referred to in this work—could generate complex 3D nano-architectures [8] that are unattainable with conventional diffractive optics. Metasurfaces consist of subwavelength features that locally modulate the phase of incoming light, with the potential for polarization-selective phase modulation. This capability enables the generation of intricate patterns, such as gyroid, rotated cubic, and diamond structures, which are not feasible with traditional diffractive masks [8]. However, the experimental realization of such patterns and the application of optical metasurfaces in holographic lithography remain largely unexplored. In this work, we present a scalable fabrication pathway based on holographic lithography for creating nano-architected materials with high specific energy dissipation, making them ideal for impact mitigation applications. Unlike previous implementations of holographic lithography, our approach leverages optical metasurfaces to expand the design space of possible nano-architectures, thereby enhancing the mechanical performance and energy absorption capabilities of the resulting materials.

2.3 Scalable Fabrication: Metasurface-based Holographic Lithography

To fabricate nano-architected materials with macroscopic lateral dimensions, we developed a customized laser scanning lithographic system (Figure 2.1a). The system was utilized to expose 1 mm thick 2×2 in² soda-lime glass slides coated with a layer of 30 to 40 μm negative tone epoxy based photoresist (SU8 2050), which was sensitized for 532 nm light and deposited by spin-coating. The system consists of a two-dimensional high-precision linear piezo-stage and a laser beam of wavelength 532 nm. The beam is directed orthogonally to the scanning plane of the stage, which sequentially rasters the metamask placed in direct contact with the photosensitive material, under the fixed laser beam (Figure 2.1b). This scanning approach enables scalable fabrication of samples with macroscale lateral dimensions, accommodating a wide range of metamask sizes.

Laser exposure parameters

As the laser exposure dose is a critical factor in determining the final geometrical resolution and the degree of crosslinking of the constituent material, we optimized the process by controlling the laser beam width w , the stage scanning speed v ,

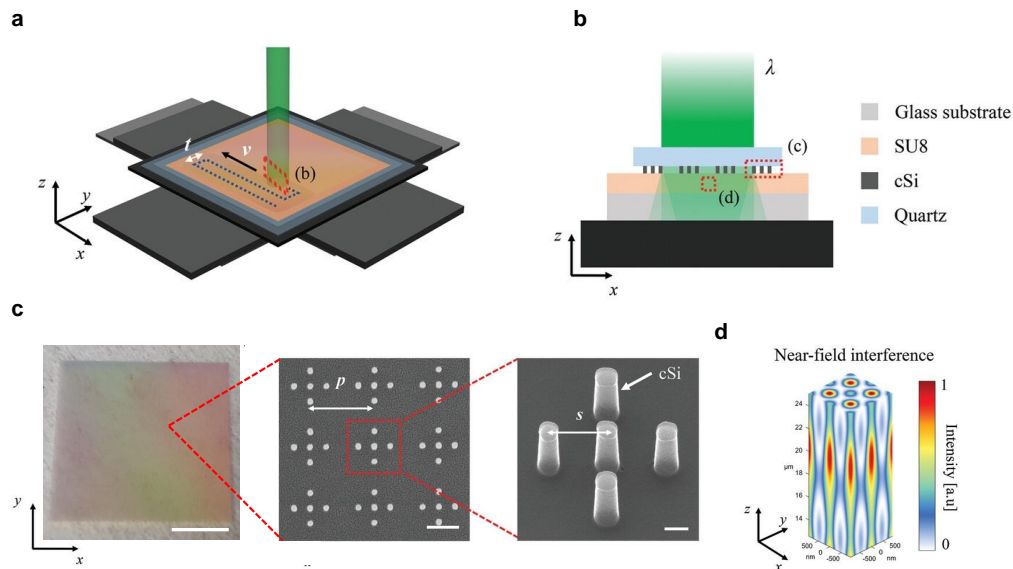


Figure 2.1: **Metasurface based holographic lithography.** **a**, Schematic representation of the lithographic setup. The scanning trajectory of a laser beam is highlighted by the dashed blue line. **b**, The metasurface is placed directly on top of the sample substrate covered with SU8 photoresist. The metamask diffracts the incoming laser beam and creates a near field 3D intensity distribution within the photoresist. **c**, The fabricated metamask (scale bar 5 mm). Insets represent a top-view helium ion microscope (HIM) image of the utilised metamask (scale bar 450 nm) and a zoomed-in tilted HIM image of the outlined region (scale bar 100 nm). **d**, Near field 3D intensity modulation generated by the fabricated metamask design, color represents light intensity normalized by the maximum intensity.

and the scanning step size t between sequential lines. The accumulated exposure dose, defined as $D = P/vt$, where P is the beam power, was uniformly distributed over the metamask (see Appendix A.1). For our experiments, we utilized laser powers in the range of 0.23 to 0.25 W, the line spacing t of 0.4 mm and the scan speed u of 1.5 mm/s, resulting in exposure doses between 0.38 to 0.41 J/mm². The printing of 3×3 cm² with feature resolution of 100s of nm took a total time of 24 minutes, demonstrating the efficiency of this method. The exact geometry of the resulting pattern was directly linked to the 3D intensity distribution generated by the metamask.

Metamask fabrication

The metamask we utilized is fabricated based on 300 nm c-Si on Quartz wafer. A 300 nm thick layer of e-beam positive resist ZEP 520A (Zeon Corporation) is spin coated on the chip. A 100 keV electron beam lithography system (Raith EBPG

5200) is used to generate the metasurface mask pattern. The pattern is developed in a developer (ZED-N50, Zeon Corporation). A 50 nm layer of Al_2O_3 is deposited using e-beam evaporator to reverse the generated pattern by lift-off process. Then the transferred Al_2O_3 pattern is used as a hard mask for $\text{SF}_6/\text{C}_4\text{F}_8$ dry etching of silicon (Oxford Plasmalab System 100). After that, the Al_2O_3 is removed by 1:1 ammonium hydroxide and hydrogen peroxide at 80 °C. Finally, a 2 μm layer of SU8 is spin coated on top of the metamask for protection. The fabricated metamask was composed of an array of 900 nm-spaced face-centered unit cells of five 115 nm-diameter 300 nm-tall crystalline Si nano-pillars spaced at $s = 225$ nm on top of 1 mm thick Quartz substrate. Figure 2.1c contains scanning electron microscopy images (SEM) of a 3×3 array of unit cells spaced by distance $p = 900$ nm (top view) and a zoomed-in view of a single unit cell (45° tilt view). The metamask covered a patterned area of 2.1×2.4 cm² and was fabricated by electron beam lithography and deep reactive ion etching as described in the experimental section. The utilized metamask generates a near field interference pattern that resembles struts organized in layered 3D brick-and-mortar-like patterns as shown in Fig. 2.1d. The light intensity pattern was calculated by finite difference time domain (FDTD) and angular spectrum propagation simulations.

Polymerization and Post-processing

Cationic polymerization was performed using the negative photoresist SU8. The SU8 was sensitized with a visible light sensitizing system, HNu 470 and HNu 254 (at mass ratio of 0.53% and 4.66%, respectively, in a 70% solids resist). The resist was spun-coated onto substrates with adhesion layers at 3000 rpm for 30 seconds to produce 40 μm uniform coatings. The sample was then pre-baked at 65 °C for 10 minutes and then at 95 °C for 30 minutes. Upon laser exposure, photoacid was generated from an onium salt-based visible light photoinitiator in concentrations proportional to exposure intensity. Following exposure, the sample was post-baked at 65°C for 270 s to promote the photoacid and polymer chain diffusion necessary for cationic polymerization of the oxirane rings. The sample was subsequently developed by suspending it inverted in a bath of propylene glycol monomethyl ether acetate (PGMEA) for 2 hours. After development, the samples were washed in a series of baths to perform a solvent exchange from PGMEA to isopropanol (IPA). After ≈ 1 hour in 100% IPA, the samples were air dried.

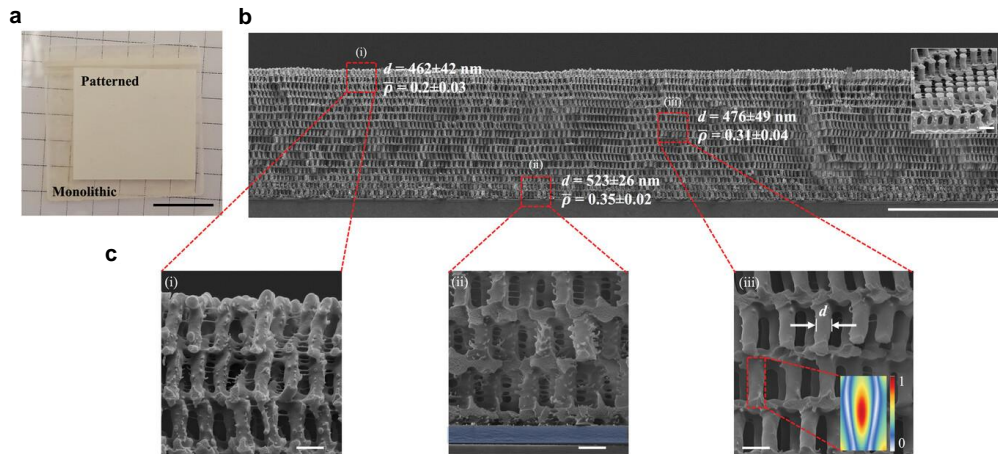


Figure 2.2: Morphology and pattern fidelity. **a**, A top view photo of the fabricated sample. White square in the middle corresponds to the patterned area, whose appearance is opaque (scale bar 1 cm). **b**, Scanning electron microscopy (SEM) image showing a typical cross section of the fabricated material. A clear pattern transfer is observed throughout the entire sample thickness (scale bar 25 μ m). The inset shows the beam arrangement within a single layer (scale bar 1 μ m). **c**, A zoomed-in SEM image of the cross section showing the generated beam structure and difference in diameter d . The blue area in (ii) corresponds to the adhesion layer (scale bar 1 μ m).

2.4 Microstructural Characterization

Figure 2.2 shows a photograph of a typical 30 μ m-thick nano-architected sheet produced via this process patterned over the area of 2.1×2.4 cm² on a glass substrate. The opaque region of the sheet corresponds to the nano-architected material, and the translucent periphery corresponds to the monolithic unpatterned SU8. The white appearance of the sheet is attributed to its strong scattering over a broad band of visible light wavelengths. Cross sectional SEM images demonstrate that the pattern was preserved and successfully developed throughout the thickness of the material (Figure 2.2b), with the resulting architecture of brick-and-mortar arrangements of beams, with each horizontal layer shifted by half a period in both lateral directions respective to the underlying one (Figure 2.2b inset). The SEM images reveal a lateral periodicity of 900 ± 10 nm, which matches the periodicity of the metamask, and a vertical periodicity of 1.62 ± 0.02 μ m, which is 30% lower than the periodicity of 2.39 μ m predicted by finite difference time domain simulations (shown in Figure 2.1d). Based on the cross-sectional images at different depths throughout the sample (Figure 2.2c), the beam diameter d increases by approximately 15% from the sample surface to base. The average beam width varied between 462 ± 42 nm in the top

layers to 523 ± 26 nm in the bottom layers. The unit cells in the upper 20% of the sample height have a fully open-cell morphology (Figure 2.2c (i)), the unit cells in the center region and below (Figure 2.2c (ii) & (iii)) preserve the laterally open-cell morphology but lose the vertical interconnectivity. Based on the measured beam diameters we estimate that the relative density (volume fraction) $\bar{\rho}$ to vary between 0.2 and 0.35 throughout the thickness of the material.

2.5 Quasi-static Characterization

To assess the mechanical properties of the nano-architected materials, we performed quasi-static mechanical characterization at a strain rate of approximately $\dot{\epsilon} \sim 10^{-4}$ s⁻¹ using nanomechanical testing techniques. Given the large separation of scales between the nano-sized unit cells and the macroscale tessellated brick-and-mortar structure, we initially examined the collective response of multiple unit cells to capture properties that more closely resemble the continuum behavior of the material.

2.5.1 Ex-situ Nanomechanical Indentation

Nanoindentation experiments were conducted with a G200 XP Nanoindenter (KLA). As shown in Figure 2.3a, the nano-architected SU-8 sheets remained attached to the glass substrate during testing. To probe the effective behavior of the overall architected material rather than individual unit cells, we employed a flat-ended cylindrical punch with a 100 μ m diameter, which compressed approximately 7,850 unit cells per test. The samples were indented to a maximum displacement of 12 μ m at a displacement rate of 20 nm s⁻¹, corresponding to a strain rate of $\dot{\epsilon} = 10^{-4}$ s⁻¹. To minimize the influence of time-dependent viscoelastic effects, the indenter was held at the peak load for 100 seconds before unloading. Continuous stiffness measurement (CSM) technique, which imposed 2 nm displacement oscillation amplitude at a frequency of 45 Hz, was utilized to detect an initial contact between the indenter tip and the sample and quasi-continuously measure contact stiffness as a function of depth. For all experiments, the effective elastic modulus was extracted by analyzing the continuous stiffness at the depth of 10% of the sheet thickness (~ 3 μ m after the full contact) following the Oliver-Pharr method [9].

2.5.2 Mechanical Response of Architected Materials

A representative indentation load vs. displacement curve is presented in Figure 2.3b, revealing three distinct mechanical response regimes: (1) an initial linear elastic regime up to a strain of 0.13 followed by (2) a plastic deformation regime with a

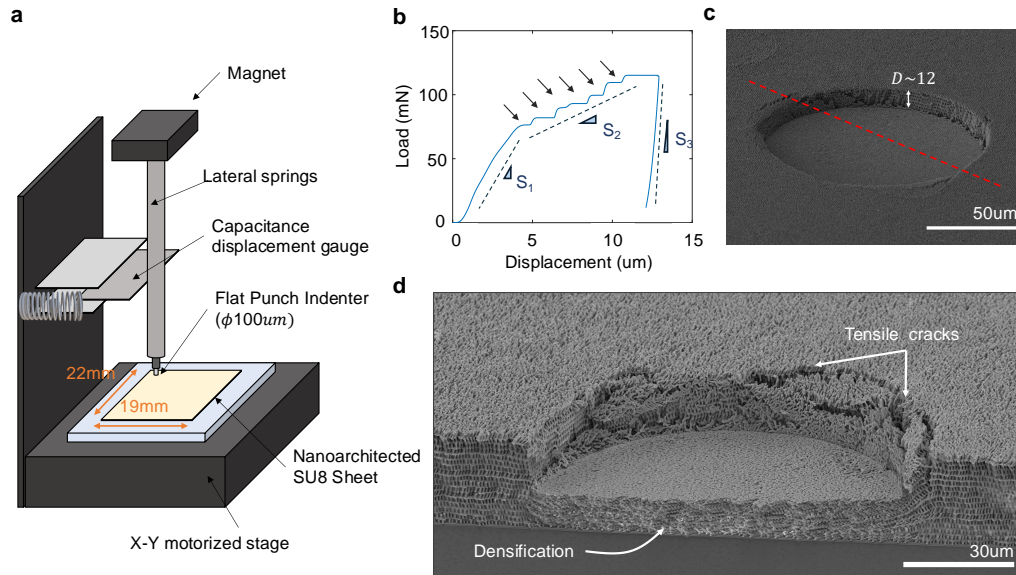


Figure 2.3: **Quasi-static nanoindentation characterization.** **a**, Schematic representation of Nanoindenter setup. **b**, Representative load-displacement response of the nanoarchitected material during compressive indentation with a $100\ \mu\text{m}$ -diameter flat punch at a strain rate of $\dot{\epsilon} \sim 10^{-4}\ \text{s}^{-1}$. The dashed lines represent the slopes of the initial elastic loading, plateau-like response, and the upper 30% of the unloading data segment. The arrows in the plateau region depict a series of displacement bursts that correspond to the collapse of individual structural layers and crack formation. **c**, SEM image of the representative indentation mark after the nanomechanical experiment, with the intended cross-sectional plane denoted by the red-dashed line (tilt 30°). **d**, SEM image of a cross-section through a $12\ \mu\text{m}$ -deep and $100\ \mu\text{m}$ -wide residual impression of the indentation mark.

gradually increasing load plateau and discrete displacement bursts up to a strain of 0.37 and (3) partial elastic recovery of 0.027 strain during unloading. The stiffness of the material in each regime, calculated as the slope of load and displacement, is indicated by the dashed lines in Figure 2.3b. This analysis revealed that the post-yield regime has a plateau-like response, characterized by a $\sim 75\%$ lower slope (S_2) compared with that in the initial elastic regime (S_1), a pronounced step-like behavior, containing a series of discrete displacement bursts, indicated by arrows in Figure 2.3b, and strain hardening. This response is attributed to indentation-induced shear stresses arising from the boundary constraints of the cylindrical punch and the densified layers beneath the indentation mark. The unloading curve indicates the significant amount of plastic deformation with the slope (S_3) being $\sim 720\%$ stiffer than the initial elastic stiffness. The full post-indentation impression mark is shown in Figure 2.3c and confirms the inclusion of multiple unit cells across the flat

punch diameter and the establishment of full parallel contact between the tip and the sample surface. The cross-sectional SEM image of the indentation imprint shown in Figure 2.3d shows that 5 to 8 layers collapsed within the densified region beneath the indenter tip and that plastic deformation was largely confined to the crushed area. Within these densified layers, nano-struts in the same layer were observed to buckle in the same direction, which alternates across the depth. This behavior suggests the presence of strong shear stresses during compressive loading. Additionally, we observed the formation of tensile cracks around the contact perimeter, indicating the development of tensile membrane stresses on the sample surface. Shear-off along the imprint perimeter occurred through severe plastic deformation, followed by deeper penetration of fracture as the load increased [10, 11].

2.5.3 In-Plane Inhomogeneity Across the Large-scale Sheet

Given that the nano-architected structures span across the macroscale, ensuring in-plane material homogeneity is essential for maintaining consistent mechanical behavior.

Spatial Mapping of Stiffness

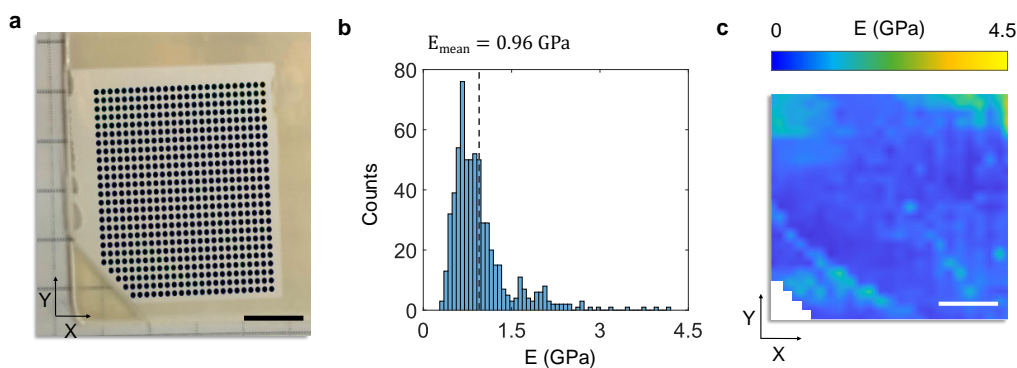


Figure 2.4: **Spatial Mapping of Stiffness Across Macroscale Architected SU8 Sheet.** **a**, Indentation mapping of the 25×25 indents conducted on the nano-architected SU8 sheet. An array of dots represents individual indents located on a $820 \mu\text{m}$ in X $840 \mu\text{m}$ in Y Cartesian grid across the sheet (scale bar 6 mm). **b**, Distribution of experimentally measured elastic modulus with an average of 0.96 GPa and a standard deviation of 0.52 GPa. **c**, Spatial mapping of in-plane modulus across the sheet (scale bar 6 mm).

To assess the mechanical uniformity across the entire sample, we performed a series of nanoindentation tests at an average spacing of $820 \mu\text{m}$ in X and $840 \mu\text{m}$ in Y on a 25×25 Cartesian grid across the sheet (Figure 2.4a). As aforementioned, the

effective indentation modulus was calculated using the Oliver-Pharr method [9] at a depth of 10% of the sheet thickness ($\sim 3 \mu\text{m}$ after the full contact) to minimize the substrate effects. The histogram in Figure 2.4b shows that the average elastic modulus across the entire sample is 0.96 ± 0.52 GPa, with a range of 300 MPa to 4 GPa. The distribution exhibits a right-skewed tail that approaches the modulus range of monolithic SU-8, reported to vary between 3.5 GPa and 6 GPa [12–17]. This right skewed histogram reveals that $\sim 88\%$ of the indents fall within a modulus range of 300 MPa to 1.5 GPa. Within this range, the distribution is more symmetric, with an average modulus of 0.80 GPa and a standard deviation of 0.25 GPa. According to the spatial modulus map in Figure 2.4c, the modulus uniformity is relatively consistent in the center of the sample, whereas stiffer regions are predominantly distributed near the edges. This observation suggests that edge effects or potential process-induced variations may contribute to the increased stiffness near the boundaries.

Stiffness Variation from Metamask Inhomogeneity

To understand the root cause of in-plane stiffness variations in the architected SU-8, we examined the diffraction efficiency, α , of the metamask by measuring the intensities of the zeroth and first diffraction orders (Appendix A.2).

The results in Figure 2.5a show that the observed mechanical pattern traces the diffraction landscape of the metamask, suggesting a strong correlation between the mechanical properties and the diffraction efficiency of the metamask. Specifically, regions with higher diffracted intensity exhibited greater stiffness. Two different sample locations, A and B, marked by black stars in Figure 2.5a, were identified to receive $\alpha \approx 0.85$ and $\alpha \approx 0.37$, which induces the modulus of 2.07 GPa and 0.73 GPa, respectively. Further analysis of the transmitted and diffracted intensities of the metamask in the marked locations reveals that the region with $\alpha \approx 0.85$ received an approximately 27% higher optical dose compared to the region with $\alpha \approx 0.37$.

This local variation in diffraction intensity and optical dose is likely to induce a non-uniform cross-linking in the underlying polymer and microstructural variations. As shown in Figure 2.5b, two locations A and B exhibit different relative densities, with stiffer regions having a higher relative density. The increased exposure is likely to result in a larger volume of cross-linked polymer, effectively filling more space and enhancing stiffness.

The laser power also significantly affects the intrinsic elastic stiffness of the material. To evaluate the extent of laser power on affecting intrinsic material properties, we

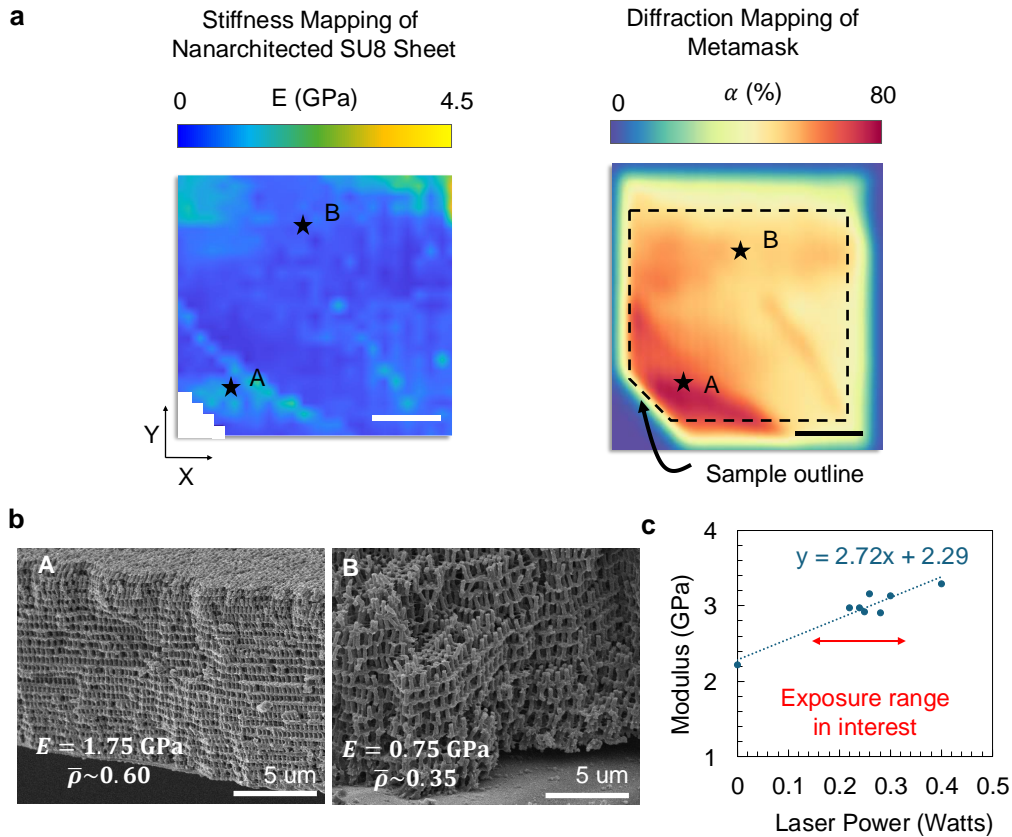


Figure 2.5: **Stiffness Variations Correlation to Metamask Inhomogeneity.** **a**, Spatial mapping of in-plane modulus across the sheet (left) and the corresponding metamask diffraction efficiency map over the same area (scale bar 6 mm). **b**, SEM images of the samples at two distinct locations, A and B. **c**, The effects of laser power on the constituent material properties. Stiffness was measured from the unpatterned, monolithic SU8 crosslinked with a different laser power attainable in the actual patterning process.

prepared unpatterned, monolithic SU-8 samples polymerized under different laser powers and measured their stiffness. Figure 2.5c demonstrates a strong correlation between laser power and elastic stiffness with a proportional relation.

Since the elastic modulus of a cellular material is influenced by both structural dimensions and the intrinsic properties of the constituent material, [18, 19]

$$E = f(\bar{\rho})E_s, \quad (2.1)$$

it is crucial to establish a precise correlation between these design factors and the diffraction efficiency (α) of the metamask.

Realistically, achieving a fully uniform diffraction pattern on the macroscale metamask is highly challenging due to the fabrication inconsistencies and the sensitivity

of diffraction efficiency to nano-scale defects. FDTD simulations (Figure 2.6) reveal that even small deviations in the nano-pillar width (e.g., ~ 5 nm or $\sim 5\%$ from the nominal width of 115 nm) can result in up to a three-fold increase in diffraction efficiency, emphasizing the practical complexity of maintaining uniformity across the metamask surface.

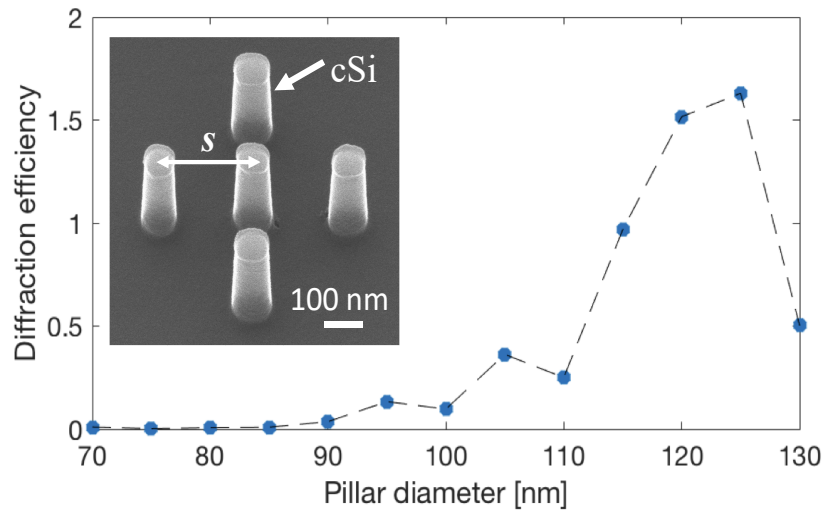


Figure 2.6: **Simulated diffraction efficiencies for varying nano-pillar width.**

Therefore, we decide to evaluate more fundamental understanding in what extent geometrical variations in mechanical properties so that we can understand the role of structural design in shaping the overall mechanical performance of nano-architected materials. The next section, we conduct a detailed study on how variations in geometrical design, particularly relative density and beam aspect ratio, affect stiffness, energy absorption, and failure mechanisms.

2.6 Effects of Structural Designs: Relative Density and Beam Aspect Ratio

2.6.1 Two-Photon Polymerization for Variations in Unit Cell Design

While metasurface-based holographic lithography provides a scalable approach for fabricating nano-architected materials, systematic variation of geometric parameters remains challenging due to the predetermined beam morphology imposed by the metamask. The multi-step metamask fabrication process makes it cumbersome to systematically modify design parameters. To overcome this limitation, we employed two-photon polymerization (2PP) direct laser writing using the Photonic Professional lithography system (Nanoscribe GmbH). Though less efficient for large-scale fabrication, 2PP enables precise control over geometric parameters with-

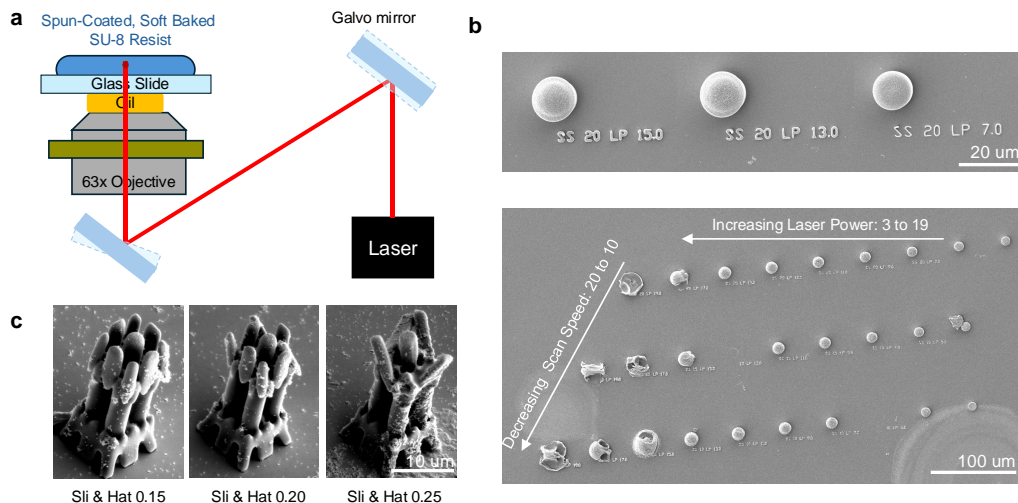


Figure 2.7: Two Photon Lithography for SU8 Photoresist. **a**, Schematic representation of the 2PP lithographic setup featuring the galvo scanning mode and oil immersion configuration. **b**, The effect of variations in scan speed (SS) and laser power (LP) on the SU-8 photoresist. Lower SS combined with high LP resulted in overexposure and, in some cases, explosive delamination due to excessive heat generation. **c**, The effect of variations in slicing and hatching distances on 2PP voxel conditions. Larger slicing and hatching distances reduced the printing time but compromised structural integrity and weakened the interfaces between subcomponents within the design.

out requiring a metamask, making it an ideal platform for systematically exploring variations in unit cell design.

The lithography process followed the same sample preparation protocol described previously, including spin-coating and post-baking steps. A soft-baked SU-8 thin film was placed in an oil immersion configuration for exposure (Figure 2.7a). Given the unconventional use of 2PP for SU-8, extensive optimization of printing parameters was necessary to achieve high-fidelity structures. As shown in Figure 2.7b, a lower scan speed (SS) combined with higher laser power (LP) resulted in overexposure and, in extreme cases, explosive delamination due to localized overheating of the photoresist. Through systematic tuning, the optimized printing parameters were identified as SS = 40 and LP = 3 (galvo scanning mode).

Additionally, slicing and hatching distances, which define the spacing between neighboring voxels, were optimized to 0.15 to maintain structural integrity and ensure interfacial cohesion (Figure 2.7c). The precise control afforded by this method enabled systematic exploration of geometrical parameters, particularly relative den-

sity and beam aspect ratio, providing valuable insights into the relationship between design and mechanical performance.

2.6.2 In-situ Nanomechanical Compression

The fabricated architected structures were characterized under quasi-static compression at a strain rate of $\sim 10^{-4} \text{ s}^{-1}$ to evaluate their mechanical behavior. Unlike ex-situ nanomechanical indentation, uniaxial compression was performed using a flat punch (100 μm diameter) mounted on a nanoindenter (InSEM, Nanomechanics Inc.) installed within an SEM (FEI Quanta 200F). This setup enabled in-situ imaging of deformation mechanisms throughout the experiment.

Compression was conducted under displacement control until full densification. Stress is calculated using $\sigma = F/A$, where F and A is the initial cross-sectional area (footprint of the sample) perpendicular to the loading direction. Engineering strain (ϵ) was determined by normalizing displacement by sample height. Effective elastic modulus (E) was extracted between strains of 0.01 and 0.04 to avoid artifacts from initial contact misalignment, and yield strength (σ_y) was measured using the 0.2% offset method.

2.6.3 Mechanical Response of Architected Materials

Relative Density

Relative density, $\bar{\rho}$ of architected material quantifies the fraction of unit cell volume occupied by solid material. As seen in Figure 2.5b, the large-scale fabricated sample exhibited relative density variations from 0.35 to 0.60. To systematically investigate the effects of $\bar{\rho}$ on mechanical performance, 3-by-4 tessellated samples with $\bar{\rho}$ ranging from 0.37 to 0.72 were fabricated using 2PP (Figure 2.8). At low $\bar{\rho}$, the samples remained open-cell, but as $\bar{\rho}$ increased, the structures gradually transitioned to closed cell morphologies at $\bar{\rho} \sim 0.72$.

In-situ quasi-static compression tests measured stress-strain responses (Figure 2.12a). At low $\bar{\rho}$, the material exhibited plateau stress indicative of buckling and layer collapse, followed by densification [20]. With increasing $\bar{\rho}$, the plateau stress became less apparent, and strain hardening occurred throughout compression.

Elastic modulus, E , and yield strength, σ_y , were determined from stress-strain curves (Figure 2.12b) and followed the expected scaling relations. Typically, strength and modulus in architected materials scale with relative density as:

$$E = BE_s(\bar{\rho})^m, \quad (2.2)$$

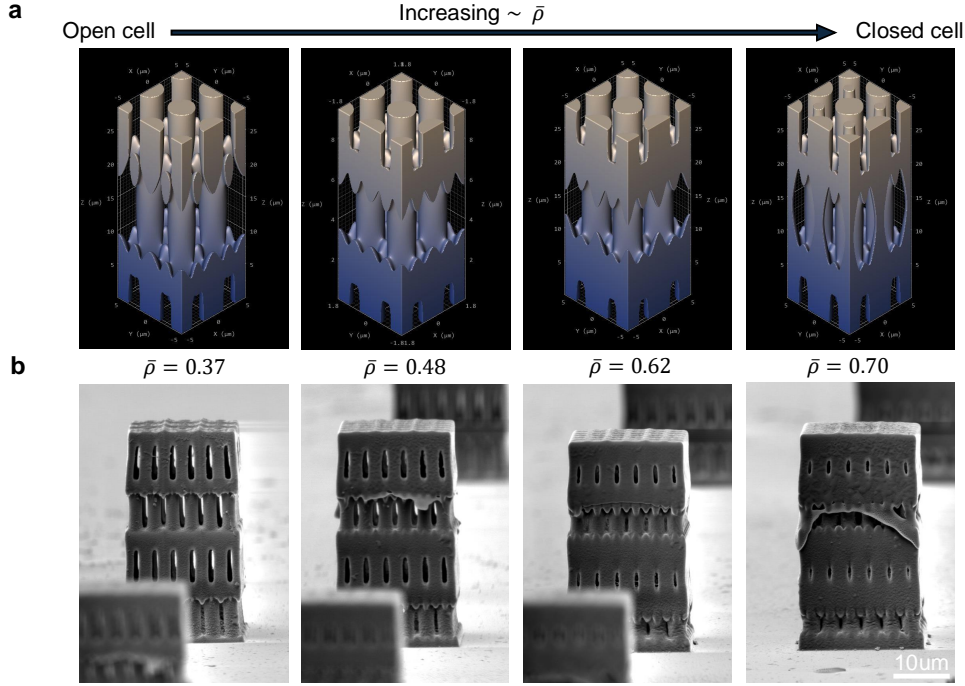


Figure 2.8: **Variations in Relative Density ($\bar{\rho}$) for Small Lattice SU8.** **a**, CAD models of unit cells illustrating different morphologies with varying relative densities. **b**, SEM images of 3-by-3 SU8 lattices fabricated using 2PP lithography, showing variations in relative density across different samples.

$$\sigma_y = C\sigma_y s(\bar{\rho})^n, \quad (2.3)$$

where E_s and σ_y are the constituent material's elastic modulus and yield strength, respectively; B and C are geometry-dependent proportionality constants, and m and n are scaling coefficients [21].

We found that the experimentally measured stiffness in our polymeric structures scales nearly linearly ($m = 1.12$) with relative density, as shown in Figure 2.10c, while the yield strength follows $\sigma_y \sim \bar{\rho}^{1.56}$. In the linear elasticity regime, where microscopic strain remains below the elastic limit of the constituent material, the scaling coefficients for a bending-dominated structure—where deformation is predominantly bending rather than stretching—are theoretically predicted as $m \sim 2$ and $n \sim 1.5$ [22]. Due to the relatively high $\bar{\rho}$ of our samples compared to conventional cellular solids ($\bar{\rho} \leq 0.3$), stiffness exhibits a weaker dependency on $\bar{\rho}$, whereas strength follows the expected scaling relation more closely.

In polymeric nano-architectures, first mode, Euler beam buckling beams serves as the dominant failure mechanism. Due to residual stresses from the substantial post-buckling deformation, materials generally have limited recovery [21]. As

shown in Figure 2.10a, post-compression SEM images indicate that the structures primarily undergo plastic deformation with minimal recovery. The stress-strain curves suggest that deformation modes shift with $\bar{\rho}$: at lower $\bar{\rho}$, the structures exhibit layer-by-layer collapse, whereas at higher $\bar{\rho}$, the failure mode transitions toward a more uniform barreling deformation. Recent studies [23] suggest that deformation mode is influenced not only by $\bar{\rho}$ but also by unit cell morphology, particularly transitioning from polymer columnar structures (at low $\bar{\rho}$) to closed-cell (porous) architectures (at high $\bar{\rho}$). The viscoelasticity of SU-8 likely contributes to the observed ductile load-displacement behavior.

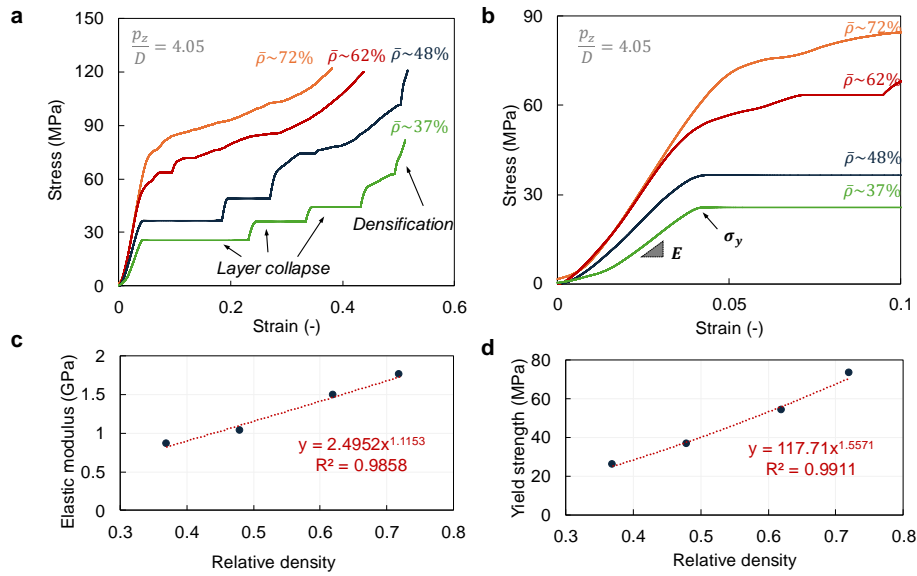


Figure 2.9: **Quasi-static compression results for nanoarchitected SU8 with different relative densities ($\bar{\rho}$).** **a**, Stress vs. strain curves measured during compression. **b**, Zoomed-in stress vs. strain curves comparing elastic modulus and yield strength. **c**, Effective elastic modulus vs. relative density. **d**, Effective yield strength vs. relative density.

To assess the energy dissipation capability of these structures, we calculated the absorbed energy density, W_v , as the area enclosed by the stress (σ) vs. strain (ε) curve:

$$W_v = \int \sigma d\varepsilon, \quad (2.4)$$

up to the densification strain, which serves as the practical limit for energy absorption applications in structured materials [24].

Figure 2.10b shows that as relative density increases, the material absorbs more energy, but saturation occurs at $\bar{\rho} > 0.48$. To quantify energy absorption efficiency,

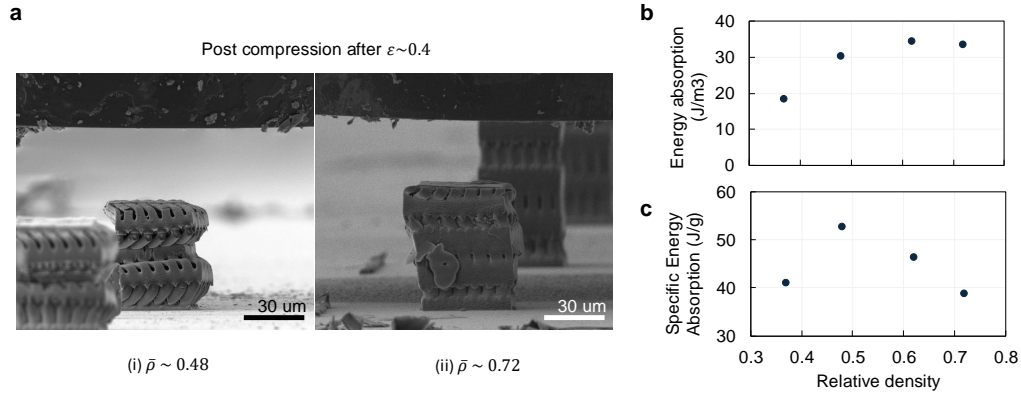


Figure 2.10: **Deformation and Energy absorption of nanoarchiated SU8 with different relative density ($\bar{\rho}$).** **a**, Post-mortem SEM images of deformed samples. Scale bar 30 μm **b**, Calculated absorbed energy (J/m^3) and **c**, specific absorbed energy (J/kg^3) for the samples with different $\bar{\rho}$.

we computed the specific energy absorption metric, ψ , defined as:

$$\psi = \frac{W_v}{\rho_s \bar{\rho}}, \quad (2.5)$$

where ρ_s is the density of the constituent SU-8 polymer ($\rho_s \approx 1200 \text{ kg}/\text{m}^3$). As shown in Figure 2.10c, the highest specific energy absorption is achieved at $\bar{\rho} \sim 0.48$, indicating an optimal balance between energy absorption and material weight. This suggests that nano-architected SU-8 structures with moderate relative densities provide the best performance for lightweight energy-absorbing applications.

Beam Aspect Ratio

As our material design relies on strut-based architectures, the geometry of individual struts plays a crucial role in mechanical performance. The strut geometries (defined in Figure 2.11a), particularly the longitudinal periodicity, p_z , is strongly modulated by the periodicity of the metasurface, such that $p_{x,y} = p$, which corresponds to the spacing between 3×3 arrays of unit cells, as shown in Figure 2.1c. The longitudinal periodicity of the metamask, p purely defines the 3D intensity distribution so that p_z , of the corresponding architected structure is governed by the Talbot effect, given by:

$$p_z = \frac{1}{2} \frac{\frac{\lambda}{n_{\text{SU-8}}}}{1 - \sqrt{1 - \left(\frac{\lambda}{pn_{\text{SU-8}}}\right)^2}}, \quad (2.6)$$

where $n_{\text{SU-8}} = 1.6$ is the refractive index of SU-8 at the operating wavelength $\lambda = 532 \text{ nm}$.

Small variations in p can significantly alter the strut geometry within the sample, allowing modulation of the beam aspect ratio for mechanical tunability. Figure 2.11b illustrates the range of achievable p_z values and corresponding beam aspect ratios (p_z/D) using this metamask design principle. To ensure accurate predictions, our design accounts for up to a $\sim 60\%$ volume shrinkage during post-processing.

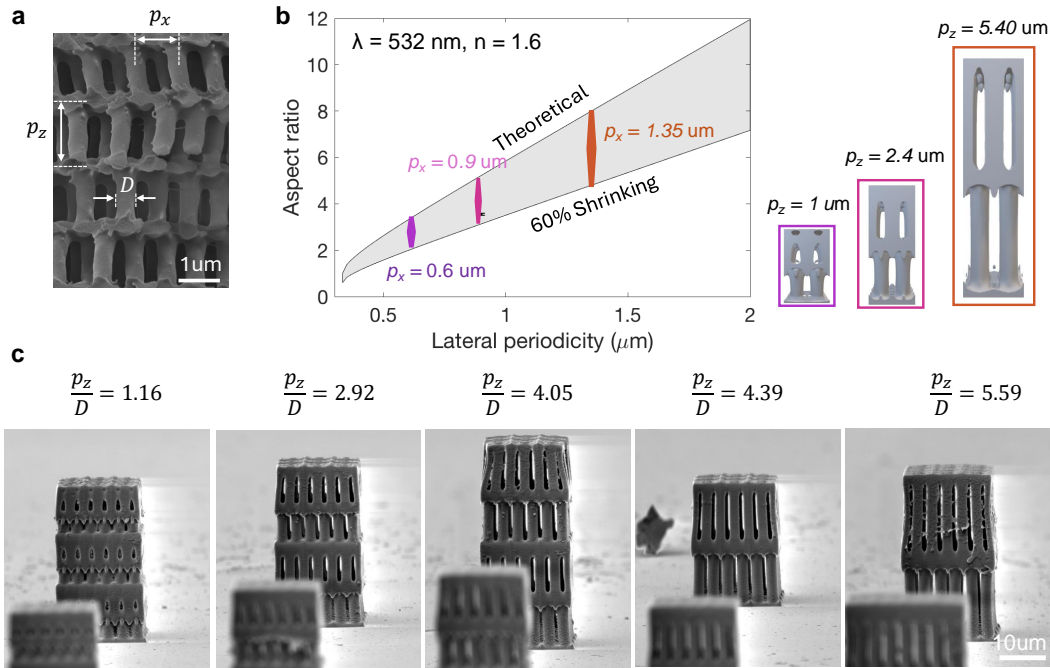


Figure 2.11: **Variations in Beam Aspect Ratio (p_z/D) for Small Lattice SU8.** **a**, The geometrical parameters, the lateral (p_x) and longitudinal (p_z) periodicity with beam diameter (D), define the aspect ratio of the nanoarchitected SU8. **b**, Theoretically attainable aspect ratio of the fabricated SU8 lattice by adjusting the lateral periodicity of metasurface (p_x) for the developed holographic setup ($\lambda = 532\text{nm}$, $n = 1.6$). The longitudinal periodicity (p_z) is a direct result of the Talbot effect. The maximum shrinkage during the post-processing can be up to 60% of the as-printed structures. **c**, SEM images of 3-by-3 or 3-by-2 SU8 lattices with $\bar{\rho} = 0.4$ fabricated using 2PP lithography, showing variations in beam aspect ratio across different samples.

Using this principle, we fabricated nanoarchitected samples with different beam aspect ratios at a fixed relative density of $\bar{\rho} \sim 37\%$ using 2PP lithography (Figure 2.11c).

The mechanical properties of periodic lattices with varying beam aspect ratios are presented in Figure 2.12a and b. As p_z/D increases (i.e., as the struts become taller), the peak stress corresponding to buckling decreases, and the plateau stress extends.

Due to the relatively slow printing speed of 2PP, larger aspect ratio samples were printed as 2-by-2 lattices instead of 3-by-3, as the latter requires significantly more fabrication time. Consequently, densification occurs earlier in high p_z/D samples.

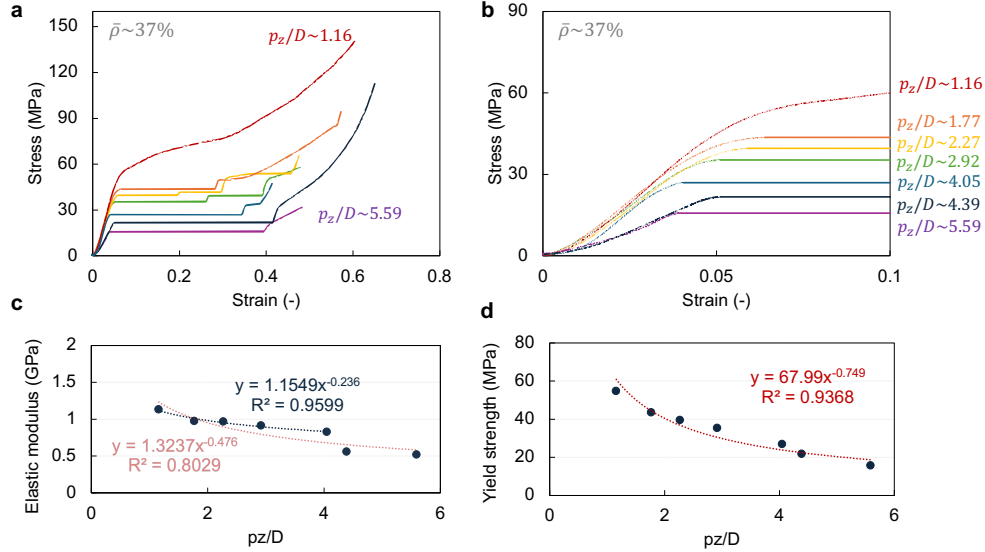


Figure 2.12: **Quasi-static compression results for nanoarchitected SU8 with different beam aspect ratios (p_z/D).** **a**, Stress vs. strain curves during compression. **b**, Zoomed-in stress vs. strain curves for elastic modulus and yield strength comparison. **c**, Effective elastic modulus vs. beam aspect ratio (p_z/D). **d**, Effective yield strength vs. beam aspect ratio (p_z/D).

For non-rigid lattices composed of solid Euler struts with characteristic cross-sectional dimension D and length L (in our notation, p_z), stiffness is expected to be dominated by beam bending, following the scaling relation:

$$E \propto (D/L)^n, \quad (2.7)$$

where n depends on the dominant deformation mechanism. Figure 2.12c plots the effective elastic modulus as a function of aspect ratio, revealing two distinct regimes with minimal stiffness variation within each. The underlying mechanisms governing the transition between these states remain unclear; however, the key observation is that beam aspect ratio has a negligible impact on effective modulus. This suggests that the stiffness variations observed in our large-scale samples are primarily driven by relative density variations and the intrinsic properties of the constituent material.

As struts become taller, additional deformation modes emerge, including shear, beam bending/buckling, and node failure due to stress concentration, collectively

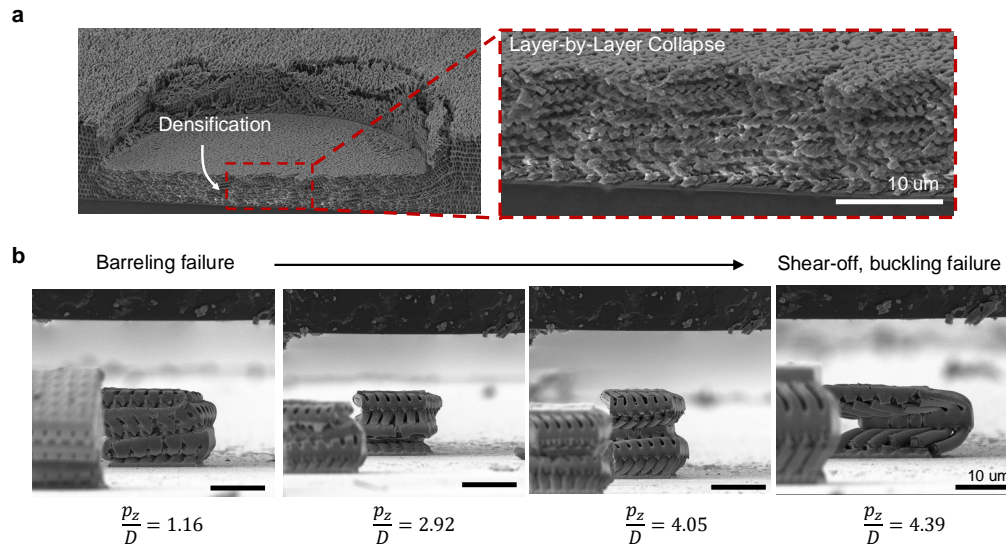


Figure 2.13: **Effects of beam aspect ratio on material deformation mode.** **a**, Post-mortem SEM images of a deformed large-scale nanoarchitected SU8 sheet fabricated via holographic lithography. Scale bar: $30 \mu\text{m}$. **b**, Post-mortem SEM images of 2PP-fabricated nanoarchitected SU8 samples with varying beam aspect ratios (p_z/D).

reducing the effective yield strength (Figure 2.12d). The activation of buckling and shear failure mechanisms leads to premature structural collapse, lowering the overall load-bearing capacity.

The effects of p_z on deformation modes are evident in Figure 2.13b, where increasing p_z/D shifts deformation from barreling failure to layer-by-layer collapse. This bifurcated deformation follows a repeating pattern across layers, with shear-driven failure propagating through the structure. Due to the high stress concentration and limited elasticity of SU-8, most failures occur at or near the nodes.

These findings are consistent with our observations in large-scale nanoarchitected sheets fabricated via holographic lithography. Cross-sectional SEM images of indentation imprints in densified regions after quasi-static indentation (Figure 2.13b) confirm that nanostruts within the same layer buckle in the same direction, alternating across the depth. This behavior suggests strong shear stress influences during compressive loading.

Overall, these results validate the scalability of our design principles. The geometrical effects and failure mechanisms observed in small-scale 2PP-fabricated lattices translate well to large-scale samples produced using holographic lithography, demonstrating the robustness of our approach to nanoarchitected material

design.

2.7 Dynamic Characterization

As demonstrated in the quasi-static characterizations, the enhanced local deformation and the multiple distinct plastic energy dissipation mechanisms available to nano-architected polymers enable these materials to have superior energy dissipation capabilities. As the scalable nano-architected SU8 is aimed for impact resistant application, understanding the material behavior under dynamic loading is of our interest. Due to the limited access to the dynamic testing set-up, the tested architected sample have an average of $p_z/D \sim 2.5$ and $\bar{\rho} \sim 50\%$.

2.7.1 Laser Induced Particle Impact Testing

To measure the impact absorbing capability of the fabricated material, we performed laser-induced particle impact tests (LIPIT) [25], on 40 μm -thick nano-architected sheets during which 14 μm -diameter SiO_2 microparticles were launched to impact the material. A selective particle was propelled from the launching pad, by rapidly expanding the polyurea layer with the ablation laser, which selectively accelerated an individual projectile. The excitation laser pulse energy was calibrated to control the projectile velocity from 50 m s^{-1} to 10^3 m s^{-1} . A laser imaging pulse (Cavilux, 640 nm wavelength, 30 μs duration) was used to illuminate the moving microparticle, and the adjacent snapshots of its trajectory captured by an ultrahigh-speed camera (SIMX16, Specialised Imaging) were used to measure the impact (v_0) and rebound velocities (v_r). These experiments were performed on a sample with a relative density, $\bar{\rho} \sim 50\%$, and the impacting particle size was approximately one order of magnitude greater than that of the unit cell (lateral periodicity of $900 \pm 10 \text{ nm}$), which allows for the separation of relative scales between the impact area and the characteristic material length scale.

2.7.2 Energy Absorption and Impact Response

Energetic performance

To evaluate the energetic performance of nano-architected SU8, we calculated the impact energy

$$W_o = \frac{1}{2} m_p v_o^2, \quad (2.8)$$

and rebound energy

$$W_r = \frac{1}{2} m_p v_r^2, \quad (2.9)$$

where the mass of a micro-projectile

$$m_p = \frac{1}{6}\pi\rho_{SiO_2}D_{SiO_2}^3, \quad (2.10)$$

is calculated to be 2.64 ng, based on the measured diameter D_{SiO_2} (13.96 μm) and the density of silica ρ_{SiO_2} (1,850 kg m^{-3}).

The dissipated energy W_d of the material during the impact was calculated from the kinetic energy loss of a projectile, W_r , and the inelastic energy due to consolidation in the microparticle, W_{i,SiO_2} , defined as

$$W_d = W_o - W_r - W_{i,SiO_2}. \quad (2.11)$$

According to [26], W_{i,SiO_2} is a function of W_r with the form of a quadratic function, $W_{i,SiO_2} = C1W_r^2 + C2W_r + C3$, where C_i are the fitting parameters.

LIPIT experiments convey that the lithographically patterned nano-architected SU8 exhibits near-ideal energy dissipation, with a linear slope of 0.992 ($R_2 = 0.99$) (Figure 2.14a). This indicates that nearly most energy was dissipated upon the impact to the material. Portela et al. [26] performed similar LIPIT experiments on nano-architected glassy carbon with similar beam dimensions in the range of 400 to 500 nm yet different relative density, $\sim 23\%$ and reported three distinct responses as a function of impact energy W_o : (1) elastic collision for impact velocities below 50 m s^{-1} , which corresponds to W_o of less than 0.003 μJ , (2) particle rebound with partial cratering beyond elastic regime, and transitioning to (3) particle embedding beyond 515 m s^{-1} with $W_o \sim 0.034 \mu\text{J}$. In the experiments in this work, no external damage was observed for impact velocities of 250 m s^{-1} with W_o of $\sim 0.08 \mu\text{J}$. Under these conditions, the impacting particles rebounded with a high coefficient of restitution, ($\epsilon = |v_r|/|v_o|$) in the range of 0.27 - 0.45. At velocities greater than 250 m s^{-1} , the higher kinetic energy and momentum of the projectile were sufficient to induce plastic deformation of the nano-lattice, forming a localized crater with no noticeable signs of fracture at the impact site. The vertical beams directly underneath the impact site plastically deformed, which bent the horizontal layers, creating a dimple on the surface. At W_o greater than $\sim 0.16 \mu\text{J}$, major cracks formed along the circumference of the projectile impact site, which deepened the crater in addition to the observed plastic distortion. These characteristics of structural layer collapse under the impact zone and tensile cracking around the compacted area are similar to those observed during quasi-static indentation experiments (2.15). Impact velocities greater than $\sim 750 \text{m s}^{-1}$ resulted in the microparticles being captured within the nanolattice with no rebound. SEM images of the characteristic regimes are shown in Figure 2.14b.

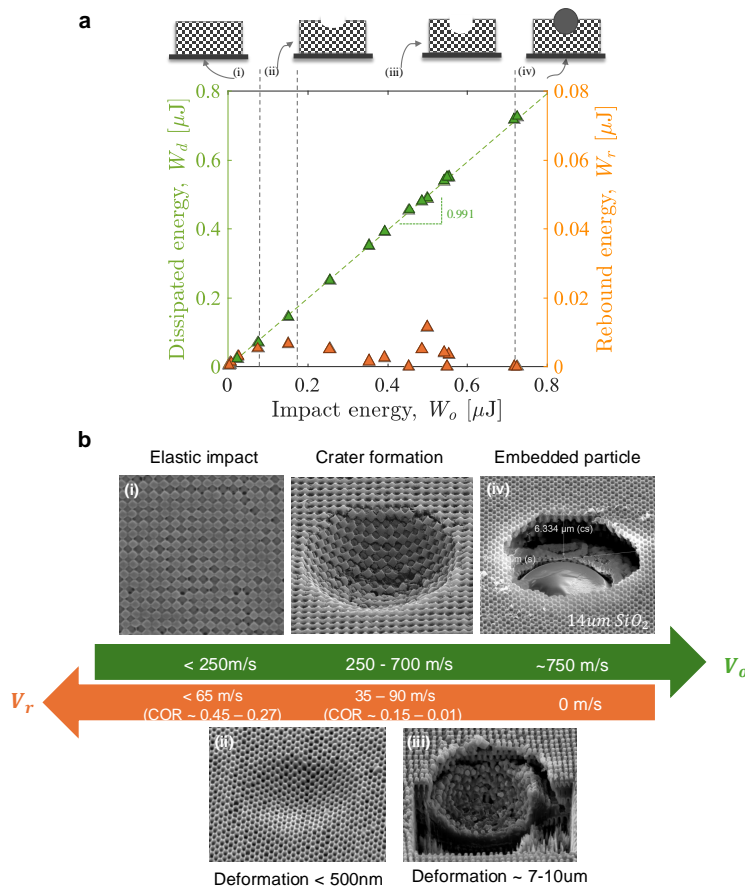


Figure 2.14: **Analysis of micro-ballistic experiments on nano-architected SU8 sheet.** **a**, Dissipated and rebound energetics versus impact energetics. A linear fit of the dissipated energy is presented with a green dashed line. As a function of impact energy, four deformation regimes were exhibited: (i) elastic rebound, (ii) shallow and (iii) deep crater formation to (iv) particle capture. **b**, Corresponding post-impact micrograph of each regime. (scale bar 5 μm).

Specific Energy Absorption

To quantitatively compare to other materials tested at different sample thicknesses and projectile sizes, the specific dissipation energy W_d^* is calculated by

$$W_d^* = \frac{W_d}{m_{crater}} = \frac{W_d}{\bar{\rho}\rho_{SU8}V_{crater}}, \quad (2.12)$$

with relative density $\bar{\rho}$ (~ 0.5), base polymer density ρ_{SU8} ($1,200 \text{ kg m}^{-3}$) and crater volume V_{crater} , which was measured via post-mortem analysis. Since the specific energy is sensitive to crater volume measurement, it is obtained for deep crater ($v_o \geq 450 \text{ m s}^{-1}$) only where the crater volume is large enough to be accurately measured from SEM-FIB post-mortem analysis.

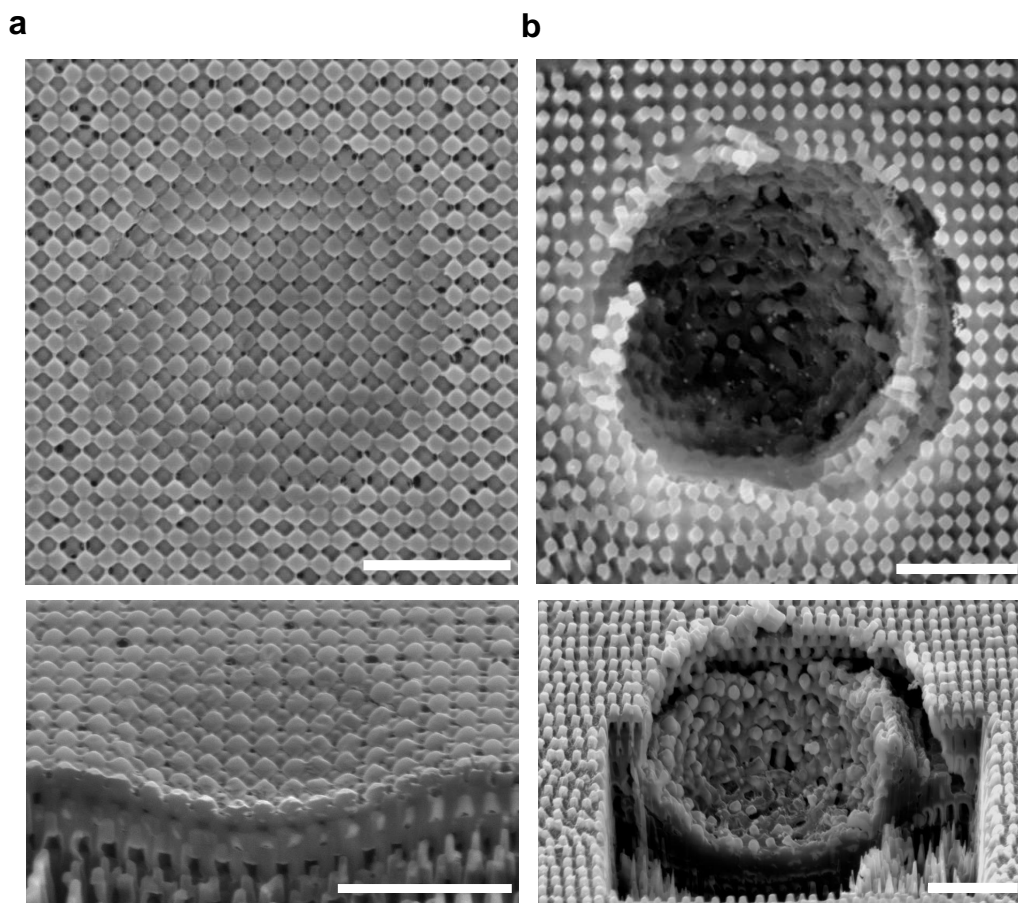


Figure 2.15: **Crater morphology and cross-sectional micrographs.** **a**, Shallow crater formed after an impact with $v_o = 345 \text{ m s}^{-1}$. **b**, Deep crater formed with impact velocity $v_o = 600 \text{ m s}^{-1}$ (scale bar $5\mu\text{m}$)

Comparing to other ballistic materials [5, 26–37], Figure 2.16 conveys that the nano-architected SU8 has the specific energy of $0.51\text{--}2.61 \text{ MJ kg}^{-1}$ across a broad range of tested velocities, a range comparable to that of other composite materials used for impact absorption, such as Kevlar/PVB composite [32], polystyrene [30], and pyrolyzed carbon nanolattices [26]. This enhanced energy dissipation is most likely enabled by the synergistic interplay between the high fracture toughness of SU8 and the structural instabilities [38, 39]. Benefitting from its nano-architecture, the patterned SU8 sheet with $\bar{\rho} \sim 50\%$ achieves the absolute density of 600 kg m^{-3} , a value 2-4 times lower than that of fully dense thin polycarbonate films [29] or multi-layer graphene [34]. The material and experimental parameters of other ballistic studies are summarized in Table 2.1.

The variability in the specific energy dissipation of nano-architected SU8 tested

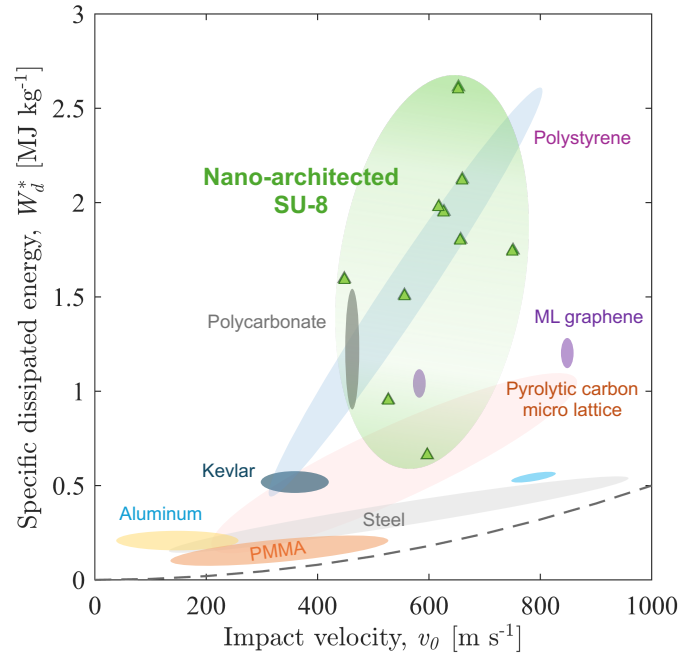


Figure 2.16: **Specific dissipation energy of nano-architected SU8 sheet.** W_d^* of nano-architected SU8 thin sheet compared with other bulk and nanomaterials [5, 26–37].

under the same experimental conditions can be attributed to uncertainties in the crater volume measurements and to the local variations of mechanical properties indicated from the indentation data, which can possibly affect the size of deformation and failure mechanisms [29]. Since the crater volume was estimated from the radial symmetric assumption of the cross-sections, which were prepared by focused ion beam (FIB) milling, the material damage or removal induced from beam local heating [40, 41] and measurement uncertainty induced from the charging issue [42] was not inevitable. Based on the rough analysis for the propagation of uncertainty from the measured values of $v_o \sim 2\%$, $v_r \sim 2\%$ and $V_{crater} \sim 30\%$,

$$\frac{\sigma_f}{f} \approx \sqrt{\sum_{i=1}^n \left(\frac{\sigma_i}{a_i}\right)^2} \approx 0.3, \quad (2.13)$$

the experimental errors from the post-mortem analysis can result in about 30% errors in the energy calculations. The local variations of mechanical properties indicated from the indentation data can possibly affect the size of deformation and failure mechanisms as well [26, 29].

In addition, it has been also reported that post-mortem inspection of residual im-

Target					Projectile		
Material	Thickness	Density	Specific E. Dissipation	Material	Diameter	Impact velocity	
[-]	[μm]/[mm]	[kg m ⁻³]	[MJ kg ⁻¹]	[-]	[μm]/[mm]	[m s ⁻¹]	
Nano-architected pyrolised carbon ^[26]	28	196, 322	0.19 - 1.1	Silica	14	30 - 1200	
Polycarbonate ^[29]	0.20	1200	0.79 - 1.69	Silica	7.6	500	
Graphene oxide/SF composites ^[28]	0.08 0.15	-	0.42 - 0.75	Silica	7.6	400	
Polystyrene ^[30]	0.075 0.29	- 1053	0.4 - 2.8	Silica	3.7	350 - 800	
Multi-layer graphene ^[34]	0.01 0.10	- 2200	0.86 - 1.26	Silica	3.7	900	
PMMA ^[27]	4 - 6	1190	0.034 - 0.23	Steele	7.8	89.3 - 670	
304 Stainless Steel ^[37]	0.4	7800	0.091 - 0.27	Steel	8	176 - 592	
304 Stainless Steel ^[35]	3	7800	0.20 - 0.68	Steel	12.5	480 - 997	
CFRP ^[33]	2, 6	1900	0.28 - 0.56	Steel	4	500 - 1230	
Kevlar/PVB composite ^[32]	7	1355	0.46 - 0.55	Tungsten carbide	12.7	296 - 422	
Aluminum ^[31]	1.27	2780	0.11 - 0.56	Steel	6.4 12.7	152 - 869	

Table 2.1: **References for Other Micro-LIPIT/Macro spherical projectile ballistic experiments on other materials**

Impact impressions in polymers often underestimate the actual deformation volume because it does not account for the time-dependent properties of the base material, for example viscoelastic recovery, elastically deformed zone [25]. This indicates that attributing the dissipation capability of the material solely to the deformed area might not capture the right physics under the impact. Therefore, we have examined the contribution of crater kinetic energy to the total dissipated energy by decomposing W_d into two terms:

$$W_d = W_{craterKE} + W_{delocalization}, \quad (2.14)$$

where the first term

$$W_{craterKE} = \frac{1}{2} m_{crater} v_o^2, \quad (2.15)$$

represents an approximate measure of kinetic energy transferred within the deformed volume of the material and the second term

$$W_{delocalization} = W_d - W_{craterKE}, \quad (2.16)$$

accounts for all other dissipation mechanisms such as intrinsic viscoelastic dissipation [25, 34, 36], adiabatic heating of polymer [30], or strain delocalization. To evaluate the delocalization capability of nano-architected SU8, the specific delocalization energy $W_{delocalization}^*$ is evaluated by decoupling the crater mass contribution,

$$W_{delocalization}^* = W_d^* - \frac{1}{2} v_o^2. \quad (2.17)$$

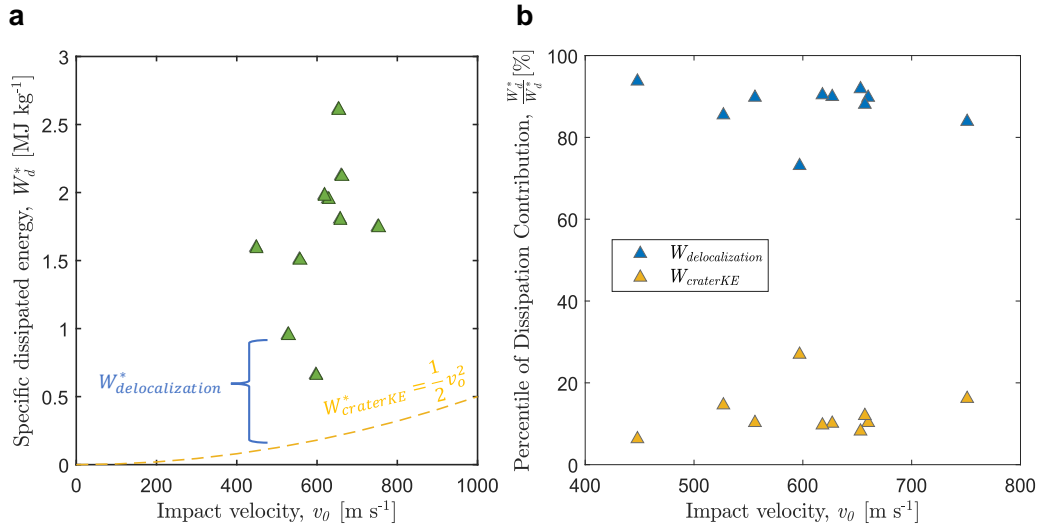


Figure 2.17: **Contribution of crater kinetic energy and delocalization energy during dissipation process.** **a**, Decomposition of W_d^* into two terms, $W_{delocalization}^*$ and $W_{craterKE}^*$. **b**, Percentile of dissipation contribution from each factor.

Figure 2.17 shows the superior impact delocalization ability of the material. In Figure 2.17 (a), the large deviation from a baseline which represents the material-independent energy dissipation term indicates that more sample volume beyond the crater size contributes to the energy dissipation. The contribution from each term is quantified to be $\sim 12.7\%$ and $\sim 87.3\%$ for $W_{craterKE}$ and $W_{delocalization}$, respectively, from the total W_d (Figure 2.17b). Quantifying the contributions of each of these factors is critical to laying out the parameter space for the energy dissipation capabilities in nano-architected materials and should be explored in future studies.

2.8 Conclusion

This chapter demonstrates that holographic lithography, enabled by optical metasurfaces and laser scanning, is a scalable and effective platform for fabricating nano-architected materials. Using this technique, we successfully produced macroscale SU8 sheets with lateral dimensions of $2.1 \times 2.4 \text{ cm}^2$, thicknesses of 30 to 40 μm , individual unit cell dimensions of 0.9 μm , and relative densities between 20% to 50%. The ability to achieve sub-micron resolution over macroscopic areas highlights the precision and scalability of this approach.

Mechanical characterization revealed that the elastic modulus of the fabricated sheets ranged from 300 MPa to 4 GPa, consistent with the scaling of modulus based on relative density. Additionally, laser-induced particle impact tests (LIPIT) demonstrated a specific energy dissipation of 0.51-2.6 MJ kg^{-1} , comparable to other bulk and nanomaterials such as Kevlar/PVB composite [32], polystyrene [30], and pyrolysed carbon nanolattice [26]. This comparison underscores the superior energy dissipation capabilities of the nano-architected sheets, attributed to the hierarchical structuring that facilitates multiple dissipation mechanisms.

The findings highlight that both unit cell design including relative density and beam aspect ratio and intrinsic material properties, such as the degree of crosslinking, are critical factors in determining the overall mechanical response of hierarchical materials. Effective control of these factors allows for tailoring mechanical properties such as stiffness, energy absorption, and failure mechanisms.

The ability to scale fabrication efficiently combined with the geometrical design principles explored in this study can be directly applied and extended to different material systems, significantly expanding the design space for nano-architected materials. While this investigation focused on polymers, the developed fabrication methodology and geometrical design principles offer a versatile pathway for extending nano-architected materials to other material classes. For instance, atomic layer deposition (ALD) can be used to apply metal or oxide coatings, and pyrolysis can convert polymer templates into amorphous carbon. Additionally, swelling the polymer network with metal salts followed by calcination and reduction could enable the creation of metallic or oxide architectures [43].

In summary, the findings of this chapter underscore the potential of holographic lithography as a scalable and adaptable fabrication platform for producing large-area nano-architected sheets with sub-micron resolution. The demonstrated ability to translate geometrical design principles across different material systems advances

our understanding of hierarchical structuring but also lays a solid foundation for future applications in impact protection, energy absorption, and functional coatings.

*Chapter 3***MULTISCALE INTERACTIONS IN METAL-COORDINATED
DYNAMIC POLYMER**

This chapter has been adapted from:

S. Lee^{*†}, P. Walker[†], S. Velling, A. Chen, Z. Taylor, C. Fiori, V. Gandhi, Z-G. Wang & J.R. Greer. “Molecular Control via Dynamic Bonding Enables Material Responsiveness in Additively Manufactured Metallo-Polyelectrolytes”. *Nature Communications* **15**, 6850 (2024). DOI: [10.1038/s41467-024-50860-6](https://doi.org/10.1038/s41467-024-50860-6)

Contributions: S.L. conceived and designed the project, fabricated samples, performed experimental characterization, analyzed the results, and wrote the manuscript.

3.1 Chapter Summary

While Chapter 2 explored structural hierarchies in architected materials to control mechanical responses through geometric design, this chapter shifts focus to the concept of hierarchical organization within polymers, emphasizing how molecular-level dynamics propagate to influence macroscale behavior. We explore how molecular-level control in metallo-polyelectrolytes (MPECs)—through dynamic bonding and reversible crosslinking—can be leveraged to dictate macroscale mechanical behavior effectively. By integrating theoretical insights with experimental investigations using stereolithography-based additive manufacturing, we examine how hierarchical interactions across multiple length scales influence stiffness, energy dissipation, and functional properties of MPECs. The findings reveal a strong coupling effect between molecular interactions and continuum-level properties, where parameters such as metal ion valency and polymer charge sparsity play a pivotal role in governing mechanical performance. This study also demonstrates how multiscale studies can predict and guide the design of adaptive and reconfigurable materials with tunable mechanical properties. By establishing a comprehensive understanding of how hierarchical structuring in MPECs can be systematically controlled, this chapter sets

the stage for extending these design principles to a broader range of soft materials.

3.2 Introduction

MPECs are a class of soft materials that exhibit unique mechanical and physical properties through reversible electrostatic interactions between dynamic crosslinkers (multivalent metal ions) and charged polymer chains. MPECs consist of polyanions that are electrostatically crosslinked by labile metal cations with secondary metal–ligand coordination [17, 62, 63]. In concert with the polymer chain conformations that arise from electrostatic interactions, these molecular-level processes govern global phenomena in the gels. For example, the local coordination environment yields distinct stiffness response [64, 65], while the oxidation state of the metal ion has a significant impact on the ionic conductivity [66]. This molecular-level control offers a wide range of opportunities to explore for a range of applications — from filtration to biomedical devices and sensors [60, 67–69].

The multiscale physical behavior of MPEC gels, ranging from local coordination environment at the atomic level to mesoscale polymer conformation to macroscopic material properties, is strongly affected by the chemical nature of metal complexation [62, 70, 71], solution pH [72], and solvent quality [73]. The knowledge gap between the molecular-level chemistry of the dynamic bonds and the continuum-level material properties, combined with the lack of mechanistic insight from theory and simulations, has limited the development and utilization of this class of materials in real-world applications [17]. Existing state-of-the-art fabrication methods are typically complicated and require multiple steps of solution-based metallo-polyelectrolyte synthesis [17, 74] to produce samples, most of which have been reported to lack long-term stability, suffering from inhomogeneity, and in some cases requiring the addition of non-dynamic covalent crosslinkers for synthesis [70, 75]. The use of theoretical methods to gain intuition of and alleviate these experimental complications is also hampered by computational challenges, arising from the large range of length and time scales involved [17, 71, 76, 77].

To close this substantial knowledge gap between the molecular-level chemistry of dynamic bonds and the continuum-level material properties, we fabricated homogeneous, stable, and long-lived poly(Acrylic Acid) MPEC gels using a single-step stereolithography and conducted a theory-guided, physically-informed multi-scale study of MPEC gels. Through holistic material characterization, we probe the relevant length scales to corroborate theoretical and computational predictions. Based

on these findings, we present a roadmap that outlines the effect of chemical composition on the MPEC gel properties that can be used to tailor their functionality and responsiveness at the material level. The overall framework and chemical species explored in this work are common in soft materials formed with dynamic bonds, which renders our findings readily applicable to different material systems.

3.3 Additive Manufacturing of MPEC Gels via Stereolithography

Conventional methods for fabricating metallo-polyelectrolytes (MPECs) often involve multi-step processes that introduce inhomogeneities, diffusion limitations, and mechanical variability [17, 74]. Additionally, these methods require equilibration and storage in water, complicating the production of stable and inert structures for ambient environments [34]. To overcome these challenges, we developed a single-step stereolithography-based approach using Liquid Crystal Display (LCD)-based 3D printing (Figure 3.1a). This one-pot method enables in situ synthesis and fabrication of MPEC structures suitable for vat polymerization, ensuring uniformity, and mechanical stability without requiring multi-step processing.

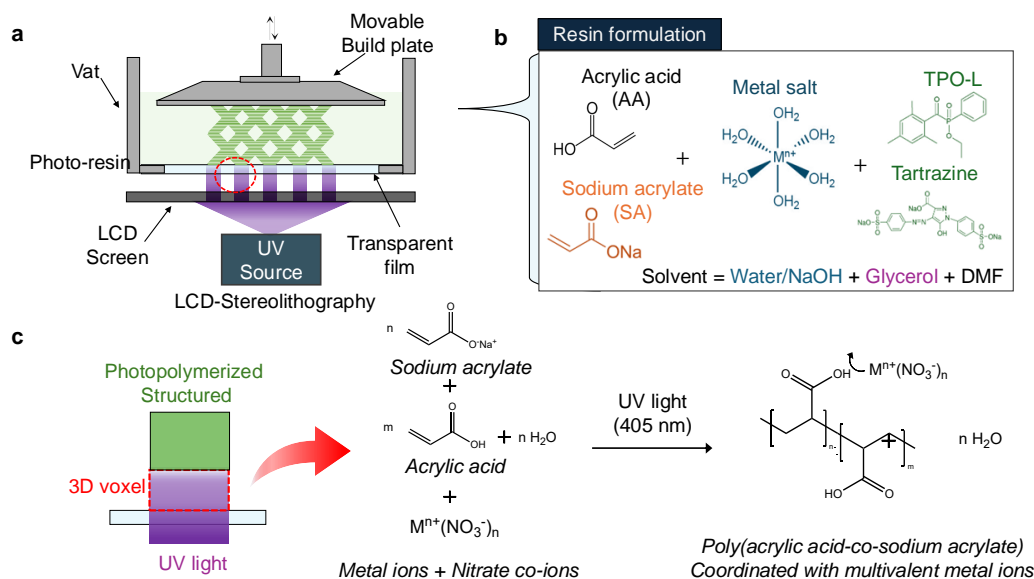


Figure 3.1: **Additive manufacturing of MPEC using stereolithography.** **a**, Schematic representation of Liquid Crystal Display (LCD) Stereolithography setup. A layer-by-layer printing is processed to produce solidified parts. **b**, Resin formulation for one-pot synthesis of MPEC. **c**, Free-radical photopolymerization reaction is initiated by projecting UV light into a liquid photoresin in the bath. The polymerized chains undergo in-situ coordination with multivalent metal ions.

Resin Preparation and Composition

We prepared a homogeneous photoresin solution consisting of Acrylic Acid (AA) monomers and Sodium Acrylate (SA) co-monomers to serve as chain builders, combined with metal ion species as dynamic crosslinkers. Poly(acrylic acid) (PAA) networks were formed in situ during photopolymerization, which was initiated by ethyl phenyl (2,4,5-trimethylbenzoyl) phosphonate (TPO-L) under 405 nm UV light. The incorporation of dynamic crosslinkers enabled in situ coordination during printing, eliminating the need for additional chemical crosslinkers (Figure 3.1c). To enable precise printing resolution for metal ions that do not absorb UV light effectively, we incorporated 1 v/v% of 30 mg/mL tartrazine (yellow-dye) as a photoblocker. Glycerol and water were used as co-solvents to prevent gel dehydration and ensure environmental stability of the fabricated structures. The total monomer

Reagent	Purpose	Amount
Acrylic acid	Monomer	15 mL
2M Sodium acrylate	Monomer/Buffer	2.18 mL
H ₂ O / 2M NaOH / 4M NaOH	Diluent/Buffer	2.40 mL
Nitrate Salt (6M for Mono, 3M for Di, 2M for Trivalent)	Binder	0.73 mL
N,N-dimethylformamide (DMF)	Diluent	1.37 mL
2,4,6-Trimethylbenzoyldi-Phenylphosphinate (TPO-L)	Photoinitiator	695.3 mg
Trisodium-5-hydroxy-1-(4-sulfonatophenyl)-4-[(E)-(4-sulfonatophenyl)diazenyl]-1H-pyrazole-3-carboxylate (Tartrazine)	UV blocker	8.15 mg
Glycerol	Plasticizer	2.40 mL

Table 3.1: **MPEC photoresin composition**

concentration was maintained at 8.8 M to ensure consistent polymerization, while the carboxylate–metal cation bond ratio was fixed at 0.02 mol% to provide uniform crosslinking density. To control the ionic strength of the metal cations, we used 0.726 mL of 6 M, 3 M, or 2 M metal nitrate solutions for mono-, di-, and tri-valent ions, respectively. The pH of the resin was adjusted using 2.4 mL of Milli-Q water and either 2 M or 4 M Sodium Hydroxide (NaOH) to modulate the degree of ion-

ization of the polyanions and influence the coordination environment of the metal crosslinkers. The detailed resin formulation is listed in Table 3.2.

Printing and Post-processing

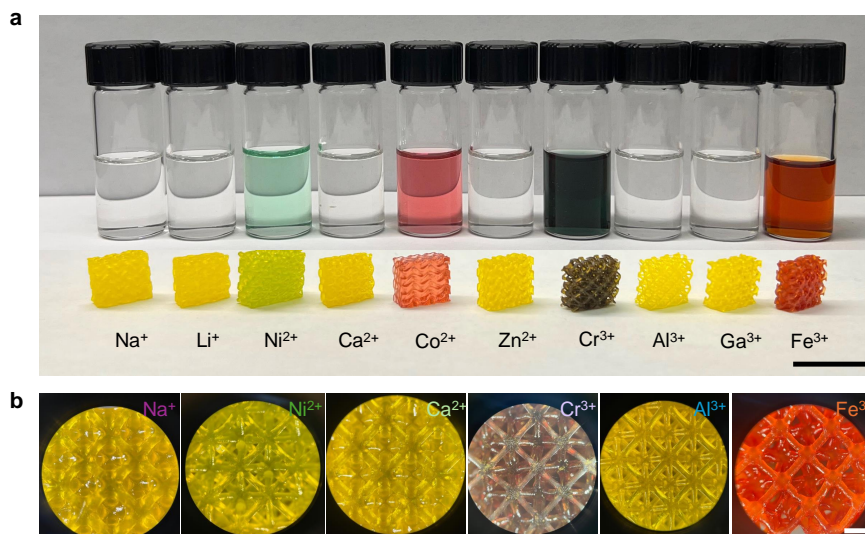


Figure 3.2: **Additive manufactured MPEC gels.** **a**, Optical images of synthesized photo resins (without tartrazine to show coordination color) and 3D-printed lattices (with tartrazine) with different metal ions. Scale bar 15 mm. **b**, Magnified images of 3D-printed octet lattices, showing multiple unit cells. Scale bar 2 mm.

The formulated resin was printed into 3D structures using a commercial 405 nm wavelength monochrome LCD-based mSLA printer (Mars 2 Pro, Elegoo Inc.). A layer thickness of 50 μm was exposed for 30 seconds at a laser power of 1.99 mW/cm^2 . The detailed printing parameters are listed in Table 3.2. To remove volatile unreacted photoresin precursors, the printed samples were placed on a PTFE (Teflon[®]) sheet and dried for 24 hours at room temperature in a vacuum oven. Following this, the samples were equilibrated under ambient conditions (22.5 $^{\circ}\text{C}$, 45% RH, 1 atm) for 48 hours prior to any characterization.

This approach enabled the successful fabrication of MPEC structures incorporating a wide range of metal ions, from sodium to iron, using a single-step stereolithographic printing process. As shown in Figure 3.2, the fabricated octet lattice structures exhibited high resolution with feature sizes in the hundreds of μm , demonstrating the versatility and precision of this method. Notably, the gels were fabricated ex-

¹High hydrophilicity of Polyacrylic acid results in high sensitivity to temperature and RH. Thus, equilibration conditions were slightly varied depending on the temperature and RH conditions.

Parameter	Setting
UV wavelength	405 nm
Layer thickness	50 μm
Exposure time	30s
Built head lifting speed	60 mm/min
Drying conditions	24hrs at 25°C, Vacuum
Ambient equilibration conditions	48-72hrs ¹ at RT, 45% RH

Table 3.2: **LCD printing and post-processing parameters.**

clusively with entanglement and metal crosslinkers, without the need for chemical crosslinkers. Consequently, it was observed that sodium ion-based MPECs exhibited reduced resolution, as their mechanical integrity relied solely on polymer entanglement rather than metal coordination.

3.4 Material Characterization for AM-Fabricated MPEC Gels

Since the rapid radical polymerization process effectively freezes the chemical species within the gel matrix, it is crucial to verify the state of the gels, especially given the focus on a multiscale study. Therefore, we conducted extensive material characterization of AM-fabricated MPEC gels to verify the following:

- Formation of metal coordination bonds and their role in creating dynamic crosslinking between polymer chains.
- Consistency in the content of metal ions and other species across different samples.
- Uniformity of the fabricated MPEC gels, ensuring that they can be considered to possess continuum properties at the macroscale.
- Thermodynamic equilibrium of MPEC gels to accurately reflect the intrinsic material properties.

Formation of Metal Coordination Bond

To confirm the formation of metal coordination bonds with carboxylate groups on PAA chains, we performed Fourier Transform Infrared (FTIR) spectroscopy on the printed MPEC gels. For simplicity, we selected Na^+ , Ca^{2+} , and Al^{3+} as representative metal species. Figure 3.3a shows that metal ions form stoichiometrically charge-balanced complexes with the polymer. The spectra display characteristic peaks for carboxyl (R-COOH) and carboxylate (R-COO^-) groups: carboxyl groups show

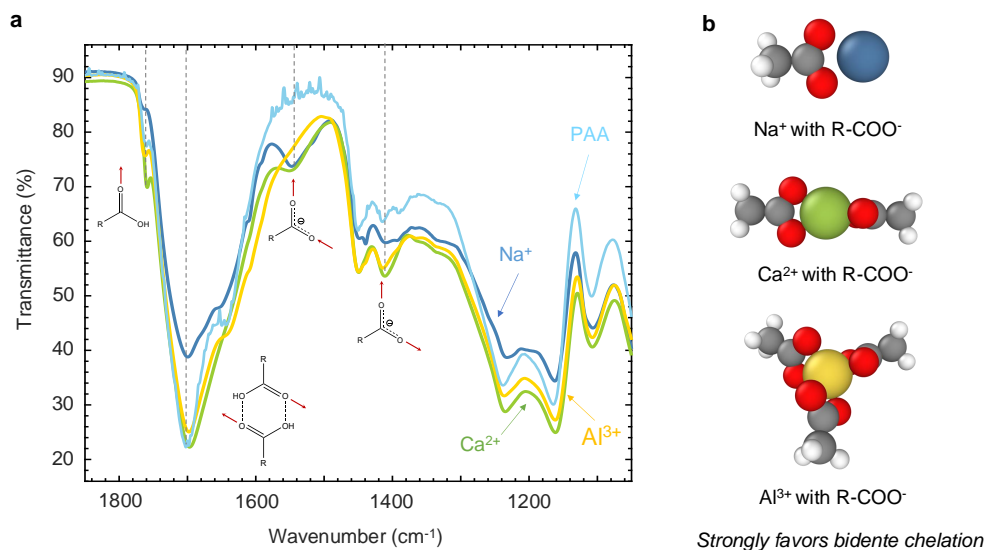


Figure 3.3: Metal-carboxylate coordination bond for AM-fabricated MPECs. **a**, FTIR spectra exhibits signatures of both carboxyl and carboxylate functional groups, with the later being associated with bidentate chelation of Na^+ , Ca^{2+} , and Al^{3+} . **b**, Visual representative of structural models of coordination for Na^+ , Ca^{2+} , and Al^{3+} .

absorption at $\sim 1760\text{ cm}^{-1}$ (monomer) and $\sim 1700\text{ cm}^{-1}$ (dimer), while the alcohol C-OH stretch appears at $\sim 1240\text{ cm}^{-1}$. The carboxylate anion shows asymmetric and symmetric stretches at $\sim 1545\text{ cm}^{-1}$ and $\sim 1410\text{ cm}^{-1}$, confirming the bond-and-a-half character. In pure PAA gels without metal crosslinkers, only carboxyl stretches were present, indicating that the polymer was fully protonated. The presence of symmetric and asymmetric carboxylate modes in MPECs at $\text{pH} \lesssim 2.5$ confirms the complexation of metal cations and the formation of metal–ligand coordination bonds.

To determine the coordination environment of metal ions, we analyzed the separation ($\Delta\nu$) between symmetric (ν_s) and asymmetric (ν_{as}) stretching frequencies of the carboxylate group. Following the methods of Deacon and Phillips and Kirwan et al. [78–80], we used sodium polyacrylate salt at $\text{pH} = 13$ as a spectral reference. The results indicated that Na^+ , Ca^{2+} , and Al^{3+} exhibit bidentate chelation, with direct coordination of metal ions to the polymer. DFT simulations of acetate anions (CH_3COO^-) bonding to each dynamic crosslinker further supported the observed local coordination environments (see Appendix B.1). These simulations confirmed that charge neutrality was maintained through a balance between the number of coordinating carboxylates and the metal cation valency (Figure 3.3b).

This validates that the printed MPEC gels successfully form metal coordination bonds and follow the valency as the coordination number for the selected species. While different metal ions may exhibit varied coordination environments, this study focuses on hard ions for consistency.

MPEC Gel Content Analysis

Understanding the actual material composition of MPEC gels is crucial for accurate modeling, as their properties are strongly influenced by multiple parameters. To quantify the gel contents, we performed Thermogravimetric Analysis (TGA). The analysis allowed us to verify:

- Solvent content in the gels: TGA confirmed that the gels contain consistent water content, which enables us to decouple the effects of solvent, ion, and pH, ensuring a fair comparison between samples.
- Metal ion content: TGA results showed that the metal ion content in the gels matches the intended resin composition, validating that the photoresin formulation accurately translates into the gel composition.

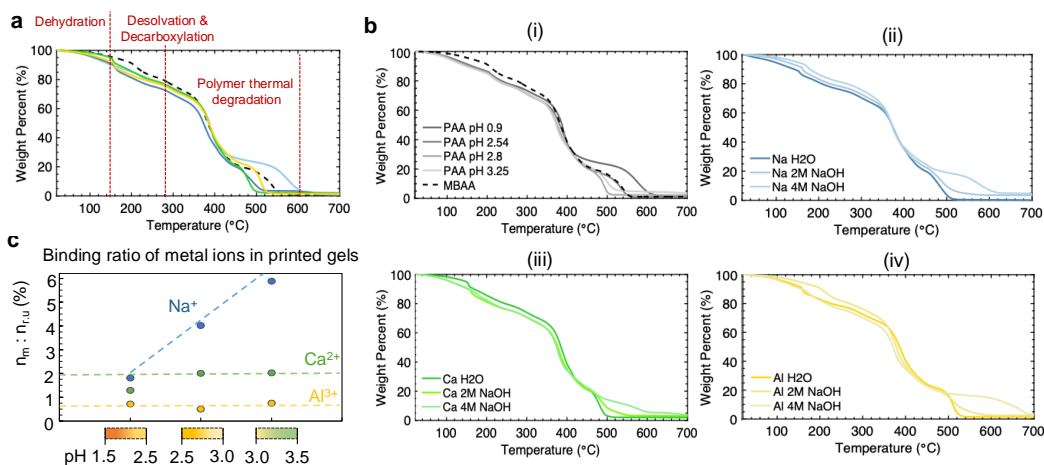


Figure 3.4: **Thermogravimetric analysis of MPEC gels for contents quantification.** **a**, Weight loss profiles of MPEC gels with different metal ions. During thermal ramp, the gels undergo dehydration-desolvation-decarboxylation-and-polymer thermal degradation. **b**, Weight loss profiles of MPEC gels for each metal ion with different pH: (i) pure PAA without any metal crosslinkers, (ii) Na⁺-MPEC, (iii) Ca⁺-MPEC, and (iv) Al⁺-MPEC. **c**, Dash lines are theoretical metal binding ratio based on the resin formulation. The markers are measured metal binding ratio as inferred from TGA using residual oxide weights.

TGA was used to quantify the water content and the metal cation (M^{n+}) to polyelectrolyte repeat unit (r.u./RCOO⁻) binding ratio in the gels by analyzing the weight loss profile during heating. As shown in Figure 3.4, the TGA curves display distinct weight loss events corresponding to different thermal decomposition stages of MPECs: dehydration, desolvation, decarboxylation, and polymer thermal degradation. Figure 3.4b illustrates these thermal transitions, regardless of metal ion type or pH, exhibited similar weight loss profiles and thermal stability.

	pH	Loosely Bound			Crystalline			Total
		Start	End	Delta	Start	End	Delta	-
PAA	0.9	100%	84.04%	15.96%	84.04%	83.66%	0.38%	16.34%
PAA	2.54	100%	85.97%	14.03%	85.97%	85.64%	0.33%	14.36%
PAA	2.8	100%	85.04%	14.96%	85.04%	84.57%	0.47%	15.43%
PAA	3.25	100%	84.48%	15.52%	84.48%	83.42%	1.06%	16.58%
Na H ₂ O	2.55	100%	88.88%	11.12%	88.88%	85.96%	2.92%	14.04%
Na 2M NaOH	2.95	100%	91.48%	8.52%	91.48%	87.68%	3.81%	12.32%
Na 4M NaOH	3.25	100%	93.44%	6.56%	93.44%	88.83%	4.61%	11.17%
Ca H ₂ O	2.15	100%	94.90%	5.10%	94.90%	90.87%	4.03%	9.13%
Ca 2M NaOH	2.72	100%	89.77%	10.23%	89.77%	85.89%	3.88%	14.11%
Ca 4M NaOH	3.1	100%	89.07%	10.93%	89.07%	85.73%	3.34%	14.27%
Al H ₂ O	1.4	100%	91.64%	8.36%	91.64%	86.90%	4.75%	13.11%
Al 2M NaOH	2.4	100%	89.00%	11.00%	89.00%	84.35%	4.66%	15.65%
Al 4M NaOH	2.97	100%	89.17%	10.84%	89.17%	84.45%	4.71%	15.55%

Table 3.3: **Quantified water contents in MPEC gels from TGA analysis.** Using inflection points in derivative data, regions of loosely bound water evaporation and tightly bound water was determined. The cumulative total of these values is reported as the total water content (wt%).

Using the first derivative of the TGA curves, we identified the contents of loosely bound water and tightly bound (crystalline) water associated with the polymer and metal cation–carboxylate bonds. The water content was consistent across all samples at approximately 14% \pm 2.14% by weight, with a median of 14.27% after post-processing (Table 3.3). This uniform water content allows us to decouple the effects of solvent, ion, and pH, ensuring a fair comparison between gels.

To determine the metal ion content, we estimated the metal cation (M^{n+}) to polyelectrolyte repeat unit (r.u./RCOO⁻) binding ratio based on the residual metal oxide weights after complete polymer degradation (Figure 3.4a). The residual metal oxide content was calculated as:

$$\text{wt}\%_{\text{MOx}} = \text{wt}\%_{\text{MPEC}} - \text{wt}\%_{\text{Soot}}$$

where residual MPEC gel, $\text{wt}\%_{\text{Soot}}$, and Soot content, $\text{wt}\%_{\text{Soot}}$, were determined by running MPEC gels and pure PAA samples to 1000°C , respectively.

The mole fraction of metal ions was determined by:

$$n_{\text{M}} = \text{wt}\%_{\text{MOx}} \times \frac{1\text{g}}{MW_{\text{MOx}}} \times \chi_{\text{M,MOx}}$$

where $\chi_{\text{M,MOx}}$ represents the stoichiometric ratio of metal to metal oxide and MW_{MOx} is the molar mass of the corresponding metal oxide.

The mole fraction of repeat unit on PAA was determined by:

$$n_{\text{r.u.}} = (\text{wt}\%_{\text{PAA}}) \times \frac{1\text{g}}{MW_{\text{AA}}} \approx (\text{wt}\%_{\text{Dried Gel}} - \text{wt}\%_{\text{MOx}}) \times \frac{1\text{g}}{MW_{\text{AA}}}$$

where MW_{AA} is the molar mass of the acetic acid. $\text{wt}\%_{\text{Dried Gel}}$ is the fully dehydrated weight of the gels ($\text{wt}\%$ at $200\text{-}260^\circ\text{C}$, depending on metal species).

As a result, the metal-to-PAA binding ratio was calculated as:

$$r = \text{M} : \text{PAA} \cong \frac{n_{\text{M}}}{n_{\text{r.u.}}}$$

As shown in Figure 3.4c, the experimentally determined binding ratios (markers) were consistent with the theoretical expectations (dashed lines) based on the resin composition. This agreement confirms that the printed MPEC gels contain the intended ion density, validating that the photoresin formulation accurately translates into the gel composition.

Material Uniformity

To assess the uniformity and homogeneity of metal crosslinkers in the dehydrated MPEC gels, we performed X-Ray Fluorescence Spectroscopy (Micro-XRF) using an M4 TORNADO Spectrometer. Mapping mode was applied to an identical sample area of $3.5\text{ mm} \times 3.5\text{ mm}$ with a thickness of 2.5 mm , a resolution of $<20\ \mu\text{m}$, and a dwell time of 40 ms/px under conditions of 50 kV and $600\ \mu\text{A}$. Spectral counts were directly recorded (see Table 3.4).

Overall, XRF mapping in Figure 3.5 confirmed that metal crosslinkers were homogeneously distributed throughout the samples for all metal ions (Na^+ , Ca^{2+} , and Al^{3+}), validating the uniformity of metal crosslinkers in the AM-fabricated MPEC gels. However, a pH-dependent variation was observed for higher-valency ions. For Na^+ (pH 2.40 to 3.20) and Ca^{2+} (pH 2.15 to 3.04), the metal ion distributions

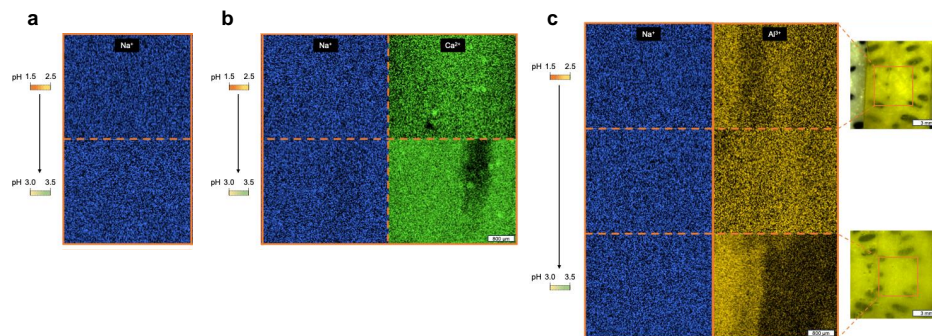


Figure 3.5: **X-Ray Fluorescence (XRF) mapping of AM-fabricated MPECs. a,** Na^+ MPEC, **b,** Ca^{2+} MPEC, and **c,** Al^{3+} with sodium counter-ion from buffer. From top to bottom in each pane shows samples fabricated in most acidic to most alkaline conditions. Outset shows large area map of XRF relative to total sample width. Spot size for all XRF maps is $20 \mu\text{m} \times 20 \mu\text{m}$.

Gel	pH	Phosphorus	Na^+	$[\text{M}^{n+}]$
PAA	0.9	7.6323E+04	2.7100E+02	
	2	3.6869E+04	7.7300E+02	
	2.54	7.1893E+04	8.6400E+02	
	2.8	5.7893E+04	1.2630E+03	
	3.25	4.5382E+04	1.6520E+03	
MBAA	0.9	2.0239E+05	5.8330E+03	
	Na^+	2.4	7.7519E+05	6.2780E+03
Ca^{2+}	3.2	1.4698E+06	6.2425E+04	
	2.15	8.0942E+04	1.8540E+03	4.7704E+05
Al^{3+}	3.04	2.6679E+06	4.5130E+04	7.2856E+06
	1.4	4.8188E+05	3.9330E+03	6.1579E+04
	2.55	1.3306E+06	3.4479E+04	4.3611E+05
	3.1	9.2093E+05	4.9520E+04	4.1606E+05

Table 3.4: **XRF Counts in constant volume mapping volume across cation and pH ranges tested.** Counts are reported for identical area ($3.5 \text{ mm} \times 3.5 \text{ mm}$), sample thickness (2.5 mm), resolution ($20 \mu\text{m}$), and dwell time (40 ms/px) under 50 kV , $600 \mu\text{A}$ conditions.

remained relatively uniform across the gels. In contrast, for Al^{3+} samples, distinct aluminum-rich and aluminum-poor regions emerged at higher pH levels, suggesting a phase separation effect.

Material Thermodynamic Equilibrium

Establishing that the MPEC gels achieved thermodynamic equilibrium is essential for accurately interpreting the results and comparing them with theoretical predictions. To address this concern, we conducted a series of experiments that provide

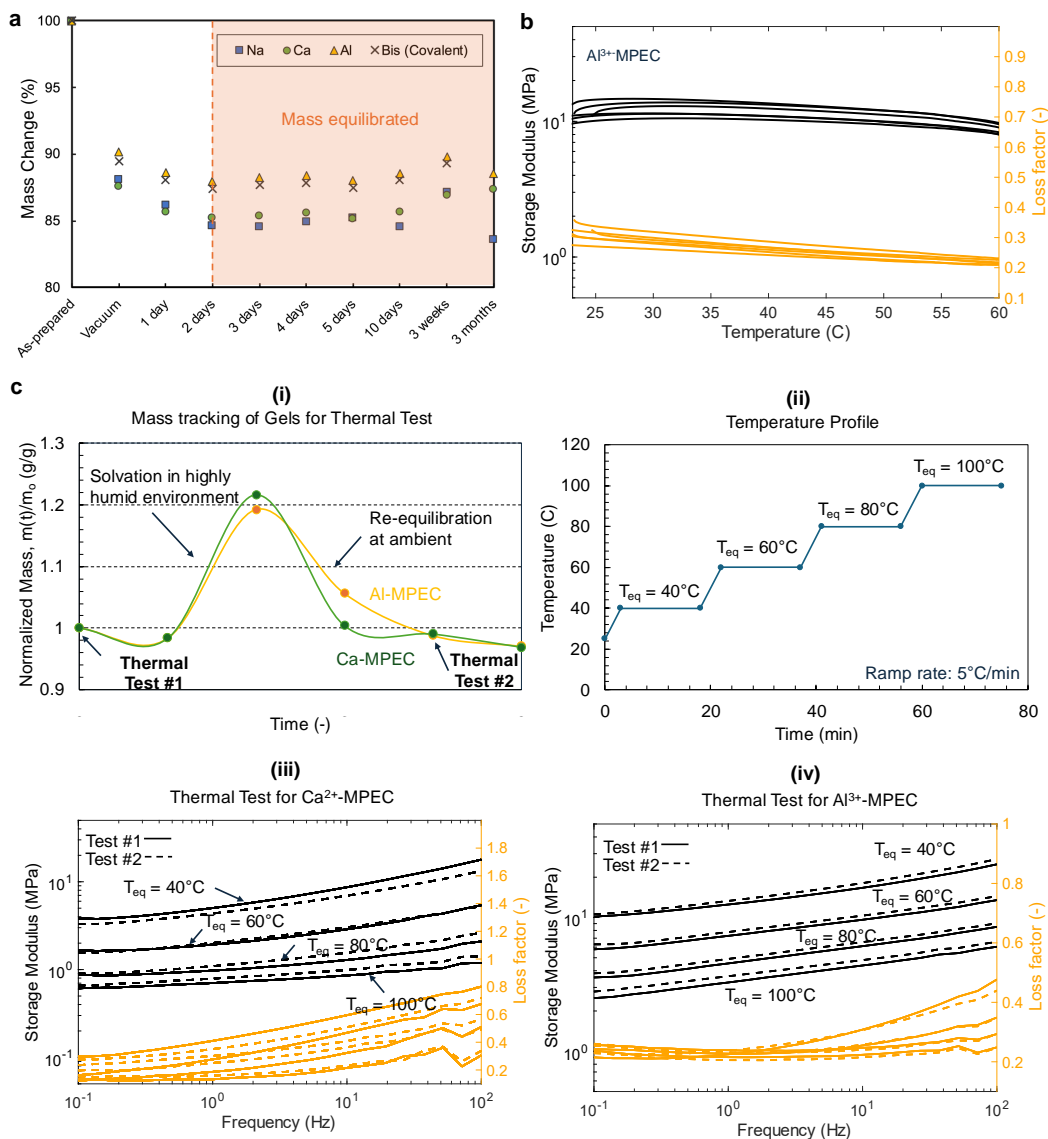


Figure 3.6: **Thermodynamic equilibrium of AM-fabricated MPECs.** **a**, Mass tracking of MPEC-gels over fabrication stages, confirming mass equilibration. **b**, Reproducible thermal cycles over $25^\circ C$ to $60^\circ C$ **c**, Reproducible thermo-mechanical behaviors of re-equilibrated gels at $T > T_g$ (i) Mass tracking of Ca^{2+} (green) and Al^{3+} -MPEC gels (yellow) to ensure constant solvent content between tests. (ii) Temperature profile applied during the test, using four different equilibration temperatures to probe the rheological behavior of (iii) Ca^{2+} (green) and (iv) Al^{3+} -MPEC gels.

multiple lines of evidence supporting the equilibrium state of the gels.

Firstly, as shown in Figure 3.6a, we monitored the mass of the gels throughout the fabrication stages and observed that they reached equilibrium densities within

three days post-processing. When exposed to a high-humidity environment (RH \sim 80%), the gels exhibited a temporary mass increase due to hydration but consistently returned to their original mass after a certain period. This behavior indicates that the solvent content likely reached an equilibrium state.

To assess the thermal stability of the gels, we subjected them to repeated heating and cooling cycles between room temperature and 60°C at a rate of 5°C/min with a fixed frequency of 1 Hz. By controlling for solvent evaporation, we observed consistent thermal signatures in storage modulus and tan delta values across more than five cycles for each gel, suggesting that the thermal properties were stable and reproducible (Figure 3.6b).

Lastly, to verify the stability of the gels at higher temperatures, we extended the analysis up to 110°C (Figure 3.6c). Before each cycle, (i) the gels were re-solvated in a high-humidity environment (RH \sim 80%) for over 24 hours to ensure consistent solvent content. (ii) The gels were then equilibrated at 40°C, 60°C, 80°C, and 100°C for 10 minutes each during the temperature ramp to minimize thermal drift. Rheological measurements were performed at each temperature, sweeping the frequency from 0.1 Hz to 100 Hz. The results showed consistent thermal signatures across all cycles, even at elevated temperatures for both (iii) Ca²⁺-MPEC and (iv) Al³⁺-MPEC.

Collectively, these findings strongly support that the MPEC gels have likely reached thermodynamic equilibrium, providing a reliable basis for interpreting the results and comparing them with theoretical models.

3.5 Molecular-Level Controls: Binding and Coordination

The fabrication platform developed in this work offers the ability to modulate several chemical parameters for MPECs, including metal identity, valency, pH, solvent content, and monomer type/concentration. To understand the influence of these molecular controllers on global material properties, we focused on the effects of metal valency and pH for the subsequent multiscale studies. The roles of solvent and metal identity are discussed in Section 3.8 for conciseness.

3.5.1 Metal Valency

Metal valency is a critical parameter that controls both binding strength and coordination number of metal cations. To screen potential metal nitrate salts, we performed Density Functional Theory (DFT) calculations to estimate the binding energy between metal cations and carboxylate (acetate) groups. Although this provides a

qualitative understanding, it serves as a useful approximation of the interactions between charged sites and metal ions. Bidentate structures were used as the initial configuration based on the FTIR spectra in Figure 3.3, with water as the solvent modeled using the Conductor-like Polarizable Continuum Model (CPCM) [81].

As shown in Figure 3.7, the binding energy scales linearly with the cation valency, demonstrating control over both the coordination number of complexed polyanion sites and the binding energy [82–84]. However, metal ions with available d-orbitals (e.g., Ni^{2+} , Cr^{3+}) deviate from this scaling behavior due to the formation of overlap π -orbitals. Detailed discussions on the effects of metal identity can be found in Section 3.8.

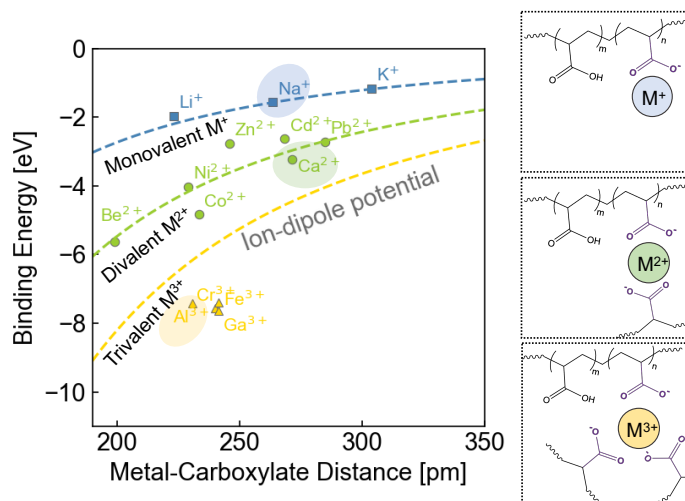


Figure 3.7: **Binding energy of multivalent metal ions.** Binding energy vs. metal-carboxylate separation of multivalent metal ions printable with the developed fabrication method. Dashed curves represent theoretical metal cation-PAA dipole interactions. The inset highlights how the different charges of metal cations lead to distinct coordination numbers around the metal center.

In our studies, we selected three representative hard ions— Na^+ , Ca^{2+} , and Al^{3+} —to isolate the effects of valency without the interference of d-orbital interactions. Due to the low binding energy of Na^+ relative to protonation, both pure PAA gels and Na^+ -MPEC gels were used as control systems depending on the pH range. The weak electrostatic interactions of Na^+ allow the monovalent gel to serve as a reference system where entanglement is the primary contributor to the material response. Additionally, we fabricated non-dynamic PAA gels covalently crosslinked with N,N'-Methylenebisacrylamide (MBAA) to highlight the contribution of dynamic

bonds. For consistency, each crosslinker is represented by a consistent color: blue for Na^+ , green for Ca^{2+} , yellow for Al^{3+} , and gray for MBAA.

As for our studies, we focus on three representative hard-ions for each valency, Na^+ , Ca^{2+} , and Al^{3+} , to isolate the effects of valency without the concomitant effects of d-orbital interactions. Owing to the low binding energy of Na^+ relative to protonation, pure PAA gels and Na^+ -MPEC gels are used as a system control, depending on the pH range explored. The weak electrostatic interactions of Na^+ ions allow the monovalent gel to serve as a reference system where entanglement is the major contributor to the material response. For comparison, non-dynamic PAA-gels covalently crosslinked with N,N'-Methylenebisacrylamide (MBAA) were also fabricated to demonstrate the contribution of the dynamic bonds. For the remainder of this article, each crosslinker is represented by a consistent color except where otherwise specified: blue for Na^+ , green for Ca^{2+} , yellow for Al^{3+} , and gray for MBAA.

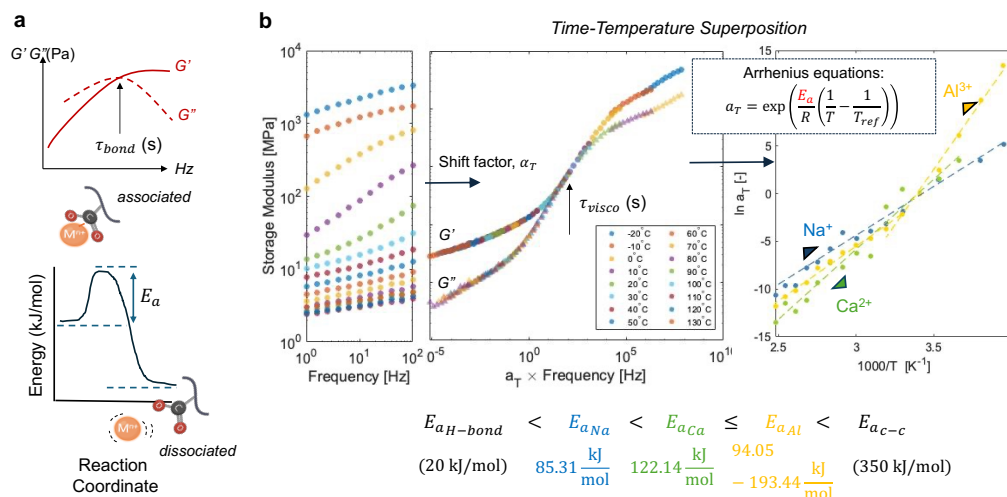


Figure 3.8: **Experimentally measured activation energy of metal.** **a**, A schematic of bond dissociation activation energy measured from rheological data. **b**, Measured rheological data for Al^{3+} -MPEC via time-temperature superposition. The data indicates that clear.

The activation energy associated with the binding strength of metal ions can be experimentally estimated by analyzing the bond relaxation time. As shown in Figure 3.8a, the rheology of transient networks allows us to assess the dissociation and reassociation dynamics of metal-coordination bonds within the network using frequency sweeps. By applying the Arrhenius Equation, we extracted the activation energy of the relevant relaxation processes [71, 85].

For MPEC gels with different metal valencies, we performed frequency sweeps to probe these dynamics. However, the rheological data in Figure 3.8b indicated that a distinct bond dissociation regime was not observed. Instead, the results showed a viscoelastic relaxation time, suggesting that the measured response is a convoluted effect of multiple network relaxations. The activation energy for the viscoelastic relaxation process was found to scale with metal valency, suggesting that binding strength influences the energy difference between relaxation processes. However, the exact contribution of bond strength remains unclear due to structural heterogeneities and the presence of other relaxation dynamics. Further investigation is required to clarify the relationship between binding strength and relaxation dynamics in the MPEC networks.

3.5.2 Polyanion Charge Density

Another key parameter is the pH of the resin, which was controlled using nitric acid and sodium hydroxide, complementary to the sodium acrylate buffer and nitrate salts. During printing, each ~50 μ m-thick layer is saturated in the resin with exposure time of 30s, allowing for equilibration with the solution. To minimize pH-dependent chain conformation effects induced from anion repulsion and the changes in hydrogen bonding [86], we maintained the pH in our experiments below the pKa of polyacrylic acid (~4.5) (Table 3.5). FTIR confirmed that the change of hydrogen bonding was minimal within the range of pH explored and the deprotonation of the polyacid as pH increases (Figure 3.9).

The high ionic strength of the gel [87, 88] allows us to correlate the pH with charge sparsity of polymerised polyanion following the Henderson–Hasselbach (HH) equation, $\langle \ell \rangle = [\text{COOH}]:[\text{COO}^-]$ (Figure 3.10a). For multivalent metal salts, their strong association with the charged sites on the polymers shifts the deprotonation equilibrium forwards [89, 90], reducing the charge sparsity of the polyanion relative to the HH expectation. Thus, we account for this effect using a modified HH equation, as shown in Figure 3.10b (see Appendix C.1 for derivations). Under the experimental conditions, the modified HH equation demonstrates the availability of sufficient number of binding sites on the polymer backbone to complex with the available metal ions ($[\text{COO}^-] \gg n[\text{M}^{n+}]$). Figure 3.10b conveys the three pH regimes experimentally explored in this work: (1) low ($1.5 < \text{pH} < 2.5$), (2) intermediate ($2.5 <$

²To keep the constant concentrations of all chemical species in the photoresin, the same volume of diluent/buffer was added as indicated on Supplementary Table 1.

³pH was measured without the photoinitiator and glycerol to avoid the reading errors induced by the organic solvents.

Metal ions	Diluent/Buffer ²	pH ³
Na ⁺	H ₂ O	2.55
	2M NaOH	2.95
	4M NaOH	3.25
Ca ²⁺	H ₂ O	2.15
	2M NaOH	2.72
	4M NaOH	3.10
Al ³⁺	H ₂ O	1.40
	2M NaOH	2.40
	4M NaOH	2.97
Ni ²⁺	H ₂ O	2.06
	2M NaOH	2.62
	4M NaOH	3.05
Co ²⁺	H ₂ O	2.15
	4M NaOH	2.95
Fe ³⁺	H ₂ O	0.70
	4M NaOH	2.84
Cr ³⁺	H ₂ O	1.55
	4M NaOH	3.00

Table 3.5: pH measurement of photoresin.

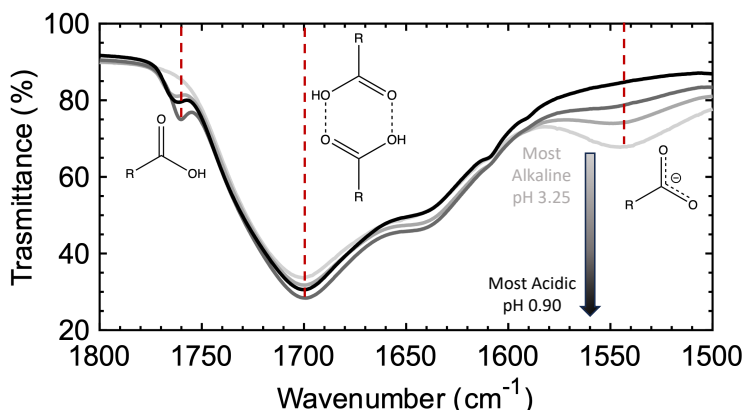


Figure 3.9: **Infrared spectrum of poly(acrylic acid) under variable pH from most acidic (pH \approx 0.9) to most alkaline (pH \approx 3.25) in region of signature bands for the carboxyl and asymmetric carboxylate stretches.** pH control of (de)protonation of the polyacid is clearly observed in the infrared spectrum via the disappearance of the monomeric R-COOH shoulder and emergence of the R-COO⁻ asymmetric mode as pH increases.

pH < 3.0), and (3) high (3.0 < pH < 3.5). Using pH measurements of the photoresin as a proxy, these values correspond to the range of polyanion charge sparsity $\langle \ell \rangle$, of approximately 100:1 to 10:1.

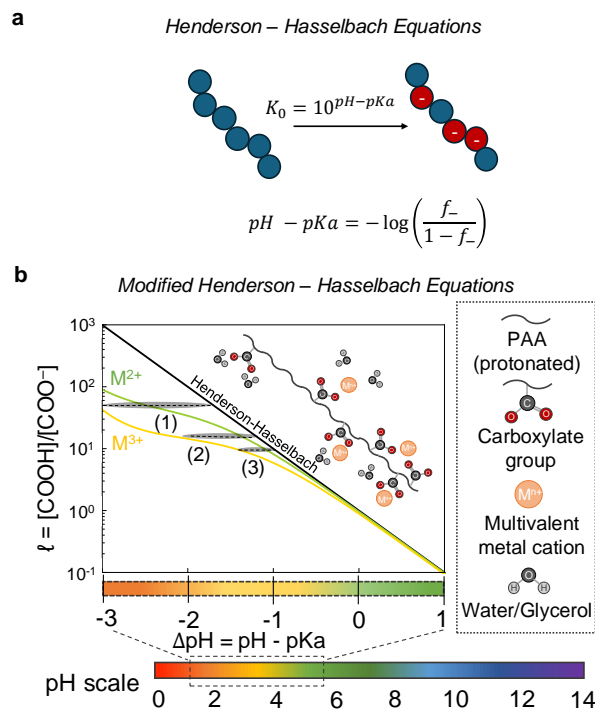


Figure 3.10: **Modified Henderson equation for polyanion charge density estimation.** **a**, Henderson Hasselbach equation estimate charge density w.r.t. the pH values. **b**, pH versus charge sparsity of polyanion chains, with varying cation valency of fixed concentration (0.02 mol%). Strong association of multivalent metal cations pushes the equilibrium forwards below the Henderson–Hasselbach theory in the range of pH of interest.

3.6 Multiscale Interactions

With our AM fabrication platform, we can precisely tune molecular parameters and fabricate macroscale MPEC gels that exhibit distinct functionalities based on molecular design choices. To fully understand how molecular-level interactions – particularly metal valency and polyanion charge density – propagate to global material properties, we perform multiscale characterization spanning from atomic interactions to continuum-scale mechanical behavior.

As illustrated in Figure 3.11, polymer structures exhibit a hierarchical organization across multiple length and time scales: from molecular-level chemistry, polymer-ion interactions, polymer network microstructures to continuum-level mechanical behavior. To capture the material response across different hierarchical levels, we combined experimental characterization, theoretical modeling, and computational simulations.

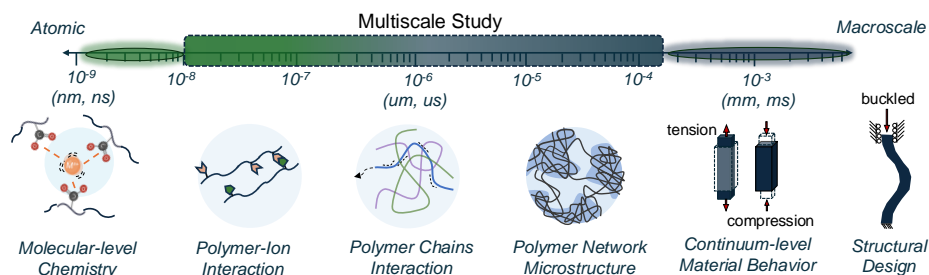


Figure 3.11: **Multiscale-span hierarchical organization of polymer structures.**

3.6.1 Chain Relaxations

To identify how the molecular controls affect the chain-level interactions, we characterized the chain relaxation. First, we performed temperature ramp to capture phase changes in the polymer as shown in Figure 3.12a. Dynamic Mechanical Analysis (DMA) results reveal that MPEC gels exhibit the expected thermoplastic phase behavior, transitioning through distinct regimes:

1. Glassy Regime ($T < 0^{\circ}\text{C}$): Polymer chains are immobilized, and the material exhibits a high storage modulus (E').
2. Glassy-to-Rubbery Transition ($5 - 50^{\circ}\text{C}$): A 2 to 3 order of magnitude decrease in E' indicates the onset of chain mobility.
3. Rubbery Regime ($50 - 70^{\circ}\text{C}$ and above): Polymer chains gain full mobility and undergo reptation, characteristic of an entangled network.

Despite the presence of dissociable metal–polymer crosslinks, a viscous flow regime was not observed at high temperatures. Instead, material embrittlement occurs beyond 170°C , attributed to water evaporation and the formation of anhydride bonds. This highlights the critical role of solvent phases in mediating polymer motion within MPEC gels.

While the thermal-phase transitions appear independent of metal valency, the rubbery regime distinctly reflects the impact of metal coordination on polymer mobility. As shown in Figure 3.12a, higher-valency metal ions restrict chain motion, leading to an increase in the plateau modulus in the rubbery phase. To quantify this effect, we estimated an effective plateau modulus from the storage modulus. Due to the incomplete rubbery regime for water evaporation, an effective plateau modulus was

defined at $T_g \ll T \sim 150^\circ\text{C} \leq T_{\text{exo-endo}}$ of the polymer in the rubbery state (Figure 3.12b). As seen in Figure 3.12c, higher valency gels induced higher plateau modulus. The plateau modulus of crosslinked polymer correlates with both polymer entanglement and crosslinking density, so to confirm the role of metal coordination and chain entanglement in governing polymer relaxation, we tried to compare our MPEC gels with the theoretical benchmarks for purely entangled polymer chains (no crosslinks) and permanently crosslinked polymer chains.

Using aqueous gel permeation chromatography (GPC), we estimated the molecular weight (M_w) of MPEC gels, which ranged from 270 kDa to 450 kDa, corresponding to a degree of polymerization of $N \sim 270 - 500$. From [91], for a long poly acrylic acid (~ 560 kDa) in theta-solvent, Small-angle X-ray scattering (SAXS) estimates the radius of gyration, $R_g \sim 227\text{\AA}$. Although our solvent system is not a theta solvent, which will non-negligibly impact the R_g of our chains, we used this measurement as a bulk part estimation for comparison. This enable us to estimate the corresponding molecular parameters [92]:

$$R_g^2 = \frac{1}{3}C_\infty n\ell^2. \quad (3.1)$$

where n is the number of repeat units, ℓ for C-C bond = 1.54\AA . This results in the Flory characteristic ratio, $C_\infty \approx 8.3$, and the Kunh length of poly(acrylic)acid, $b \approx 8.3\text{\AA}$.

$$v_o = b^2 d \sim \frac{1}{2}b^3 \sim 1.93\text{nm}^3. \quad (3.2)$$

The entanglement is

$$N_e \sim 100 \frac{v_o^2}{b^6} \sim 25. \quad (3.3)$$

The effective entanglement (G_e) and crosslinking plateau modulus (G_x) at fixed temperature, $T = 150^\circ\text{C}$, where the experimental modulus confidently reaches the plateau, can be analytically approximated [93]:

$$G_e = \frac{\rho RT}{M_e} \sim \frac{kT}{v_o N_e} \sim 0.12\text{ MPa}. \quad (3.4)$$

$$G_x = \rho RT \frac{1}{M_e + M_x} \sim \frac{kT}{v_o} \left(\frac{1}{N_e} + \frac{1}{N_x} \right) \sim 0.87\text{ MPa}. \quad (3.5)$$

Pure PAA and Na^+ -MPEC gels at all pH have almost identical values to to G_e , owing to the lack of crosslinking and indicating completely driven by modulus. Multivalent gels deviate from this limit where the plateau modulus scales with

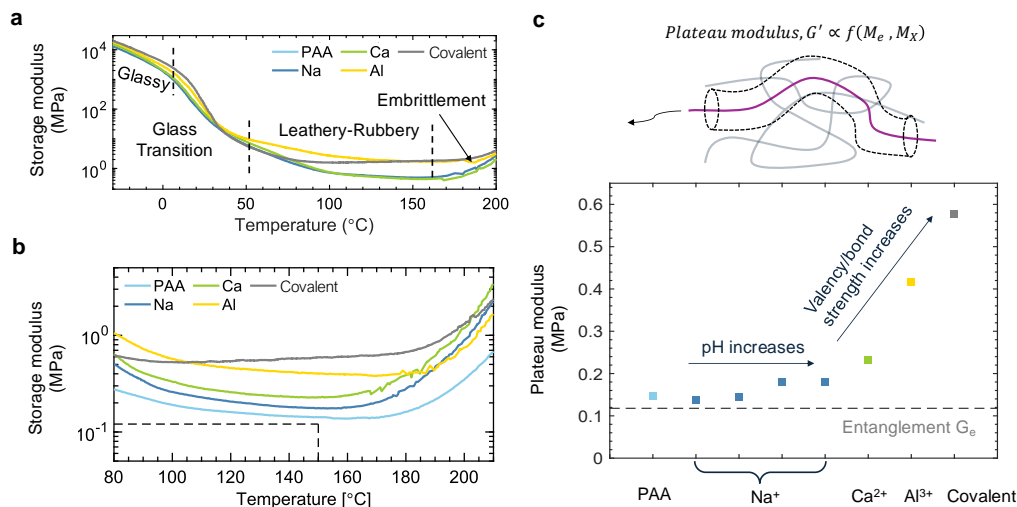


Figure 3.12: **Chain relaxation and plateau modulus.** **a**, Thermomechanical analysis of MPEC gels (storage modulus vs. temperature) showing distinct phase transitions of MPECs during a temperature ramp at $\sim 5^\circ\text{C min}^{-1}$. **b**, Zoomed-in thermogram of the leathery-to-rubbery transition in the temperature range of 80°C to 200°C , highlighting differences in relaxation behavior. **c**, Influence of pH and metal ion valency on the plateau modulus of MPECs in the rubbery state. Plateau modulus values were extracted from Figure 3.12b and compared with analytically estimated plateau modulus.

valency (Figure 3.12c). As expected, covalent gels observe the most-limited polymer motion available with the largest plateau modulus. It is noteworthy that all gels have lower modulus than G_x , confirming that ion dissociation partially releases chain constraints, allowing dynamic polymer mobility. This mechanism could be further corroborated from the Molecular Dynamic (MD) simulations of the gel systems.

The simulations were carried-out using the Large-scale Atomic/Molecular Massively Parallel Simulator (LAMMPS) [94]. The Kremer–Grest [95] coarse-grained force-field was used to model the polymer chains. All simulations were performed with 50 polyelectrolyte chains each with 300 beads. An implicit solvent model was used where the effects of the solvents were taken into account by using the dielectric constant and pressure of the system. This effectively models all solvents present as just two parameters. Following energy minimization and equilibration in an NpT ensemble, the production simulations were performed: an NVE simulation to analyse the relaxation modes. We computed the autocorrelation functions for ion-pair relaxation, $\rho_{\text{ion}}(0, t)$ and polymer end-to-end vector relaxation, $\rho_{\text{poly.}}(0, t)$. (physical interpretation is depicted in Figure 3.13a, b, respectively). Figure 3.13c show that higher valency ions (Al^{3+} , Ca^{2+}) exhibit significantly slower ion-pair relaxation

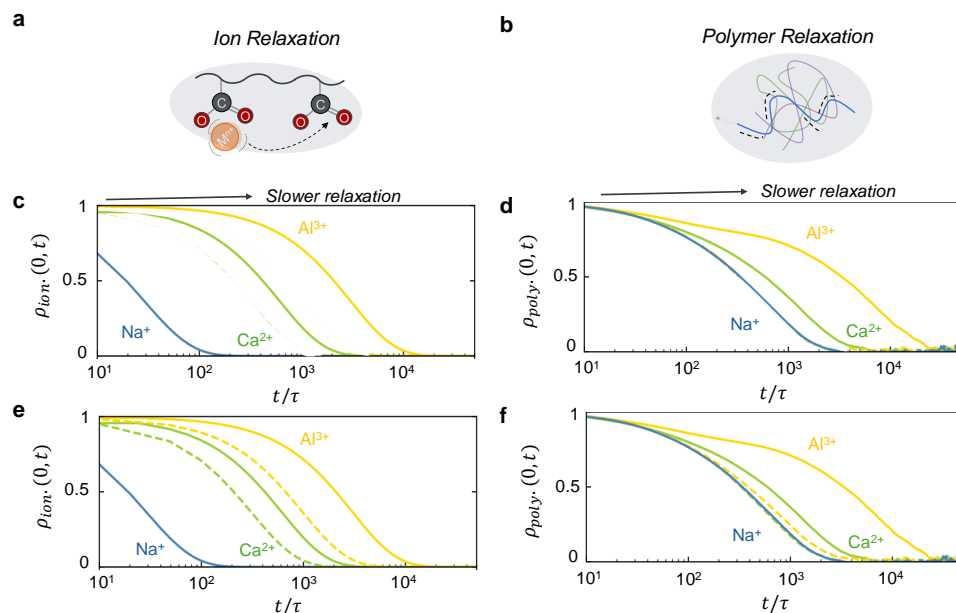


Figure 3.13: **MD simulated ion-pair and polymer chain relaxations.** **a**, Schematic representation of ion-pair relaxation. **b**, Schematic representation of polymer relaxation. Autocorrelation functions of the **c**, ion-pair and **d**, polymer end-to-end vector for MPECs with different ion valencies at low charge sparsity. Effects of high pH to the autocorrelation functions of the **e**, ion-pair and **f**, polymer end-to-end vector for MPECs with different ion valencies (solid lines correspond to the low pH and dashed ones correspond to high pH).

($\rho_{\text{ion}}(0, t)$), by almost an order of magnitude, than monovalent Na^+ , suggesting stronger and longer-lived coordination bonds. Polymer relaxation times ($\rho_{\text{poly}}(0, t)$) follow a similar trend, where the longer bond lifetime of the higher valency ions impose larger energy barriers for polymer motion, restricting chain relaxation (Figure 3.13d).

MD simulations (Figures 3.13e and f) reveal that both ion-pair $\rho_{\text{ion}}(0, t)$ and polymer relaxation $\rho_{\text{poly}}(0, t)$ are also affected by polyanion charge sparsity. Higher pH (higher charge density) accelerates ion-pair relaxation, $\rho_{\text{ion}}(0, t)$ as the increased availability of binding sites (R-COO^-) enhances competition and ion mobility to next sites. This faster ion mobility can be also propagated for $\rho_{\text{poly}}(0, t)$, affecting polymer relaxation gets faster as well.

The discrepancies between experimental and simulated charge density effects on relaxation may arise from several factors. In simulations, ion-site binding occurs in an idealized system where all binding sites are equally accessible, allowing for unrestricted ion hopping between coordination sites. However, in real MPEC net-

works, microstructural constraints introduce steric hindrance and local competition for binding sites, limiting the dynamic rearrangement of the metal-polymer interactions. Additionally, inter-chain connectivity and polymer entanglements impose topological constraints that may further affect chain mobility and relaxation dynamics, guiding us to investigate chain configurations in greater detail.

3.6.2 Chain Configurations

The configuration of polymer chains within a network plays a critical role in determining polymer integrity, mechanical properties, and final material morphology. As illustrated in Figure 3.14a, depending on metal ion valency and local charge environment, polymer chains can form two distinct crosslinking modes: intra-crosslinking, where metal ions coordinate within the same polymer chain or inter-crosslinking, bridging between different polymer chains.

To quantify the competition between inter- and intra-chain crosslinking, we employed a statistical mechanics framework based on Semenov and Rubinstein's approach [96]. In assumptions that all negative sites are fully associated (i.e. $X_i = 1$) and that intra-crosslinks are only formed between nearest neighbors, we can estimate the entropic penalty for forming an intra-crosslink: [97]:

$$\Delta S_{\text{intra.}} = m_{\text{intra.}} k_B \ln \ell^{3/2}, \quad (3.6)$$

where m_{intra} is the number of intra-crosslinked pairs, k_B is the Boltzmann constant, and ℓ is the polymer segment length.

By incorporating this entropic cost with metal ions-polymer association equilibrium, and the combinatorial probability of intra-crosslinks formation, we can analytically estimate the fraction of inter-chain f_{inter} vs. intra-chain crosslink (f_{intra}) in MPEC systems as a function of metal valency and polyanion charge density. The theoretical estimate is shown in Figure 3.14b (see Appendix C.2 for full derivations). As shown in Figure 3.14b, the fraction of inter-crosslinks (f_{inter}) is strongly dependent on metal valency. Trivalent ions (Al^{3+}) exhibit a higher f_{inter} compared to divalent ions (Ca^{2+}). This indicates that higher valency metals provide more probability in forming inter-crosslinked coordination sites, whereas divalent systems favor intra-crosslinking due to lower coordination numbers and higher entropic costs for inter-chain bonding.

Beyond metal valency, polyanion charge density strongly influences crosslinking distribution as well. Initially, increasing charge density enhances f_{inter} , as more metal ions bind to available sites, promoting inter-chain bonding. However, past an

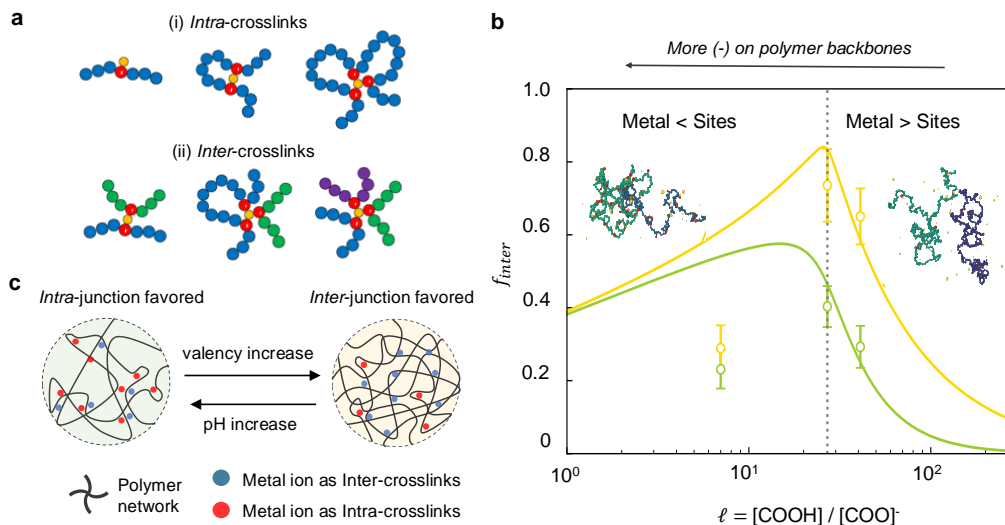


Figure 3.14: **Chain configurations.** **a**, Different possible configurations for intra- and inter-crosslinks. Different colors represent different chains. **b**, Theoretically- (lines) and computationally- (markers with 95% confidence interval) predicted fraction of inter-crosslinked ions for divalent (green) and trivalent (yellow) systems at different charge sparsity. Dotted line corresponds to the sparsity where the metal ions perfectly neutralize the polyanion. **c**, Schematic representation of the effects of metal ion valency and charges sparsity on the distribution of intra- vs. interchain crosslinks.

optimal charge density, f_{inter} begins to decline, as excess negative charges introduce electrostatic repulsion and increase the entropic cost of inter-chain bridging. This transition occurs at the critical charge density where metal ions perfectly neutralize the polyanion (dotted line in Figure 3.14b). Beyond this point, intra-crosslinking dominates, leading to more localized polymer folding rather than inter-chain connectivity. These trends are also corroborated by MD simulations (symbols), which closely match theoretical predictions.

For our experimental case, the high-pH MPEC gels correspond to the left region of Figure 3.14b with an excess of charged sites relative to metal ion concentration. As pH increases, charge density increases, and the excess charges reduce inter-chain connectivity, leading to higher intra-crosslinking fractions. These findings reveal a complex interplay between metal valency and charge density in governing MPECs chain connectivity (Figure 3.14c)

3.6.3 Network Topology

The inter-chain crosslinks play a crucial role in the formation of MPEC gel networks. To better understand how metal valency and polyanion charge sparsity influence network formation, we performed MD simulations to observe percolation and clustering behavior under different molecular design conditions (Figure 3.15a).

For this study, we define clusters as percolating networks formed by dynamic crosslinks between polymer chains, rather than localized ion aggregation from electrostatic interactions [98]. To quantify the clustering behavior, we computed the fraction of polymer within the largest cluster, f_{cluster} , by measuring its radius of gyration (R_g) for the largest cluster and estimating its volume fraction within the total simulation box (V_{box}):

$$f_{\text{cluster}} = \frac{8(R_{g,xx}^2 + R_{g,yy}^2 + R_{g,zz}^2)}{V_{\text{box}}}, \quad (3.7)$$

where $f_{\text{cluster}} = 1$ represents a fully percolated gel network in which all chains are interconnected, while $f_{\text{cluster}} = 0$ indicates isolated polymer chains without network formation.

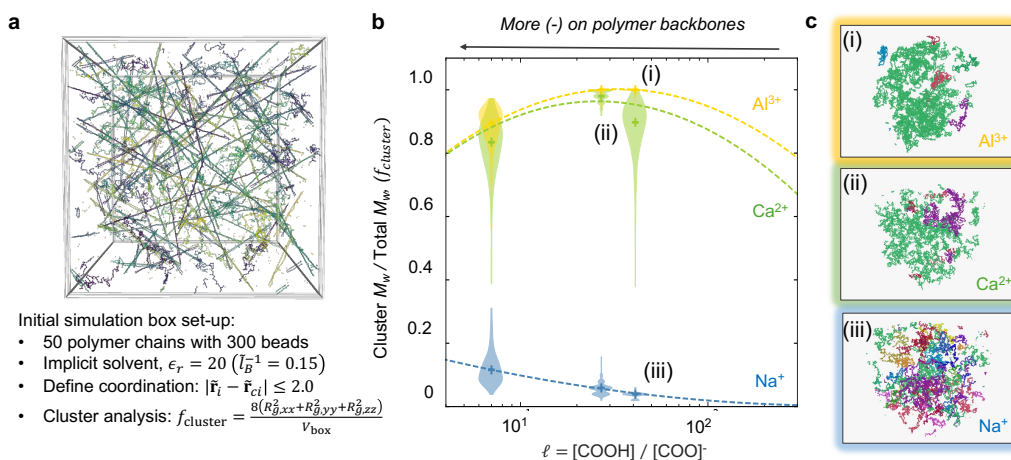


Figure 3.15: **Polymer network.** **a**, MD simulation set-up for cluster analysis. **b**, Violin plot of simulated cluster distribution across different metal valencies and charge sparsity. The wider distributions represent greater fluctuations in cluster formation. **c**, Representative MD snapshots illustrating the percolation of polymer chains under different valency conditions. The same color represents polymer chains that are interconnected.

Figure 3.15b demonstrates the effects of metal valency and charge sparsity. The results indicate that divalent and trivalent ions promote extensive polymer crosslinking, leading to percolated networks where nearly all polymer chains are intercon-

nected (Figure 3.15c). In contrast, monovalent systems exhibit significantly lower f_{cluster} , as Na^+ ions lack the ability to directly form inter-chain crosslinks, resulting in smaller clusters primarily stabilized by polymer entanglements. Trivalent MPECs exhibit the narrowest cluster distribution, suggesting more uniform, stable network formation due to stronger binding and slower relaxation dynamics. The trend in cluster size with respect to charge sparsity mirrors the previously observed fraction of inter-chain crosslinking (f_{inter}) in Figure 3.14b. This suggests that inter-chain crosslinking serves as a fundamental driving force for the evolution of polymer network topology.

Experimentally verifying percolation in MPECs poses challenges, as traditional X-ray scattering techniques are limited in resolving such large-scale clusters. Both simulated and experimental small-angle X-ray scattering (SAXS) results show no significant peaks at low structural factor (q) (Figure 3.16), indicating that polymer clusters in MPEC gels are too large to be detected by this method.

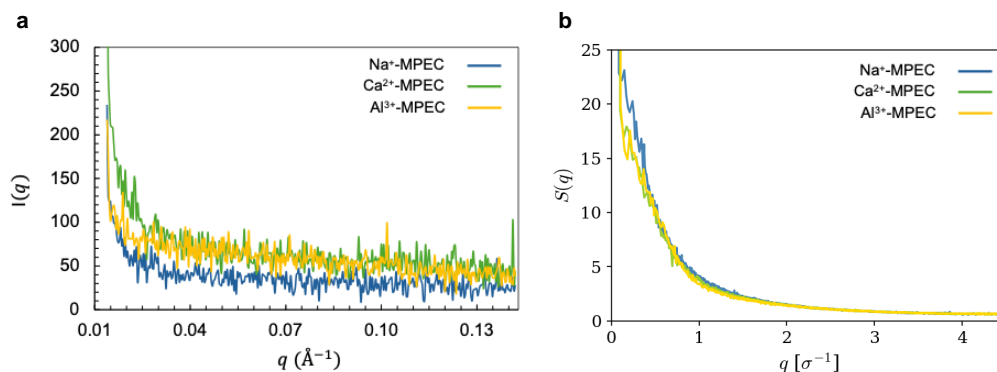


Figure 3.16: **Small-angle X-ray Scattering for cluster size estimation.** **a**, Simulated X-ray scattering signatures for mono-, di-, and trivalent gels. **b**, Experimentally measured SAXS spectrum for Na^+ , Ca^{2+} , and Al^{3+} -MPEC gels.

Instead of directly measuring the cluster size and distributions in the gels, we observe macroscale differences in optical opacity as an indirect signature of network interactions and phase behavior. As shown in Figure 3.17a, higher pH MPECs exhibit increased opacity, suggesting greater phase separation between the polymer-rich network and surrounding solvent. This phase separation becomes most apparent in the as-printed state, where the gel retains the highest solvent content. After air-drying and equilibration, opacity is reduced but remains pH-dependent (Figure 3.17b). These findings suggest that network connectivity and interactions with the surrounding environment strongly influence MPEC properties.

Scanning electron microscopy (SEM) further corroborates these observations, revealing distinct microstructural phase separation in high-pH MPECs (Figure 3.17c). At low pH, gels exhibit a uniform amorphous polymer matrix, whereas increasing charge density induces phase-separated morphologies. The interplay between

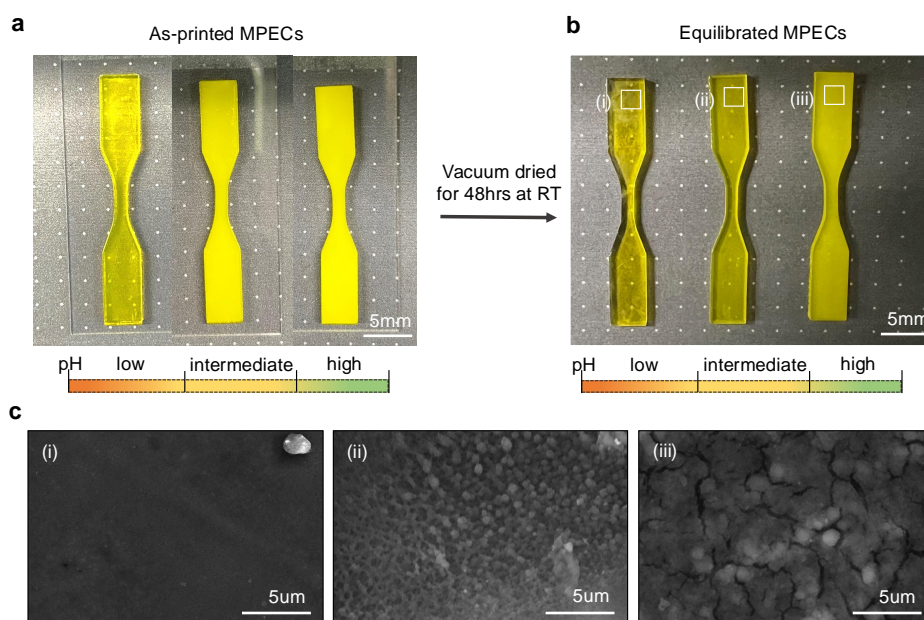


Figure 3.17: Charge-density-dependent opacity and microstructure in MPECs. **a**, Optical images of as-printed MPECs at different pH values, showing increased opacity at higher pH. **b**, Equilibrated MPECs after air drying. **c**, SEM micrographs capturing the transition from uniform microstructures at low pH to phase-separated morphologies at high pH. Regardless of the cation types, all MPECs exhibit similar responses. Ca^{2+} -MPECs were shown as a representative.

polymer charge density, metal coordination, and network topology significantly impacts the mesoscale phase behavior of MPECs. Given the observed trends in optical opacity and microstructure, understanding how metal valency and polyanion charge sparsity dictate phase separation becomes crucial for controlling bulk material properties.

3.6.4 Phase Behavior

To better understand the phase behavior of MPECs, we developed a mean-field theoretical framework for sparsely charged polyelectrolyte systems in the presence of multivalent ions. Building on the mean-field theory developed in prior works [99, 100], we accounts for three key contributions: (1) excluded-volume effects, (2) long-range electrostatic interactions, and (3) short-range association between charged polymer sites and the metal crosslinkers. The total free energy for this

system is then expressed as:

$$F = F_{\text{id.}} + F_{\text{exc.}} + F_{\text{ele.}} + F_{\text{assoc.}}, \quad (3.8)$$

where $F_{\text{id.}}$ is the free energy from ideal system, $F_{\text{exc.}}$ accounts the excluded volume effects for polymer chains treating with hard-sphere contribution, $F_{\text{ele.}}$ captures the charged species (metal ions, polyelectrolytes, solvents, other co-ions) interactions and activities using the Debye–Hückel equation [101], and $F_{\text{assoc.}}$ reflect the association interaction between metal ions and the charged polyelectrolyte backbone. A

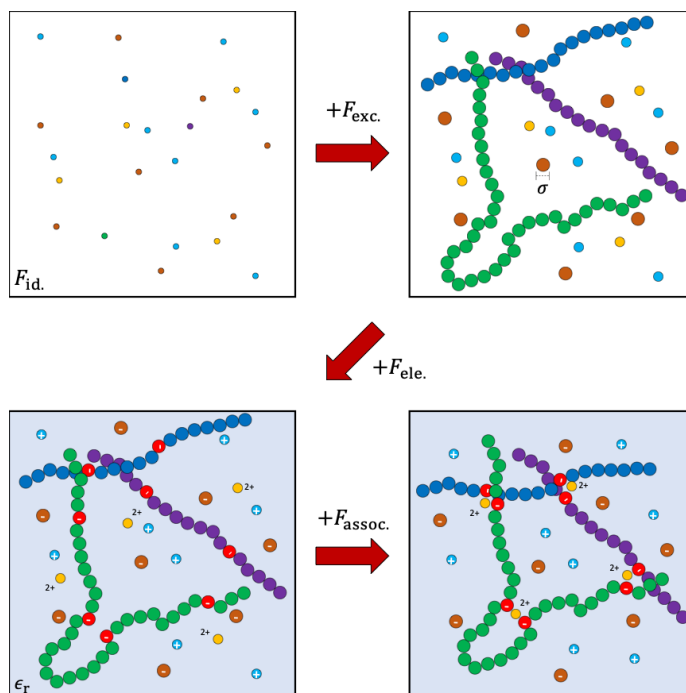


Figure 3.18: **Mean-field representation of MPEC phase behavior.** The excluded-volume, electrostatic, and metal-polyelectrolyte association interactions determine the overall phase behavior. Different species are represented: polymer chains (colored), charged polyelectrolyte sites (red), metal crosslinkers (yellow), polyelectrolyte counterions (light blue), and metal co-ions (brown).

visual representation of the contributions from each term is shown in Figure 3.18. The detailed derivation of this framework and the governing equation of state are provided in Appendix C.2.

Using this theoretical framework, we constructed phase diagrams for MPEC gels formulated with different metal valencies and polyanion charge densities (Figure 3.19). These phase diagrams delineate the conditions under which the system

remains in a single-phase gel state versus undergoing phase separation, with the boundaries marked by contour lines. Figure 3.19a illustrates the impact of metal

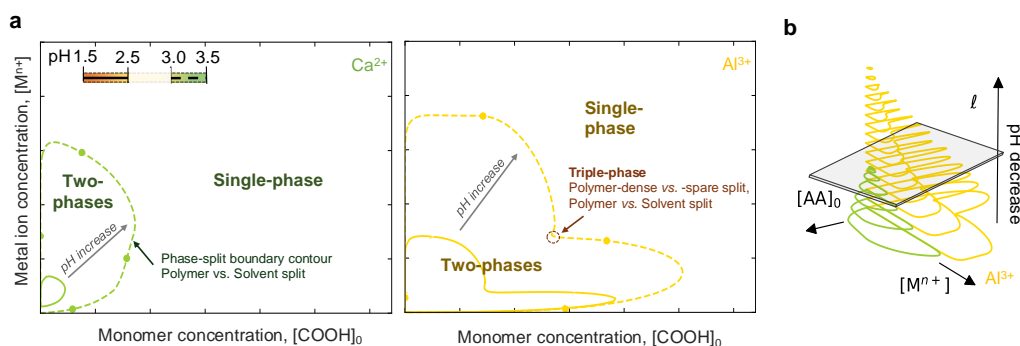


Figure 3.19: **Phase diagram of MPEC systems.** **a**, Comparison of divalent (left) and trivalent (right) metal ions, showing that trivalent gels develop a ‘notch’ feature at low concentrations, indicating gel-gel phase separation. **b**, Influence of charge sparsity (pH) on phase stability. Through-the-height contour plot demonstrate an expanded two-phase region at higher charge density (higher pH).

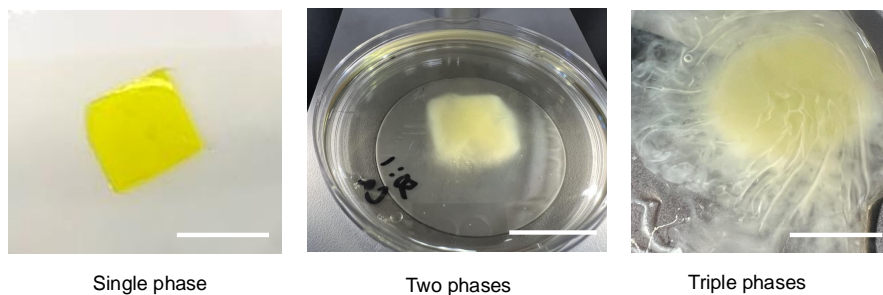


Figure 3.20: **Optical images of different phases in MPEC.** Optical images of gels at each phase from Figure 3.19a. Scale bar 20 mm.

valency on the phase boundary. While both divalent and trivalent gels exhibit the classical supernatant-coacervate phase split characteristic of polyelectrolyte systems, a distinct ‘notch’ feature emerges at low metal ion concentrations in trivalent systems. This indicates the onset of a gel-gel phase separation, where two gel-like phases with different polymer and ion concentrations coexist. The increased tendency for trivalent systems to undergo phase separation is attributed to the stronger electrostatic correlations and higher crosslinking density imposed by Al^{3+} ions.

The impact of pH, which modulates polyanion charge sparsity, is reflected in the expansion or contraction of the phase envelope. As seen in Figure 3.19b, increasing charge density (higher pH) dramatically expands the two-phase region, leading to

a greater propensity for phase separation. This trend aligns with our previous macroscopic observations of opacity and microstructural phase separation in SEM (Figure 3.17). It further demonstrates that at sufficiently low charge density (low pH), the two-phase region disappears due to the decrease in electrostatic correlations, and the system remains single-phase.

The theoretical phase diagrams were experimentally validated by direct observations of phase-separated regions (Figure 3.20) and more details in Appendix B.3). Optical images confirm that AM-fabricated MPEC gels exhibit visible phase transition from single-, two-, and triple- phases depending on the fabrication conditions, supporting the predicted phase behaviors.

Furthermore, confocal microscopy of thin-film MPECs (Figure 3.21) reveals increased phase separation at high pH, as evidenced by the autofluorescent polymer matrix (purple) becoming more discontinuous due to solvent-rich void regions (black).

3.6.5 Multiscale Study Summary

The investigation into MPECs spanned multiple scales, beginning with (1) defining molecular-level parameters, specifically metal valency and polyanion charge sparsity (pH), and (2) examining their effects on microscale interactions, including ion-pairing dynamics and chain relaxations. These molecular interactions translated into (3) chain configurations, dictating the balance between intra- and inter-chain crosslinks, which in turn shaped (4) micro- and mesoscale network structures and ultimately governed (5) the macroscale phase behavior and mechanical properties of the gels. A comprehensive summary of these interconnected effects is presented in Figure 3.22, highlighting how molecular-scale parameters dictate polymer network morphology and dynamic properties. Strong metal-polymer association (high-valency ions and low charge sparsity) leads to slow chain relaxation and a highly interconnected polymer network, forming a coalescent, percolated structure. In contrast, weak associations (low-valency ions and high charge sparsity) result in fast relaxation and a more phase-separated polymer network, favoring segregated morphologies.

With this fundamental understanding, we now shift our focus to how these structural and relaxation variations manifest in macroscale mechanical properties, such as elasticity and fracture resistance, as observed in bulk material testing. By tuning molecular parameters, we can engineer MPECs with tailored mechanical behaviors.

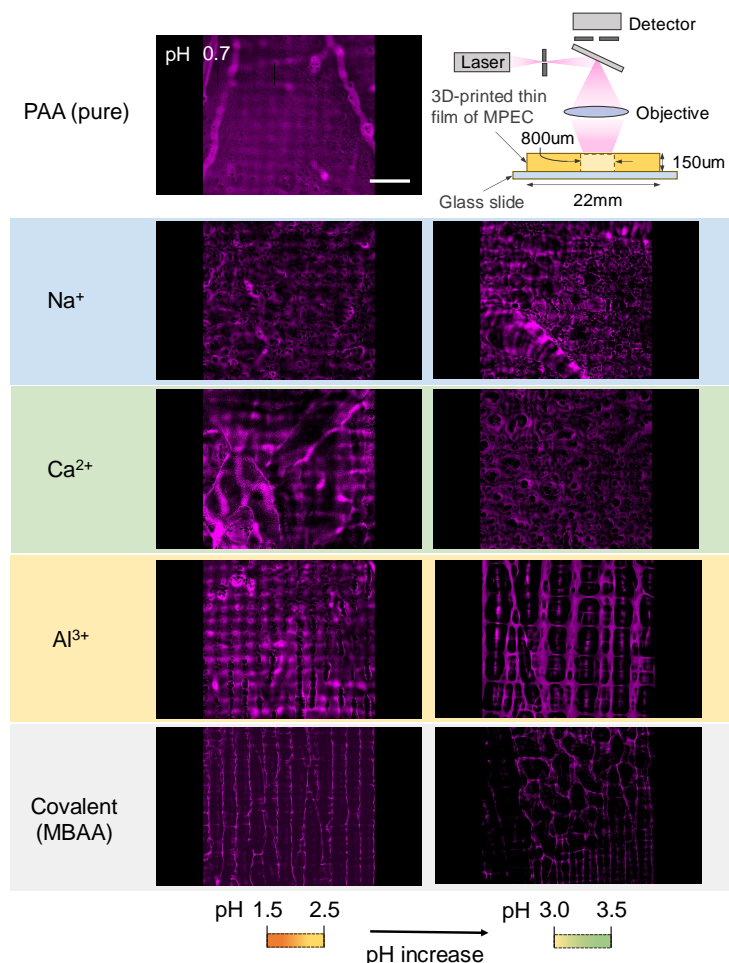


Figure 3.21: **Confocal microscope images for phase separation observation** Confocal microscopy (LSM 800, Zeiss) conducted on pH-controlled MPEC samples. It shows poly(acrylic acid) autofluorescence (purple) at 640 nm whereas negative void space corresponds to fluid filled regions. All samples are imaged across $800\ \mu\text{m}$ by $800\ \mu\text{m}$ at the depth of $50 \pm 25\ \mu\text{m}$. Higher pH of the gels demonstrating severe phase separation of fluid filled regions from polymeric region for similar molecular weight network. Scale bar for all images $150\ \mu\text{m}$.

3.7 Macroscale Mechanical Behavior

3.7.1 Uniaxial Tensile Testing

The bulk mechanical properties of MPEC gels are significantly influenced by their relaxation dynamics and structural morphologies. During tensile deformation, the mechanical response at low strain is predominantly governed by the structural topology of the network, crosslinking degree, and crosslinker functionality. As the strain increases, the influence shifts towards chain mobility and relaxation dynamics, where the rupture of crosslinkers allows stress relaxation of the stretched chains.

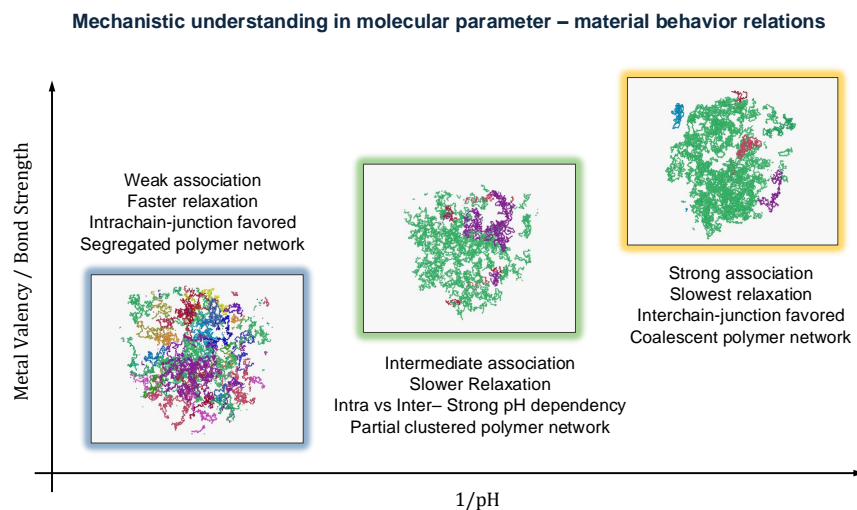


Figure 3.22: **Summary of multiscale studies.** The mechanistic correlation between molecular parameters (metal valency and polyanion charge sparsity) and macroscale gel properties. Stronger metal association leads to slow relaxation and coalescent polymer networks, while weaker association promotes faster relaxation and segregated networks. The intermediate regime exhibits a mixed behavior.

In the case of dynamically-coordinated polymers, the bond relaxation – such as the metal-ligand bond exchange rate – plays a crucial role in determining the mechanical response. Weak interactions with low association constants can facilitate chain relaxation during deformation, enhancing stretchability and modulating the stress-strain response (Figure 3.23). In contrast, strong interactions behave more like covalent bonds, leading to chain rupture under high strain. As we now understand the different relaxation and microstructure driven from the multiscale interactions from molecular species in MPEC gels, we conducted uniaxial tensile experiments on dog bone-shaped specimens to exemplify distinct mechanical response. A uniaxial test is applied a constant strain rate, $\dot{\epsilon} \approx 0.03 \text{ s}^{-1}$ at 25°C (Figure 3.24a). In Figure 3.24b, we show the stress–strain data for MPEC gels infused with different metal ions for $T \gtrsim T_g$ and within the low pH regime. This figure demonstrates a valency-dependent effect: gels with higher valency metal ions have greater stiffness and strength, and a lower stretchability. The Young’s modulus, estimated as the slope of the initial linear regime up to 10% strain, increases from 0.92 MPa Na^+ -MPEC gel to 1.30 MPa for Ca^+ -MPEC gel to 2.82 MPa for Al^+ -MPEC gel. The stresses and strains at rupture are 2.68 MPa and 1750% for the Na^+ -MPEC gel, 3.12 MPa and 1600% for the Ca^{2+} -MPEC gel, and 3.56 MPa and 870% for

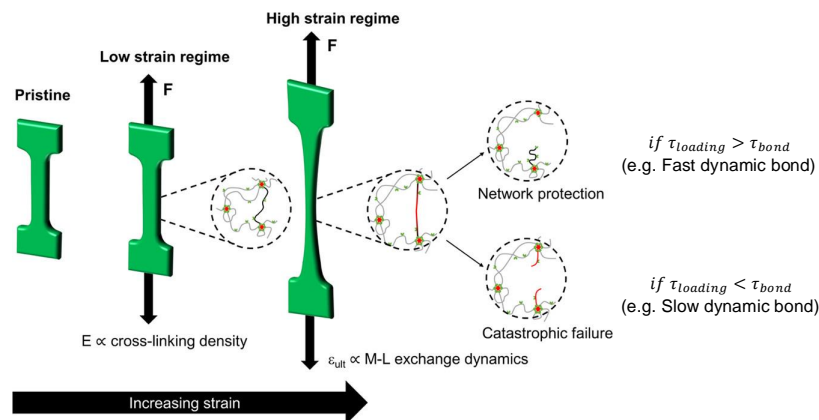


Figure 3.23: **The dependence of bulk tensile response to weakly associated bonds.** The mechanical response under load is dominated by: the initial structural topology of the network at low strain regime and the dynamics of bond relaxation at higher strain which determines the tensile failure mode. Reprinted by permission from [102]. Copyright ©2016, American Chemical Society.

the Al^{3+} -MPEC gel. These results reveal that despite the maximum number of potential carboxylate–metal bonds being kept constant for all gels, local functionality induces a noticeable difference in mechanical response. The covalently-crosslinked gel, shown in Figure 3.24b, has a similar elastic modulus to the mono- and divalent gels, most probably due to similar molecular network connectivity, which governs the material properties at low strains as described in Figure 3.23. The permanent nature of covalent bonds leads to stiffening of the gel at larger strains and results in limited stretchability of 550%.

To further interpret the mechanical behavior, we applied the Mooney-Rivlin model, a phenomenological model of elasticity, to the stress-strain data [93].

Starting with the free energy density of the ideal polymer network,

$$\frac{F}{V} = C_0 + C_1(I_1 - 3) + C_2(I_2 - 3) + C_3(I_3 - 3) + \dots, \quad (3.9)$$

where I_1 , I_2 , and I_3 are strain invariants and C_0 , C_1 , C_2 , and C_3 are stiffness tensors.

For uniaxial deformation of incompressible network,

$$I_3 = \lambda_x^2 \lambda_y^2 \lambda_z^2 = 1. \quad (3.10)$$

$$\lambda_x = \lambda, \lambda_y = \lambda_z = \frac{1}{\sqrt{\lambda}}. \quad (3.11)$$

The Mooney-Rivlin free energy density can be written in λ

$$\frac{F}{V} = C_0 + C_1\left(\lambda^2 + \frac{2}{\lambda} - 3\right) + C_2\left(2\lambda + \frac{1}{\lambda^2} - 3\right), \quad (3.12)$$

and the true stress can be obtained from eqn 3.12,

$$\sigma_{true} = \lambda \frac{\partial(F/V)}{\partial\lambda} = \left(2C_1 + \frac{2C_2}{\lambda}\right)\left(\lambda^2 - \frac{1}{\lambda}\right). \quad (3.13)$$

This leads to the Mooney-Rivlin equation with reduced stress:

$$\frac{\sigma_{true}}{\lambda^2 - 1/\lambda} = \frac{\sigma_{eng}}{\lambda - 1/\lambda^2} = 2C_1 + \frac{2C_2}{\lambda}. \quad (3.14)$$

The parameter C_2 in the Mooney-Rivlin model describes deviations from the classical dependence observed in ideal polymer networks. In the Mooney-Rivlin plot, a positive C_2 value ($C_2 > 0$) suggests a reduction in the constraining potential for surrounding chains, which is indicative of strain softening. Physically, for transiently crosslinked gels, this behavior implies that the dynamic bonds can dissociate during deformation, allowing the polymer chains to slip and relax from the surrounding crosslinking points. The Mooney-Rivlin parameters revealed that $C_2 > 0$ for MPEC gels, indicating strain softening and bond dissociation during the deformation at the applied strain rate. This bond dissociation enables the release of local constraints, facilitating chain mobility and energy dissipation under stress, thereby enhancing stretchability and preventing premature failure. In contrast, the covalently-crosslinked gels showed strain hardening due to the permanent nature of the crosslinks, which restricts chain relaxation under stress. This analysis confirms that the fast dynamics of metal coordination bonds enable the protection of chains during deformation, resulting in enhanced stretchability and lower stiffness at high strains.

In Figure 3.25e, the mechanical response of the experimentally-equivalent polyelectrolyte gel networks in the low pH regime obtained from coarse-grained Molecular-Dynamics (MD) simulations is shown. These simulations qualitatively reproduce the trends of metal ion valency on gel stiffness. The evolution of the polymer network at different strains (Figure 3.24d) reveals that polymer chains in the divalent gels are able to re-orient along the loading direction during uniaxial deformation; in the trivalent gels, the polymer chains are more-closely packed and tend to form large percolating structures through the dynamic crosslinks (clusters) that inhibit re-orientation. This behavior is supported by the observation that trivalent gels maintain a higher fraction of inter-crosslinked metal ions, f_{inter} than that of divalent gels under high strains (Figure 3.24e).

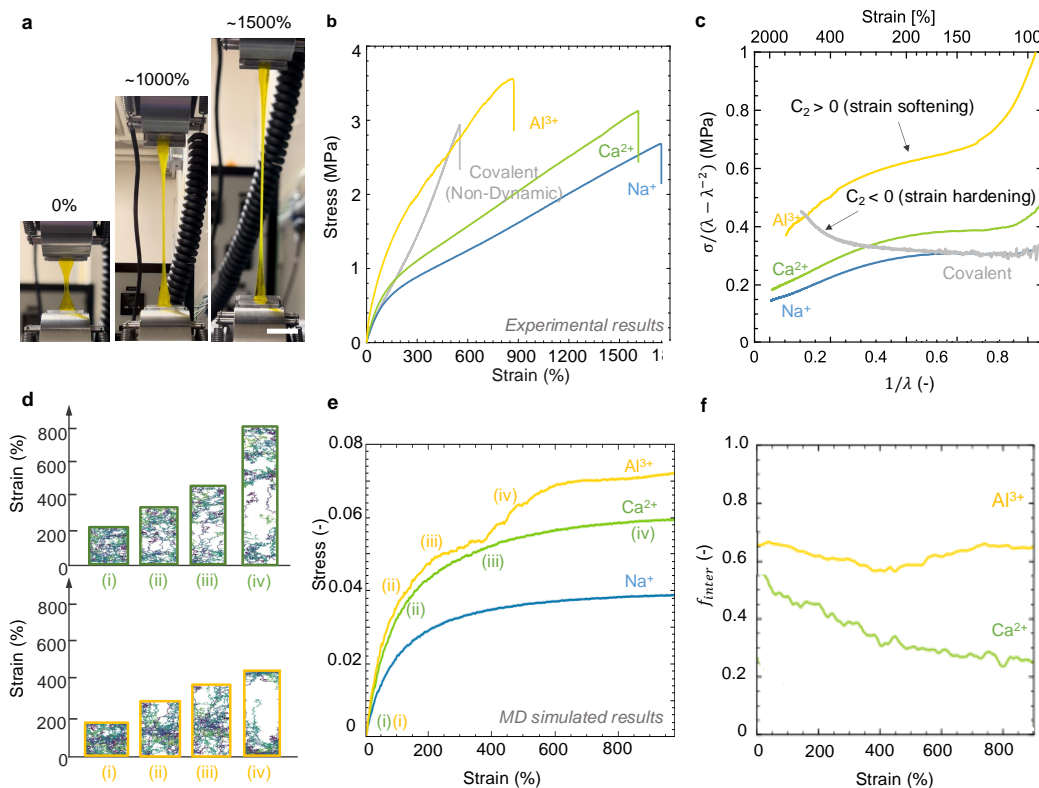


Figure 3.24: Uniaxial tensile response of bulk MPEC gels with different metal valency. **a**, Optical image of uniaxial tensile test for Ca^{2+} -MPEC gels. **b**, Experimental stress–strain data of gels crosslinked with each metal crosslinks versus with MBAA under uniaxial tensile loading. **c**, Mooney-Rivlin representation of the stress-strain curves. **d**, MD simulation snapshots of divalent(top) and trivalent (bottom) gels under uniaxial loading. **e**, MD simulation stress-strain data for different metal valency under uniaxial loading. **f**, The change in fraction of inter-crosslinked divalent and trivalent ions during elastic deformations obtained using MD simulations.

In addition to the influence of metal ions, the charge sparsity of polyanions plays a critical role in determining the mechanical behavior of MPEC gels. The distribution of negative charges along the polymer backbone affects the crosslinking density, chain conformation, and network topology, which collectively govern the gel's stiffness, stretchability. As shown in Figure 3.25a, the increase in pH (charge density) induces all gels to exhibit a $2\times$ reduction in modulus and tensile strength and a concomitant decrease of tensile strain from $> 1600\%$ to 1000% for Na^{+} - and Ca^{2+} -MPEC samples.

The MD simulations also predict that reducing the charge sparsity on the polyanion (increasing pH) leads to a reduction in f_{inter} relative to the high sparsity system,

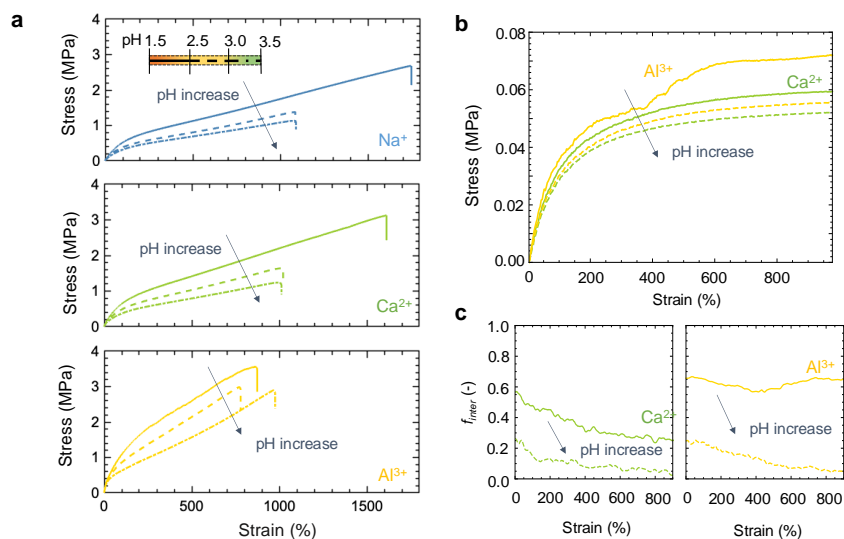


Figure 3.25: Uniaxial tensile response of bulk MPEC gels with different polyanion charge sparsity. **a**, Experimental stress—strain data as a function of pH, which shows degradation in mechanical performance in increasingly alkaline environments. **b**, MD simulation stress-strain data for different pH gels under uniaxial loading. **c**, The change in fraction of inter-crosslinks for high pH gels during elastic deformations obtained using MD simulations.

with a corresponding reduction in gel stiffness (Figures 3.25b,c). This non-intuitive shift where all stress-strain curves collapse to that of a Na^+ -MPEC gel appears to be correlated with the evolution of network topology, comprised of intrachain-molecular and interchain-molecular junctions and loops. The reduction in inter-crosslinks and the formation of a more segregated polymer network lead to a more compliant response and reduced stretchability. The stiffness and stretchability of Al^{3+} -MPEC gels are reduced by a lesser amount, indicating that trivalent ions may offer some resistance to charge sparsity effects due to their ability to form multiple crosslinks per ion.

These findings highlight how the multiscale effects of molecular choices, such as metal ion valency and polyanion charge sparsity, are manifested in the global material properties of MPEC gels. Understanding these hierarchical interactions provides valuable insights into the mechanisms governing the bulk mechanical response of MPEC gels.

3.7.2 Fracture Toughness

The mechanical response of MPEC gels under tensile deformation provides valuable insights into how molecular-level interactions influence the bulk properties of these

materials. While significant progress has been made, a key challenge remains: translating this mechanistic knowledge into guidelines for designing hydrogels with targeted mechanical properties, particularly fracture toughness which is a critical mechanical properties in the field of polymers and soft materials.

Thus, we aim to extend the current mechanistic understanding to design tougher MPEC gels by tuning metal valency and polyanion charge sparsity. The goal is to develop a comprehensive understanding of how molecular interactions at the nano-scale correlate with the bulk-level energy dissipation capabilities and fracture resistance of these gels.

Fracture toughness in soft gels is significantly influenced by the ability of the network to dissipate energy through multiple mechanisms, including bond dissociation, chain relaxation, and reversible crosslinking. Given the complexity and multi-factor nature of these behaviors, it is essential to revisit the general design principles for tough gels. As illustrated in Figure 3.26, the fracture energy for a tough gel is dependent on how much energy is required to fracture a layer of polymer chains (crack surface) and how much mechanical energy can be dissipated within the process zone around the crack tip.

Based on the Lake-Thomas model and recent advancements in the field [103], this can be quantitatively expressed as:

$$\Gamma = \Gamma_0 + \Gamma_D, \quad (3.15)$$

where Γ is the total fracture toughness of a tough gel, Γ_0 is the intrinsic fracture energy and Γ_D the mechanical dissipation energy within the process zone.

The intrinsic fracture energy represents the energy required to break polymer chains lying across the crack plane per unit area:

$$\Gamma_0 = \frac{n\sqrt{N}b}{\lambda_s^2} \cdot NU_f, \quad (3.16)$$

where n is the number of polymer strands per unit volume, N is the degree of polymerization, b is Kuhn length of the polymer chain, λ_s is the swelling ratio if solvent exists, and U_f is the energy required to fracture a polymer chain. The first term ($n\sqrt{N}b/\lambda_s^2$) represents the density of polymer chains per unit area at the crack plane, while the second term (NU_f) denotes the energy needed to fracture these chains.

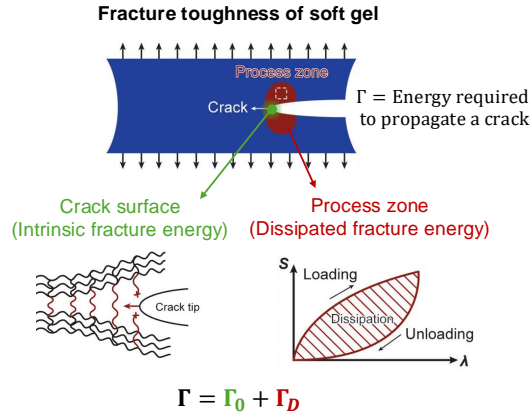


Figure 3.26: **Design principles for fracture toughness in soft gels.** The total fracture toughness of the tough hydrogel, Γ is contributed from the intrinsic fracture energy, Γ_0 from fracturing a layer of polymer chains and the mechanical dissipation in the process zone around the crack tip, Γ_D . Reprinted by permission from [104]. Copyright ©2021, American Chemical Society.

The mechanical dissipation energy in the process zone (Γ_D) accounts for the energy dissipated through bond dissociation, chain relaxation, and hysteresis in the vicinity of the crack tip:

$$\Gamma_D \approx 2V \oint \sigma d\lambda \cdot h, \quad (3.17)$$

where: V is the volume fraction of polymer chains in the process zone, σ is the stress in the material, λ is the stretch ratio and h is the size of the process zone. The line integral ($\oint \sigma d\lambda$) represents the hysteresis loop in the stress-strain curve, capturing the energy dissipation due to multiscale relaxation mechanisms. The factor of 2 accounts for energy dissipation on both sides of the crack plane for pure shear test set-up.

Based on the analytical expressions for fracture toughness, several key strategies can be proposed to optimize the balance between crosslinking density and bond dynamics in MPEC gels. For instance:

1. Maximize chain density and network integrity within the gels, which increases both $n\sqrt{Nb}/\lambda_s^2$ in Γ_0 and V in Γ_D . A denser network provides more load-bearing polymer strands per unit area, enhancing the energy required to break polymer chains and increasing the volume fraction of load-bearing chains in the process zone.

2. Enhance stress distribution and increase the effective size of the process zone (h) in Γ_D by promoting inter-crosslinking efficiency and facilitating fast bond and chain relaxations. Efficient stress distribution prevents localized stress accumulation and delays the onset of crack propagation by spreading the mechanical load more evenly throughout the network.
3. Maximize the hysteresis loop in Γ_D by promoting efficient energy dissipation mechanisms that enable the gels to absorb high amounts of energy without undergoing catastrophic failure. For example, strong bond dissociation and entanglement friction can induce a wider hysteresis loop in the stress-strain curve, reflecting greater energy dissipation during deformation.

The Mooney-Rivlin analysis from Figure 3.24c reveals a clear strain-softening behavior in all MPEC gels, suggesting that the dynamically-coordinated bonds can dissociate and reform under stress. This mechanism enables the gels to absorb energy efficiently without undergoing catastrophic failure. These findings lead to the hypothesis that:

1. Higher valency metal ions at low pH and low solvent will exhibit higher fracture toughness due to their ability to form multiple inter-crosslinks, compact network, while sustaining dynamic bond exchange allowing for dissipation from strong bond dissociation and delayed fracture.
2. Reducing metal valency or increasing pH will lead to a decrease in fracture toughness by reducing inter-crosslink density and network integrity.

To test this hypothesis, we fabricated and measured the fracture toughness of Na^+ -, Ca^{2+} -, and Al^{3+} -MPEC gels at both low pH and high pH. Due to experimental limitations, the solvent content was fixed at 10 v/v% for all gels, and the monomer concentrations were kept constant to be 8.8M. This approach ensures that the observed differences in fracture toughness can be attributed primarily to variations in metal valency and pH rather than solvent content or monomer concentration.

The fracture toughness of MPECs was evaluated using pure shear fracture experiments (Figure 3.27). In these experiments, we used notched thin gel sheets and tested them in an MTS load frame (MTS Systems Co., Eden Prairie, MN). The methodology followed the approach first developed by Thomas, Rivlin, and Lake [105, 106] and later adapted for probing the fracture behavior of tough hydrogels

[26]. During the experiments, a thin MPEC sample with dimensions ($W \times H_0 \times th$)

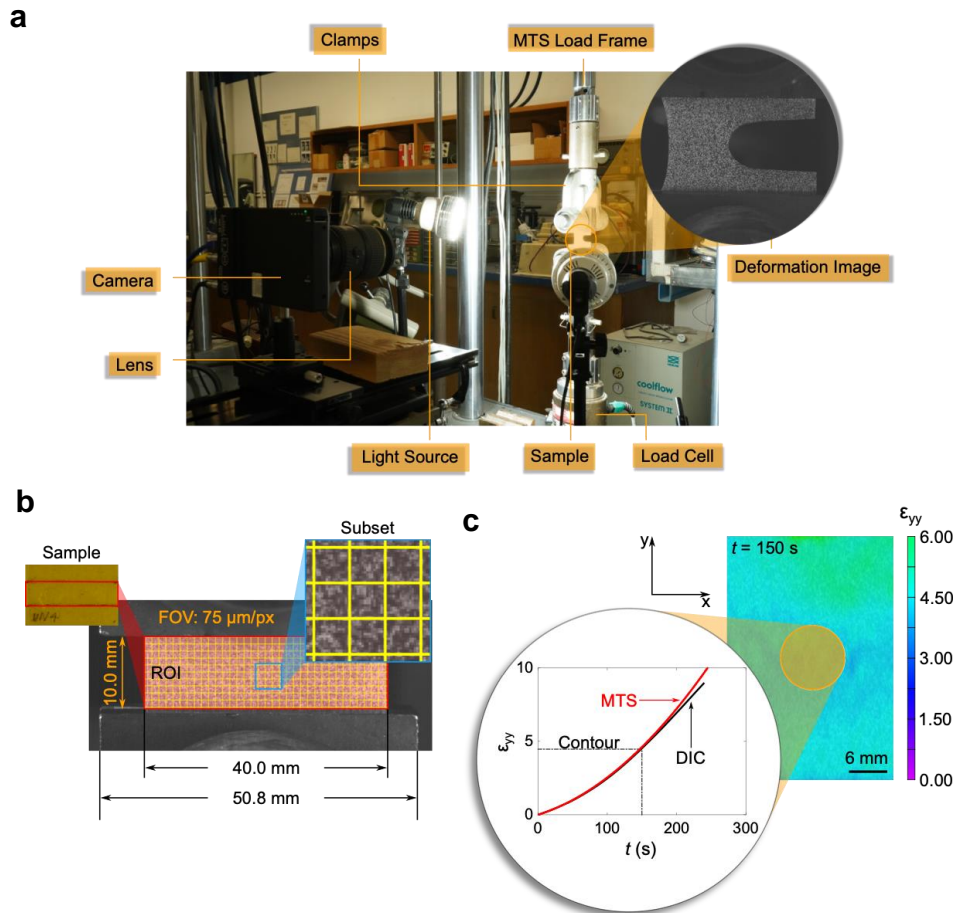


Figure 3.27: **Fracture test set-up and DIC analysis.** **a**, Experimental setup for tension testing using the MTS load frame. A series of flashlights are used to sufficiently and uniformly illuminate the sample for image capture using the high-resolution camera and DIC analysis. **b**, Overview of the DIC analysis with the region of interest (ROI), dimensions of the samples, cross-head width for calibration, and labeled subsets. **c**, Comparison of ϵ_{yy} calculated from actuator displacement data and averaged DIC data within the orange circle as a function of time for an un-notched sample undergoing uniaxial tension. Additionally, the strain field at $t = 150$ s is shown to demonstrate the uniform distribution of ϵ_{yy} indicating no slip occurred.

of $40 \times 10 \times 1.5 \text{ mm}^3$ and an initial notch length (a_0) of 16 mm ($a_0/W = 0.4$) was stretched uniaxially at a strain rate of $\dot{\epsilon} \approx 0.02 \text{ s}^{-1}$ to induce crack propagation until complete sample rupture. We used Digital Image Correlation (DIC) using a commercial software, VIC-2D (Correlated Solutions, Columbia, SC) [107] to capture the gel slippage and exact moment of crack initiation. The stress-strain curves for both notched and un-notched samples are shown in Figure 3.28.

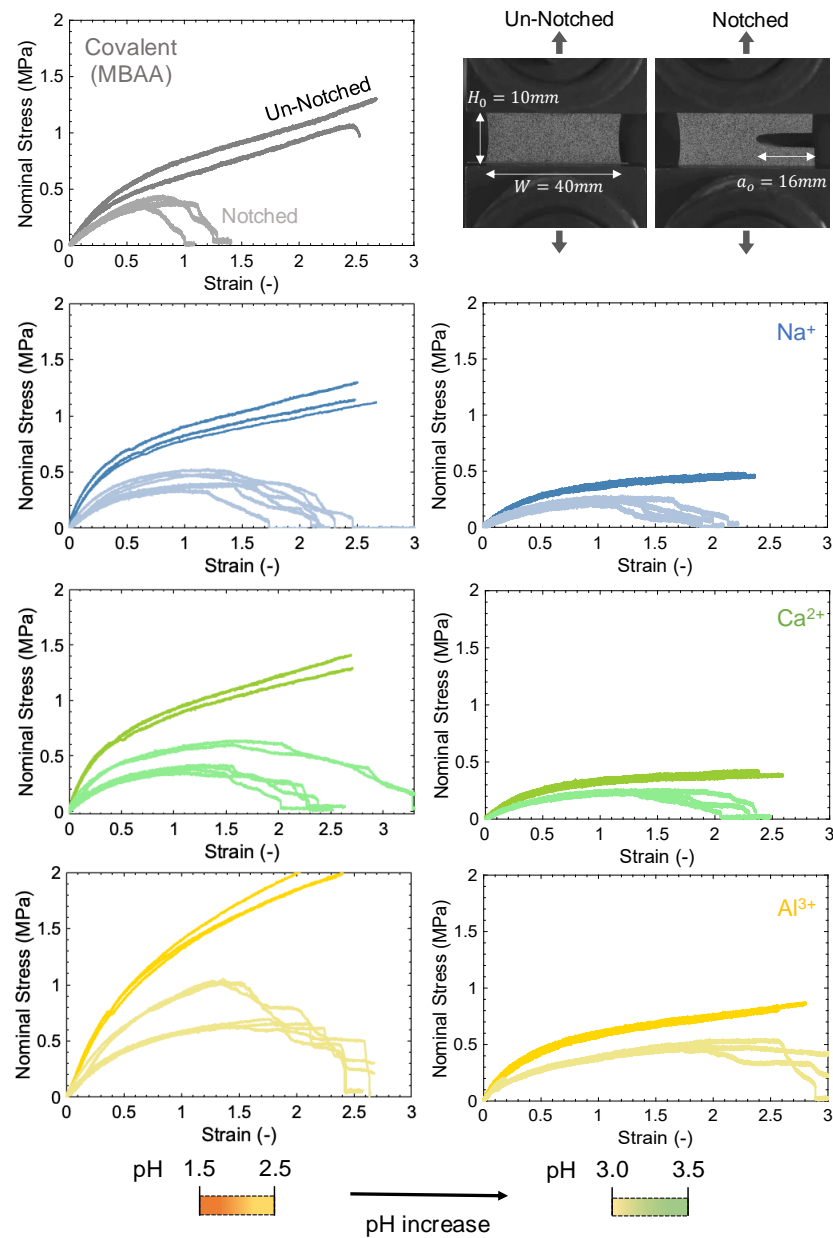


Figure 3.28: **Stress-strain curves for un-notched and notched MPEC for fracture experiment.** Un-notched and notched samples were stretched uniaxially at a strain rate of $\dot{\epsilon} \approx 0.02 \text{ s}^{-1}$.

From the DIC analysis, we defined the critical strain (λ_{crit}) as the point at which the pixels around the crack tip were lost, indicating the initiation of a crack. The fracture energy (Γ) was calculated using:

$$\Gamma = H_0 \int_0^{\lambda_{crit}} \sigma d\lambda, \quad (3.18)$$

where σ is the stress response of the corresponding un-notched samples as described in Figure 3.29b.

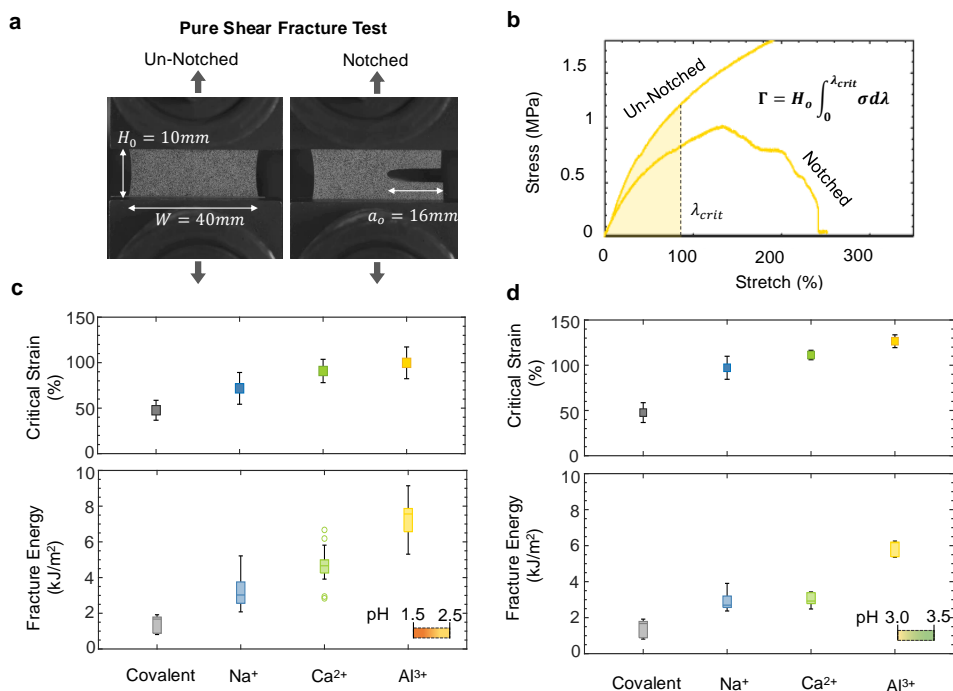


Figure 3.29: **Fracture energy of MPEC gels.** **a**, Sample dimensions of un-notched and notched samples for pure shear test. **b**, Fracture energy, Γ measured using the initial gauge length (H_0 , the un-notched sample stress-strain curve, and critical strain, λ_{crit} as per [108]. Box plots for Γ and λ_{crit} for crack initiation for **c**, charge-sparsely MPEC and **d**, charge-dense MPEC.

As shown in Figure 3.29c, the fracture energy (Γ) and critical strain (λ_c) for MPEC gels cross-linked with different metal ions demonstrate that the fracture energy increases with metal valency as we hypothesized. In the low pH range (1.5–2.5), the Al³⁺-MPEC gels exhibited the highest fracture energy of $7.32 \pm 1.04 \text{ kJ/m}^2$, which is approximately 50% greater than that of Ca²⁺-MPEC gels ($4.66 \pm 0.98 \text{ kJ/m}^2$) and about 120% higher than that of Na⁺-MPEC gels ($3.27 \pm 0.94 \text{ kJ/m}^2$). A similar trend was observed at higher pH (Figure 3.29d).

In Figure 3.29c, we show the Γ and λ_c for MPEC samples cross-linked with each metal ion and demonstrate that the fracture energy increases with stiffness. In a range of pH of 1.5–2.5 (left panel), the Al³⁺-PEC gels achieve fracture energies of $7.56 \pm 1.25 \text{ kJ/m}^2$, $\approx 50\%$ greater than that of the Ca²⁺ MPEC, whose fracture energy is $4.66 \pm 0.98 \text{ kJ/m}^2$ and $\approx 120\%$ higher than that of the Na⁺-MPEC gel, $3.03 \pm 0.94 \text{ kJ/m}^2$. We observed a similar trend for higher pH (Figure 3.29d). It is also

noteworthy that the critical strain for crack propagation (λ_c) correlates strongly with the fracture energy, suggesting that the higher fracture energy is not only a result of greater stiffness and energy dissipation but also due to delayed fracture in the higher-valency systems. This implies that the dynamic bond exchange and slower bond relaxation rates in higher-valency systems allow for more effective energy absorption before fracture, enhancing both fracture toughness and crack resistance.

Consistent with our hypothesis, the increase in pH resulted in a reduction of fracture energy for all gels regardless of metal valency. Specifically, at high pH, the fracture energy of Al^{3+} -MPEC, Ca^{2+} -MPEC, and Na^+ -MPEC gels decreased to 6.16 ± 0.58 kJ/m^2 , 2.92 ± 0.82 kJ/m^2 , and 2.69 ± 0.77 kJ/m^2 , respectively. This corresponds to a reduction of approximately 20%, 38%, and 11% compared to the low pH gels. The observed decrease in fracture energy suggests that the loss of connectivity and network integrity at higher pH levels reduces the ability of the gels to resist fracture effectively. Interestingly, despite the reduction in fracture energy, the critical strain increased at higher pH, indicating delayed fracture. This suggests that the gels may still retain the ability to dissipate energy efficiently; however, the compromised network integrity and reduced inter-crosslinking density at higher pH likely counteract the benefits of energy dissipation. Further investigation is needed to gain a more concrete understanding of the mechanisms underlying this behavior. Remarkably, all MPEC gels demonstrated 2–10 times higher fracture toughness compared to their covalently crosslinked counterparts. This significant enhancement highlights the crucial role of bond dynamics. The transient nature of these bonds enables chain relaxations, delayed fracture, and higher mechanical dissipation, which collectively contribute to the superior fracture toughness of MPEC gels.

Due to the complex stress field and large deformations in soft gels, we focused primarily on crack initiation, which determines the total fracture energy. However, the crack propagation behavior also presents an intriguing avenue for understanding how multiscale interactions influence macroscale mechanical responses. As shown in Figures 3.30a and b, the DIC analysis reveals different degrees of crack blunting and the corresponding strain (ϵ_{yy} ; y-axis is along the loading direction) distribution around the crack tip during propagation. As shown in Figure 3.30c, initially, the crack shape and local stress concentration between Ca^{2+} - and Al^{3+} -MPEC gels appear comparable at crack initiation. However, their propagation behaviors diverge significantly. For Ca^{2+} -MPEC gels, the faster local bond dissociation at the crack tip allows chains to slip, reducing stress concentration and blunting the crack. Ca^{2+} -

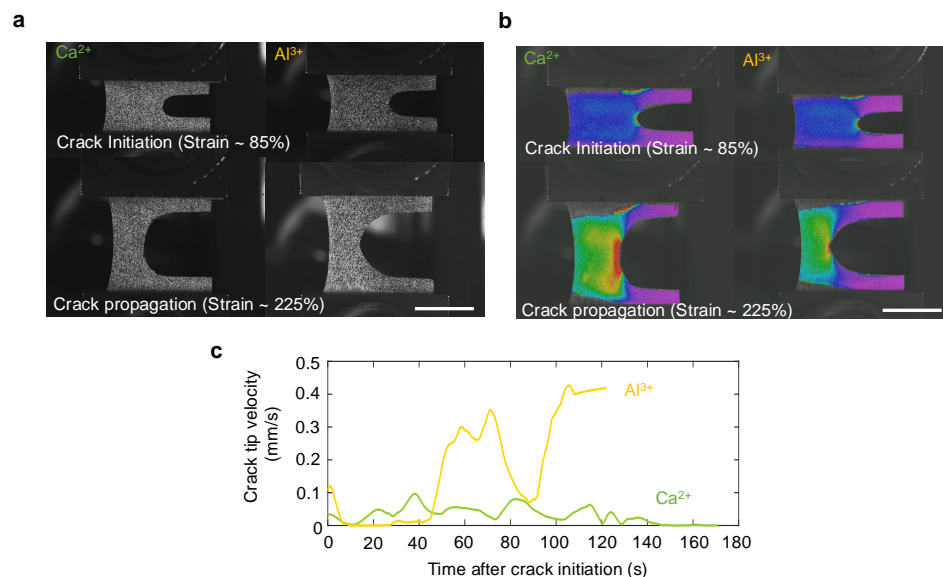


Figure 3.30: **Crack propagation behavior of MPEC gels.** **a**, High-resolution images of MPEC gels at crack initiation and crack propagation. Scale bar 20 mm. **b**, the corresponding spatial mapping of ϵ_{yy} from DIC analysis, applied with a subset size of $15 \times 15 \text{ px}^2$, a step size of 1, and a strain filtering radius of 15 px [107]. Scale bar 20 mm. **c**, Crack tip velocity during the propagation.

MPEC gels show a constant steady crack propagation with continuous crack blunting until the rupture. In contrast, Al³⁺-MPEC gels exhibit a sharper crack tip with more localized energy dissipation, leading to multiple crack velocity jumps.

This difference in crack propagation behavior is likely linked to the bond and chain dynamics—specifically, the bond exchange rates and chain relaxation mechanisms—which influence how effectively energy dissipation and stress distribution are managed at the crack tip. Since crack propagation involves multiple strain rates and a complex stress field, further investigation would be necessary to identify the dominant factors. Nevertheless, the observed behaviors suggest that a more detailed mechanistic understanding could provide valuable insights into designing MPEC gels with desired fracture behavior.

3.8 Additional Molecular-Level Controls: Solvent and Metal Identity

3.8.1 Solvent Effects

Solvent content is a critical parameter that significantly influences the material behavior of MPEC gels. While we kept the solvent content constant across all samples in the previous sections to isolate other variables, we conducted additional studies to understand the effects of solvent using both experimental and computational

approaches.

Experimental results

The primary solvents used in the fabricated MPEC gels are water and glycerol. TGA analysis in Figure 3.4 confirmed that all equilibrated gels, regardless of metal ions and system pH, contained approximately $14\% \pm 2.14\%$ water by weight and 10 v/v% glycerol. To assess the impact of water content, we placed the equilibrated gels in a high-humidity environment ($RH \sim 80\%$) to vary the water content. Figure 3.31a shows that the gels absorbed different amounts of water, which significantly influenced their mechanical properties.

Quasi-static tensile tests indicated that increasing the water content from 10% to 20% and 30% by weight reduced the modulus by a factor of 1.41 and 4.80 for Al-MPEC and 1.86 and 3.92 for Ca-MPEC, as shown in Figure 3.31b. The increased water content led to a more flexible network with lower stiffness and higher energy dissipation.

The glycerol content was varied by adjusting the amount introduced into the photoresin. For fair comparison the total solvent amount is kept same instead the volume fraction between water and glycerol varied. As shown in Figure 3.32, reducing the glycerol fraction resulted in the overall solvent remained in the gels after post processing decreased due to more volatile nature of water compared to glycerol. The impact of this reduction is demonstrated in Figure 3.32 where gels exhibit stiffer responses with earlier failure. 3.32.

Theoretical results

To identify the molecular mechanisms of the effect of solvents on MPEC gels, we performed molecular dynamics simulations using an implicit solvent model. The simulations varied the dielectric constant and system pressure to account for changes in solvent composition. As there is a high concentration of polyelectrolyte, varying the solvent composition is not likely to have a dramatic effect on the system dielectric. On the other hand, by replacing glycerol with water, the overall free volume of the system is expected to decrease, leading to an increase in osmotic pressure. This effect is expected to be more substantial when varying the solvent. 3.33.

As shown in Figure 3.33, increasing the system pressure (equivalent to increasing the water fraction) led to higher stress responses across all valencies, which agrees

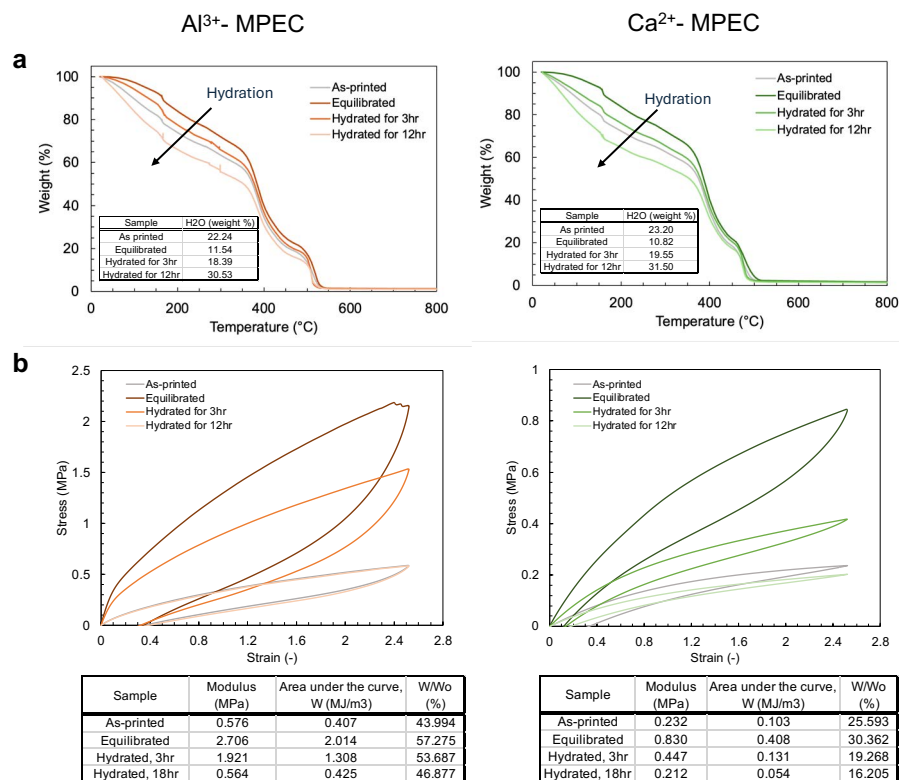


Figure 3.31: Effects of solvent content in MPEC gels. Different amount of water included in trivalent (left) and divalent (right) MPEC gels by equilibrating the gels in high-humidity environment (RH~80%). **a**, TGA analysis confirms that the gels contain different amount of water contents. **b**, Stress-strain curves obtained for different water contents on. The respective young's moduli, area enclosed by the loading-unloading curve (hysteresis) and energy dissipation percent (hysteresis normalized by the total energy induced from the applied loading) of each gel have been given in the tables above.

well with the experimental results in Section 3.8.1. Figures 3.33b and 3.33d indicate that the reduced free volume significantly hindered polymer motion, resulting in a narrower distribution of cluster sizes for divalent and trivalent gels and a longer end-to-end vector relaxation time. In contrast, the monovalent gel exhibited a wider cluster distribution due to the absence of dynamic crosslinks. The ion-pair relaxation times showed only a slight decrease despite the change in free volume (Figure 3.33c). This suggests that while the solvent content strongly influences polymer motion and mechanical properties, its impact on ion-pair dynamics is limited. The enhanced stiffness and mechanical hysteresis can be attributed to the much hindered polymer motions which dissipate energy from extensive frictions and make the system more

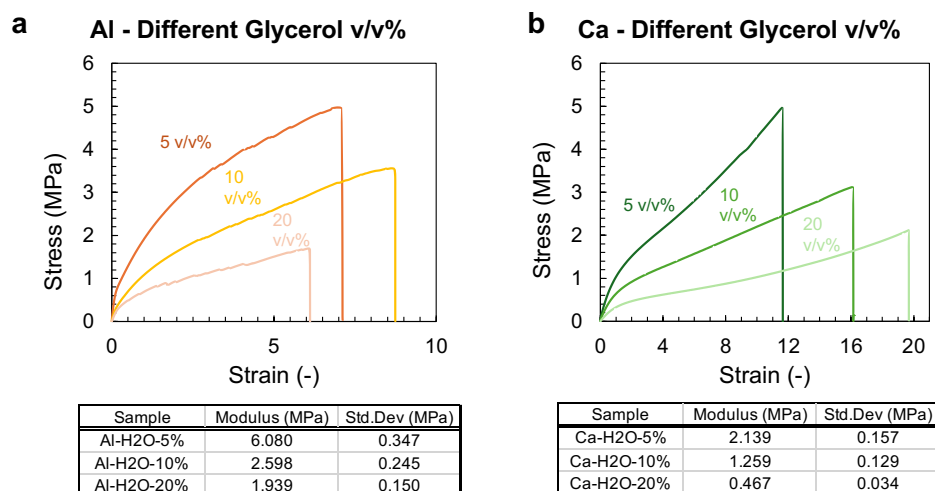


Figure 3.32: **Stress-strain curves obtained for different co-solvent contents.** For **a**, the trivalent and **b**, the divalent MPEC gels. The respective storage moduli and standard deviations of each gel have been given in the tables above. The same protocol was used to print and perform the experiments on the gels as described in the main text.

compact.

3.8.2 Metal Identity Effects

As shown in Figure 3.7, metal identity can influence the coordination environment and binding strength of MPEC gels, primarily due to differences in ion size and the ability to form shared molecular orbitals. To explore the effects of metal ions beyond hard ions, we conducted both experimental studies and MD simulations to assess how metal identity impacts the mechanical properties of the gels.

Experimental observations

To investigate the impact of metal ion identity on the mechanical properties of MPEC gels, we printed gels using different metal ions from the same pre-gel solutions and confirmed their bidentate chelation by carboxylate. We then performed quasi-static tensile tests to measure their mechanical responses. The results are summarized in Figures 3.34 and 3.35.

For divalent ions (Ca^{2+} , Zn^{2+} , Ni^{2+}) shown in Figure 3.34, the gels became stiffer as the ionic radius decreased from Ca^{2+} to Zn^{2+} to Ni^{2+} , particularly at medium to high pH (Figures 3.34b and 3.34c). This trend aligns with theoretical predictions at the subsequent section. The significantly higher stiffness observed for Ni^{2+} -MPEC

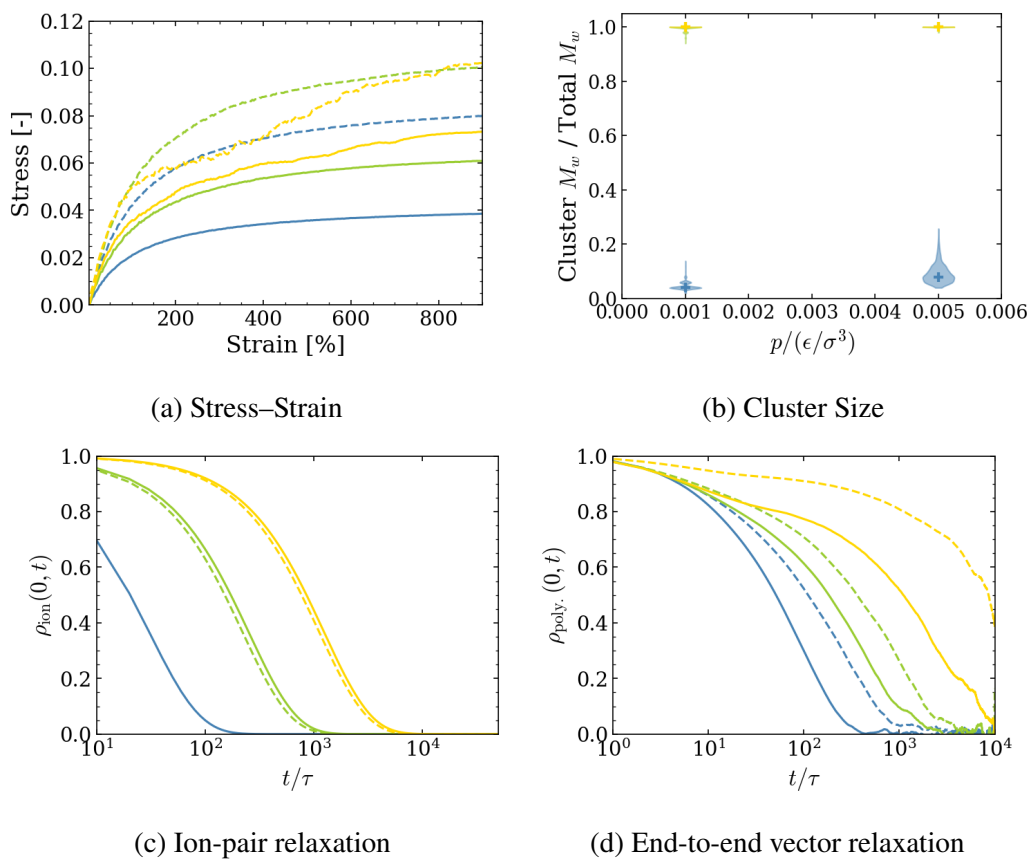


Figure 3.33: **MD simulations of MPEC gels with varying applied pressure.** **a**, Stress-strain curves from uniaxial stretching. **b**, Cluster size distribution under different system pressure. **c**, Ion-pair relaxation and **d**, end-to-end vector relaxation. Solid curves correspond to pressures of $0.001\epsilon/\sigma^3$ and dashed curves correspond to pressures of $0.005\epsilon/\sigma^3$. The color scheme used in this figure follow the scheme used in the main text (blue: monovalent, green: divalent and yellow: trivalent ions).

gels is likely due to the presence of half-filled d-orbitals, which enhance binding strength and relaxation dynamics.

Interestingly, there appears to be a maximum in the tensile critical strain as we vary the ionic radius, likely resulting from a balance between the binding strength of the coordinating bonds and the polymer relaxation time. An interesting exception to the stiffness trend occurs at low pH, where the trend does not strictly follow ion size. This suggests that protonation and other charge interactions become more dominant, and the difference in binding strength becomes less detectable, especially in the low pH regime where the number of available binding sites is reduced and protonation becomes strongly favored.

For the trivalent ions shown in Figure 3.35, the binding strength across different

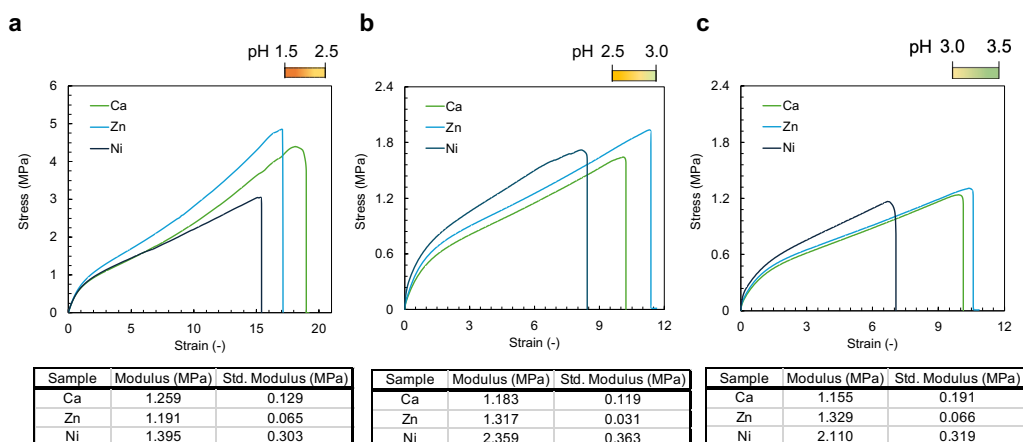


Figure 3.34: **Stress-strain curves obtained for different divalent metal ions (Ca^{2+} , Zn^{2+} and Ni^{2+}) at varying pH. (a, low, b, medium, c, high).** The respective young's moduli and standard deviations of each gel have been given in the tables above. The same protocol was used to print and perform the experiments on the gels as described in the main text.

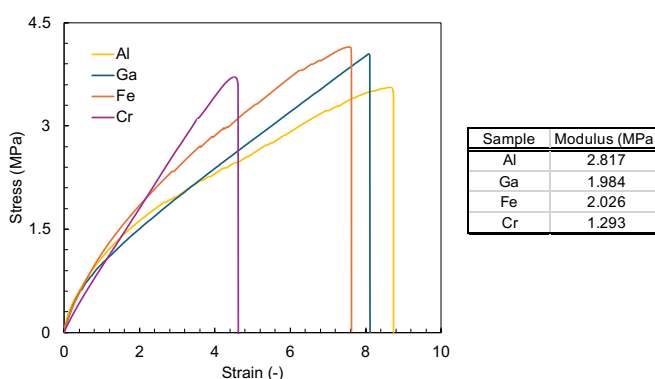


Figure 3.35: **Stress-strain curves obtained for different trivalent metal ions (Al^{3+} , Ga^{3+} , Fe^{3+} and Cr^{3+}).** The respective young's moduli and standard deviations of each gel have been given in the table on the right. The same protocol was used to print and perform the experiments on the gels as described in the main text.

species is relatively similar as predicted by Figure 3.7, yet the gels exhibited distinct mechanical responses. Cr^{3+} -MPEC and Fe^{3+} -MPEC gels initially showed a lower elastic modulus compared to hard ions such as Al^{3+} and Ga^{3+} but became stiffer at larger strains and failed earlier than the other trivalent gels. The observed elastic modulus is likely driven more by the polymer microstructure, while the response at larger strains reflects the influence of relaxation dynamics. This suggests that the metal identity affects both the microstructure and the relaxation behavior of the gels.

Cr^{3+} -MPEC gels can be printed with finer resolution than other gels, likely due

to the presence of multiple half-filled d-orbitals in Cr^{3+} . This promotes a binding characteristic closer to covalent than ionic, resulting in stronger bonds and a more static crosslinking network. Consequently, the gels exhibit strain stiffening and earlier failure due to altered cluster formation and distribution. Similarly, Fe^{3+} -MPEC gels also contain multiple half-filled d-orbitals, which contribute to a stiffer response at larger strains.

However, transition metal species are known to undergo photo-reduction in the presence of supporting electrolytes (Na^+), carboxylic acids, hydroxycarboxylic acids, and other weak-field ligands, resulting in the reduction of metal cations such as Fe^{3+} to Fe^{2+} [109–111]. Additionally, many transition metal salts exhibit a broader UV absorbance band extending to higher wavelength, overlapping with the exposure wavelength (405 nm) used for photopolymerization. This overlap could influence the degree of polymerization or chelation degree in the gel matrix, thereby affecting the mechanical properties. Therefore, the mechanical response of transition metal species likely requires further investigation to account for photo-induced effects and polymerization dynamics, beyond just binding strength.

Theoretical predictions

To explore the impact of metal identity on MPEC gels, we conducted theoretical investigations by assessing the effect of ion diameter on mechanical behavior. Due to the complexity of capturing local asymmetries in coordination environments and mixed ligand-fields, a more sophisticated computational model would be required for a detailed understanding, which is beyond our current capabilities. As shown in Figure 3.36, increasing the ion diameter resulted in different extents of effects depending on metal valency. For monovalent gels, changes in ion diameter had minimal impact on their mechanical properties. This can be attributed to the fact that monovalent ions do not form crosslinks between chains. Consequently, variations in binding strength had little effect on polymer motion. The stress-strain response in monovalent gels is likely governed more by chain entanglement and electrostatic repulsion rather than by metal coordination.

In contrast, for divalent and trivalent gels, increasing the ion diameter resulted in faster relaxation times for both ion-pair and end-to-end vector dynamics. This behavior is attributed to the larger metal-acetate distances, which lead to weaker binding strength (Figures 3.36b–3.36d). The reduced binding strength also manifested as a decrease in cluster size, indicating that larger ions promote a more mobile

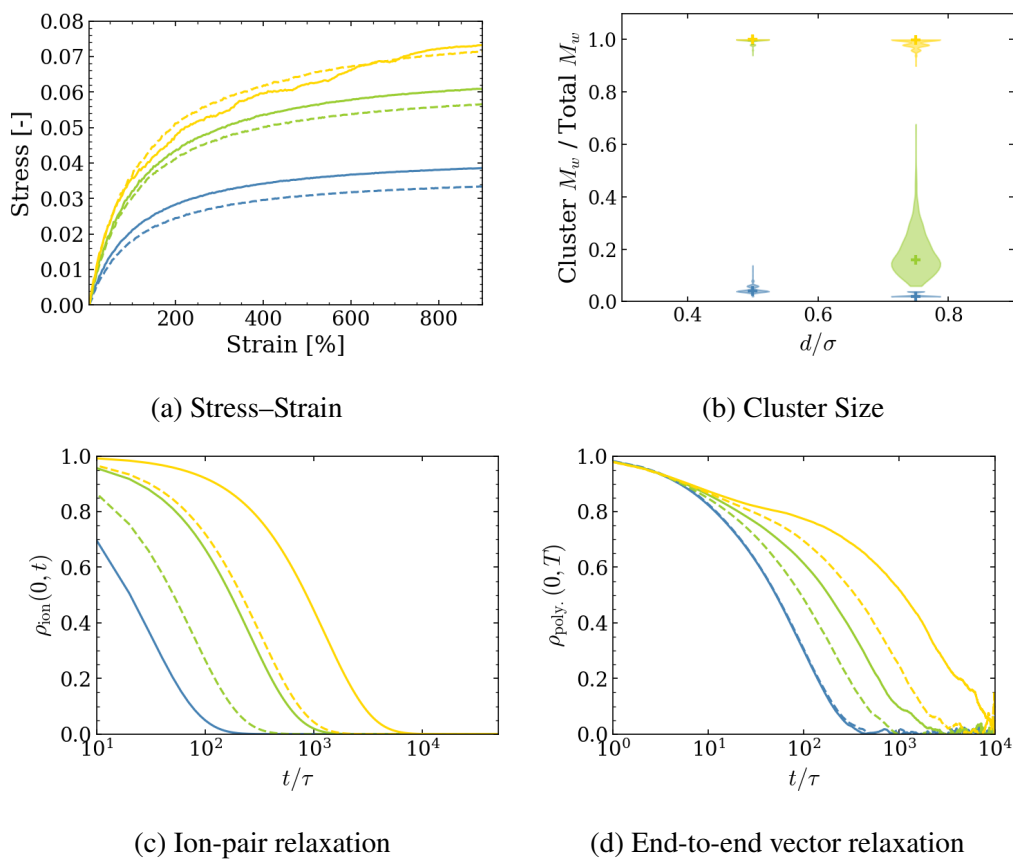


Figure 3.36: **MD simulations of MPEC gels with varying ion diameters.** **a**, Stress-strain curves from uniaxial stretching. **b**, Cluster size distribution over different ion diameters. **c**, Ion-pair relaxation and **d**, end-to-end vector relaxation. Solid curves correspond to diameters of 0.5σ and dashed curves correspond to diameters of σ . The color scheme used in this figure follow the scheme used in the main text (blue: monovalent, green: divalent and yellow: trivalent ions).

and less interconnected network.

Divalent gels were particularly sensitive to ion diameter, with larger ions causing the cluster size and mechanical behavior to resemble those of monovalent gels. This suggests a shift towards a less crosslinked network as the ion diameter increases. These findings highlight the role of ion size in modulating both binding strength and the extent of crosslinking in divalent MPEC gels.

In contrast, for trivalent gels, despite the faster relaxation dynamics, the cluster size and mechanical response of aluminum ions were less affected by changes in ion diameter. This suggests that the experimentally observed stiffness variations for trivalent gels may be influenced by factors beyond ion size and binding strength alone. The results imply that coordination geometry and the ability to form multiple

crosslinks per ion may play a more significant role in determining the mechanical properties of trivalent MPEC gels.

3.9 Conclusion

In summary, we present the design, characterization, and multiscale modeling of additively manufactured metallo–polyelectrolyte gels. The advanced characterizations through the lens of thermodynamics and mechanics demonstrate the remarkable interplay of dynamic crosslinker valency and polyanion charge sparsity in governing material properties of MPEC gels. The use of theoretical and computational approaches led to a fundamental understanding of the experimental findings and provided insights into the underlying mechanisms from local bond relaxation to mesoscale polymer network topology. The theory developed for this work is capable of extension to other material systems using the key chemical levers identified/explored herein. The development of a simple synthesis pathway and integration to additive manufacturing offers a large parameter space for material design of MPEC gels and an abundance of applications of metallo-polyelectrolytes.

*Chapter 4***BRIDGING MOLECULAR-TO-MECHANICS: MOLECULAR CONTROL FOR GLOBAL MATERIAL RESPONSE**

This chapter has been adapted from:

S. Lee^{*†}, P. Walker[†], S. Velling, A. Chen, Z. Taylor, C. Fiori, V. Gandhi, Z-G. Wang & J.R. Greer. “Molecular Control via Dynamic Bonding Enables Material Responsiveness in Additively Manufactured Metallo-Polyelectrolytes”. *Nature Communications* **15**, 6850 (2024). DOI: [10.1038/s41467-024-50860-6](https://doi.org/10.1038/s41467-024-50860-6)

Contributions: S.L. conceived and designed the project, fabricated samples, performed experimental characterization, analyzed the results, and wrote the manuscript.

S. Lee, Z. Liu, K. Funk, X. He & J.R. Greer. "Cation-Induced Pattern Transformation of Additively Manufactured Polyelectrolytes". *In Preparation*.

Contributions: S.L. conceived and designed the project, fabricated samples, performed experimental characterization, analyzed the results, and wrote the manuscript.

4.1 Chapter Summary

Building on the insights from Chapter 3, this chapter explores how multiscale knowledge of hierarchical interactions in MPECs can be leveraged to control global material behavior. By employing multiscale knowledge of hierarchical interactions, we explore how molecular-level control such as dynamic bonding and reversible crosslinking can dictate global material/structural behavior such as controllable deformation, shape transformation, and multifunctionality. The findings provide a comprehensive understanding of how molecular design strategies can be extended to develop adaptive and reconfigurable materials with tailored mechanical and functional properties.

4.2 Introduction

A critical frontier in polymer research is the integration of adaptability and responsiveness into soft materials to enable functional responses to external stimuli. MPECs have emerged as a promising class of responsive and adaptive materials due to their reversible and tunable bonding interactions. Recent studies have highlighted the versatility of MPECs. For instance, their dynamic bonding enables reversible network formation, facilitating reprocessing and recycling by dissolving and reshaping the gels under controlled conditions [112]. The tunable metal-ligand coordination imparts adaptable mechanical properties and enables drastic alterations in their physical and chemical characteristics positioning them as strong candidates for applications in soft robotics [13] or tunable adhesives [59].

However, while the constituent dynamic polymers offer potential for responsiveness, programming these responses in a controlled manner or tailoring them to specific functionalities remains a significant challenge. As observed in Chapter 2, not only do the constituent material properties matter, but the structural design also plays a crucial role in determining the global material response. Therefore, an integrated approach that combines dynamic chemistry with solid/structural mechanics is essential to achieve controllable adaptability in functional material systems.

This chapter addresses this challenge by combining molecular-level controls, including dynamic bonds and phase transitions, with nonlinear structural responses such as buckling and reconfigurability to program global material behavior. The central premise is that molecular interactions dictate local responsiveness, while structural geometries can amplify or suppress these responses through localized deformation or stress redistribution. This synergistic interplay is anticipated to enable programmable material responses that can self-reconfigure under external stimuli, unlocking capabilities such as tailored viscoelasticity, controlled instabilities, and environmental adaptability.

4.3 Mechanical Stimuli: Controllable Deformation of Bilayer Structure

The deformation and buckling behavior of slender structures is governed by fundamental principles of structural mechanics, where factors such as beam geometry, material properties, boundary conditions, and applied loads collectively dictate structural stability. For example, in Euler-Bernoulli beam theory, the critical buckling load, P_c , which marks the transition from a stable to an unstable state under

axial compression, is given by:

$$P_c = \frac{\pi^2 EI}{L_e^2}, \quad (4.1)$$

where E is elastic modulus, I is the moment of inertia, and L_e is the effective beam length. This equation accurately predicts when a beam will buckle; however, it does not provide insight into the direction of deflection (i.e., whether the beam buckles left or right). This directional uncertainty stems from stochastic factors, such as material heterogeneity, geometric imperfections, or small perturbations in experimental conditions. In this study, we leverage the rich dynamic properties enabled by molecular controls in MPECs to intentionally guide nonlinear deformation behaviors in flexible structures. Specifically, we fabricate bi-material structures in which two MPEC gels—crosslinked by different metal ions—introduce controlled mismatches in viscoelastic relaxation dynamics. These mismatches create predictable asymmetries in stiffness evolution and stress relaxation, biasing the direction of buckling. This approach enables programmed instability-driven mechanical deformation.

Fabrication of the bilayer MPECs

We used the same fabrication process described in Chapter 3.3. Due to the limitation of printing resolution, we only explored mm-scale structural response. To fabricate

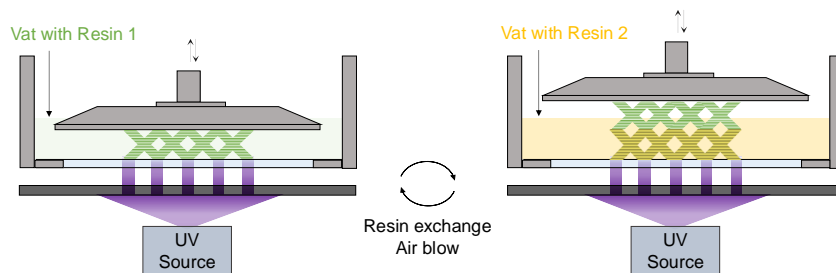


Figure 4.1: **Vat polymerization set-up for bimaterial/composite structure of MPECs.**

the bi-material MPEC constructs with spatially controlled dynamic crosslinking, we employed a resin-exchange vat polymerization approach, as illustrated in Figure 4.1. The first material was first printed via layer-by-layer photopolymerization. Once the designated portion was printed, the resin vat was replaced with a second precursor solution. During the exchange, an air-jet method was used to blow away residual precursor solution from the exposed surface, minimizing material contamination

at the interface and limiting cross-diffusion of chemical species. The construct underwent post-processing and curing to stabilize the polymer network. This resin-exchange AM technique enables the fabrication of bi-material MPEC structures with sharp material transitions, allowing us to program distinct mechanical relaxation behaviors at the interface. This controlled heterogeneity serves as a mechanism for directing structural deformations, which will be explored in subsequent sections.

4.3.1 Strain-rate Dependent Buckling

Inspired by the work of Janbaz et al.[113], we introduce a bilayer beam system in which two chemically identical MPEC matrices are crosslinked with different metal ions to induce distinct time-dependent viscoelastic relaxations (Figure 4.2). This engineered mismatch allows us to predictably switch buckling direction depending on the applied strain rate.

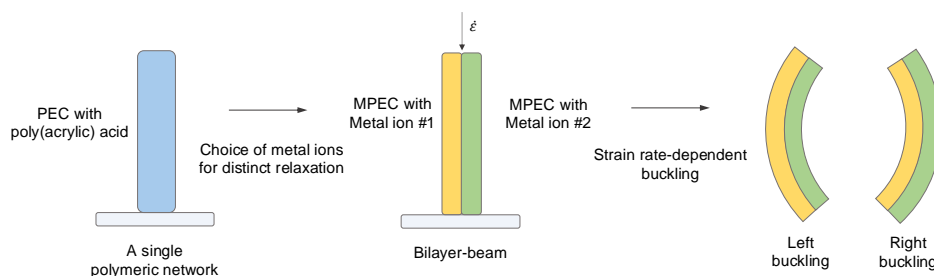


Figure 4.2: **Controllable buckling mode under compressive stress.**

To introduce a controllable mismatch in viscoelastic relaxation, we fabricated bilayer beams composed of:

- Al^{3+} -MPEC: Exhibits slow, highly viscoelastic relaxation with a lower equilibrium modulus.
- Ni^{2+} -MPEC: Exhibits faster relaxation with a higher equilibrium modulus.

We first conducted stress relaxation experiments under an instantaneous tensile load to quantify the time-dependent mechanical response of each gel. As shown in Figure 4.3, Al^{3+} -MPEC exhibits slower relaxation with prolonged stress dissipation, while Ni^{2+} -MPEC relaxes more rapidly with a higher equilibrium modulus. This mismatch in viscoelastic behavior introduces a strain-rate dependency in the buckling response. Since the effective stiffness of each layer depends on the deformation timescale, the softer side under a given strain rate will preferentially buckle.

The buckling transition criteria of the bilayer beam is first evaluated. To model the distinct visco-hyperelastic behavior of MPEC gels, the Neo-Hookean model and Prony series are used. The strain energy density function for the model can be expressed as:

$$W = C_1^0(I_1 - 3) \left(1 - \sum_{i=1}^n g_i (1 - e^{-\frac{t}{\tau_i}}) \right) + p(I_3 - 1), \quad (4.2)$$

where I_1 and I_3 are the first and third invariants of left Cauchy-Green deformation tensor. C_1^0 , g_i , τ_i , and n are the Prony parameters representing instantaneous modulus, dimensionless coefficients, relaxation time and number of series terms. p is the hydrostatic pressure component.

For incompressible material ($J = \det \mathbf{F} = 1$) under uniaxial deformation, the deformation gradient can be expressed as:

$$\mathbf{F} = \text{diag}(\lambda, \frac{1}{\lambda}, \frac{1}{\lambda}), \quad (4.3)$$

and the left Cauchy-Green deformation tensor:

$$\mathbf{B} = \mathbf{F} \cdot \mathbf{F}^T = \text{diag}(\lambda^2, \frac{1}{\lambda}, \frac{1}{\lambda}), \quad (4.4)$$

where λ is the applied stretch in principal direction 1.

The corresponding Cauchy stress can be obtained from the following expression:

$$\sigma = \frac{1}{J} \mathbf{F} \frac{\partial W}{\partial \mathbf{F}} = C_1^0 \left(1 - \sum_{i=1}^n g_i (1 - e^{-\frac{t}{\tau_i}}) \right) \left(\lambda^2 - \frac{1}{\lambda} \right). \quad (4.5)$$

and the material properties in the loading direction can be described as:

$$E(t) = \frac{\partial \sigma}{\partial \lambda} = E_0 \left(1 - \sum_{i=1}^n g_i (1 - e^{-\frac{t}{\tau_i}}) \right) \left(2\lambda + \frac{1}{\lambda^2} \right). \quad (4.6)$$

The stress relaxation data were fitted with a four-term prony series using lsqcurvefit algorithms. As shown in the inset of Figure 4.3a, four terms provided highly accurate results for both materials and the corresponding prony parameters were provided in Figure 4.3b.

To model the buckling criteria, the Euler buckling conditions for a finite beam on elastic foundation with fixed ends were used [114]. The implicit equation for the

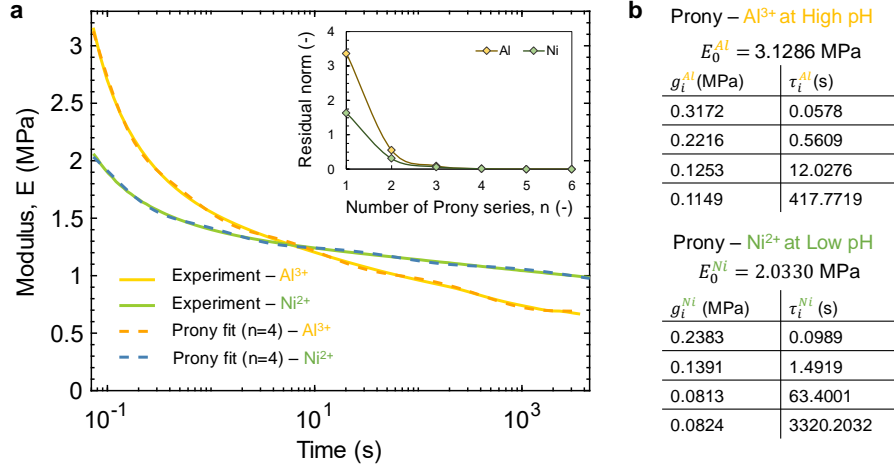


Figure 4.3: **Stress relaxation of selected MPECs and Prony series fitting.** **a**, Fitting of experimental data of relaxation modulus for Al³⁺ at high pH (yellow) and Ni²⁺ at low pH (green). A four-term Prony series (n=4) was selected for fitting based on the residual norm analysis (inset). **b**, The Prony parameters determined for each material.

buckling was given as:

$$\frac{\sin(\frac{1}{2}\sqrt{\pi^2x + 2y})}{\sin(\frac{1}{2}\sqrt{\pi^2x - 2y})} = \mp \frac{\sqrt{\pi^2x + 2y}}{\sqrt{\pi^2x - 2y}}, \quad (4.7)$$

$$\text{where } x = \frac{P_{cr}l^2}{\pi^2EI} \text{ and } y = \sqrt{\frac{k_f l^4}{EI}}.$$

which can be approximated with a mathematical fitting equation [114]:

$$y = \frac{\pi^2}{2}(x - 4), \quad (4.8)$$

which simplifies into an analytical solution for the critical buckling load, P_{cr} and/or critical buckling strain, ε_{cr} is given as:

$$P_{cr} = \frac{2EI}{l^2} \left(\sqrt{\frac{k_f l^2}{EI}} + 2\pi^2 \right). \quad (4.9)$$

$$\varepsilon_{cr} = \frac{P_{cr}}{EA} = \frac{2I}{l^2 A} \left(\sqrt{\frac{k_f l^4}{EI}} + 2\pi^2 \right), \quad (4.10)$$

where E , k_f , l , I , A are elastic modulus of the beam, stiffness of the elastic foundation, effective length of buckling, and the moment of inertia, and the cross section area of a beam.

From the equation 4.10, if we assume the same geometry of each layer on the beam (l, I , and A are identical for both materials), the buckling direction criteria can be:

$$\sqrt{\frac{E_{Ni}l^4}{E_{Al}I}} > \sqrt{\frac{E_{Al}l^4}{E_{Ni}I}} \text{ for left buckling ,} \quad (4.11)$$

$$\sqrt{\frac{E_{Ni}l^4}{E_{Al}I}} < \sqrt{\frac{E_{Al}l^4}{E_{Ni}I}} \text{ for right buckling .} \quad (4.12)$$

Combining with the visco-hyperelastic model (equation 4.6), the criterion for left buckling – buckling towards the side of Al³⁺-MPEC – can be given as:

$$\frac{E_{0,Ni}}{E_{0,Al}} > \frac{\left(1 - \sum_{i=1}^n g_{i,Al}(1 - e^{-\frac{t}{\tau_{i,Al}}})\right)}{\left(1 - \sum_{i=1}^n g_{i,Ni}(1 - e^{-\frac{t}{\tau_{i,Ni}}})\right)}. \quad (4.13)$$

For the lower ($t \rightarrow \infty$) and higher ($t \rightarrow 0$) limits of strain rates, equation 4.13 can be simplified as

$$\frac{E_{0,Ni}}{E_{0,Al}} > \frac{(1 - \sum_{i=1}^n g_{i,Al})}{(1 - \sum_{i=1}^n g_{i,Ni})} \text{ for lower strain rate } (t \rightarrow \infty), \quad (4.14)$$

$$\frac{E_{0,Ni}}{E_{0,Al}} > 1 \text{ for high strain rate } (t \rightarrow 0). \quad (4.15)$$

By fitting the material parameters from Figure 4.3b into equation 4.13, we can construct the critical buckling strain plot as a function of the strain rate, $\dot{\epsilon}$ as shown in Figure 4.4a.

It indicates that the critical buckling strain for the bilayer beam of Al³⁺-Ni²⁺, $\dot{\epsilon}_c$ is transitioned at $\sim 4e-3$: if $\dot{\epsilon} > \dot{\epsilon}_c$ (fast compression), the beam buckles to the left and if $\dot{\epsilon} < \dot{\epsilon}_c$ (slow compression), the beam buckles to the right.

To verify this prediction, we fabricated bilayer beams ($20 \times 4 \times 4 \text{ mm}^3$) using resin-exchange printing (see Figure 4.1). Due to the same polymer matrix, the interface between Al³⁺ and Ni²⁺ gels remained chemically stable, preventing delamination. We performed uniaxial compression experiments at a strain rate of 10^{-3} s^{-1} (slow loading) and 10^{-1} s^{-1} (fast loading). As shown in Figure 4.4, the bilayer beam predictably buckled left under fast compression and right under slow compression, validating our strain-rate-dependent instability control.

4.3.2 Relaxation Dependent Curling

In dynamic materials, post-deformation shape recovery is largely governed by relaxation dynamics and polymer network reconfiguration. The rate and degree of

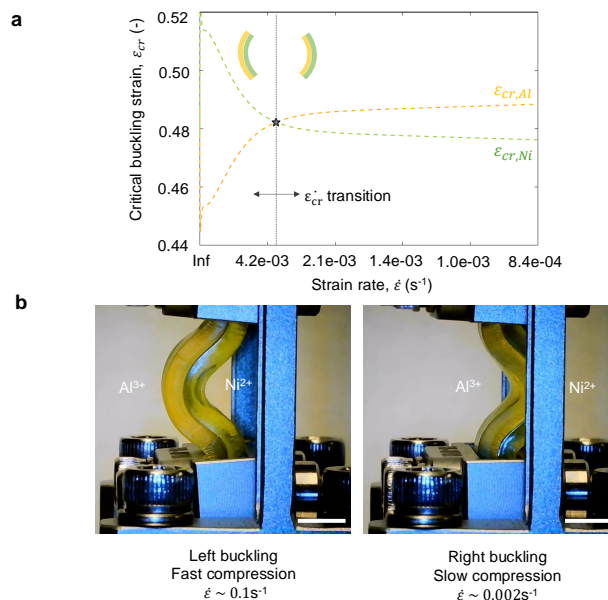


Figure 4.4: **Strain-rate-dependent buckling direction control in MPEC bilayer beams.** **a**, Calculated critical buckling strain as a function of strain rate for the fabricated MPEC bilayer beam. **b**, Experimental validation demonstrating controlled buckling direction under different strain rates. Scale bar 4 mm.

relaxation dictate their ability to recover from applied strain. This property can be exploited to induce shape transformations, where mismatch strain can drive programmable out-of-plane bending upon release. Building on our findings in strain-rate-dependent buckling, we introduce a bilayer system composed of Al^{3+} -MPEC and Ni^{2+} -MPEC gels, where the mismatch in viscoelastic relaxation generates a strain-dependent curvature change. This approach allows us to program stretch-release curling behavior as shown in Figure 4.7. To quantify the recovery properties

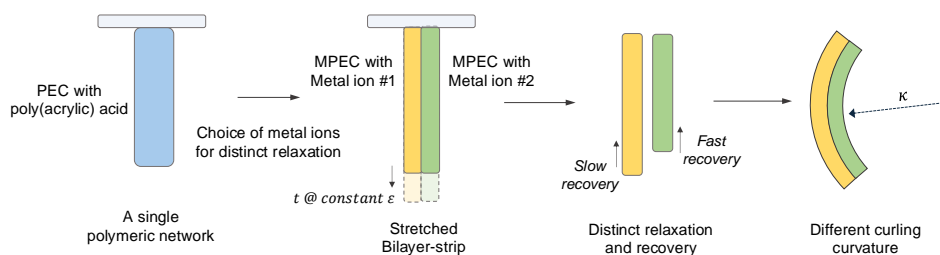


Figure 4.5: **Controllable curling curvature induced by tensile stress in MPEC bilayer strips.**

of the individual gels, we conducted stress relaxation and recovery (creep at zero load) experiments for individual gel. As shown in Figure 4.6b, a constant strain is

applied to stretch the gel, hold the strain for a fixed period of time (t_{hold}), and then release the stretch and track the recovery time.

To quantify the extent of permanent deformation, we define the plastic strain, $\lambda_{plastic} = (L(t_{recovery}) - L_0)/L_0$, where L_0 is the initial strip length before stretching, and $L(t_{recovery})$ is the length after release. Thus, if the gel fully recovers, then $L(t_{recovery}) = L_0$, meaning $\lambda_{plastic} = 0$.

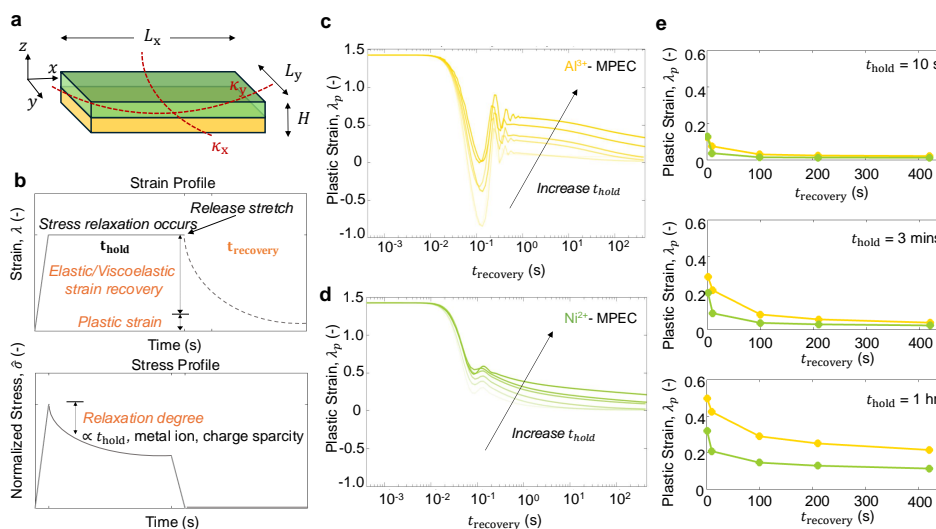


Figure 4.6: Distinct recovery strain of selected MPEC gels. **a**, Schematic representation of the bilayer strip. **b**, Representative strain and stress profiles, with colored annotations indicating material-dependent properties. Measured plastic strain evolution for **c**, Al^{3+} -MPEC and **d**, Ni^{2+} -MPEC over recovery time ($t_{recovery}$) after being stretched by $\lambda = 1.4$ for various hold times (t_{hold}). **e**, Induced mismatch strain resulting from differences in relaxation rate and degree between the two material systems.

As shown in Figures 4.6c,d, both Al^{3+} -MPEC and Ni^{2+} -MPEC exhibit an initial elastic snap-back response upon release due to stored elastic energy from the polymer network. The high polymer density and strong crosslinking in Al^{3+} -MPEC lead to a greater initial elastic recovery force, but over time, greater relaxation occurs compared to Ni^{2+} -MPEC. The strong recovery forces induces out of plane bending on the strip due to fixed boundary end, so $\lambda_{plastic} \leq 0$ does not mean the gel is shorten and then elongated again. After that, it soon equilibrate into its final plastic strain. Over t_{hold} time, greater relaxation occurs for both gels in Figure 4.6e. Due to prolonged relaxation of Al^{3+} -MPEC, observed from Figure 4.3a, it had a larger $\lambda_{plastic}$ compared to Ni^{2+} -MPEC. This evolving mismatch in residual strain drives increasing curvature formation as t_{hold} increases.

To predict the achievable curvature from the mismatch strain, we employ a saddle bending model based on the mechanics of bilayer beams [115, 116].

Assuming incompressibility ($J = \det \mathbf{F} = 1$), the deformation gradient, \mathbf{F} is composed of stretch contribution, \mathbf{F}_s and bending contribution, \mathbf{F}_b :

$$\mathbf{F} = \mathbf{F}_s \cdot \mathbf{F}_b, \quad (4.16)$$

where:

$$\mathbf{F}_s = \text{diag}(\lambda_{mis,x}, \lambda_{mis,y}, \frac{1}{\lambda_1 \lambda_2}), \quad (4.17)$$

$$\mathbf{F}_b = \text{diag}(1 + \kappa_y z + (1 - \cos(-\kappa_x y))(\kappa_y z - \frac{\kappa_y}{\kappa_x}), 1 + \kappa_x z, \frac{1}{\lambda_1 \lambda_2}), \quad (4.18)$$

where $\lambda_{mis,x}$ and κ_y are the mismatch strain and gaussian curvature along the stretch direction, $\lambda_{mis,y}$ and κ_x are the lateral contraction and gaussian curvature across the width of the strip, z is the coordinate in the current configuration along the thickness.

For a thin and slender rectangular strip ($L_x \gg L_y$ and $L_x \gg H$), plane strain conditions apply with uniaxial kinematic ($\lambda_{mis,y} = 1/\sqrt{\lambda_{mis,x}}$ and $\kappa_x \approx 0$), which simplifies the deformation gradient to a case for pure bending deformation:

$$\mathbf{F} = \text{diag}((1 + \kappa_y z)\lambda_{mis,x}, \frac{1}{\sqrt{\lambda_{mix,x}}}, \frac{1}{\sqrt{\lambda_{mix,x}}}). \quad (4.19)$$

Using the Neo-hookean hyperelastic model:

$$\psi(\lambda_1, \lambda_2, \lambda_3) = C_1(\lambda_1^2 + \lambda_2^2 + \lambda_3^2 - 3), \quad (4.20)$$

where C_1 is the material elasticity coefficient. The total strain energy for the entire volume of the strip ($\Omega = \Omega_{Al} + \Omega_{Ni}$) can be evaluated:

$$U = U_{Al} + U_{Ni} = \int_{\Omega} \psi_{Al} d\Omega_{Al} + \int_{\Omega} \psi_{Ni} d\Omega_{Ni}. \quad (4.21)$$

Given the strip dimensions ($L_x \times L_y \times H = 18 \times 4 \times 2 \text{ mm}^3$) and the mismatch strain (Figure 4.6e), we estimate the curvatures (κ_y, κ_x) minimizing U . Due to the slender and thin shape of the fabricated bilayer strip, it was estimated that $\kappa_x \approx 0$. The estimated curvature of κ_y (marker) is highly dependent on t_{hold} due to the evolution of mismatch as demonstrated in Figure 4.7a. To experimentally verify the predicted curvature evolution, we fabricated Al^{3+} - Ni^{2+} bilayer strips using resin-exchange printing (same as for the buckling experiment). Using a static displace-controlled loading in Dynamic Mechanical Analyzer, we applied an

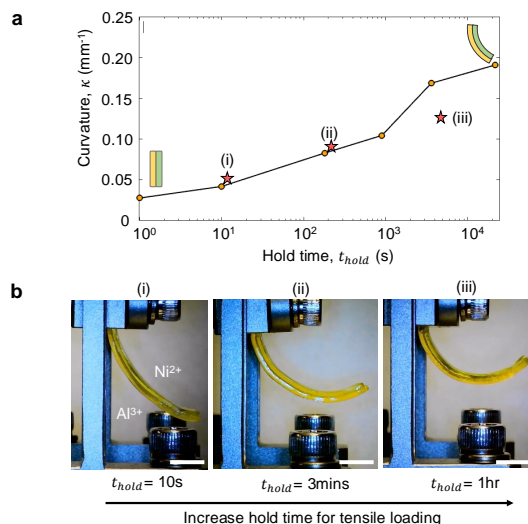


Figure 4.7: **Relaxation-dependent curling curvature from stretch-release shape change.** **a**, Calculated curvature (markers) for the constructed MPEC bilayer strip at $t_{\text{recovery}} = 100$ s. A line curve is included as a visual guide. **b**, Experimental verification of curling curvature variation depending on t_{hold} . The measured curvatures (stars) are plotted in Figure 4.7a. Scale bar 4 mm.

instantaneous stretch of $\lambda = 1.4$ held for a predefined t_{hold} , and then released the load. Figure 4.7b confirms that as t_{hold} increases, the induced curvature grows, and ImageJ curvature measurements from post-release strip deformation closely match analytically estimated values. The strong mismatch strain in Al^{3+} -MPEC and Ni^{2+} -MPEC generates a pronounced curling effect.

4.4 Solvent Stimuli: Swelling-induced Shape Transformation

The interplay between metal ions and charge interactions in MPECs not only dictates their mechanical properties but also significantly influences their interactions with surrounding solvents. When MPEC gels come into contact with solvents such as water, metal solutions, toluene, acetone, or isopropanol (IPA), solvent molecules diffuse into the polymer network, leading to volume expansion (swelling) or contraction (shrinking) of the elastomeric structure. These solvent-polymer interactions provide a versatile design tool, enabling precise control over swelling behavior through adjustments in metal ion coordination and polyanion charge density, which in turn facilitates topological transformations.

The swelling degree of polymer networks can be systematically tuned through a combination of chemical composition and processing parameters. The careful selection of solvent-polymer interactions by tailoring monomer type, charge density,

and hydrophilicity allows for programmable expansion or contraction. Additionally, structural parameters such as crosslinking density, polymer molecular weight, and network architecture serve as constraints to modulate swelling behavior. In this study, we exploited the delicate balance between metal coordination and charge interactions in MPECs to induce metal valency-specific swelling responses.

Fabrication of the swellable MPECs

To achieve swelling-induced shape transformations, we adopted a two-step fabrication process. As shown in Figure 4.8, instead of directly printing MPEC gels with metal ions pre-coordinated to polyelectrolytes, we first fabricated polymer matrices with controlled charge sparsity as described in Chapter 3.3. The printed structures were then subjected to a post-processing step, where they were immersed in water to remove residual resins, equilibrated in water-acetone mixture with targeted volume ratio, and then metal solutions, allowing for precise control over the introduction of metal ions into the gel network. Additionally, to maintain structural integrity in solvent environments, we incorporated partial chemical crosslinking using N,N'-Methylenebisacrylamide (MBAA). This approach enabled preventing premature gel dissolution while preserving spatially controlled ion diffusion and the stability of the printed constructs.

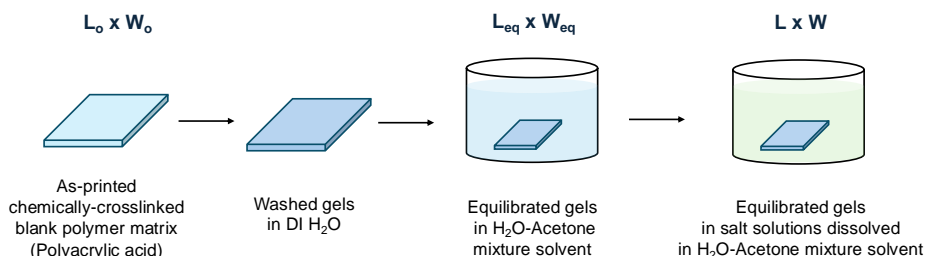


Figure 4.8: Fabrication processes for swellable MPECs.

4.4.1 Charge Density, Metal Valency Dependent Swelling

As discussed in Chapter 3.6.4, polyanion charge sparsity significantly influences polymer microstructure and phase behavior. Confocal microscopy images of printed blank PAA gels reveal that higher pH formulations exhibit more pronounced phase separation between the polymer matrix and surrounding solvent (Figure 4.9). This phase separation suggests that the charge density of polymer chains affects polymer-solvent and polymer-metal ion interactions. To systematically investigate these

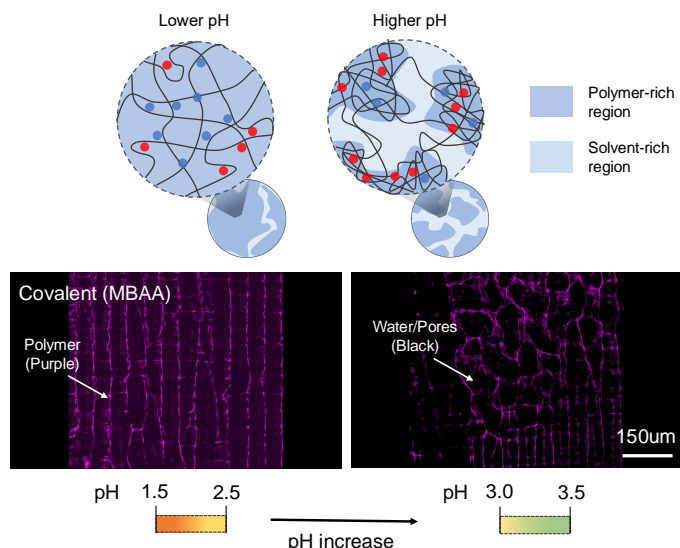


Figure 4.9: **Confocal microscope image of printed blank PAA gel with different pH.** Increased phase separation is observed in high pH gels.

effects, we conducted swelling experiments on free-standing blank PAA gels printed at low pH (pH 1.8) and high pH (pH 3.1). Thin square samples ($12.7 \times 12.7 \times 1 \text{ mm}^3$) were printed and immersed in different environments:

- Solvent Effect: Water-acetone mixture without metal ions to examine swelling dependency on solvent composition.
- Metal Ion Effect: Solutions of Na^+ , Ca^{2+} , and Al^{3+} in a water-acetone mixture to evaluate the effect of metal valency on swelling.

After equilibrium swelling, the gel dimensions were measured using ImageJ software, and the swelling ratio λ_s was calculated as:

$$\lambda_s = \frac{L}{L_0}, \quad (4.22)$$

where L_0 is the initial length of the as-printed gel, and L is the swollen gel dimension at different conditions. Figure 4.10 and Figure 4.11 highlight the distinct swelling behavior of gels in different solvent compositions and metal ion solutions. The high-pH gels swelled significantly more than their low-pH counterparts in water, highlighting charge-density-driven solvent interactions. This behavior is because the more charges on the high-pH gels need the more counter ions to exist in the gel for electroneutrality. As a consequence, the more solvents will enter for the larger excess

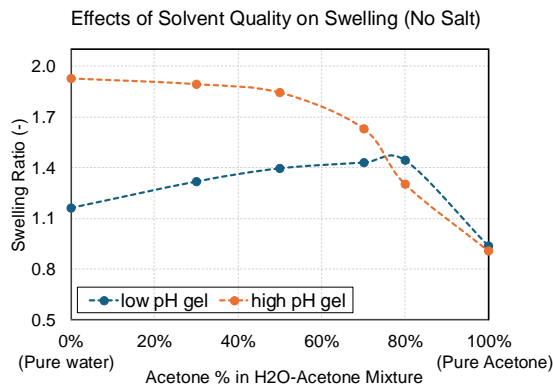


Figure 4.10: **Swelling ratio of low vs. high pH PAA gels in a water-acetone mixture.** The gel pH modulates solvent interaction, influencing swelling behavior.

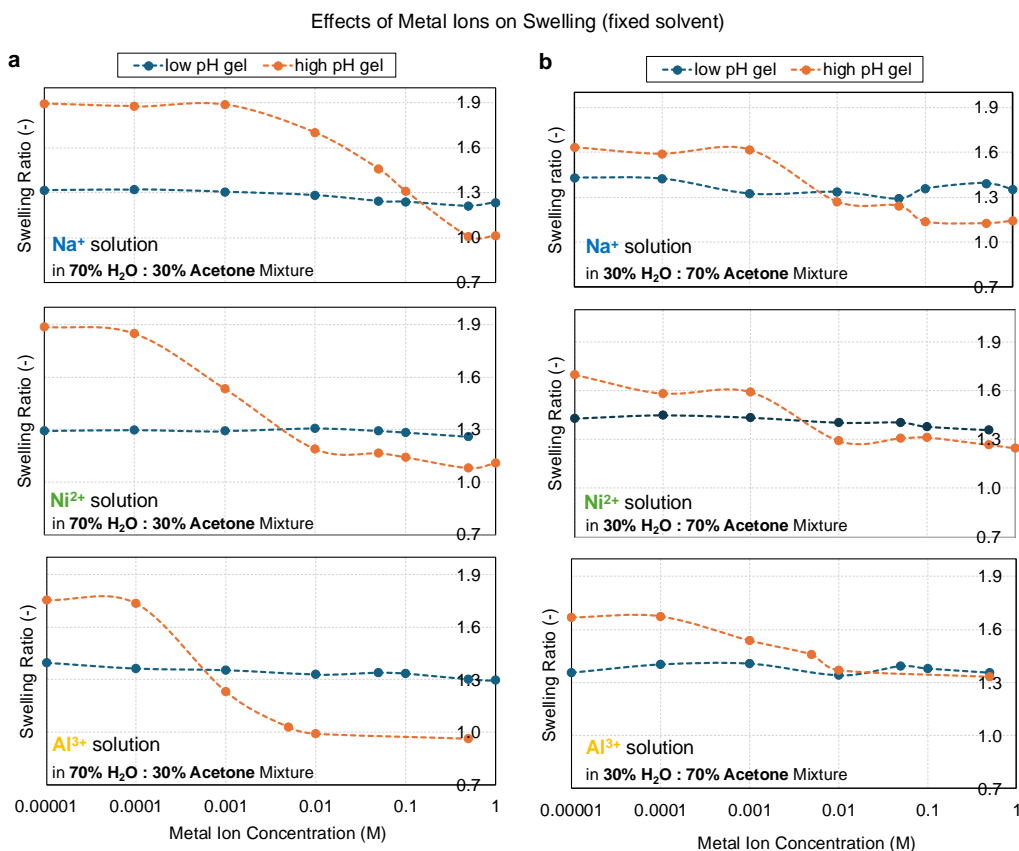


Figure 4.11: **Swelling ratio of low vs. high pH PAA gels in Na^+ , Ni^{2+} , and Al^{3+} solutions.** Salt concentrations were varied in **a**, a 70% water - 30% acetone mixture and **b**, a 30% water - 70% acetone mixture to analyze metal valency effects.

of mobile ions in the gel. The swelling response was confirmed to be repeatable over multiple drying and re-swelling cycles, indicating thermodynamically equilibrated behavior.

To probe solvent interaction effects, gels were immersed in water-acetone mixtures with varying volume fractions. Since acetone has a lower dielectric constant than water, it is expected to screen charge interactions more effectively, inducing further phase separation. As shown in Figure 4.10, high-pH gels remained insensitive to acetone concentrations up to 60 v/v% but shrank sharply beyond this threshold, as demixing and solvent exclusion occurred. Conversely, low-pH gels initially expanded, exhibiting increased solvent compatibility, until they reached the same 60 v/v% threshold, beyond which they also contracted.

Low-pH gels showed minimal response to metal ions and their concentrations, while high-pH gels exhibited sharp swelling transitions at critical metal ion concentrations (Figure 4.11). Due to the high ionic strength of trivalent systems and their stronger metal-polymer coordination, gels displayed a lower critical concentration threshold for higher-valency systems. This transition could be attenuated by increasing the acetone volume fraction, which globally weakens network-solvent affinity. At higher acetone concentrations, the swelling behavior of high-pH gels approached that of low-pH gels, suggesting that solvent composition globally regulates swelling responses.

4.4.2 Qualitative Bi-material Shape Transformation

The distinct swelling response of MPEC gels can be exploited for controlled shape transformations. To demonstrate this, we printed a bilayer beam composed of a blank PAA gel with low pH (left) and high pH (right). The bending direction depended on the solvent environment. The higher swelling degree of high-pH gels in water caused the structure to bend toward the low-pH side, whereas the bending direction reversed as immersed in metal solutions. The higher propensity of metal coordination for higher-pH gels constrained swelling, leading to preferential expansion of the low-pH side. Beyond bilayer designs, spatially controlling bi-material composition enables cooperative shape transformations. In an in-plane arrangement, circular high-pH regions within a low-pH matrix generated out-of-plane buckling due to differential swelling. The circular patterns experienced expansive forces, while the surrounding low-pH gel constrained deformation, promoting buckling as the energetically favorable response.

These qualitative demonstrations validate that charge density and metal valency-dependent swelling can serve as effective mechanisms for shape transformation. However, swelling-induced shape transformations involve large nonlinear deforma-

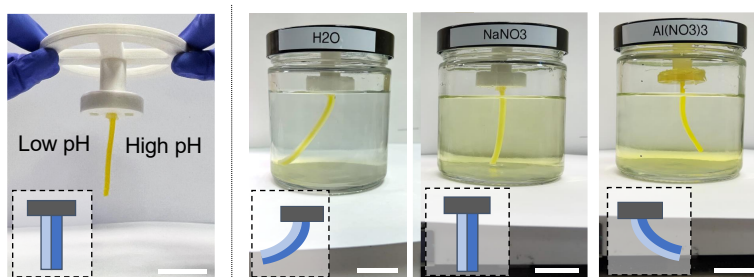


Figure 4.12: **Metal-valency selective bending direction.** Swelling-induced deformation of a bilayer beam composed of Na^+ -MPEC with low pH (left) and high pH (right). Scale bar 30 mm.

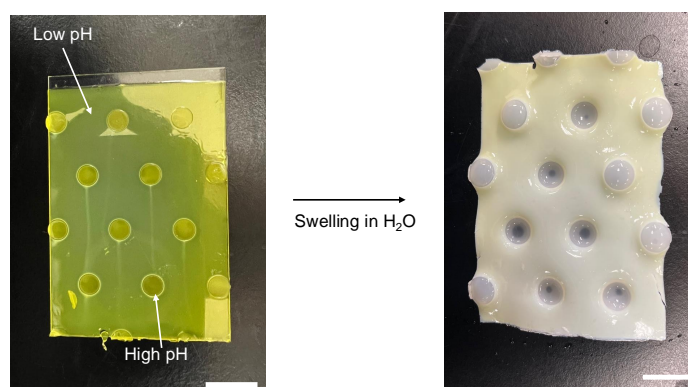


Figure 4.13: **In-plane bimaterial design for cooperative buckling.** Spatially controlled swelling patterns induce out-of-plane buckling. Scale bar 15 mm.

tions, making analytical predictions challenging. To achieve robust and controllable shape transformations, computational modeling is essential to accurately guide structural evolution by accounting for nonlinear mechanics and dynamic swelling behaviors.

Currently, swelling-induced shape transformations are often simulated using finite element analysis (FEA), where the experimentally measured equilibrium swelling strain is applied as a predefined input, and material behavior is approximated using simplified models such as Neo-Hookean hyperelasticity. This approach is effective when the swelling strain is well-characterized and can be directly prescribed, allowing for predictions of the final transformed shape under specific conditions. However, it does not capture the underlying dynamic physics governing swelling transitions, particularly the sharp, nonlinear swelling responses observed in metal solutions (Figure 4.11).

To bridge this gap, a more advanced constitutive framework is needed that integrates large deformation mechanics, electrochemistry, and polymer-solvent interactions in MPECs. Instead of using swelling strain as a direct input, the model should describe shape transformation and evolution as a function of key environmental factors, such as metal ion concentration, solvent composition, or metal valency. By coupling mechanical deformation with the governing stimuli parameters, this framework would enable dynamic predictions of swelling behavior, capturing nonlinear transitions and providing a more powerful tool for designing shape-programmable materials.

4.4.3 Large Deformation Coupled With Molecular Interactions

We are developing a constitutive framework that integrates large deformation mechanics with electrochemistry in MPECs, based on field theory and a modified Flory-Rehner free-energy function [117]. The following section presents some of our preliminary results and ongoing efforts toward establishing this framework, with the ultimate goal of enabling predictive design and control of complex shape transformations in MPEC structures.

Constitutive law framework: free-energy function

Following the work from [117], the swelling behavior of polyelectrolyte system can be expressed with three field variables: deformation gradient (\mathbf{F}), which models the mechanical response of the polymer network; the chemical compositions (C^a), which accounts for mobile ion effects and chemical potential gradients; and the nominal electric displacements ($\tilde{\mathbf{D}}$), which incorporates electrostatic interactions arising from charged species.

$$\mathbf{F} = \frac{\partial \mathbf{x}}{\partial \mathbf{X}}, \quad (4.23)$$

where \mathbf{X} is material points in reference configuration (dry state), \mathbf{x} is the points in current configuration. The true electric displacement, $D(\mathbf{x}, t)$ due to charge interactions, is related to the nominal electric displacement by:

$$\mathbf{D}(\mathbf{x}, t) = \frac{1}{\det \mathbf{F}} \tilde{\mathbf{D}}. \quad (4.24)$$

The number of mobile particles of species per unit volume, C^a is assumed to be conserved (no chemical reaction assumption).

The total free-energy density W of the gel is extended from the Flory-Rehner model and decomposed into four primary contributions:

$$W = W_{net} + W_{sol} + W_{ion} + W_{pol}, \quad (4.25)$$

where W_{net} , W_{sol} , W_{ion} , W_{pol} are the contributions from network stretching, mixing the polymers with the solvent and ions, and polarizing the gel.

The free-energy of stretching the polymer network is assumed to be:

$$W_{net} = \frac{1}{2}NkT(I - 3 - \log(\det \mathbf{F})), \quad (4.26)$$

where $I = \text{tr}(\mathbf{F}^T \mathbf{F})$ the first invariant of Cauchy Green deformation tensor, N is the number density of polymer chains in the dry state, k is the Boltzmann constant and T is the absolute temperature.

The free energy of mixing the solvent and the polymer is taken to be [118, 119]:

$$W_{sol} = \frac{kT}{v^s} (v^s C^s \log \frac{v^s C^s}{1 + v^s C^s} - \frac{\chi}{1 + v^s C^s}), \quad (4.27)$$

where v^s is the volume of the solvent molecule, C^s is the nominal concentration of solvent, χ is the Flory-Huggins parameter for polymer–solvent interactions. For highly swollen gel, $v^s C^s \gg 1$ and $\det \mathbf{F} \gg 1$.

Assuming the concentrations of the mobile ions to be low so that their contribution to the free energy is due entirely to the entropy of mixing with the solvent, W_{ion} is approximately:

$$W_{ion} = kT \sum_b C^b \left(\log \frac{C^b}{v^s C^s c_b^0} - 1 \right), \quad (4.28)$$

where C_b is the nominal concentration of mobile ions, and c_b^0 is the reference state concentration. The true concentration of mobile ions is $c^b = C^b / v^s C^s$.

By treating the polyelectrolyte gel as an ideal dielectric [120], the free energy of polarization is given by [121]:

$$W_{pol} = \frac{1}{2\varepsilon} \frac{1}{\det \mathbf{F}} |\mathbf{F}\tilde{\mathbf{D}}|^2, \quad (4.29)$$

where ε is the the effective dielectric constant of the gel. Due to the different dielectric constants of the polymer and the solvent, the effective dielectric constant of the gel in in function of the concentration of the solvent, but is assumed to be a constant in this study for simplicity.

Although the gel undergoes large volume change ($\det \mathbf{F} \gg 1$), each ions and individual polymer chain are assumed to be incompressible. As a result the volume of the swollen gel is represented as the sum of the volume of dry polymer and volume of all mobile species (i.e. solvents and ions):

$$1 + \sum v^a C^a = \det \mathbf{F}. \quad (4.30)$$

To enforce this volume constraint, the final free-energy expression introduces a Lagrange multiplier term Π

$$\tilde{W} = W + \Pi(1 + 1 + \sum v^a C^a - \det \mathbf{F}), \quad (4.31)$$

where W is equation 4.25 and $\Pi(\mathbf{X}, t)$ is a field of Lagrange multiplier.

Constitutive law framework: constitutive equations

The governing equations for true stress σ , solvent chemical potential μ_{sol} , and ion electrochemical potential μ_{ion} are obtained by differentiating \tilde{W} (equation 4.31) with respect to \mathbf{F} , C_s , and C_b , respectively:

$$\begin{aligned} \sigma &= \frac{\partial \tilde{W}}{\partial \mathbf{F}} \frac{\mathbf{F}^T}{\det \mathbf{F}} \\ &= \frac{NkT}{\det \mathbf{F}} (\mathbf{F}\mathbf{F}^T - \mathbf{I}) + \frac{1}{\varepsilon} (\mathbf{D} \otimes \mathbf{D} - \frac{1}{2} (|\mathbf{D}|^2) \mathbf{I}) - \Pi \mathbf{I}, \end{aligned} \quad (4.32)$$

where

$$\mathbf{D} = \tilde{D} \frac{\mathbf{F}^T}{\det \mathbf{F}}. \quad (4.33)$$

The solvent chemical potential is given by:

$$\begin{aligned} \mu_{\text{sol}} &= \frac{\partial \tilde{W}}{\partial C^s} \\ &= kT \left[\log \frac{v^s C^s}{1 + v^s C^s} + \frac{1}{1 + v^s C^s} + \frac{\chi}{(1 + v^s C^s)^2} - \sum_{b \neq s} \frac{C^b}{C^s} \right] + \Pi v^s. \end{aligned} \quad (4.34)$$

Similarly, the ion electrochemical potential is:

$$\begin{aligned} \mu_{\text{ion}} &= \frac{\partial \tilde{W}}{\partial C^b} + e z^b \Phi \\ &= kT \log \frac{C^b}{v^s C^s c_0^b} + \Pi v^b + e z^b \Phi, \end{aligned} \quad (4.35)$$

where e is the elementary charge, z_b is the valency of the mobile ions, and Φ is the electric potential.

The constitutive equations can be obtained for external solutions with the same approach but the free-energy function is modified to be:

$$W^{\text{ext.sol}} = W_{\text{ion}} + W_{\text{pol}}. \quad (4.36)$$

With an assumption that the external solution is an infinitely large reservoir, we set $\Phi = 0$ for the regions far away from the gel. Then, the constitutive equation for external solutions are:

$$\mu_{ion}^{ext,sol} = kT \left[\log(v^b c_0^b) - \sum_{b \neq s} v^b c_0^b \right], \quad (4.37)$$

$$\mu_{sol}^{ext,sol} = -v^s kT \sum_{b \neq s} c_0^b. \quad (4.38)$$

Constitutive law framework: equilibrium state for free swelling

As we model the equilibrium states for the gel undergoing free swelling, the following equilibrium conditions must be satisfied:

1. Stress balance (zero stress in free swelling gel)

The true stress balance for the gel (far away from the gel-solution interface), the equation 4.32 becomes:

$$\sigma = \frac{NkT}{\det \mathbf{F}} (\mathbf{F}\mathbf{F}^T - \mathbf{I}) - \Pi \mathbf{I} = 0. \quad (4.39)$$

2. Electrochemical equilibrium for mobile ions

Electrochemical potential of all mobile ions are uniform throughout the gel and the external solution require $\mu_{ion} = 0$ at chemical equilibrium so that equation 4.35 becomes:

$$C^b = v^s c^s c_0^b \exp\left(\frac{-\Pi v^b + e z^b \Phi}{kT}\right). \quad (4.40)$$

3. Solvent chemical potential balance between gel and external solution

Equation 4.34) balances with external solution equation 4.38):

$$\mu_{sol} = \mu_{sol}^{ext,sol}. \quad (4.41)$$

4. Electroneutrality conditions:

$$C_{fix} + C^{OH^-} + C^{NO_3^-} = C^{H^+} + C^{ZM^+}, \quad (4.42)$$

where C_{fix} is the nominal concentration of the fixed charges on the polymer network.

5. Volume constraint (isotropic swelling assumption: $\mathbf{F} = \lambda \mathbf{I}$) The incompressible relation is represented as:

$$1 + v^s C^s = \lambda^3. \quad (4.43)$$

By solving these equilibrium conditions with experimental parameters (e.g., polymer charge density, N , charge density, C_{fix} , ion concentrations, c_b^0 , Flory-Huggins parameter, χ), we can predict the swelling ratio, λ and electrochemical interactions in MPEC gels.

Material parameters for modeling

To implement the constitutive framework for MPEC swelling behavior, we determine four key input parameters:

1. Mobile ion concentration (c_b^0)

The mobile ion concentration in the external solution, c_b^0 , is obtained directly from the known concentrations of the metal salt solutions used in swelling experiments.

2. Fixed charge concentration (C_{fix})

The fixed charge density (f) on polymer is determined using the Henderson-Hasselbalch relation (Figure 3.10a) based on measured resin pH values. Table 4.1 presents the estimated the fixed charge density for different MPEC gel formulations. C_{fix} values are estimated from f .

PAA gel	Measured resin pH	$f = \frac{[\text{COO}^-]}{[\text{COOH}]} = 10^{\text{pH} - \text{pKa}}$
Low-pH	1.81	0.003
High-pH	3.46	0.145

Table 4.1: **Estimated fixed charge density (f) for modeling in MPEC gels.**

3. Polymer-solvent interaction (χ)

In this study, the Flory-Huggins interaction parameter (χ) represents an effective polymer-solvent interaction depending on the solvent composition. It is determined by fitting experimental swelling data (Figure 4.10). To account the co-solvent, we treat the mixed solvent following the rule of mixture and fitted the effective χ as [122]:

$$\chi = \bar{\chi}_0 + \frac{\bar{\chi}_1}{\det \mathbf{F}}, \text{ where } \bar{\chi}_i = \chi_i^a \varphi + \chi_i^w (1 - \varphi) - \chi_i^{aw} \varphi (1 - \varphi) \quad (4.44)$$

represent polymer-acetone, polymer-water, and mixed solvent interactions, respectively, and φ is the volume fraction of acetone.

4. Effective Polymer Chain Density (N)

The effective density of polymer chains in the dry polymer state, N , is extracted from poroelastic characterization using macroindentation tests [117, 123]. The indentation setup, illustrated in Figure 4.14a, involves applying a fixed displacement δ to a fully swollen gel while measuring force relaxation over time. This relaxation is driven by solvent migration within the deformed region, governed by the chemical potential gradient (Figure 4.14b).

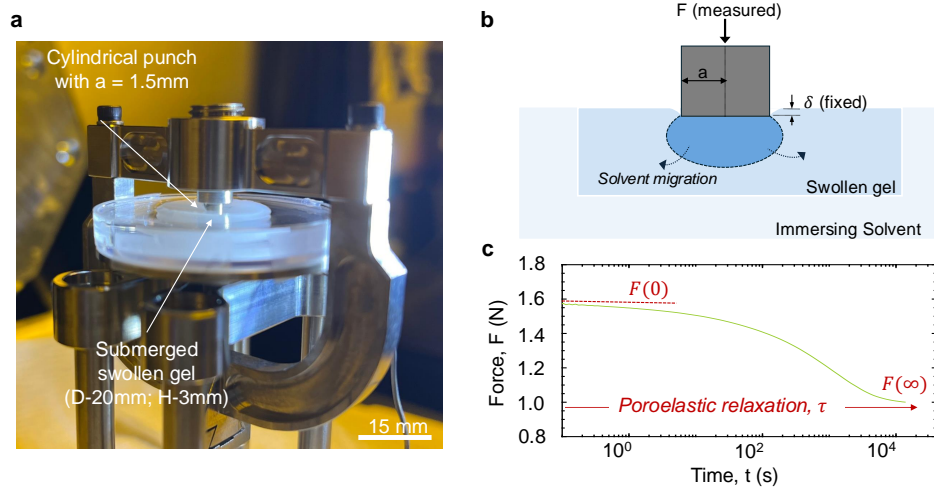


Figure 4.14: **Poroelastic relaxation via indentation.** **a**, Experimental indentation setup for submerged swollen gels. **b**, A cylindrical indenter (radius = 1.5 mm) applies a fixed displacement $\delta=0.3$ mm, inducing solvent migration within the gel. **c**, Measured force relaxation over time for a low-pH PAA gel in water.

At the instant of indentation, the gel behaves as an incompressible elastic solid due to the absence of immediate solvent migration. Over time, solvent redistributes within the gel, transitioning it to a compressible state. Using Hertzian contact mechanics of an elastic layer with flat punch indenter [124], the measured load relaxation is correlated with the gel's shear modulus (G_{gel})[125]:

$$F(0) = 8G_{gel}\delta a, \quad (4.45)$$

where a is the indenter radius, and G_{gel} is the share modulus of the fully swollen gel and is related to the polymer chain density as [125]:

$$G_{gel} = \frac{NkT}{\lambda_{eq}}, \quad (4.46)$$

where λ_{eq}^* is the equilibrium swelling ratio of fully dried and fully swollen gel in water.

PAA gel	Measured G_{gel} (kPa)	Measured λ_{eq}^* (in water)	Estimated N ($\times 10^{25} \text{ m}^{-3}$)
Low-pH	160.6	1.71	6.68
High-pH	119.8	2.73	7.96

Table 4.2: **Estimated polymer chain density (N) from indentation experiments.**

Table 4.2 summarizes the extracted G_{gel} and N values. While this approach effectively estimates the bulk polymer network density, it should be noted that it does not fully account for charge interactions [126], which influence the swelling response of polyelectrolyte gels. Thus, while N provides a useful approximation, a more refined method incorporating electrostatic interactions is needed for future studies. The Poisson's ratio of the gels is assumed to be $\nu = 0.5$, as most hydrogels exhibit near-incompressible behavior in the swollen state.

Preliminary results for complex shape transformation

The preliminary results for modeling the swelling response of low-pH and high-pH gels immersed in Na^+ solutions (70% water:30% acetone mixture) are presented in Figure 4.15. The model captures key swelling trends observed in both gel systems, particularly the insensitivity of low-pH gels to Na^+ and the swelling-to-shrinkage transition in high-pH gels. While these initial results are promising, additional validation and refinements are required to improve accuracy and predictive capability.

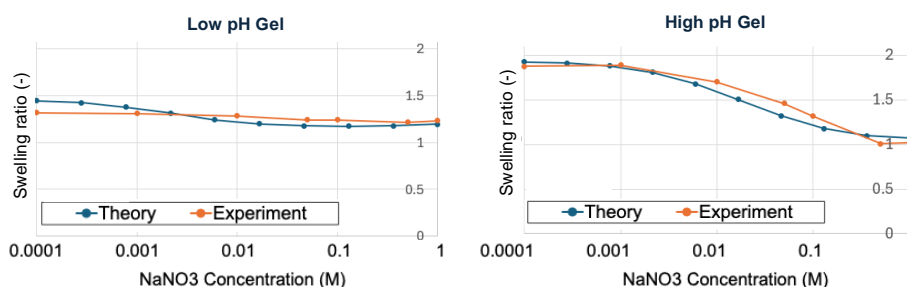


Figure 4.15: **Comparison of experimental and theoretical swelling of PAA gels in Na^+ solution.** The developed model effectively captures the swelling behavior of low-pH (left panel) and high-pH (right panel) gels immersed in Na^+ solutions, demonstrating the experimentally observed insensitivity of low-pH gels and the swelling-to-shrinkage transition in high-pH gels.

Building on these insights, we explore the potential of integrating the constitutive model to describe swelling-induced geometrically confined buckling shape

transformations. Inspired by the work of Wu et al.[127], where interconnected hydrogel pores were shown to transition between open and closed states under swelling-induced buckling, we aim to extend this concept by directly linking shape transformation to sodium ion concentration.

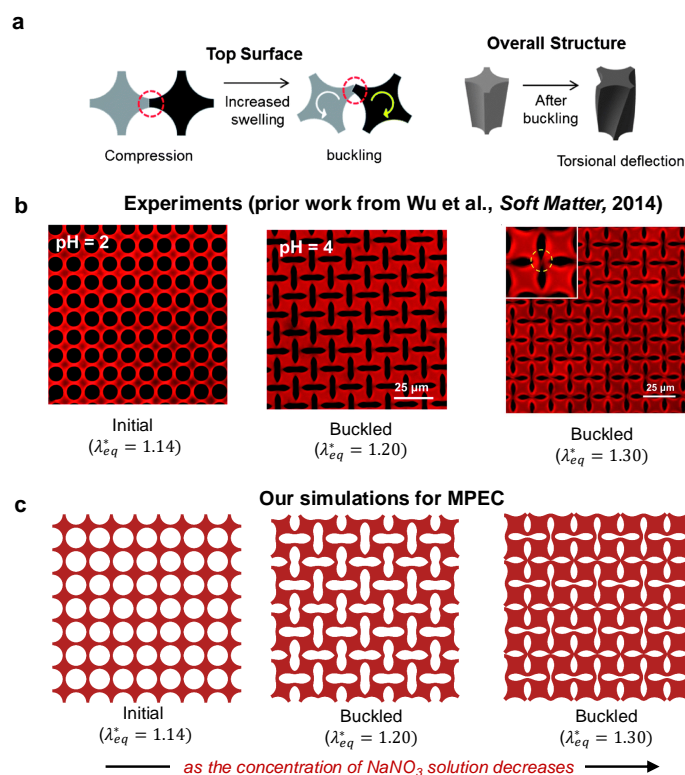


Figure 4.16: **Geometrically confined shape transformation.** **a**, The swelling-induced buckling instability mechanism, where interconnected and geometrically confined pores exert compressive forces on neighboring domains, triggering coordinated structural rotation. **b**, Experimental observations of shape-transformed hydrogels as a function of swelling degree (Reproduced from [127] with permission from the Royal Society of Chemistry). **c**, Simulated MPEC shape transformation as a function of sodium ion concentration, demonstrating continuous shape evolution rather than discrete transitions.

In [127], swelling a pH-responsive gel at low pH (pH 2) generated minimal compressive stress at the joint regions due to limited swelling ratio, leading to minor pore shrinkage without significant structural transformation. However, at pH 4, increased osmotic pressure drove buckling at the interconnecting joints, leading to simultaneous structural rotation (Figure 4.16a). When interconnected hydrogel pores were arranged in a tessellated pattern, the collective mechanical instability enabled a large-scale pattern transformation of the hydrogel membrane (Figure 4.16b).

This experiment demonstrated that differential swelling strain can be harnessed for programmable structural responses.

Our approach builds upon this concept and demonstration by incorporating ion-responsive swelling behavior into shape evolution dynamics. We first capture the Na^+ responsive swelling response of the high pH gel via the developed constitutive models. Then, the predicted swelling response is represented with a modified Neo-hookean model with the Lagrangian multiplier, which can smoothly integrated into a commercial FEA using COMSOL. By changing the Lagrangian multiplier, which represents Na^+ ion concentration change in real system, the morphology transformation can be demonstrated as a continuous change in solvent environment. We demonstrate some of preliminary results that decreasing Na^+ concentration leads to increased corresponding swelling ratios, which in turn drive a gradual transition from open to closed pore states following similar transformed shape to the experimental work (Figure 4.16c).

Unlike prior approaches that rely on experimentally measured equilibrium swelling strains as pre-defined input parameters, our model actively couples large deformation mechanics with environmental condition changes. This preliminary work demonstrates a potential advancement in predictive control over dynamic shape transitions, rather than relying solely on empirical fitting. However, the current model is still in an early stage, requiring further refinement and validation.

4.4.4 Outlook for Complex Shape Transformation

The ability to design materials that dynamically transform in response to environmental stimuli holds great promise for next-generation functional materials. While the model successfully predicts key swelling trends, several key refinements are required for full development:

- **Parameter Sensitivity:** The accuracy of the model depends on input parameters such as polymer-solvent interaction (χ), which is determined through empirical fitting. Further refinement is required to improve parameter estimation.
- **Multivalent Ion Effects:** The current model is primarily validated for monovalent ion solutions (Na^+). Additional modifications are needed to account for the complex electrostatic interactions and coordination chemistry of multivalent metal ions.

- **Dynamic Swelling Transitions:** While the model captures equilibrium swelling well, transient swelling kinetics, including sharp phase transitions observed in high-pH gels, require further refinement. A time-dependent diffusion-reaction framework could improve predictions.

By leveraging this computational-experimental framework, we will be able to design self-adaptive materials capable of responding dynamically to environmental changes, with potential applications in self-regulating filtration membranes, salt-responsive soft robotics, and bio-mimetic sensing systems.

4.5 Beyond Mechanics: Towards Multifunctionality

The dynamic and reversible nature of molecular bonds in MPEC gels allows them to extend beyond mechanical tunability, enabling functionalities such as reprocessability, shape memory, and stimuli-responsive behavior. By leveraging reversible crosslinking and thermally-driven relaxation of these materials, this section explores two key functionalities that highlight the broader applications of dynamic chemistry: reprocessability via guided dissolution and shape memory behavior.

4.5.1 Dissolution and Reprocessing

The reversibility of metal–polymer electrostatic interactions enables complete dissolution and reprocessing of MPEC gels, offering a pathway toward sustainable and recyclable soft materials. Unlike conventional covalently crosslinked networks, which degrade irreversibly or require chemical scission for recycling, MPECs dissolve controllably in response to solvent and pH stimuli, allowing material reuse and reshaping.

Molecular choice dependent dissolution

To validate the reprocessability of MPEC gels, we tested their solvent-assisted dissolution in aqueous environments. As shown in Figure 4.17, AM-fabricated MPEC gels with different metal ions were prepared and immersed in DI water to monitor their dissolution behavior. The mass change, ΔM , was tracked over time using the equation:

$$\Delta M\% = \frac{M(t) - M_0}{M_0} \times 100 \quad (4.47)$$

where M_0 is the initial mass of equilibrated MPECs and $M(t)$ is the mass at a given time. Initially, all gels exhibited swelling as solvent diffusion and polymer network expansion occurred. However, their dissolution behavior varied depending on the

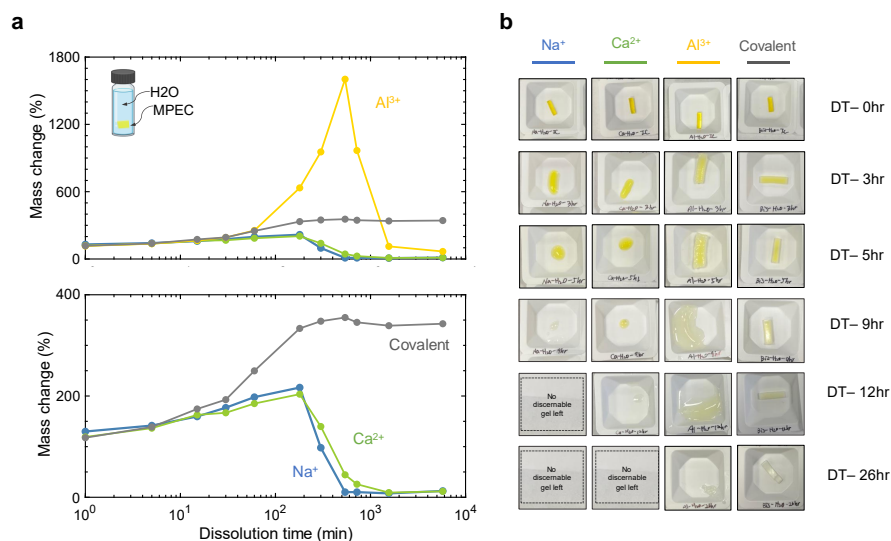


Figure 4.17: Gel dissolution of MPECs with varied metal ions. **a**, The swelling and dissolution progress of MCPs crosslinked with different metal species were monitored. **b**, Optical images of the remaining MPEC gels extracted from the supernatant liquid during the dissolution time (DT).

metal coordination strength. For Na^+ and Ca^{2+} -MPECs, dissolution began once the metal coordination number dropped below two, leading to complete dissolution within 9–12 hours for Na^+ and 15–20 hours for Ca^{2+} . The stronger polymer association of Ca^{2+} resulted in a slower dissolution rate compared to Na^+ . In contrast, Al^{3+} -MPECs exhibited significant swelling ($\sim 1600\%$ of M_0) before dissolution. The slow relaxation of Al^{3+} ions allowed the gel to retain its shape, while progressive polymer disentanglement enabled a larger swelling degree. Once maximum swelling was reached, the network gradually collapsed, leading to dissolution. As expected, the covalently crosslinked network reached equilibrium swelling without dissolving, demonstrating its permanent and non-reprocessable nature. Charge sparsity further influenced the dissolution dynamics, significantly altering swelling and dissolution rates. As shown in Figure 4.18, MPEC gels fabricated at high pH (resulting in higher charge density on the polymer) exhibited distinct dissolution behaviors. Na^+ and Ca^{2+} gels dissolved more rapidly, whereas Al^{3+} gels experienced extreme swelling, reaching nearly 6000% of their original mass before dissolution. Notably, even a small pH adjustment from 1.4 to 2.4 resulted in a dramatic difference in dissolution behavior, emphasizing the sensitivity of charge density in dictating material stability.

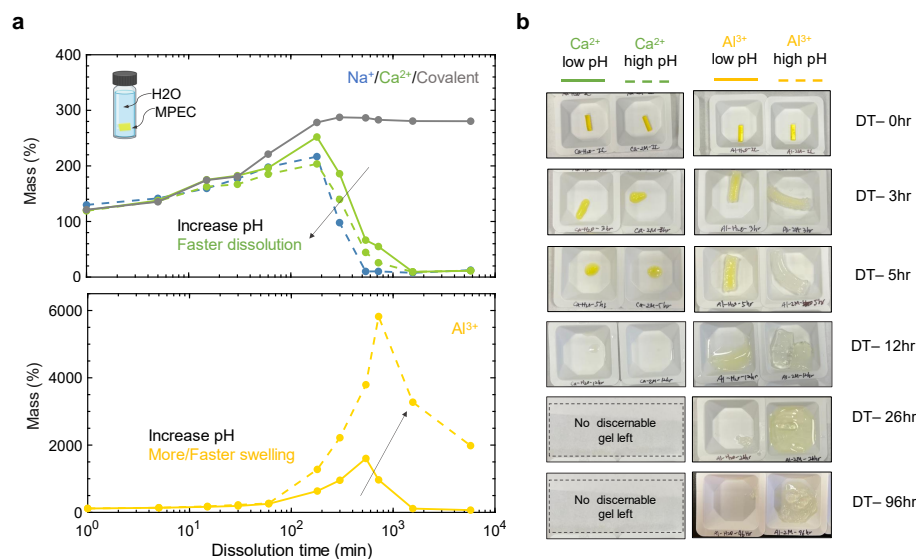


Figure 4.18: **Gel dissolution of MPECs with varied charge sparsity.** **a**, The swelling and dissolution progress of MCPs crosslinked with Ca²⁺ and Al³⁺ at different pH (solid: low pH, dashed: high pH) were monitored. **b**, Optical images of the remaining MPEC gels extracted from the supernatant liquid during the dissolution time (DT).

Guided dissolution pathway

For homogeneous and efficient reprocessability, a guided dissolution pathway is necessary to systematically account for the molecular composition of MPEC gels and navigate phase transitions during dissolution. The phase diagrams constructed in previous chapters through multiscale studies and mean-field theory provide a valuable framework for predicting dissolution behaviors, enabling precise control over reprocessing conditions.

Directly correlating fabricated gels to phase diagrams is challenging due to the complexity of precisely quantifying all components, including polymer repeat units, metal ion concentrations, and solvent composition in printed MPECs. Therefore, we experimentally mapped the dissolution behavior by exposing MPEC gels to different dissolution conditions, backtracking their relative position in the constructed phase diagram (additional data in Appendix B.3) This allowed us to determine the printed state of MPECs within the phase space (Figure 3.19).

Figure 4.19a illustrates the initial phase state of printed Al³⁺-MPECs (yellow marker). Upon submersion in water, the chemical potential drives water penetration into the gels, leading to a decrease in both COOH and metal ion concentrations. The

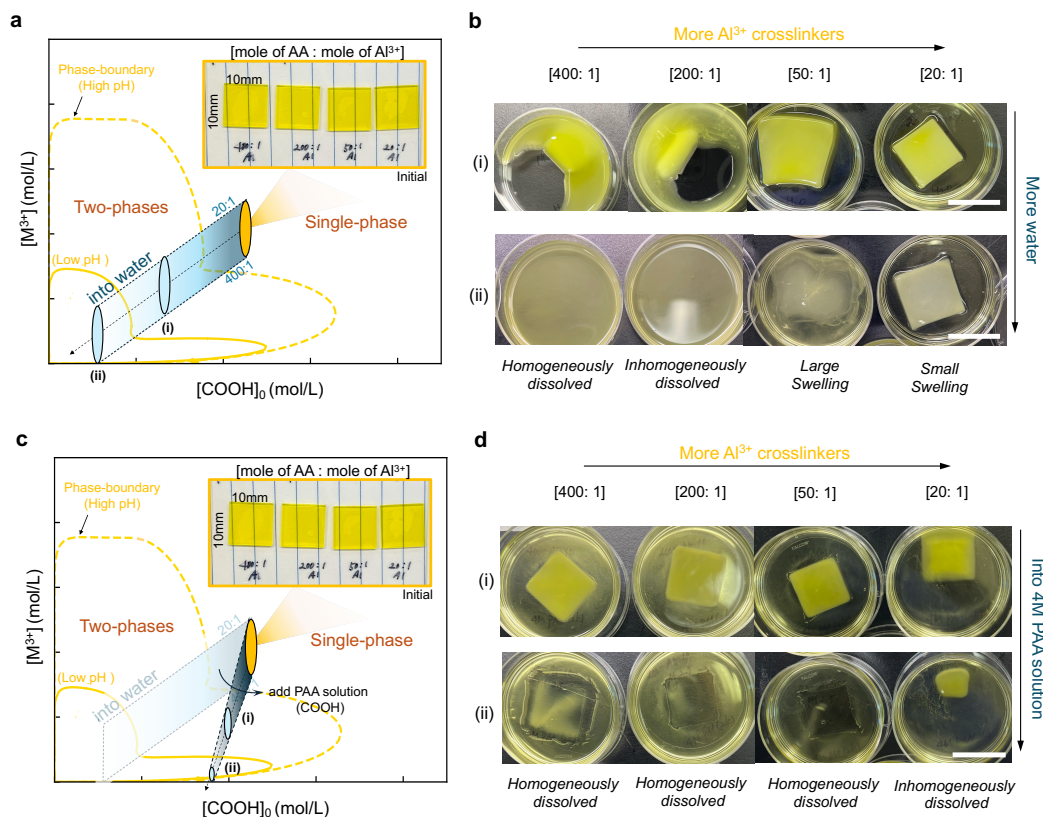


Figure 4.19: **Guided dissolution pathway for Al^{3+} -MPEC.** **a, b,** Dissolution path of printed Al^{3+} -MPECs with varied crosslinking densities upon submersion in water. The yellow markers represent the initial phase states of the printed gels, while the blue markers indicate the subsequent phases achieved during dissolution. The inset shows images of printed Al^{3+} -MPECs with different crosslinking densities. Scale bar 10 mm. **c, d,** Modified dissolution pathway by introducing pre-polymerized poly(acrylic acid) solutions in water to navigate controlled phase transitions. This adjustment enables more homogeneous dissolution while preventing excessive swelling. Scale bar 10 mm.

blue markers represent subsequent phases achieved during dissolution. As shown in Figure 4.19b, the transition from a transparent initial state to an opaque phase indicates that all gels underwent phase separation upon dissolution.

The dissolution behavior varied depending on the crosslinking density of the gels:

- At low crosslinking density (400:1 ratio): Achieves homogeneous and rapid dissolution due to its lower crosslinking, reaching a polymer-sparse state quickly.
- At moderate crosslinking density (200:1 ratio): Reaches a triple-phase bound-

ary where metal solution, polymer-dense, and polymer-sparse regions coexist, verified by heterogeneous dissolution patterns. While the gel eventually reaches a fully dissolved state, the dissolution occurs inhomogeneously, with visible phase-separated domains persisting before complete breakdown.

- At high crosslinking density (50:1 & 20:1 ratio): Experiences a polymer-metal solution phase split, significantly slowing dissolution and inducing extreme swelling due to the competition between slow ion dissociation and polymer disentanglement.

To ensure uniform and efficient dissolution across all gels, we modified the dissolution path by introducing pre-polymerized polyacrylic acid (R-COOH) into the water. This altered the phase transition pathway, guiding all gels through a polymer-dense to polymer-sparse transition, which facilitated homogeneous dissolution (Figure 4.19c). As shown in Figure 4.19d, this approach successfully dissolved all gels without excessive swelling. While the highly crosslinked (20:1) gels required more time to fully dissolve, they eventually underwent complete dissolution, demonstrating the effectiveness of the guided dissolution strategy.

Reprocessing of dissolved gels

Once dissolved, the polymer network remains chemically intact, allowing reformation into new geometries. We recast dissolved MPECs into molds to demonstrate the ability to reshape the material into new forms without loss of integrity. As shown in Figure 4.20, the gels were successfully reprinted and reprocessed. However, for the reprocessed MPEC gels, maintaining identical mechanical properties after reprocessing proved challenging due to difficulties in precisely controlling solvent content and composition. As discussed in Chapter 3.8.1, solvent effects play a critical role in governing the mechanical behavior of MPEC gels. Even small variations in solvent composition and quantity can introduce multiscale effects, influencing molecular-level charge interactions, polymer chain mobility through changes in free volume, and phase behavior as predicted by the phase diagram. These subtle yet impactful changes contribute to variability in mechanical responses after reprocessing, underscoring the necessity for precise solvent control and post-processing optimization in future studies.

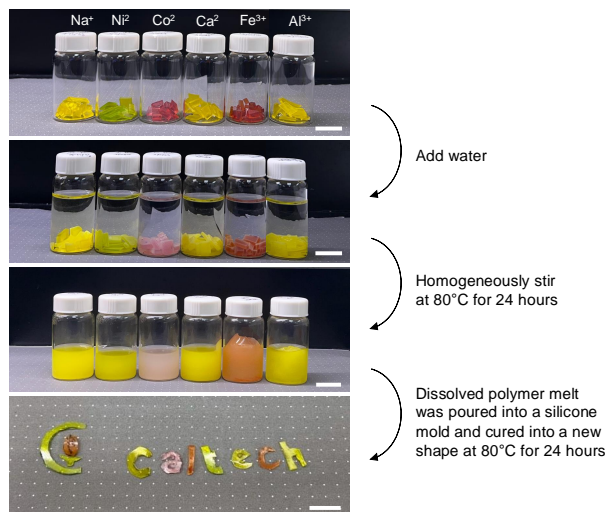


Figure 4.20: **Reprocessability of 3D-printed MPECs.** The dynamic nature of metal-coordination bonds enables complete dissolution and reprocessing of MPECs. AM-fabrication MPEC gels with various metal cations were dissolved in water and recast into different shapes. Scale bar 10 mm.

4.5.2 Shape Memory Effects

The inherent dynamic and thermal dependence of MPEC gels provides a mechanism for programmable shape memory effects, where external stimuli, such as heat or solvent exposure, trigger controlled shape recovery. The shape memory rate and recoverable strain are dictated by the interplay between bond relaxation, polymer network reconfiguration, and elastic energy storage/release. Upon heating, polymer chains become mobile, dynamic crosslinkers weaken, and the polymer network undergoes reconfiguration. Upon cooling, the crosslinks reform, stabilizing the new shape until reactivation. Similar to mechanically induced relaxation, the extent and rate of thermally triggered relaxation govern the recovery kinetics.

To demonstrate this effect, a flower-shaped MPEC gel with open petals was heated to 90°C, deformed into a closed shape for 5s (‘programming’), and subsequently cooled to -5°C to fix the programmed shape. When reheated to 90°C, the gel returned to its original shape, mimicking the blooming of a flower (Figure 4.21a). Figure 4.21b highlights how metal valency influences the rate of shape recovery. Upon reheating to 90°C, MPEC gels restored their original shape at different rates depending on their metal crosslinkers (Na⁺ - 90s, Ca²⁺ - 72s, Al³⁺ - 30s). The differences in recovery speed arise from variations in relaxation dynamics. As discussed in Figure 3.13c, ion-pairing kinetics and polymer relaxation times vary with metal valency, influencing the driving force for shape recovery. During ‘programming’ at elevated

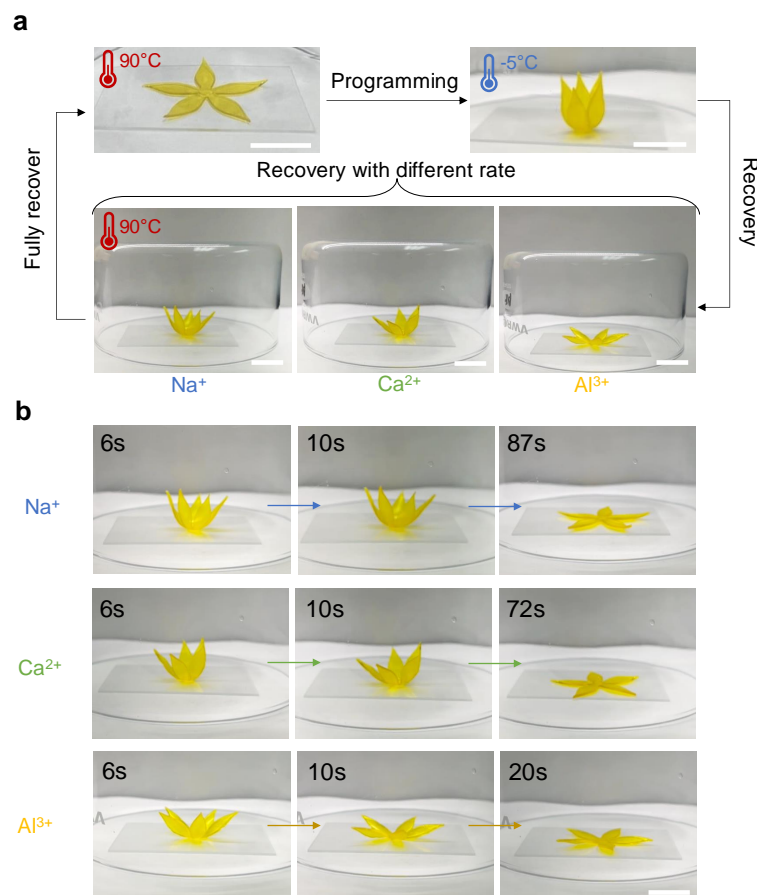


Figure 4.21: **Controlled shape recovery in MPECs.** **a**, Heating-induced shape memory behavior of a flower-shaped MPEC gel. **b**, Influence of metal valency on shape recovery rates. Scale bars 20 mm.

temperatures, the slow relaxation of Al³⁺ ions results in gels being further from equilibrium, leading to a faster recovery upon reheating.

This demonstration expands the stimuli-responsive capabilities of MPECs beyond mechanical activation, highlighting their potential for thermally driven functionalities.

4.6 Conclusion

This chapter explored how molecular-level control in MPECs can be leveraged to program deformation and different functionality. By integrating experimental characterization, theoretical modeling, and computational simulations, we demonstrated how charge interactions, metal coordination, and relaxation dynamics govern deformation modes, shape transformations, and multifunctional properties. The ex-

perimental findings reveal that strain-rate-dependent buckling and relaxation-driven curling can be programmed by controlling molecular relaxation timescales, demonstrating the ability to precisely guide nonlinear mechanical instabilities. Solvent-driven deformations further highlight the critical role of charge sparsity and metal valency in dictating swelling transitions, which were successfully captured using a field-theory-based constitutive model. The preliminary modeling results provide an important step toward predicting complex shape transformations by directly coupling swelling mechanics with external chemical stimuli. Beyond mechanical responses, we demonstrate the multifunctionality of MPEC gels, including guided dissolution for reprocessing and thermally activated shape memory effects, enabled by the reversible nature of metal-polymer coordination. The ability to dynamically reconfigure material properties and structures through controllable swelling and relaxation mechanisms presents a promising pathway toward adaptive soft materials, reconfigurable actuators, and self-healing systems. We hope this work provides fundamental insights into how molecular interactions dictate global material responses and provide a comprehensive understanding of how molecular design strategies can be extended to develop adaptive and reconfigurable materials with tailored mechanical and functional properties.

SUMMARY AND OUTLOOK

5.1 Summary

This work explores hierarchical material design by integrating scalable fabrication, multiscale characterization, and predictive modeling to connect molecular-level interactions with macroscale material performance. By addressing challenges in architected materials and dynamically crosslinked polymer networks (MPECs), this work advances the understanding of how structural organization across multiple length scales dictates mechanical properties, energy dissipation, and adaptive functionality.

The first study develops a scalable fabrication strategy for nano-architected polymeric materials using metamask-based holographic lithography, enabling the seamless tessellation of nano-architected unit cells into centimeter-scale architectures. By systematically tuning unit cell geometries, including relative density and beam aspect ratio, we demonstrate their impact on the stiffness, impact resistance, and energy dissipation mechanisms. These findings highlight the potential of hierarchical structuring in scalable manufacturing, offering design principles for impact mitigation and lightweight, high-performance structures.

The second study shifts the focus from geometrical hierarchies to polymer hierarchical organization. Dynamically crosslinked MPECs are investigated by leveraging metal coordination and polyanion charge density as molecular design parameters. Through multiscale experimental characterization and theoretical modeling, the study reveals how charge sparsity and metal valency govern chain relaxation, crosslinking dynamics, and network topology. The findings elucidate the critical role of ion-pairing kinetics and polymer network interactions in determining macroscale stiffness, stretchability, and fracture toughness. The multiscale insights provide a framework for designing functional materials with tunable and programmable mechanical properties.

The final study extends molecular design principles to global material responses, integrating them with continuum mechanics to control mechanical instabilities and shape transformations. We demonstrate strain-rate-dependent buckling and relaxation-driven curling, enabling nonlinear deformations. Solvent-responsive

swelling transitions illustrate how charge density and metal valency drive programmable shape transformations. Beyond mechanical functionality, the study demonstrates reprocessability and guided dissolution, allowing MPECs to be fully dissolved and reformed into new geometries. Thermal activation also enables shape-memory effects, broadening the scope of stimuli-responsive materials.

Through these studies, we highlight the importance of hierarchical structuring as a fundamental design principle in material science. By bridging fundamental material physics with additive manufacturing, we can expand the material design space for functional polymers, enabling a more robust and versatile approach to material development.

5.2 Outlook

As the field of functional materials progresses, the ability to design, fabricate, and predict the behavior of adaptive and functional material systems remains a key challenge. This thesis has demonstrated how hierarchical structuring, dynamic crosslinking, and molecular-level interactions can be leveraged to program material responses. Moving forward, three critical research directions emerge that will enable to contribute for the next generation of material systems.

Expanding Additive Manufacturing for Functional Materials

Achieving precise multi-scale structuring in hierarchical materials remains a major challenge. This work demonstrated holographic lithography and stereolithography-based fabrication for both nano-architected and dynamically crosslinked materials. However, achieving scalable, high-resolution, and multi-material integration remains an ongoing pursuit.

Current AM techniques are largely optimized for structural and passive materials, whereas functional polymers require precise control over crosslinking dynamics, phase separation, and bond exchange kinetics. Expanding AM processing capabilities to accommodate dynamic chemistry will enable the fabrication of gradient architectures and spatially heterogeneous materials, where mechanical stiffness, relaxation rates, and molecular mobility vary locally to enable programmed deformations and shape evolution.

Integrating chemically responsive materials into scalable AM platforms will allow spatiotemporal programming of material properties, leading to adaptive structures with site-specific mechanics and tunable functionalities. Future work should focus

on developing AM techniques that enable precise spatial control of polymerization kinetics, reaction-diffusion behavior, and dynamic bond exchange, unlocking new opportunities in wearable devices, biomedical applications, and soft robotics.

Linking Molecular Dynamics with Structural Mechanics for Adaptive Systems

The final phase of this thesis demonstrated how molecular relaxation mechanisms can be leveraged to program strain-rate-dependent buckling, relaxation-driven curling, and solvent-responsive shape transformations. These studies establish a critical synergy between material chemistry and structural instabilities, where molecular interactions dictate local responsiveness, while structural geometries amplify or suppress these effects through localized deformation or stress redistribution. This interplay enables programmable architectures that dynamically reconfigure under external stimuli, unlocking applications where materials autonomously respond, conform, and recover under external forces.

Future research should fine-tune molecular bond lifetimes, relaxation dynamics, and chemo-mechanical coupling to develop materials with on-demand adhesion, self-regulating interfaces, and programmable mechanical properties. By integrating molecular-scale dynamics with structural mechanisms such as buckling, snap-through instabilities, and nonlinear deformations via origami/kirigami, future functional material systems can be precisely engineered for tailored topologies, controlled instabilities, and enhanced environmental adaptability. This will enable stimuli-responsive, adaptive behaviors to serve as self-monitoring systems for environmental sensing, shape-morphing soft robotics, and dynamically conforming biomedical implants.

Advancing Multiscale Understanding for Predictive Material Design

A fundamental challenge in dynamic polymer design is establishing a predictive and reliable framework that links molecular parameters to bulk material properties. The complexity arises from the interplay of chemical composition, crosslinking dynamics, solvent interactions, and additive manufacturing (AM) flexibility, often leading to unpredictable outcomes. To bridge this gap, it is essential to understand how molecular-scale interactions propagate across length scales, influencing network topology, mesoscale phase behavior, and macroscopic mechanical properties.

Developing reliable parameter-structure-property relationships requires a synergistic integration of experiments and computational modeling. While experiments capture physical phenomena across different scales, computational tools provide

mechanistic insights beyond experimental reach. For example, our molecular dynamics simulations and mean-field theory successfully decoded dynamic polymer networks, phase behavior, and relaxation mechanisms in charged polymer, enabling rational material design.

To fully harness hierarchical functional materials, constitutive models must integrate fundamental material physics with continuum mechanics, linking molecular physics, geometric design, and environmental stimuli. This will enable materials to exhibit continuous, tunable responses, rather than discrete transitions, for programmable deformation. Such efforts will further expand material design possibilities by generating large-scale datasets, allowing data-driven inverse design and AM-driven rapid prototyping. By leveraging machine-learning-assisted frameworks, we can accelerate materials discovery and predictive optimization. Refining multiscale predictive frameworks will drive design-driven engineering of adaptive, reconfigurable materials.

Future vision

The true potential of hierarchical, functional materials lies in the seamless integration of dynamic molecular mechanisms with larger-scale architectures, where chemical adaptability and mechanical tunability work in tandem. Achieving this vision requires not only advancing fabrication techniques and computational models but also developing a deeper, physics-based understanding of how multiscale interactions dictate emergent material behaviors. By marrying fundamental material physics with engineering design, we can push beyond conventional limits, paving the way for next-generation materials that autonomously adapt to their environment and revolutionize applications in robotics, healthcare, and beyond.

BIBLIOGRAPHY

1. Harinarayana, V. & Shin, Y. Two-photon lithography for three-dimensional fabrication in micro/nanoscale regime: A comprehensive review. *Optics & Laser Technology* **142**, 107180. ISSN: 00303992. <https://linkinghub.elsevier.com/retrieve/pii/S0030399221002681> (Oct. 2021).
2. Bauer, J. *et al.* Nanolattices: An Emerging Class of Mechanical Metamaterials. *Advanced Materials* **29**, 1701850. ISSN: 09359648. <http://doi.wiley.com/10.1002/adma.201701850> (Oct. 2017).
3. Zheng, X. *et al.* Multiscale metallic metamaterials. en. *Nature Materials* **15**. Publisher: Nature Publishing Group, 1100–1106. ISSN: 1476-4660. <https://www.nature.com/articles/nmat4694> (2025) (Oct. 2016).
4. Spadaccini, C. M. Additive manufacturing and processing of architected materials. en. *MRS Bulletin* **44**, 782–788. ISSN: 0883-7694, 1938-1425. <https://www.cambridge.org/core/journals/mrs-bulletin/article/additive-manufacturing-and-processing-of-architected-materials/83785D6DAD5B623944F8AA2A17C9DEB9> (2025) (Oct. 2019).
5. Chowdhury, S., Shrivastava, S., Kakati, A. & Sangwai, J. S. Comprehensive Review on the Role of Surfactants in the Chemical Enhanced Oil Recovery Process. *Industrial & Engineering Chemistry Research* **61**, 21–64. ISSN: 0888-5885. (2023) (Jan. 2022).
6. Zhang, L. *et al.* Topology-optimized lattice structures with simultaneously high stiffness and light weight fabricated by selective laser melting: Design, manufacturing and characterization. *Journal of Manufacturing Processes* **56**, 1166–1177. ISSN: 1526-6125. <https://www.sciencedirect.com/science/article/pii/S1526612520303789> (2025) (Aug. 2020).
7. Frenzel, T., Findeisen, C., Kadic, M., Gumbsch, P. & Wegener, M. Tailored Buckling Microlattices as Reusable Light-Weight Shock Absorbers. *Advanced Materials* **28**, 5865–5870. ISSN: 09359648. <https://onlinelibrary.wiley.com/doi/10.1002/adma.201600610> (July 2016).
8. Li, S. *et al.* Liquid-induced topological transformations of cellular microstructures. *Nature* **592**, 386–391. ISSN: 0028-0836. <http://www.nature.com/articles/s41586-021-03404-7> (Apr. 2021).
9. Greer, J. R. & De Hosson, J. T. Plasticity in small-sized metallic systems: Intrinsic versus extrinsic size effect. *Progress in Materials Science* **56**, 654–724. ISSN: 00796425. <https://linkinghub.elsevier.com/retrieve/pii/S0079642511000065> (Aug. 2011).

10. Meza, L. R., Das, S. & Greer, J. R. Strong, lightweight, and recoverable three-dimensional ceramic nanolattices. *Science* **345**, 1322–1326. ISSN: 0036-8075. <http://www.sciencemag.org/cgi/doi/10.1126/science.1255908> (Sept. 2014).
11. Crook, C. *et al.* Plate-nanolattices at the theoretical limit of stiffness and strength. *Nature Communications* **11**, 1579. ISSN: 2041-1723. <http://www.nature.com/articles/s41467-020-15434-2> (Dec. 2020).
12. Portela, C. M. *et al.* Supersonic impact resilience of nanoarchitected carbon. *Nature Materials*. ISSN: 1476-1122. <http://www.nature.com/articles/s41563-021-01033-z> (June 2021).
13. Zhuo, S. *et al.* Complex multiphase organohydrogels with programmable mechanics toward adaptive soft-matter machines. *Science Advances* **6**. Publisher: American Association for the Advancement of Science, eaax1464. <https://www.science.org/doi/10.1126/sciadv.aax1464> (2025) (Jan. 2020).
14. Wanasinghe, S. V., Dodo, O. J. & Konkolewicz, D. Dynamic Bonds: Adaptable Timescales for Responsive Materials. en. *Angewandte Chemie International Edition* **61**. eprint: <https://onlinelibrary.wiley.com/doi/pdf/10.1002/anie.202206938>, e202206938. ISSN: 1521-3773. <https://onlinelibrary.wiley.com/doi/abs/10.1002/anie.202206938> (2025) (2022).
15. Jangizehi, A. *et al.* Metal–ligand complexation and clustering in mussel-inspired side-chain functionalized supramolecular hydrogels. en. *Soft Matter* **18**. Publisher: The Royal Society of Chemistry, 6836–6847. ISSN: 1744-6848. <https://pubs.rsc.org/en/content/articlelanding/2022/sm/d2sm00666a> (2022) (Sept. 2022).
16. Burnworth, M. *et al.* Optically healable supramolecular polymers. en. *Nature* **472**. Publisher: Nature Publishing Group, 334–337. ISSN: 1476-4687. <https://www.nature.com/articles/nature09963> (2025) (Apr. 2011).
17. Zhu, T. *et al.* Metallo-polyelectrolytes as a class of ionic macromolecules for functional materials. en. *Nature Communications* **9**. Number: 1 Publisher: Nature Publishing Group, 4329. ISSN: 2041-1723. <https://www.nature.com/articles/s41467-018-06475-9> (2023) (Oct. 2018).
18. Kloxin, C. J. & Bowman, C. N. Covalent adaptable networks: smart, reconfigurable and responsive network systems. en. *Chemical Society Reviews* **42**. Publisher: The Royal Society of Chemistry, 7161–7173. ISSN: 1460-4744. <https://pubs.rsc.org/en/content/articlelanding/2013/cs/c3cs60046g> (2025) (Aug. 2013).
19. Kloxin, C. J., Scott, T. F., Adzima, B. J. & Bowman, C. N. Covalent Adaptable Networks (CANs): A Unique Paradigm in Cross-Linked Polymers. *Macromolecules* **43**. Publisher: American Chemical Society, 2643–2653. ISSN: 0024-9297. <https://doi.org/10.1021/ma902596s> (2025) (Mar. 2010).

20. Xi, W., Scott, T. F., Kloxin, C. J. & Bowman, C. N. Click Chemistry in Materials Science. en. *Advanced Functional Materials* **24**. eprint: <https://onlinelibrary.wiley.com/doi/pdf/10.1002/adfm.201302847> (2025) (2014). ISSN: 1616-3028.
21. Elling, B. R. & Dichtel, W. R. Reprocessable Cross-Linked Polymer Networks: Are Associative Exchange Mechanisms Desirable? *ACS Central Science* **6**. Publisher: American Chemical Society, 1488–1496. ISSN: 2374-7943. <https://doi.org/10.1021/acscentsci.0c00567> (2025) (Sept. 2020).
22. Webber, M. J. & Tibbitt, M. W. Dynamic and reconfigurable materials from reversible network interactions. en. *Nature Reviews Materials* **7**. Publisher: Nature Publishing Group, 541–556. ISSN: 2058-8437. <https://www.nature.com/articles/s41578-021-00412-x> (2025) (July 2022).
23. Chang, T.-M. & Billeck, S. E. Structure, Molecular Interactions, and Dynamics of Aqueous [BMIM][BF₄] Mixtures: A Molecular Dynamics Study. en. *The Journal of Physical Chemistry B* **125**, 1227–1240. ISSN: 1520-6106, 1520-5207. <https://pubs.acs.org/doi/10.1021/acs.jpcc.0c09731> (2022) (Feb. 2021).
24. Ying, H., Zhang, Y. & Cheng, J. Dynamic urea bond for the design of reversible and self-healing polymers. en. *Nature Communications* **5**. Publisher: Nature Publishing Group, 3218. ISSN: 2041-1723. <https://www.nature.com/articles/ncomms4218> (2025) (Feb. 2014).
25. Delebecq, E., Pascault, J.-P., Boutevin, B. & Ganachaud, F. On the Versatility of Urethane/Urea Bonds: Reversibility, Blocked Isocyanate, and Non-isocyanate Polyurethane. *Chemical Reviews* **113**. Publisher: American Chemical Society, 80–118. ISSN: 0009-2665. <https://doi.org/10.1021/cr300195n> (2025) (Jan. 2013).
26. Sun, J. Y. *et al.* Highly stretchable and tough hydrogels. *Nature* **489**. Publisher: Nature Publishing Group, 133–136. ISSN: 00280836. <http://dx.doi.org/10.1038/nature11409> (2012).
27. Wang, S. *et al.* Facile mechanochemical cycloreversion of polymer cross-linkers enhances tear resistance. *Science* **380**. Publisher: American Association for the Advancement of Science, 1248–1252. <https://www.science.org/doi/10.1126/science.adg3229> (2023) (June 2023).
28. Kim, J., Zhang, G., Shi, M. & Suo, Z. Fracture, fatigue, and friction of polymers in which entanglements greatly outnumber cross-links. *Science* **374**, 212–216. ISSN: 10959203 (2021).
29. Daniel, W. F. M. *et al.* Solvent-free, supersoft and superelastic bottlebrush melts and networks. en. *Nature Materials* **15**. Publisher: Nature Publishing Group, 183–189. ISSN: 1476-4660. <https://www.nature.com/articles/nmat4508> (2025) (Feb. 2016).

30. C. Stuparu, M., Khan, A. & J. Hawker, C. Phase separation of supramolecular and dynamic block copolymers. en. *Polymer Chemistry* **3**. Publisher: Royal Society of Chemistry, 3033–3044. <https://pubs.rsc.org/en/content/articlelanding/2012/py/c2py20368e> (2025) (2012).
31. Wang, M. *et al.* Tough and stretchable ionogels by in situ phase separation. en. *Nature Materials* **21**. Number: 3 Publisher: Nature Publishing Group, 359–365. ISSN: 1476-4660. <https://www.nature.com/articles/s41563-022-01195-4> (2023) (Mar. 2022).
32. Nonoyama, T. *et al.* Instant Thermal Switching from Soft Hydrogel to Rigid Plastics Inspired by Thermophile Proteins. en. *Advanced Materials* **32**. _eprint: <https://onlinelibrary.wiley.com/doi/pdf/10.1002/adma.201905878>, 1905878. ISSN: 1521-4095. <https://onlinelibrary.wiley.com/doi/abs/10.1002/adma.201905878> (2023) (2020).
33. Zhang, X. *et al.* Progress on the layer-by-layer assembly of multilayered polymer composites: Strategy, structural control and applications. *Progress in Polymer Science* **89**, 76–107. ISSN: 0079-6700. <https://www.sciencedirect.com/science/article/pii/S007967001830279X> (2025) (Feb. 2019).
34. Richardson, J. J. *et al.* Innovation in Layer-by-Layer Assembly. *Chemical Reviews* **116**. Publisher: American Chemical Society, 14828–14867. ISSN: 0009-2665. <https://doi.org/10.1021/acs.chemrev.6b00627> (2025) (Dec. 2016).
35. Deshmukh, P. K. *et al.* Stimuli-sensitive layer-by-layer (LbL) self-assembly systems: Targeting and biosensory applications. *Journal of Controlled Release* **166**, 294–306. ISSN: 0168-3659. <https://www.sciencedirect.com/science/article/pii/S0168365913000060> (2025) (Mar. 2013).
36. Zema, L., Loreti, G., Melocchi, A., Maroni, A. & Gazzaniga, A. Injection Molding and its application to drug delivery. *Journal of Controlled Release* **159**, 324–331. ISSN: 0168-3659. <https://www.sciencedirect.com/science/article/pii/S0168365912000041> (2025) (May 2012).
37. Bajpai, A. K., Shukla, S. K., Bhanu, S. & Kankane, S. Responsive polymers in controlled drug delivery. *Progress in Polymer Science* **33**, 1088–1118. ISSN: 0079-6700. <https://www.sciencedirect.com/science/article/pii/S0079670008000609> (2025) (Nov. 2008).
38. Shi, L. *et al.* Self-Healing Polymeric Hydrogel Formed by Metal–Ligand Coordination Assembly: Design, Fabrication, and Biomedical Applications. en. *Macromolecular Rapid Communications* **40**. _eprint: <https://onlinelibrary.wiley.com/doi/pdf/10.1002/marc.201800837>. ISSN: 1521-3927. <https://onlinelibrary.wiley.com/doi/abs/10.1002/marc.201800837> (2025) (2019).
39. Lei, Z. Q., Xiang, H. P., Yuan, Y. J., Rong, M. Z. & Zhang, M. Q. Room-Temperature Self-Healable and Remoldable Cross-linked Polymer Based on

- the Dynamic Exchange of Disulfide Bonds. *Chemistry of Materials* **26**. Publisher: American Chemical Society, 2038–2046. ISSN: 0897-4756. <https://doi.org/10.1021/cm4040616> (2025) (Mar. 2014).
40. Andreu, A. *et al.* 4D printing materials for vat photopolymerization. *Additive Manufacturing* **44**, 102024. ISSN: 2214-8604. <https://www.sciencedirect.com/science/article/pii/S2214860421001895> (2025) (Aug. 2021).
 41. Shaukat, U., Rossegger, E. & Schlögl, S. A Review of Multi-Material 3D Printing of Functional Materials via Vat Photopolymerization. en. *Polymers* **14**. Number: 12 Publisher: Multidisciplinary Digital Publishing Institute, 2449. ISSN: 2073-4360. <https://www.mdpi.com/2073-4360/14/12/2449> (2025) (Jan. 2022).
 42. Tariq, A. *et al.* Recent Advances in the Additive Manufacturing of Stimuli-Responsive Soft Polymers. en. *Advanced Engineering Materials* **25**. eprint: <https://onlinelibrary.wiley.com/doi/pdf/10.1002/adem.202301074>, 2301074. ISSN: 1527-2648. <https://onlinelibrary.wiley.com/doi/abs/10.1002/adem.202301074> (2025) (2023).
 43. Lai, J.-C. *et al.* A rigid and healable polymer cross-linked by weak but abundant Zn(II)-carboxylate interactions. en. *Nature Communications* **9**. Number: 1 Publisher: Nature Publishing Group, 2725. ISSN: 2041-1723. <https://www.nature.com/articles/s41467-018-05285-3> (2023) (July 2018).
 44. Cai, H., Wang, Z., Utomo, N. W., Vidavsky, Y. & Silberstein, M. N. Highly stretchable ionically crosslinked acrylate elastomers inspired by polyelectrolyte complexes. en. *Soft Matter* **18**. Publisher: The Royal Society of Chemistry, 7679–7688. ISSN: 1744-6848. <https://pubs.rsc.org/en/content/articlelanding/2022/sm/d2sm00755j> (2023) (Oct. 2022).
 45. Murphy, S. V. & Atala, A. 3D bioprinting of tissues and organs. en. *Nature Biotechnology* **32**. Publisher: Nature Publishing Group, 773–785. ISSN: 1546-1696. <https://www.nature.com/articles/nbt.2958> (2025) (Aug. 2014).
 46. Grindy, S. C. *et al.* Control of hierarchical polymer mechanics with bioinspired metal-coordination dynamics. *Nature Materials* **14**, 1210–1216. ISSN: 1476-1122. <http://www.nature.com/articles/nmat4401> (Dec. 2015).
 47. Yuk, H. *et al.* Hydraulic hydrogel actuators and robots optically and sonically camouflaged in water. en. *Nature Communications* **8**. Publisher: Nature Publishing Group, 14230. ISSN: 2041-1723. <https://www.nature.com/articles/ncomms14230> (2025) (Feb. 2017).
 48. Palleau, E., Morales, D., Dickey, M. D. & Velev, O. D. Reversible patterning and actuation of hydrogels by electrically assisted ionoprinting. en. *Nature Communications* **4**. Publisher: Nature Publishing Group, 2257. ISSN: 2041-

1723. <https://www.nature.com/articles/ncomms3257> (2025) (Aug. 2013).
49. Morales, D., Palleau, E., D. Dickey, M. & D. Velev, O. Electro-actuated hydrogel walkers with dual responsive legs. en. *Soft Matter* **10**. Publisher: Royal Society of Chemistry, 1337–1348. <https://pubs.rsc.org/en/content/articlelanding/2014/sm/c3sm51921j> (2025) (2014).
50. Stayton, P. S. *et al.* Control of protein–ligand recognition using a stimuli-responsive polymer. en. *Nature* **378**. Publisher: Nature Publishing Group, 472–474. ISSN: 1476-4687. <https://www.nature.com/articles/378472a0> (2025) (Nov. 1995).
51. Tokarev, I. & Minko, S. Multiresponsive, Hierarchically Structured Membranes: New, Challenging, Biomimetic Materials for Biosensors, Controlled Release, Biochemical Gates, and Nanoreactors. *Advanced Materials* **21**. _eprint: <https://onlinelibrary.wiley.com/doi/pdf/10.1002/adma.200801408>, 241–247. ISSN: 1521-4095. <https://onlinelibrary.wiley.com/doi/abs/10.1002/adma.200801408> (2025) (2009).
52. Weng, W., Beck, J. B., Jamieson, A. M. & Rowan, S. J. Understanding the Mechanism of Gelation and Stimuli-Responsive Nature of a Class of Metallo-Supramolecular Gels. *Journal of the American Chemical Society* **128**. Publisher: American Chemical Society, 11663–11672. ISSN: 0002-7863. <https://doi.org/10.1021/ja063408q> (2025) (Sept. 2006).
53. Ionov, L. *et al.* Reversible Chemical Patterning on Stimuli-Responsive Polymer Film: Environment-Responsive Lithography. *Journal of the American Chemical Society* **125**. Publisher: American Chemical Society, 8302–8306. ISSN: 0002-7863. <https://doi.org/10.1021/ja035560n> (2025) (July 2003).
54. Boudou, T., Crouzier, T., Ren, K., Blin, G. & Picart, C. Multiple Functionalities of Polyelectrolyte Multilayer Films: New Biomedical Applications. en. *Advanced Materials* **22**. _eprint: <https://onlinelibrary.wiley.com/doi/pdf/10.1002/adma.200901327>, 441–467. ISSN: 1521-4095. <https://onlinelibrary.wiley.com/doi/abs/10.1002/adma.200901327> (2025) (2010).
55. Stuart, M. A. C. *et al.* Emerging applications of stimuli-responsive polymer materials. en. *Nature Materials* **9**. Publisher: Nature Publishing Group, 101–113. ISSN: 1476-4660. <https://www.nature.com/articles/nmat2614> (2025) (Feb. 2010).
56. Liu, J., Miao, J., Zhang, Z., Liu, Z. & Yu, Y. Programmable shape deformation actuated bilayer hydrogel based on mixed metal ions. en. *European Polymer Journal* **175**, 111375. ISSN: 0014-3057. <https://www.sciencedirect.com/science/article/pii/S0014305722003792> (2023) (July 2022).

57. Li, C. H. *et al.* A highly stretchable autonomous self-healing elastomer. *Nature Chemistry* **8**. Publisher: Nature Publishing Group, 618–624. ISSN: 17554349 (2016).
58. I. Dzhardimalieva, G., C. Yadav, B., Singh, S. & E. Uflyand, I. Self-healing and shape memory metallopolymers: state-of-the-art and future perspectives. en. *Dalton Transactions* **49**. Publisher: Royal Society of Chemistry, 3042–3087. <https://pubs.rsc.org/en/content/articlelanding/2020/dt/c9dt04360h> (2022) (2020).
59. Liu, J. *et al.* Reconfiguring hydrogel assemblies using a photocontrolled metallopolymer adhesive for multiple customized functions. en. *Nature Chemistry* **16**. Publisher: Nature Publishing Group, 1024–1033. ISSN: 1755-4349. <https://www.nature.com/articles/s41557-024-01476-2> (2025) (June 2024).
60. Gao, Y., Wu, K. & Suo, Z. Photodetachable Adhesion. en. *Advanced Materials* **31**. eprint: <https://onlinelibrary.wiley.com/doi/pdf/10.1002/adma.201806948>, 1806948. ISSN: 1521-4095. <https://onlinelibrary.wiley.com/doi/abs/10.1002/adma.201806948> (2024) (2019).
61. Yang, F., Tadepalli, V. & Wiley, B. J. 3D Printing of a Double Network Hydrogel with a Compression Strength and Elastic Modulus Greater than those of Cartilage. *ACS Biomaterials Science & Engineering* **3**. Publisher: American Chemical Society, 863–869. <https://doi.org/10.1021/acsbiomaterials.7b00094> (2025) (May 2017).
62. Dong, H., Snyder, J. F., Williams, K. S. & Andzelm, J. W. Cation-Induced Hydrogels of Cellulose Nanofibrils with Tunable Moduli. *Biomacromolecules* **14**. Publisher: American Chemical Society, 3338–3345. ISSN: 1525-7797. <https://doi.org/10.1021/bm400993f> (2024) (Sept. 2013).
63. Neumann, L. N. *et al.* Dynamics and healing behavior of metallosupramolecular polymers. *Science Advances* **7**. Publisher: American Association for the Advancement of Science, eabe4154. <https://www.science.org/doi/10.1126/sciadv.abe4154> (2023) (Apr. 2021).
64. Zhong, M. *et al.* Dually cross-linked single network poly(acrylic acid) hydrogels with superior mechanical properties and water absorbency. en. *Soft Matter* **12**. Publisher: The Royal Society of Chemistry, 5420–5428. ISSN: 1744-6848. <https://pubs.rsc.org/en/content/articlelanding/2016/sm/c6sm00242k> (2024) (June 2016).
65. Vidavsky, Y. *et al.* Tuning the Mechanical Properties of Metallopolymers via Ligand Interactions: A Combined Experimental and Theoretical Study. *Macromolecules* **53**. Publisher: American Chemical Society, 2021–2030. ISSN: 0024-9297. <https://doi.org/10.1021/acs.macromol.9b02756> (2023) (Mar. 2020).

66. Kim, T. H. *et al.* Flexible biomimetic block copolymer composite for temperature and long-wave infrared sensing. *Science Advances* **9**. Publisher: American Association for the Advancement of Science, eade0423. <https://www.science.org/doi/10.1126/sciadv.ade0423> (2023) (Feb. 2023).
67. Durmaz, E. N. *et al.* Polyelectrolytes as Building Blocks for Next-Generation Membranes with Advanced Functionalities. *ACS Applied Polymer Materials* **3**. Publisher: American Chemical Society, 4347–4374. <https://doi.org/10.1021/acsapm.1c00654> (2023) (Sept. 2021).
68. Zhu, T. *et al.* Rational Synthesis of Metallo-Cations Toward Redox- and Alkaline-Stable Metallo-Polyelectrolytes. *Journal of the American Chemical Society* **142**. Publisher: American Chemical Society, 1083–1089. ISSN: 0002-7863. <https://doi.org/10.1021/jacs.9b12051> (2023) (Jan. 2020).
69. Tang, S., Gong, J., Shi, Y., Wen, S. & Zhao, Q. Spontaneous water-on-water spreading of polyelectrolyte membranes inspired by skin formation. en. *Nature Communications* **13**. Number: 1 Publisher: Nature Publishing Group, 3227. ISSN: 2041-1723. <https://www.nature.com/articles/s41467-022-30973-6> (2023) (June 2022).
70. Zhu, Q., Barney, C. W. & Erk, K. A. Effect of ionic crosslinking on the swelling and mechanical response of model superabsorbent polymer hydrogels for internally cured concrete. en. *Materials and Structures* **48**, 2261–2276. ISSN: 1871-6873. <https://doi.org/10.1617/s11527-014-0308-5> (2024) (July 2015).
71. Khare, E., Holten-Andersen, N. & Buehler, M. J. Transition-metal coordinate bonds for bioinspired macromolecules with tunable mechanical properties. en. *Nature Reviews Materials* **6**. Number: 5 Publisher: Nature Publishing Group, 421–436. ISSN: 2058-8437. <https://www.nature.com/articles/s41578-020-00270-z> (2023) (May 2021).
72. Hiller, J., Mendelsohn, J. D. & Rubner, M. F. Reversibly erasable nanoporous anti-reflection coatings from polyelectrolyte multilayers. en. *Nature Materials* **1**. Number: 1 Publisher: Nature Publishing Group, 59–63. ISSN: 1476-4660. <https://www.nature.com/articles/nmat719> (2023) (Sept. 2002).
73. Michaels, A. S. POLYELECTROLYTE COMPLEXES. *Industrial & Engineering Chemistry* **57**. Publisher: American Chemical Society, 32–40. ISSN: 0019-7866. <https://doi.org/10.1021/ie50670a007> (2022) (Oct. 1965).
74. Baumberger, T. & Ronsin, O. Cooperative Effect of Stress and Ion Displacement on the Dynamics of Cross-Link Unzipping and Rupture of Alginate Gels. *Biomacromolecules* **11**. Publisher: American Chemical Society, 1571–1578. ISSN: 1525-7797. <https://doi.org/10.1021/bm1002015> (2024) (June 2010).

75. Zheng, S. Y. *et al.* Metal-Coordination Complexes Mediated Physical Hydrogels with High Toughness, Stick–Slip Tearing Behavior, and Good Processability. *Macromolecules* **49**. Publisher: American Chemical Society, 9637–9646. ISSN: 0024-9297. <https://doi.org/10.1021/acs.macromol.6b02150> (2023) (Dec. 2016).
76. Glisman, A. *et al.* Multivalent Ion-Mediated Polyelectrolyte Association and Structure. *Macromolecules* **57**. Publisher: American Chemical Society, 1941–1949. ISSN: 0024-9297. <https://doi.org/10.1021/acs.macromol.3c02437> (2024) (Mar. 2024).
77. Mantha, S. *et al.* Adsorption Isotherm and Mechanism of Ca²⁺ Binding to Polyelectrolyte. *Langmuir* **40**. Publisher: American Chemical Society, 6212–6219. ISSN: 0743-7463. <https://doi.org/10.1021/acs.langmuir.3c03640> (2024) (Mar. 2024).
78. Deacon, G. B. & Phillips, R. J. Relationships between the carbon-oxygen stretching frequencies of carboxylato complexes and the type of carboxylate coordination. *Coordination Chemistry Reviews* **33**, 227–250. ISSN: 0010-8545. <https://www.sciencedirect.com/science/article/pii/S0010854500804555> (2023) (Oct. 1980).
79. Deacon, G. B., Huber, F. & Phillips, R. J. Diagnosis of the nature of carboxylate coordination from the direction of shifts of carbon-oxygen stretching frequencies. *Inorganica Chimica Acta* **104**, 41–45. ISSN: 0020-1693. <https://www.sciencedirect.com/science/article/pii/S0020169300837834> (2023) (Oct. 1985).
80. Kirwan, L. J., Fawell, P. D. & van Bronswijk, W. In Situ FTIR-ATR Examination of Poly(acrylic acid) Adsorbed onto Hematite at Low pH. *Langmuir* **19**. Publisher: American Chemical Society, 5802–5807. ISSN: 0743-7463. <https://doi.org/10.1021/la027012d> (2023) (July 2003).
81. Mennucci, B. & Tomasi, J. Continuum Solvation Models: A New Approach to the Problem of Solute's Charge Distribution and Cavity Boundaries. *The Journal of Chemical Physics* **106**, 5151–5158. ISSN: 0021-9606. (2023) (Mar. 1997).
82. Pearson, R. G. Hard and soft acids and bases, HSAB, part II: Underlying theories. en. *Journal of Chemical Education* **45**, 643. ISSN: 0021-9584, 1938-1328. <https://pubs.acs.org/doi/abs/10.1021/ed045p643> (2023) (Oct. 1968).
83. Schwarzenbach, G. en. in *Advances in Inorganic Chemistry and Radiochemistry* (eds Emeleus, H. J. & Sharpe, A. G.) 257–285 (Academic Press, Cambridge, MA, Jan. 1961). <https://www.sciencedirect.com/science/article/pii/S0065279208602423> (2023).

84. Stumm, W. & Morgan, J. J. *Aquatic chemistry: chemical equilibria and rates in natural waters* 3rd ed. eng. OCLC: 31754493. ISBN: 978-0-471-51184-7. <http://catdir.loc.gov/catdir/toc/onix05/94048319.html> (2023) (Wiley, New York, 1996).
85. Katashima, T. *et al.* Experimental Comparison of Bond Lifetime and Viscoelastic Relaxation in Transient Networks with Well-Controlled Structures. *ACS Macro Letters* **11**. Publisher: American Chemical Society, 753–759. <https://doi.org/10.1021/acsmacrolett.2c00152> (2025) (June 2022).
86. Swift, T., Swanson, L., Geoghegan, M. & Rimmer, S. The pH-responsive behaviour of poly (acrylic acid) in aqueous solution is dependent on molar mass. *Soft matter* **12**. Publisher: Royal Society of Chemistry, 2542–2549 (2016).
87. Gallegos, A., Ong, G. M. C. & Wu, J. Thermodynamic non-ideality in charge regulation of weak polyelectrolytes. en. *Soft Matter* **17**. Publisher: The Royal Society of Chemistry, 9221–9234. ISSN: 1744-6848. <https://pubs.rsc.org/en/content/articlelanding/2021/sm/d1sm00848j> (2023) (Oct. 2021).
88. Gallegos, A. & Wu, J. Hierarchical Model of Weak Polyelectrolytes with Ionization and Conformation Consistency. en. *Macromolecules* **56**, 4760–4772. ISSN: 0024-9297, 1520-5835. <https://pubs.acs.org/doi/10.1021/acs.macromol.2c01910> (2023) (June 2023).
89. Landsgesell, J. *et al.* Simulations of ionization equilibria in weak polyelectrolyte solutions and gels. en. *Soft Matter* **15**. Publisher: Royal Society of Chemistry, 1155–1185. <https://pubs.rsc.org/en/content/articlelanding/2019/sm/c8sm02085j> (2022) (2019).
90. Landsgesell, J. *et al.* Grand-Reaction Method for Simulations of Ionization Equilibria Coupled to Ion Partitioning. *Macromolecules* **53**. Publisher: American Chemical Society, 3007–3020. ISSN: 0024-9297. <https://doi.org/10.1021/acs.macromol.0c00260> (2022) (Apr. 2020).
91. Taylor, T. J. & Stivala, S. S. Small-angle X-ray scattering of poly(acrylic acid) in solution: 1. Dioxane. *Polymer* **37**, 715–719. ISSN: 0032-3861. <https://www.sciencedirect.com/science/article/pii/0032386196872454> (2023) (Jan. 1996).
92. Miquelard-Garnier, G., Creton, C. & Hourdet, D. Strain induced clustering in polyelectrolyte hydrogels. en. *Soft Matter* **4**. Publisher: The Royal Society of Chemistry, 1011–1023. ISSN: 1744-6848. <https://pubs.rsc.org/en/content/articlelanding/2008/sm/b717460h> (2023) (Apr. 2008).
93. Rubinstein, M. & Colby, R. H. *Polymer Physics* ISBN: 978-0-19-852059-7 (Oxford University Press, Oxford, New York, Aug. 2003).

94. Thompson, A. P. *et al.* LAMMPS - a flexible simulation tool for particle-based materials modeling at the atomic, meso, and continuum scales. en. *Computer Physics Communications* **271**, 108171. ISSN: 0010-4655. <https://www.sciencedirect.com/science/article/pii/S0010465521002836> (2023) (Feb. 2022).
95. Kremer, K. & Grest, G. S. Dynamics of entangled linear polymer melts: A molecular-dynamics simulation. en. *The Journal of Chemical Physics* **92**, 5057–5086. ISSN: 0021-9606, 1089-7690. <http://aip.scitation.org/doi/10.1063/1.458541> (2022) (Apr. 1990).
96. Rubinstein, M. & Semenov, A. N. Thermoreversible Gelation in Solutions of Associating Polymers. 2. Linear Dynamics. en. *Macromolecules* **31**, 1386–1397. ISSN: 0024-9297, 1520-5835. <https://pubs.acs.org/doi/10.1021/ma970617%2B> (2022) (Feb. 1998).
97. Semenov, A. N. & Rubinstein, M. Thermoreversible Gelation in Solutions of Associative Polymers. 1. Statics. *Macromolecules* **31**, 1373–1385. ISSN: 0024-9297, 1520-5835. (2022) (Feb. 1998).
98. Dautzenberg, H. Polyelectrolyte Complex Formation in Highly Aggregating Systems. 1. Effect of Salt: Polyelectrolyte Complex Formation in the Presence of NaCl. *Macromolecules* **30**. Publisher: American Chemical Society, 7810–7815. ISSN: 0024-9297. <https://doi.org/10.1021/ma970803f> (2025) (Dec. 1997).
99. Semenov, A. N. & Rubinstein, M. Thermoreversible Gelation in Solutions of Associative Polymers. 1. Statics. en. *Macromolecules* **31**, 1373–1385. ISSN: 0024-9297, 1520-5835. <https://pubs.acs.org/doi/10.1021/ma970616h> (2022) (Feb. 1998).
100. Zhang, P., Alsaifi, N. M., Wu, J. & Wang, Z.-G. Salting-Out and Salting-In of Polyelectrolyte Solutions: A Liquid-State Theory Study. en. *Macromolecules* **49**, 9720–9730. ISSN: 0024-9297, 1520-5835. <https://pubs.acs.org/doi/10.1021/acs.macromol.6b02160> (2022) (Dec. 2016).
101. Debye, P. & Hückel, E. Zur Theorie Der Elektrolyte. I. Gefrierpunktserniedrigung Und Verwandte Erscheinungen. *Physikalische Zeitschrift* **24**, 185–206 (1923).
102. Mozhdghi, D. *et al.* Tuning Dynamic Mechanical Response in Metallopolymer Networks through Simultaneous Control of Structural and Temporal Properties of the Networks. en. *Macromolecules* **49**, 6310–6321. ISSN: 0024-9297, 1520-5835. <https://pubs.acs.org/doi/10.1021/acs.macromol.6b01626> (2022) (Sept. 2016).
103. Zhao, X. Multi-scale multi-mechanism design of tough hydrogels: building dissipation into stretchy networks. en. *Soft Matter* **10**. Publisher: Royal Society of Chemistry, 672–687. <https://pubs.rsc.org/en/content/articlelanding/2014/sm/c3sm52272e> (2025) (2014).

104. Zhao, X. *et al.* Soft Materials by Design: Unconventional Polymer Networks Give Extreme Properties. *Chemical Reviews* **121**. Publisher: American Chemical Society, 4309–4372. ISSN: 0009-2665. <https://doi.org/10.1021/acs.chemrev.0c01088> (2022) (Apr. 2021).
105. Rivlin, R. S. & Thomas, A. G. Rupture of rubber. I. Characteristic energy for tearing. *Journal of Polymer Science* **10**, 291–318. ISSN: 00223832, 15426238. <https://onlinelibrary.wiley.com/doi/10.1002/pol.1953.120100303> (2023) (Mar. 1953).
106. Lake, G. J., Thomas, A. G. & Tabor, D. The strength of highly elastic materials. *Proceedings of the Royal Society of London. Series A. Mathematical and Physical Sciences* **300**, 108–119. <https://royalsocietypublishing.org/doi/10.1098/rspa.1967.0160> (2023) (Jan. 1997).
107. Sutton, M. A., Orteu, J.-J. & Schreier, H. W. *Image correlation for shape, motion and deformation measurements : basic concepts, theory and applications* <https://imt-mines-albi.hal.science/hal-01729219> (2023) (Springer, New York, NY, 2009).
108. Lin, S., Londono, C. D., Zheng, D. & Zhao, X. An extreme toughening mechanism for soft materials. en. *Soft Matter*, 10.1039.D2SM00609J. ISSN: 1744-683X, 1744-6848. <http://xlink.rsc.org/?DOI=D2SM00609J> (2022) (2022).
109. Abrahamson, H. B., Rezvani, A. B. & Brushmiller, J. G. Photochemical and spectroscopic studies of complexes, of iron (III) with citric acid and other carboxylic acids. *Inorganica Chimica Acta* **226**, 117–127 (1994).
110. Kuma, K., Nakabayashi, S., Suzuki, Y., Kudo, I. & Matsunaga, K. Photo-reduction of Fe (III) by dissolved organic substances and existence of Fe (II) in seawater during spring blooms. *Marine Chemistry* **37**, 15–27 (1992).
111. Lueder, U., Jørgensen, B. B., Kappler, A. & Schmidt, C. Photochemistry of iron in aquatic environments. *Environmental Science: Processes & Impacts* **22**, 12–24 (2020).
112. Deng, Y., Zhang, Q. & Feringa, B. L. Dynamic Chemistry Toolbox for Advanced Sustainable Materials. en. *Advanced Science* **11**. _eprint: <https://onlinelibrary.wiley.com/doi/10.1002/adv.202308666>. ISSN: 2198-3844. <https://onlinelibrary.wiley.com/doi/abs/10.1002/adv.202308666> (2025) (2024).
113. Janbaz, S., Narooei, K., van Manen, T. & Zadpoor, A. A. Strain rate–dependent mechanical metamaterials. *Science Advances* **6**. Publisher: American Association for the Advancement of Science, eaba0616. <https://www.science.org/doi/10.1126/sciadv.aba0616> (2023) (June 2020).
114. Hetényi, M. *Beams on Elastic Foundation: Theory with Applications in the Fields of Civil and Mechanical Engineering* en. ISBN: 978-0-472-08445-6 (University of Michigan Press, Ann Arbor, Michigan, 1946).

115. Ramachandran, R. G., de Cortie, J., Maiti, S., Deseri, L. & Velankar, S. S. Uniaxial stretch-release of rubber-plastic bilayers: Strain-dependent transition to stable helices, rolls, saddles, and tubes. *Extreme Mechanics Letters* **48**, 101384. ISSN: 2352-4316. <https://www.sciencedirect.com/science/article/pii/S2352431621001231> (2025) (Oct. 2021).
116. Wissman, J., Finkenauer, L., Deseri, L. & Majidi, C. Saddle-like deformation in a dielectric elastomer actuator embedded with liquid-phase gallium-indium electrodes. *Journal of Applied Physics* **116**, 144905. ISSN: 0021-8979. <https://doi.org/10.1063/1.4897551> (2025) (Oct. 2014).
117. Hong, W., Zhao, X. & Suo, Z. Large deformation and electrochemistry of polyelectrolyte gels. *Journal of the Mechanics and Physics of Solids* **58**, 558–577. ISSN: 0022-5096. <https://www.sciencedirect.com/science/article/pii/S0022509610000062> (2025) (Apr. 2010).
118. Flory, P. J. Thermodynamics of High Polymer Solutions. *The Journal of Chemical Physics* **10**, 51–61. ISSN: 0021-9606. <https://doi.org/10.1063/1.1723621> (2025) (Jan. 1942).
119. Huggins, M. L. Solutions of Long Chain Compounds. *The Journal of Chemical Physics* **9**, 440. ISSN: 0021-9606. <https://doi.org/10.1063/1.1750930> (2025) (May 1941).
120. Zhao, X., Hong, W. & Suo, Z. Electromechanical hysteresis and coexistent states in dielectric elastomers. *Physical Review B* **76**. Publisher: American Physical Society, 134113. <https://link.aps.org/doi/10.1103/PhysRevB.76.134113> (2025) (Oct. 2007).
121. Suo, Z., Zhao, X. & Greene, W. H. A nonlinear field theory of deformable dielectrics. *Journal of the Mechanics and Physics of Solids* **56**, 467–486. ISSN: 0022-5096. <https://www.sciencedirect.com/science/article/pii/S002250960700110X> (2025) (Feb. 2008).
122. Yu, Y., Landis, C. M. & Huang, R. Salt-Induced Swelling and Volume Phase Transition of Polyelectrolyte Gels. *Journal of Applied Mechanics* **84**. ISSN: 0021-8936. <https://doi.org/10.1115/1.4036113> (2025) (Mar. 2017).
123. Kalcioğlu, Z. I., Mahmoodian, R., Hu, Y., Suo, Z. & Vliet, K. J. V. From macro- to microscale poroelastic characterization of polymeric hydrogels via indentation. en. *Soft Matter* **8**. Publisher: The Royal Society of Chemistry, 3393–3398. ISSN: 1744-6848. <https://pubs.rsc.org/en/content/articlelanding/2012/sm/c2sm06825g> (2025) (Feb. 2012).
124. Hu, Y., Zhao, X., Vlassak, J. J. & Suo, Z. Using indentation to characterize the poroelasticity of gels. *Applied Physics Letters* **96**, 121904. ISSN: 0003-6951. <https://doi.org/10.1063/1.3370354> (2025) (Mar. 2010).

125. Hu, Y., Chen, X., Whitesides, G. M., Vlassak, J. J. & Suo, Z. Indentation of polydimethylsiloxane submerged in organic solvents. en. *Journal of Materials Research* **26**, 785–795. ISSN: 2044-5326. <https://doi.org/10.1557/jmr.2010.35> (2025) (Mar. 2011).
126. Hu, Y., You, J.-O., Auguste, D. T., Suo, Z. & Vlassak, J. J. Indentation: A simple, nondestructive method for characterizing the mechanical and transport properties of pH-sensitive hydrogels. en. *Journal of Materials Research* **27**, 152–160. ISSN: 2044-5326, 0884-2914. <https://www.cambridge.org/core/journals/journal-of-materials-research/article/indentation-a-simple-nondestructive-method-for-characterizing-the-mechanical-and-transport-properties-of-ph-sensitive-hydrogels/590199AC0EBFEE0B16BB81E2F80A7597> (2025) (Jan. 2012).
127. Wu, G., Xia, Y. & Yang, S. Buckling, symmetry breaking, and cavitation in periodically micro-structured hydrogel membranes. en. *Soft Matter* **10**. Publisher: The Royal Society of Chemistry, 1392–1399. ISSN: 1744-6848. <https://pubs.rsc.org/en/content/articlelanding/2014/sm/c3sm51640g> (2025) (Feb. 2014).
128. Landsgesell, J. *et al.* Simulations of Ionization Equilibria in Weak Polyelectrolyte Solutions and Gels. *Soft Matter* **15**, 1155–1185. (2022) (2019).
129. Landsgesell, J. *et al.* Grand-Reaction Method for Simulations of Ionization Equilibria Coupled to Ion Partitioning. *Macromolecules* **53**, 3007–3020. ISSN: 0024-9297. (2022) (Apr. 2020).
130. Chapman, W., Gubbins, K., Jackson, G. & Radosz, M. SAFT: Equation-of-state Solution Model for Associating Fluids. *Fluid Phase Equilib.* **52**, 31–38. ISSN: 03783812. (2022) (Dec. 1989).
131. Carnahan, N. F. & Starling, K. E. Equation of State for Nonattracting Rigid Spheres. *The Journal of Chemical Physics* **51**, 635–636. ISSN: 0021-9606. (2023) (Sept. 2003).
132. Zhang, P., Alsaifi, N. M., Wu, J. & Wang, Z.-G. Salting-Out and Salting-In of Polyelectrolyte Solutions: A Liquid-State Theory Study. *Macromolecules* **49**, 9720–9730. ISSN: 0024-9297, 1520-5835. (2022) (Dec. 2016).
133. Silva, W., Zanatta, M., Ferreira, A. S., Corvo, M. C. & Cabrita, E. J. Revisiting Ionic Liquid Structure-Property Relationship: A Critical Analysis. *International Journal of Molecular Sciences* **21**, 7745. ISSN: 1422-0067. (2022) (Oct. 2020).
134. Ylitalo, A. S., Balzer, C., Zhang, P. & Wang, Z.-G. Electrostatic Correlations and Temperature-Dependent Dielectric Constant Can Model LCST in Polyelectrolyte Complex Coacervation. *Macromolecules* **54**, 11326–11337. ISSN: 0024-9297, 1520-5835. (2022) (Dec. 2021).
135. Blum, L. Mean Spherical Model for Asymmetric Electrolytes. *Molecular Physics* **30**, 1529–1535. ISSN: 0026-8976. (2023) (Nov. 1975).

136. Maribo-Mogensen, B., Kontogeorgis, G. M. & Thomsen, K. Modeling of Dielectric Properties of Complex Fluids with an Equation of State. *The Journal of Physical Chemistry B* **117**, 3389–3397. ISSN: 1520-6106, 1520-5207. (2022) (Mar. 2013).
137. Blum, L. & Hoeye, J. S. Mean Spherical Model for Asymmetric Electrolytes. 2. Thermodynamic Properties and the Pair Correlation Function. *The Journal of Physical Chemistry* **81**, 1311–1316. ISSN: 0022-3654, 1541-5740. (2023) (June 1977).
138. Jiang, J. W., Blum, L., Bernard, O. & Prausnitz, J. M. Thermodynamic Properties and Phase Equilibria of Charged Hard Sphere Chain Model for Polyelectrolyte Solutions. *Molecular Physics* **99**, 1121–1128. ISSN: 0026-8976. (2022) (July 2001).
139. Dufal, S. *et al.* The A in SAFT: Developing the Contribution of Association to the Helmholtz Free Energy within a Wertheim TPT1 Treatment of Generic Mie Fluids. *Mol. Phys.* **113**, 948–984. ISSN: 13623028 (2015).
140. Gross, J. & Sadowski, G. Application of the Perturbed-Chain SAFT Equation of State to Associating Systems. *Ind. Eng. Chem. Res.* **41**, 5510–5515. ISSN: 0888-5885, 1520-5045. (2022) (Oct. 2002).

Appendix A

FABRICATION OPTIMIZATION FOR SCALABLE HOLOGRAPHIC LITHOGRAPHY

A.1 Scanning Step Size Optimization for Holographic Lithography

To optimize the scanning step size for a given beam size we implemented a numerical simulation that quantifies the uniformity of the deposited dose distribution. We used the TaperCamD-uCD23 beam profiles to record the 2D beam intensity (Figure A.1a). The beam width was estimated around 2.14 mm. In order to simulate the scanning procedure, temporal discretization was applied, therefore the final intensity distribution could be approximated by a sequential summation of Gaussian beams shifted in the horizontal and vertical directions. The horizontal shift was assumed to be d which is the scanning step, and the vertical $1/v\delta t$, where v the scanning speed and δt the temporal step size. To access the uniformity of the resulting intensity distribution I we calculate the reverse contrast given by

$$U = 1 - \frac{I_{max} - I_{min}}{I_{max} + I_{min}}. \quad (\text{A.1})$$

A higher value of U corresponds to a higher uniformity. For our simulation we utilized a time step of $0.1 \mu\text{s}$ and a scanning speed of 1.5 mm s^{-1} , the beam spacing was varied between 0.1 and 1 mm in steps of 0.0091 mm.

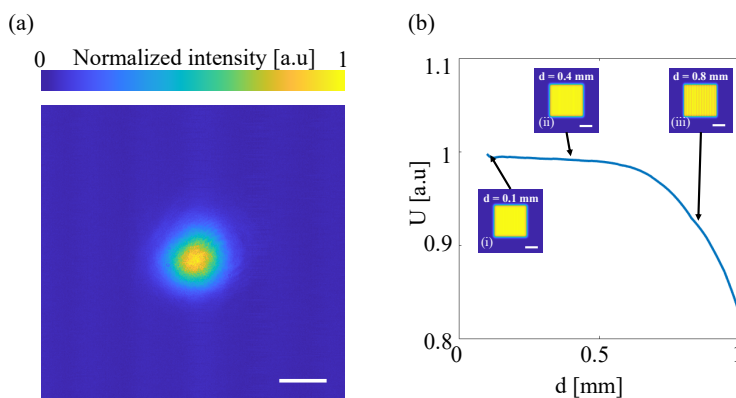


Figure A.1: **Scanning step size optimization for holographic lithography.** **a**, Recorded beam profile/ Scale bar 1 mm. **b**, Uniformity factor for various beam step sizes. The insets show the resulting intensity distributions at step sizes 0.1 mm, 0.4 mm, and 1 mm respectively. Scale bar 4 mm.

The uniformity factor (Figure A.1b) is close to unity and relatively stable for beam step sizes up to 0.5 mm. After that a rapid decline is observed together with a deterioration of the intensity distribution. Therefore we choose a step size of 0.4 mm.

A.2 Diffraction efficiency measurements and mask uniformity

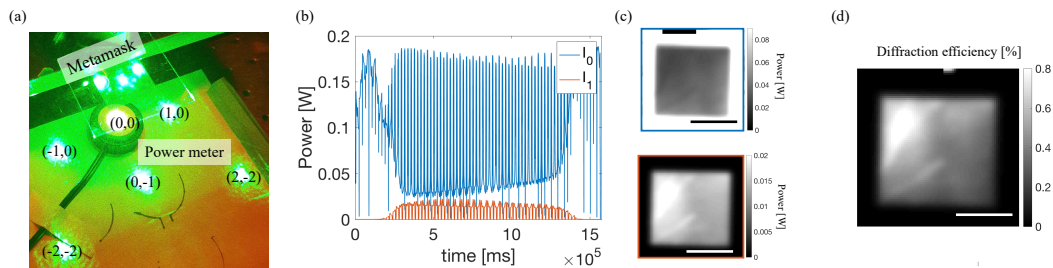


Figure A.2: **Metamask diffraction efficiency measurement.** **a**, Photograph of measurement setup. **b**, Raw power data for the first and zeroth diffraction orders. **c**, Reconstructed images of the two measured orders. Scale bar 1 cm. **d**, Computed diffraction efficiency map. Scale bar 1 cm.

To map the diffraction efficiency of the metamask we measured the intensities of the zeroth and first diffraction orders. We utilised the PM100D THOR labs optical power meter equipped with a Si photodiode (S121C). We place the metamask 5.9 cm above the power meter (Figure A.2a) and performed two sequential scans: one for measuring the zeroth order and one for measuring the first diffracted order. The laser was operated at 0.2 W. Since the power meter is not measuring with a constant frequency the temporal data (Figure A.2b) had to be interpolated and rearranged in order to form 2D images (Figure A.2c). By dividing the intensities of the first and zeroth orders we retrieved the diffraction efficiency map is generated (Figure A.2d). The metamask is not fully uniform due to fabrication inconsistencies. The observed difference in diffraction efficiency can be attributed to fine variations in the nano-pillar width.

Appendix B

EXPERIMENTAL CHARACTERIZATION FOR MULTIVALENT IONS AND POLYELECTROLYTE SYSTEM

B.1 Vibrational Spectroscopy for Metal-Carboxylate Coordination

Quantum DFT simulation of IR spectra for metal complexation environment

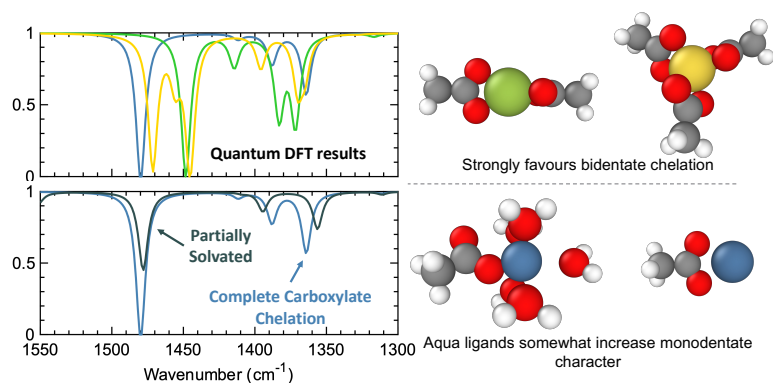


Figure B.1: **Quantum DFT simulated infrared spectra of acetate (RCOO^-) complexation of Na^+ , Ca^{2+} , and Al^{3+} in vacuo and with explicit coordinating aqua (H_2O) ligands.** Simulations demonstrate agreement with asymmetric and symmetric stretching modes of carboxylates seen experimentally. Representative structural models of coordination generated by simulation show a clear bidentate chelation coordinating environment in vacuo, while increasing explicit water in the ligand field appears to introduce some monodentate chelation to otherwise predominantly bidentate metal cation chelation, in agreement with experimental conclusions.

The complexation environment of metal cations was simulated using Quantum DFT methods. From these simulations, vibrational spectra and associated lowest energy coordinating geometries were produced allowing comparison with experimental findings. Energy minimization showed clear distinct coordination geometries between metal bonding based on valence, which was affected further as a result of competitive inclusion of water ligands in the crystal field of the cation, as captured in Supplementary Figure B.1. Representative structural models of coordination show clear bidentate chelation of the cations in vacuo, while introducing explicit water in the ligand field appears to introduce some monodentate chelation to otherwise predominantly bidentate chelation, seemingly consistent with experimental findings. These simulations, which are intentionally absent other species in MPEC gels (e.g.,

glycerol), are in generally good agreement with asymmetric and symmetric stretching modes of carboxylates seen experimentally: $\Delta\nu_0^{\text{DFT}}$ values for Na^+ , Ca^{2+} , and Al^{3+} corresponding to 116.04 cm^{-1} , 77.36 cm^{-1} and 76.02 cm^{-1} , respectively. This provided us with sufficient confidence to consider the binding energies obtained from these calculations to be somewhat representative of the real system.

B.2 Effects of Entanglement in AM-Fabricate MPEC Gels

We conducted an extended study by synthesizing Na^+ -MPEC gels with varying monomer concentrations. These variations result in different chain densities and lengths, thereby impacting the degree of entanglement within each system. The mechanical data for these gels is provided below. While more careful study is needed to ensure uniform solvent content across all systems, our preliminary findings suggest that the degree of entanglement significantly influences the mechanical response in sodium gels. Both modulus and tensile stress-strain responses exhibit noticeable variations with different degrees of entanglement.

[AA+SA]	M_0 (8.9M)	$0.8M_0$ (7.1M)	$0.67M_0$ (5.9M)	$0.6M_0$ (5.3M)	$0.5M_0$ (4.4M)
pH	2.43	2.42	2.48	2.52	2.56
Na^+					

Figure B.2: **Different monomer concentrations were used to fabricate Na^+ -MPEC gels with different polymerization degree.** The measured pH for each photoresin was included. Images of as-printed gels with the corresponding conditions.

B.3 Experimental Tracking in the Constructed MPEC Phase Diagrams

Quantitatively validating the phase diagrams presented in Figure 3.19 proved challenging due to the highly dense phase of the gel in our system. However, we conducted qualitative comparisons to verify the constructed phase diagrams for both Al and Ca. To explore different phase regions on the diagram, equilibrated gels were immersed in various solutions, including water, metal salt solutions with different concentrations, and poly(acrylic) acid solutions with different concentrations,

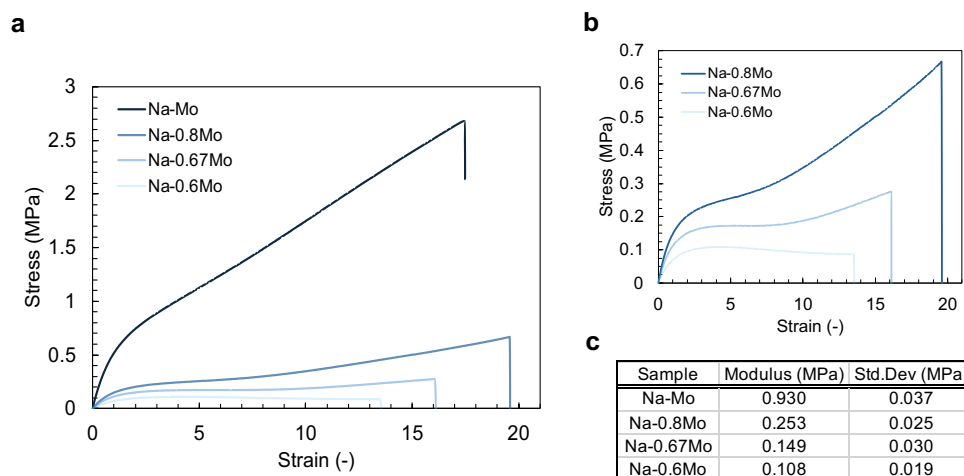


Figure B.3: **Quasi-static tensile test for the fabricated Na⁺-MPEC gels.** All gels were post-processed to the same conditions described in the main text. **a**, all samples, **b**, zoomed-in axes for samples with lower concentration to show stress-strain curve shape change, and **c**, summary of the measured young's modulus.

until equilibrium was reached.

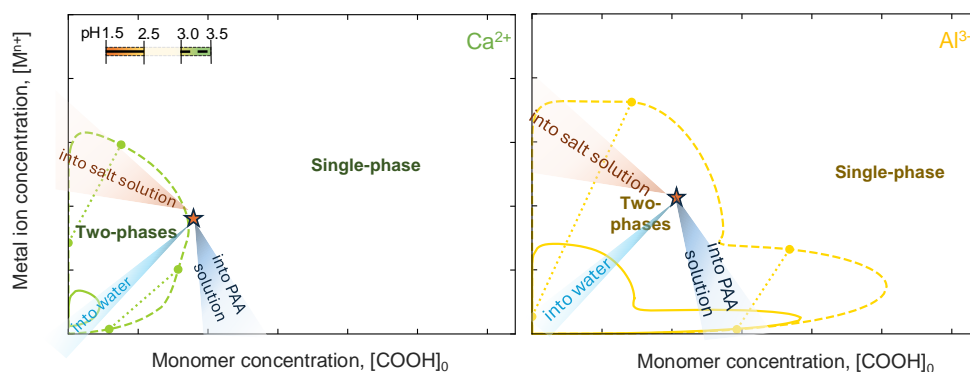


Figure B.4: **Experimental plan for exploring different phase regions on the constructed phase diagram for Ca²⁺ (left) and Al³⁺-MPEC (right).** The star marker represents an arbitrarily chosen starting gel condition. Different phases were observed depending on the solution type and concentration, aligning with the behavior predicted from the phase diagram.

We have summarized all results from these tests below. Regarding the solvent consistency, we ensured that the theoretical calculations used implicit solvent parameters to match the experimental conditions, facilitating direct comparison between theory and experiment. We hope this clarifies the approach taken to validate the phase

diagrams.

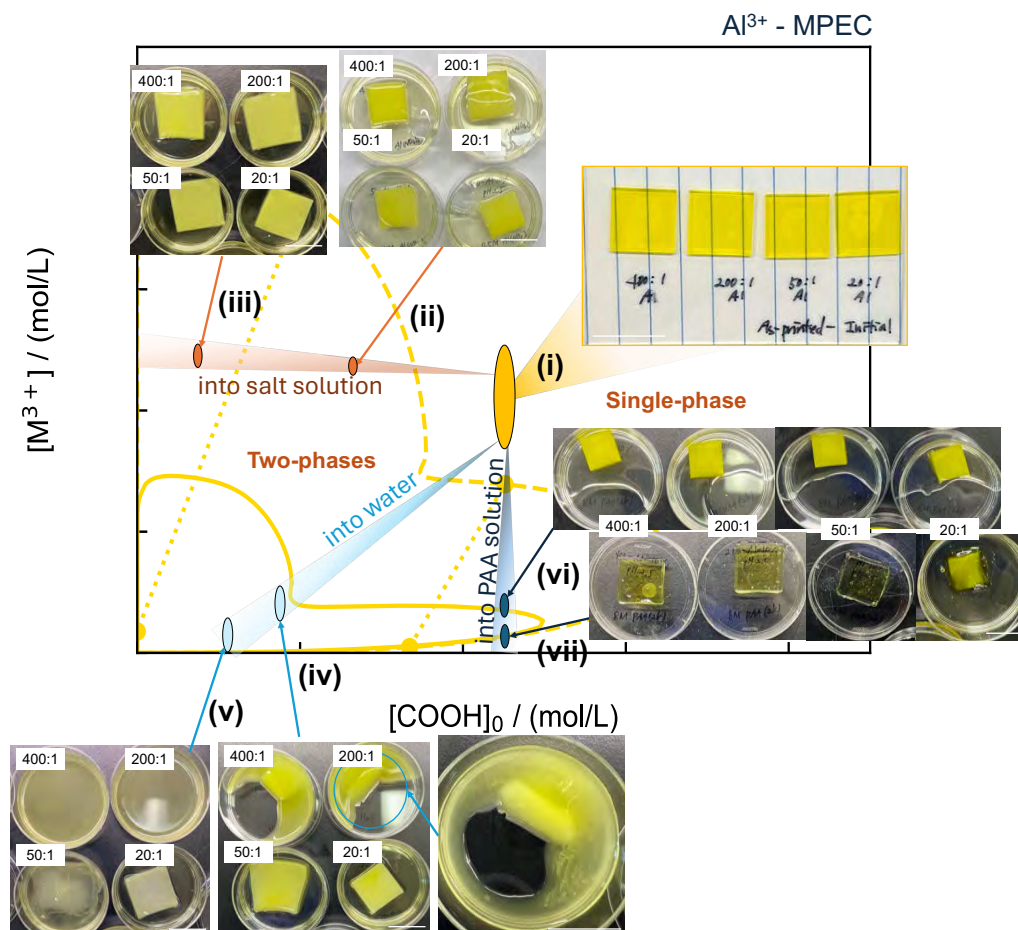


Figure B.5: **Experimental validation of the phase diagram for Al^{3+} -MPEC.** To explore different phase regions on the diagram, equilibrated Al-gels with different density (400:1, 200:1, 50:1, 20:1 for AA:Metal ratio) were immersed in various solutions, including water, calcium nitrate solutions with different concentrations, and polyacrylic acid solutions with different concentrations, until equilibrium was reached. Different phases were observed depending on the solution type and concentration, aligning with the behavior predicted from the phase diagram. Gels become opaque in two-phase region whereas remain transparent in the single-phase region. (i) Equilibrated gels after post-processing; (ii) and (iii) immersed in 3 ml and 6 ml of 1M $\text{Al}(\text{NO}_3)_3$ solution; (iv) and (v) immersed in 4 ml and 8 ml of water; (vi) and (vii) immersed in 3 ml, 6 ml of 8M PAA solution ($M_w \sim 5$ kDa). Scale bar for all images 10 mm.

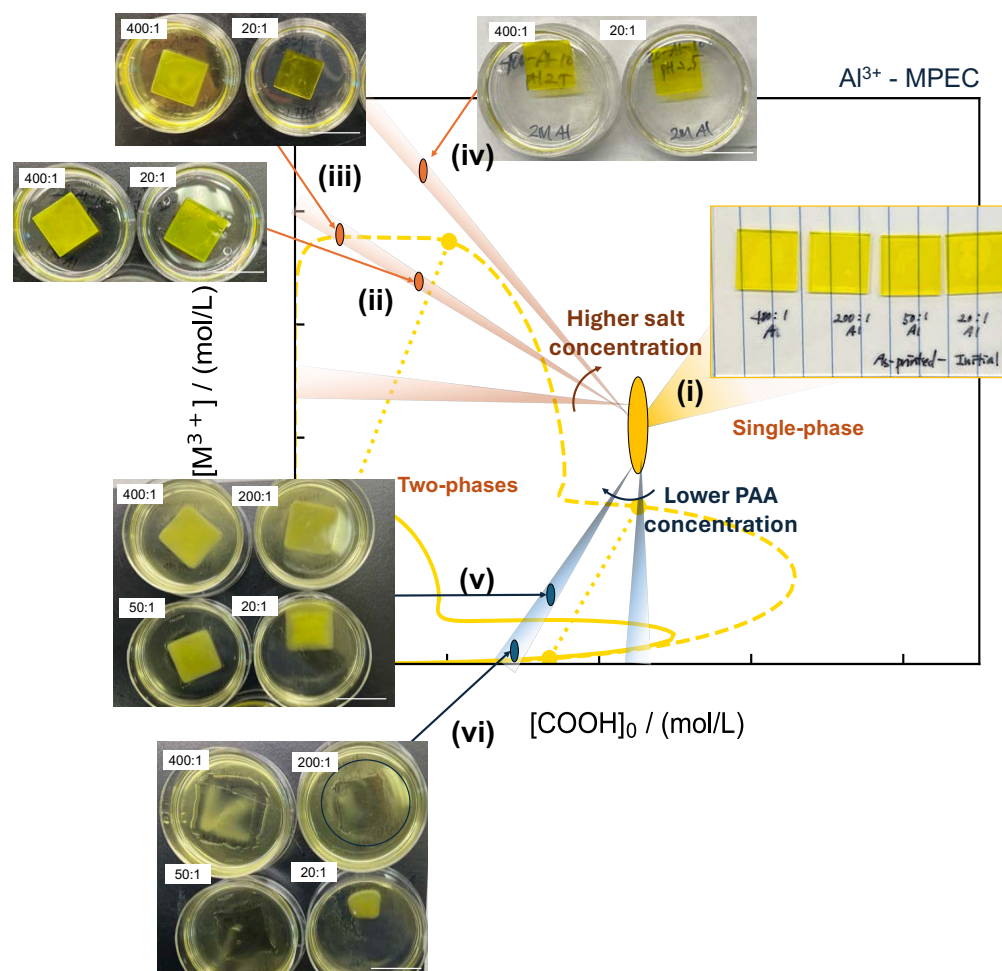


Figure B.6: **Additional experimental validation of the constructed phase diagram for Al^{3+} -MPEC.** (i) Equilibrated gels after post-processing; (ii), (iii), (iv) immersed in 3 ml of 1.5M, 1.75M and 2M $\text{Al}(\text{NO}_3)_3$ solution; (v) and (vi) immersed in 4 ml and 8 ml of 4M PAA solution ($M_w \sim 5$ kDa). Scale bar for all images 10 mm.

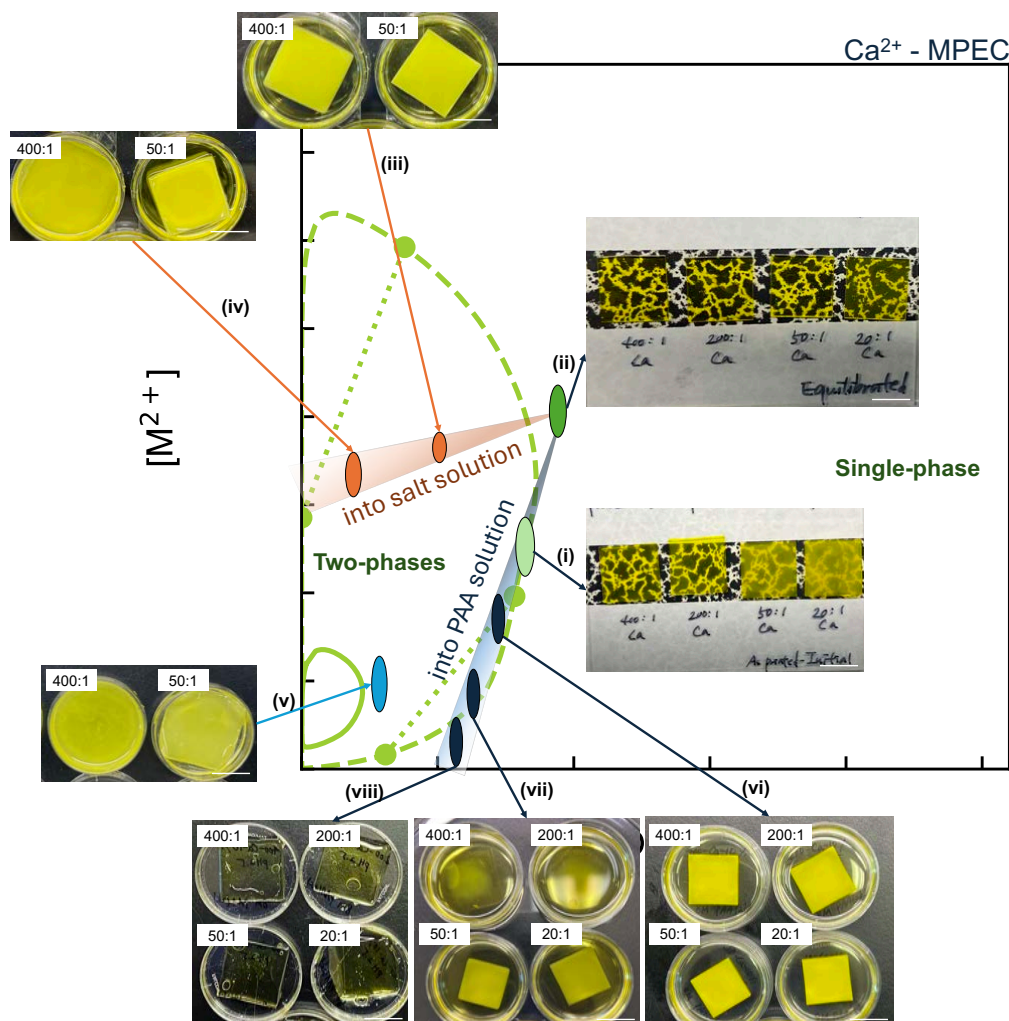


Figure B.7: **Experimental validation of the phase diagram for Ca^{2+} -MPEC.** To explore different phase regions on the diagram, equilibrated Ca-gels with different density (400:1, 200:1, 50:1, 20:1 for AA:Metal ratio) were immersed in various solutions, including water, calcium nitrate solutions with different concentrations, and polyacrylic acid solutions with different concentrations, until equilibrium was reached. Different phases were observed depending on the solution type and concentration, aligning with the behavior predicted from the phase diagram. Gels become opaque in two-phase region whereas remain transparent in the single-phase region. (i) As-printed gels; (ii) Equilibrated gels after post-processing; (iii) and (iv) immersed in 3 ml and 6 ml of 1.5M $\text{Ca}(\text{NO}_3)_2$ solution; (v) immersed in water; (vi), (vii) and (viii) immersed in 3 ml, 6 ml, 8 ml of 8M PAA solution ($M_w \sim 5$ kDa). Scale bar for all images 10 mm.

Appendix C

**THEORETICAL FRAMEWORK FOR MULTIVALENT IONS
AND POLYELECTROLYTE SYSTEM**

C.1 Modified Henderson–Hasselbach Equation

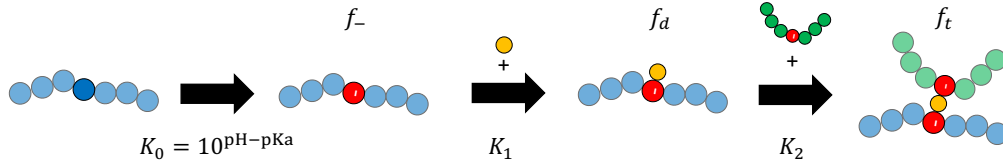


Figure C.1: **Visual representation of the possible associations of a weak polyelectrolyte in the presence of multivalent cations.** Association constants are denoted by K_i and the fraction of polymers existing in state i are denoted by f_i .

If we treat our deprotonation equilibrium as a simple acid-base reaction, then the ratio of deprotonated (f_-) and protonated ($1 - f_-$) PAA sites can be obtained using the Henderson–Hasselbach equation:

$$\text{pH-pKa} = -\log\left(\frac{f_-}{1 - f_-}\right). \quad (\text{C.1})$$

While this equation has origins within solution chemistry, it can also be derived using statistical mechanics. Starting from a chain with m_p beads, we assume that m_- have been deprotonated. As such, the partition function for this system is given by:

$$Z_- = Z_{\text{ref.}} P_{-, \text{comb.}} K_0^{m_-}, \quad (\text{C.2})$$

where $Z_{\text{ref.}}$ is our reference partition function. The combinatorial term, $P_{-, \text{comb.}}$ is given by:

$$P_{-, \text{comb.}} = \frac{m_p!}{(m_p - m_-)! m_-!}, \quad (\text{C.3})$$

and the equilibrium constant, K_0 , is simply given by:

$$K_0 = \rho_p 10^{(\text{pH-pKa})}. \quad (\text{C.4})$$

If we were to minimize equation C.2 with respect to m_- and define a new variable, $f_- = m_-/m_p$, we would recover the Henderson–Hasselbach equation:

$$\text{pH-pKa} = -\log\left(\frac{f_-}{1 - f_-}\right). \quad (\text{C.5})$$

However, if we want to modify this equation accounting for the fact that the deprotonated sites can subsequently bind to metal ions (and form crosslinks), we need to modify our partition function. We now assume that, from m_m metal cations and of the m_- charged sites on the polyelectrolyte backbone, m_d have formed dimers. Our partition function, now starting from Z_- as the reference system, is given by:

$$Z_d = Z_- P_{d,\text{comb.}} K_1^{m_d}, \quad (\text{C.6})$$

where the combinatorial term is given by:

$$P_{d,\text{comb.}} = \frac{m_-!}{(m_- - m_d)! m_d!} \frac{m_m!}{(m_m - m_d)! m_d!} m_d!. \quad (\text{C.7})$$

The additional $m_d!$ contribution arises from the fact that there are $m_d!$ ways to select the dimers. The equilibrium constant for this association, following equation C.43, is given by:

$$K_1 = \rho_p \kappa_d \sigma_{pm}^3 g^{\text{EXP}}(\sigma_{pm}) \left[\exp\left(\frac{l_B Z_m}{\sigma_{pm}}\right) - 1 \right], \quad (\text{C.8})$$

where κ_d is the bonding volume for this association. We can repeat the above process to account for the formation of m_t trimers from m_d dimers and $m_- - m_d$ unassociated charged sites, and even for higher-order 4-mers. Saving some unnecessary algebra, the resulting expression, starting from the original reference partition function $Z_{\text{ref.}}$, is:

$$Z_q = Z_{\text{ref.}} K_0^{m_-} K_1^{m_d} K_2^{m_t} K_3^{m_q} \times \frac{m_p! m_m!}{(m_p - m_-)! (m_m - m_d)! (m_t - m_q)! (m_- - m_d - m_t - m_q)! m_q!}, \quad (\text{C.9})$$

where:

$$K_2 = \rho_p \kappa_t \sigma_{pm}^3 g^{\text{EXP}}(\sigma_{pm}) \left[\exp\left(\frac{l_B}{\sigma_{pm}} \left[Z_m - \frac{1}{2} \right]\right) - 1 \right], \quad (\text{C.10})$$

$$K_3 = \rho_p \kappa_q \sigma_{pm}^3 g^{\text{EXP}}(\sigma_{pm}) \left[\exp\left(\frac{l_B}{\sigma_{pm}} \left[Z_m - \frac{2}{\sqrt{3}} \right]\right) - 1 \right], \quad (\text{C.11})$$

where κ_t and κ_q are the bonding volume for each association. Note that, with each incremental association, the binding energy is reduced due to the local repulsions from the sites that are already associated. The magnitude of these reductions was determined by the configurations which resulted in the least repulsion between charged sites (linear for the trimer and triangular planar for the 4-mer). This will lead to a situation where $K_3 < K_2 < K_1$, which should make sense as, when forming

additional associations, both the local repulsion and steric hindrance will make these interactions less favorable.

If we now minimize the above expression with respect to m_- , m_d , m_t and m_q , and normalise these variables with respect to the number of beads ($f_i = m_i/m_p$), we obtain the following:

$$K_0 = \frac{f_- - f_d - f_t - f_q}{1 - f_-}, \quad (\text{C.12})$$

$$K_1 = \frac{f_d - f_t}{(f_m - f_d)(f_- - f_d - f_t - f_q)}, \quad (\text{C.13})$$

$$K_2 = \frac{f_t - f_q}{(f_d - f_t)(f_- - f_d - f_t - f_q)},$$

$$K_3 = \frac{f_q}{(f_t - f_q)(f_- - f_d - f_t - f_q)}.$$

Unfortunately, the variables f_i are not particularly useful as, for example, f_d measures the fraction of sites that have at least formed a dimer, not only. As such, we define the following fractions, X_i , which measure the fraction of sites in state i only:

$$X_- = f_- - f_d - f_t - f_q, \quad (\text{C.14})$$

$$X_d = f_d - f_t - f_q, \quad (\text{C.15})$$

$$X_t = 2(f_t - f_q),$$

$$X_q = 3f_q.$$

We can also define the fraction of metal ions not associated as:

$$X_{m,\text{free}} = f_m - X_d - X_t/2 - X_q/3. \quad (\text{C.16})$$

Substituting into equations C.12 gives:

$$K_0 = \frac{X_-}{1 - X_- - X_d - X_t - X_q}, \quad (\text{C.17})$$

$$K_1 = \frac{X_d}{X_{m,\text{free}}X_-}, \quad (\text{C.18})$$

$$2K_2 = \frac{X_t}{X_dX_-},$$

$$\frac{3}{2}K_3 = \frac{X_q}{X_tX_-}.$$

As we can see in the above system of equations, we are representing the set of associations in Figure C.1 as sequential, reversible reactions. Indeed, without even

implementing the above system of equations, we can see that, if the pH is below the pKa, then $K_0 \ll K_1, K_2, K_3$, which will push the equilibrium forward above the Henderson–Hasselbach result to increase the fraction of dimers, trimers and 4-mers present.

Interplay between pH and metal valency

Without forming the full free energy equation, we are able to use this modified Henderson–Hasselbach equation to examine the interplay between pH and metal valency. Indeed, if we assume, to test the impact of additional associations, that $K_1 = K_2 = K_3 = 1000$, and examine how the charge sparsity of the polyelectrolytes varies with pH under different conditions, we obtain Figure C.2.

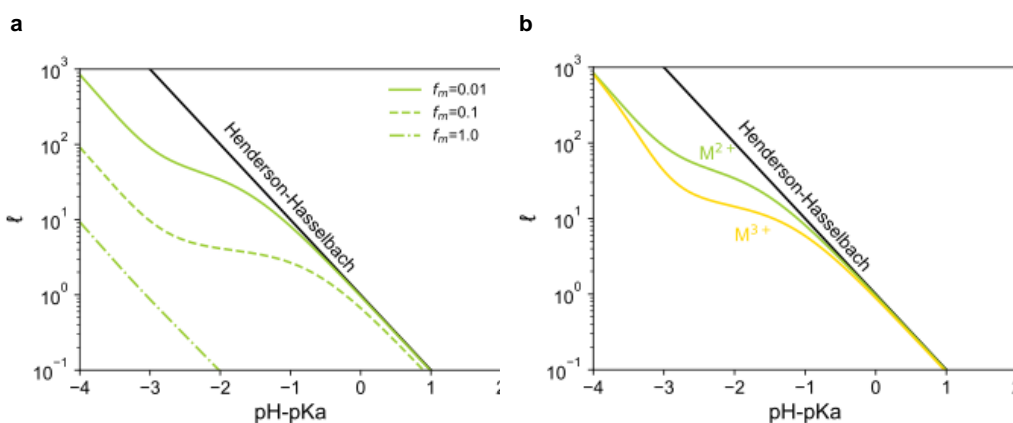


Figure C.2: **Theoretically estimated charge sparsity of a polyelectrolyte chain** at **a**, different divalent metal concentrations and **b**, different valency metals at the same concentration, $f_m = 0.01$.

If we consider Figure C.2a for a moment, we can see that the introduction of metal ions has led to a downwards shift of the charge sparsity curve at low pH. This is expected as, given the equilibrium for associating with metal ions is so strong, whatever metal ions are present will force the deprotonation equilibrium forward such that there are enough charged sites to bind all charged sites. However, as we reach high pH where there are now more charged sites than metal ions, K_0 now becomes the determinant equilibrium constant where all curves eventually converge towards the Henderson–Hasselbach equation. This occurs until the metal ion concentration becomes equal to the polymer bead concentration ($f_m = 1$); at this point, there will always be enough metal ions to bind all polyelectrolyte beads, leading to a constant offset from the Henderson–Hasselbach equation.

If we next consider the impact of the metal valency in Figure C.2b, we can see that the ability to form a 4-mer has allowed the trivalent system to maintain a lower sparsity at the same pH as the divalent system. This would make sense as, with a fourth association, the deprotonation equilibrium is pushed further forward. The exceptions to this are at the very low and very high pH regime. As mentioned previously, at very low pH, the equilibrium is dominated by the metal ion associations. However, as there are so few charged sites, these metal ions are only able to associate once, meaning that the dominating equilibrium constant is K_1 , which is identical in both systems. At very high pH, like the divalent system, we now have more charged sites than metal ions, leading to the deprotonation equilibrium dominating. All of these observations are commensurate with prior work using Monte Carlo simulations [128, 129].

C.2 Mean-field Theory of Multivalent Ions and Polyelectrolyte Systems

The theory we develop to model multivalent ions and polyelectrolyte systems accounts for three effects: 1. excluded-volume effects, 2. long-range electrostatic effects and 3. short-range association between charged sites on the polyelectrolyte backbone and the metal crosslinkers. The resulting representation resembles that shown in Figure C.3. The total free energy (no longer free energy density) for this system is then expressed as:

$$F = F_{\text{id.}} + F_{\text{exc.}} + F_{\text{ele.}} + F_{\text{assoc.}} \quad (\text{C.19})$$

Excluded Volume Effects

To account for the excluded volume contribution, $F_{\text{exc.}}$, we take inspiration from the Statistical Associating Fluid Theory (SAFT), developed by Chapman et al. [130], where one treats species as fused chains of m hard-sphere monomers with beads of diameter σ . This hard-chain contribution to the free energy is obtained from:

$$\frac{F_{\text{exc.}}}{Nk_{\text{B}}T} = \bar{m} \frac{F_{\text{HS}}}{Nk_{\text{B}}T} - \sum_i x_i (m_i - 1) \ln[g_{\text{HS}}(\sigma_i)], \quad (\text{C.20})$$

where x_i , m_i and σ_i are the mole fraction, number of beads and bead diameter of species i , respectively. \bar{m} is the molar-average number of segments in the system:

$$\bar{m} = \sum_i x_i m_i \quad (\text{C.21})$$

Note that the symbol N will now refer to the total number of particles in the system, rather than polymer chain length. The hard-sphere contribution to the free energy,

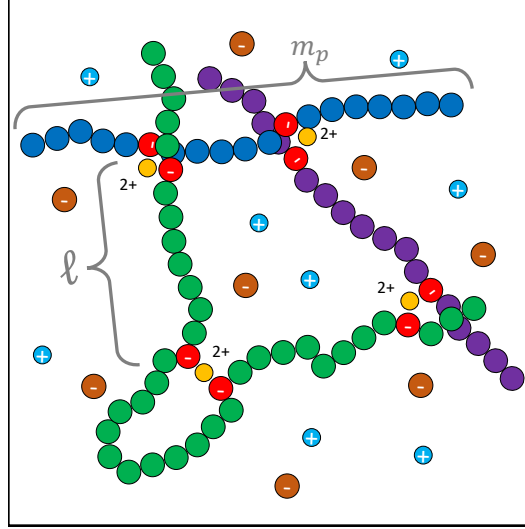


Figure C.3: **Visual representation of the proposed theory.** Colors have been used to distinguish between chains. Charged sites on the polymer backbone have been highlighted in red. The metal crosslinker, polyelectrolyte counter-ion and metal co-ion have been highlighted in yellow, light blue and brown, respectively.

F_{HS} , is obtained from the Carnahan-Starling equation of state [131]:

$$\frac{F_{\text{HS}}}{Nk_{\text{B}}T} = \frac{1}{\zeta_0} \left[\frac{3\zeta_1\zeta_2}{(1-\zeta_3)} + \frac{\zeta_2^3}{\zeta_3(1-\zeta_3)^2} + \left(\frac{\zeta_2^3}{\zeta_3^2} - \zeta_0 \right) \ln(1-\zeta_3) \right], \quad (\text{C.22})$$

where the packing fractions, ζ_n , are obtained from:

$$\zeta_n = \frac{\pi}{6} \rho \sum_i x_i m_i \sigma_i^n, \quad n \in 0, 1, 2, 3, \quad (\text{C.23})$$

where ρ is the total number density (N/V) of the system. The hard-sphere pair distribution function, $g_{\text{HS}}(\sigma_i)$, is also obtained using the Carnahan-Starling equation of state:

$$g_{\text{HS}}(\sigma_i) = \frac{1}{1-\zeta_3} + \frac{\sigma_i}{2} \frac{3\zeta_2}{(1-\zeta_3)^2} + \frac{\sigma_i^2}{4} \frac{2\zeta_2^2}{(1-\zeta_3)^3}. \quad (\text{C.24})$$

We note that, unlike Zhang et al. [132], we only use the hard-sphere pair distribution function in equation C.20 to model the formation of chains, despite the presences of charges in the chain. In Zhang et al.'s work [132], all beads in the chain are charged whereas, in our work, the charged beads are separated by ℓ uncharged beads. As such, the beads in direct contact with one another will only interact via hard-sphere interactions. However, if the spacing between charged beads is reduced to the point of being below the screening length of the system, long-range interactions within the chain will play a role. For this reason, we will avoid such low charge sparsities.

Electrostatic Effects

The electrostatic contribution, $F_{\text{ele.}}$, is obtained using the Debye–Hückel equation [101], given by:

$$\frac{F_{\text{ele.}}}{Nk_{\text{B}}T} = -\frac{\rho}{3}l_{\text{B}}\kappa \sum_i x_i f_i Z_i^2 \chi(\kappa\sigma_i), \quad (\text{C.25})$$

where f_i and Z_i are the number and valency of charges on species i . l_{B} is the Bjerrum length:

$$l_{\text{B}} = \frac{\beta e_c^2}{4\pi\epsilon_0\epsilon_{\text{r}}}, \quad (\text{C.26})$$

where e_c is the charge of an electron, ϵ_0 is the permittivity of free space and ϵ_{r} is the dielectric constant of the medium. The Debye inverse screening length, κ , is given by:

$$\kappa^2 = 4\pi l_{\text{B}}\rho \sum_i x_i f_i Z_i^2. \quad (\text{C.27})$$

The function $\chi(y)$ can be obtained from:

$$\chi(y) = \frac{3}{y^3} \left[\frac{3}{2} + \ln(1+y) - 2(1+y) + \frac{1}{2}(1+y)^2 \right]. \quad (\text{C.28})$$

We note that a few approximations are made when using the Debye–Hückel equation. Firstly, as part of the derivation for the Debye–Hückel equation, we assume that we are in a regime where the inverse screening length is large. Silva et al. [133] have shown that, even when this approximation is not made and the Poisson–Boltzmann expression is solved in full, the differences between this and the Debye–Hückel equation remain minor up to high salt concentrations. One limitation of this is when considering that charges on the polymer backbone separated by ℓ monomers. In the case of a freely jointed chain, so long as the distance between monomers exceeds the screening length ($\kappa\ell\sigma \gg 1$), it is still valid to use the Debye–Hückel expression in this context. Following a similar line of thought, we also assume that our solvent, that is, the dielectric medium, can be treated implicitly.

Finally, as done in the work by Zhang et al. [132] and, more recently, Ylitalo et al. [134], one could also capture electrostatic effects using Blum [135] implicit mean-spherical approximation (MSA). Based on the work by Maribo-Mogensen et al. [136], we note that the differences between the MSA and Debye–Hückel expression can be accounted for using a simple rescaling of the bead diameter, σ_i . As such, given we are aiming to analyse this system qualitatively and that the Debye–Hückel term is less computationally demanding, we shall use this term instead.

Association Effects

When modelling the association between the metal crosslinker and charged site on the polyelectrolyte backbone, we assume that the number of sites on the metal crosslinker is equal to its valency ($Z_m = f_m$). That is, it cannot crosslink with more charged sites than its charge can compensate for; this would be intuitive as, once the crosslink has become locally neutral, it will be energetically unfavorable to crosslink with an additional charge on the backbone. As for the polyelectrolyte, we will treat each charged site as an association site; given all charged sites are monovalent, each polyelectrolyte then has f_p association sites.

At this point, we note that the theory developed by Semenov and Rubinstein [97] can be reproduced using the first-order Wertheim Thermodynamic Perturbation Theory (WTPT1) in the case where we assume the binding energy is large and the fluid is ideal ($g(r) \approx 1$). Given we are now modeling the chain as having both excluded volume and electrostatic effects, this approximation is no longer appropriate. As such, we will now rigorously re-derive the association contribution, $F_{\text{assoc.}}$. We start with a system where no sites are associated; in this case, we define the local number density of the sites as:

$$\rho_i(\mathbf{r}_i) = \frac{N_i(\mathbf{r}_i)f_i}{V}, \quad (\text{C.29})$$

where $N_i(\mathbf{r}_i)$ is the local number density of species i at the position vector \mathbf{r}_i . We now assume that some of these sites have been associated such that the local number density of sites not associated, $\rho_{i0}(\mathbf{r}_i)$, is given by:

$$\rho_{i0}(\mathbf{r}_i) = \frac{N_i(\mathbf{r}_i)f_i}{V} X_i(\mathbf{r}_i), \quad (\text{C.30})$$

where $X_i(\mathbf{r}_i)$ is the local fraction of sites on species i not associated. As a result, the free energy change of these sites associating is given by:

$$\begin{aligned} \frac{F_{\text{assoc.}}}{k_B T} = & \sum_i \int \rho_i(\mathbf{r}_i) \ln \left(\frac{\rho_{i0}(\mathbf{r}_i)}{\rho_i(\mathbf{r}_i)} \right) + \rho_i(\mathbf{r}_i) - \rho_{i0}(\mathbf{r}_i) d\mathbf{r}_i \\ & - \int \int \rho_{p0}(\mathbf{r}_p) \rho_{m0}(\mathbf{r}_m) g(r_{pm}) f(r_{pm}) d\mathbf{r}_p d\mathbf{r}_m, \end{aligned} \quad (\text{C.31})$$

where the indices p and m refer to the polyelectrolyte and metal sites, and r_{pm} is the distance between the polyelectrolyte and metal sites. $g(r)$ is the pair distribution function and $f(r)$ is the Mayer- f function given by:

$$f(r) = [\exp -\beta\phi(r) - 1], \quad (\text{C.32})$$

where $\phi(r)$ is the potential characterizing the association interaction. To simplify our expression for the free energy, we will assume the system is homogeneous (that is our number densities have no positional dependence), giving:

$$\begin{aligned} \frac{F_{\text{assoc.}}}{k_{\text{B}}T} &= \sum_i \left[\rho_i \ln \left(\frac{\rho_{i0}}{\rho_i} \right) + \rho_i - \rho_{i0} \right] \int d\mathbf{r}_i \\ &\quad - \rho_p \rho_0 \rho_{m0} \int \int g(r_{pm}) f(r_{pm}) d\mathbf{r}_p d\mathbf{r}_m, \end{aligned} \quad (\text{C.33})$$

$$\begin{aligned} \frac{F_{\text{assoc.}}}{k_{\text{B}}T} &= \sum_i N_i f_i [\ln X_i + 1 - X_i] \\ &\quad - 4\pi \rho_p \rho_0 \rho_{m0} V \int g(r_{pm}) f(r_{pm}) r_{pm}^2 dr_{pm}, \end{aligned} \quad (\text{C.34})$$

$$\frac{F_{\text{assoc.}}}{Nk_{\text{B}}T} = \sum_i x_i f_i [\ln X_i + 1 - X_i] - \rho x_p x_m f_p f_m X_p X_m \Delta_{pm}. \quad (\text{C.35})$$

For clarity, we have defined the association strength between the polyelectrolyte and metal, Δ_{pm} , as:

$$\Delta_{pm} = 4\pi \int g(r_{pm}) f(r_{pm}) r_{pm}^2 dr_{pm}. \quad (\text{C.36})$$

If we now minimize equation C.35 with respect to all X_i , we obtain:

$$\frac{\partial}{\partial X_p} \left(\frac{F_{\text{assoc.}}}{Nk_{\text{B}}T} \right) = x_p f_p \left[\frac{1}{X_p} - 1 \right] - \rho x_p x_m f_p f_m X_m \Delta_{pm} = 0, \quad (\text{C.37})$$

$$\frac{\partial}{\partial X_m} \left(\frac{F_{\text{assoc.}}}{Nk_{\text{B}}T} \right) = x_m f_m \left[\frac{1}{X_m} - 1 \right] - \rho x_p x_m f_p f_m X_p \Delta_{pm} = 0, \quad (\text{C.38})$$

which we can re-arrange to give a set of mass-action equations:

$$X_p = \frac{1}{1 + \rho x_m f_m \Delta_{pm} X_m}, \quad (\text{C.39})$$

$$X_m = \frac{1}{1 + \rho x_p f_p \Delta_{pm} X_p}. \quad (\text{C.40})$$

Substituting these expressions to equation C.35 will give:

$$\frac{F_{\text{assoc.}}}{Nk_{\text{B}}T} = \sum_i x_i f_i \left[\ln X_i + \frac{1 - X_i}{2} \right]. \quad (\text{C.41})$$

At this stage, we note the similarities between equation C.41 and the sticker contribution from Semenov and Rubinstein [97]'s work. Indeed, if we had allowed the polyelectrolyte sites to associate directly with each other and defined $p = 1 - X_p$,

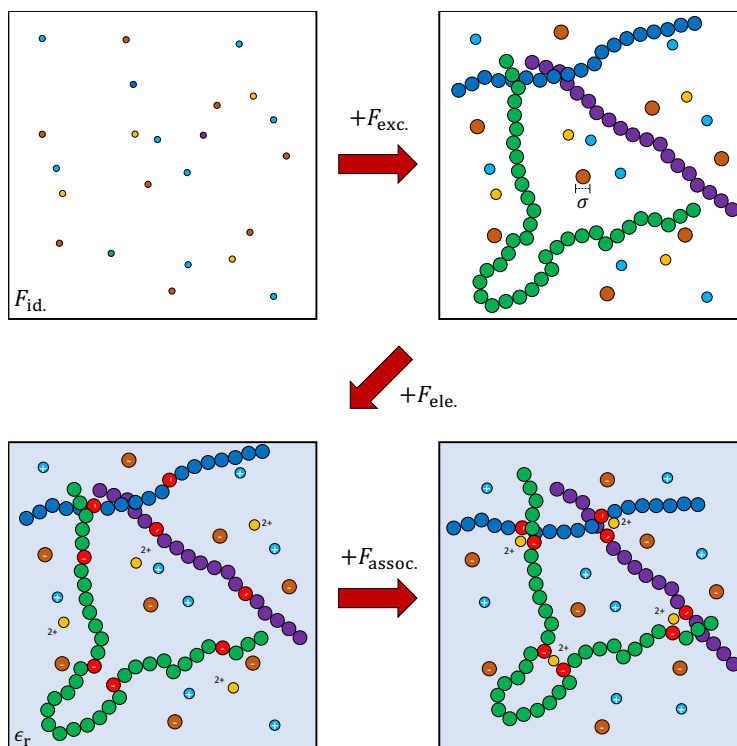


Figure C.4: **Summary of the impact of each term in the proposed theory.** The dielectric medium is represented with a change in the background color. Color scheme is identical to that in Figure C.3.

the above expression would reduce to that of Semenov and Rubinstein [97], with one key difference. Our association strength, given in equation C.36 now requires information from the pair distribution function of our reference system (charged hard-spheres). We will assume that the association between sites is characterized by Coulomb's potential such that:

$$\phi(r_{pm}) = \frac{l_B Z_m}{r_{pm}}. \quad (\text{C.42})$$

Expressions for the pair distribution function between charged species do exist, as obtained from Blum's implicit MSA model [137], which was further simplified by Jiang et al. [138] to what is known as the exponential approximation of the implicit MSA pair distribution function ($g^{\text{EXP}}(r)$). However, the integral in equation C.36 is not trivial and would be numerically expensive to evaluate. Typically, within SAFT-type approaches, this is dealt with by either developing correlations for the association strength [139], or by treating the pair distribution function and Mayer- f function as constants (evaluated at contact). We can then introduce a fudge-factor (also known as the 'bonding volume', $\kappa_{pm}\sigma_{pm}^3$) to approximate the association

strength [130, 140]:

$$\Delta_{pm} = \kappa_{pm} \sigma_{pm}^3 g^{\text{EXP}}(\sigma_{pm}) \left[\exp\left(\frac{l_B Z_m}{\sigma_{pm}}\right) - 1 \right]. \quad (\text{C.43})$$

This now gives us a full set of equations to describe our system. The development of this theory is summarized in Figure C.4.

Definition of phase equilibrium

In the case where a phase split occurs between phases α and β at a specified density for each species, ρ_{i0} , and temperature, the total free energy density ($\Psi = F/V$) will be given by:

$$\Psi = \varphi \Psi_\alpha(\boldsymbol{\rho}_\alpha, T) + (1 - \varphi) \Psi_\beta(\boldsymbol{\rho}_\beta, T), \quad (\text{C.44})$$

where φ is the volume fraction of phase α and $\boldsymbol{\rho}_j$ is the vector containing the density of each species in phase j . In order to conserve the total density of each species, we must introduce the Lagrangian multiplier, μ_i , for each species. Furthermore, as we are now including charged species, we must ensure electroneutrality in all phases. Given the input densities must satisfy electroneutrality, then we only require one more Lagrangian multiplier, ψ , to ensure this will be satisfied. As a result, the total Lagrangian for this system is:

$$\begin{aligned} \ell = & \varphi \Psi_\alpha(\boldsymbol{\rho}_\alpha, T) + (1 - \varphi) \Psi_\beta(\boldsymbol{\rho}_\beta, T) \\ & + \sum_i \mu_i (\varphi \rho_{i\alpha} + (1 - \varphi) \rho_{i\beta} - \rho_{i0}) \\ & + \psi \varphi \sum_i \rho_{i\alpha} f_i Z_i. \end{aligned} \quad (\text{C.45})$$

To determine the composition of each phase, we must minimize equation C.45 with respect to all densities (ρ_{ij}), volume fraction (φ), and all Lagrangian multipliers. In doing so, we find the following system of equations:

$$\mu_i = \frac{\partial \Psi_\alpha}{\partial \rho_{i\alpha}} + \psi f_i Z_i = \frac{\partial \Psi_\beta}{\partial \rho_{i\beta}}, \quad \forall i \quad (\text{C.46})$$

$$0 = \Psi_\alpha - \Psi_\beta + \sum_i \mu_i (\rho_{i\alpha} - \rho_{i\beta}) + \psi \sum_i \rho_{i\alpha} f_i Z_i, \quad (\text{C.47})$$

$$0 = \varphi \rho_{i\alpha} + (1 - \varphi) \rho_{i\beta} - \rho_{i0}, \quad \forall i \quad (\text{C.48})$$

$$0 = \sum_i \rho_{i\alpha} f_i Z_i. \quad (\text{C.49})$$

As we can see above, the choice of notation for the Lagrangian multipliers was intentional as μ_i corresponds to the chemical potential of each species and ψ corresponds to the electrochemical potential difference between phase α and β .

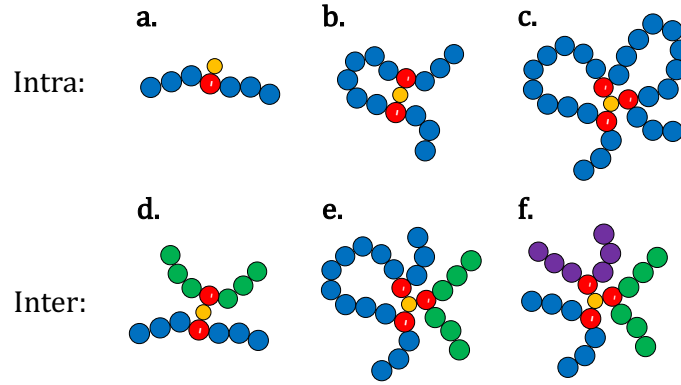


Figure C.5: **Visual representation of different possible chain configurations.** for intra- (a-c) and inter- (d-f) crosslinks. Different colors represent different chains.

Determining fraction of inter-chain crosslinked sites

One aspect of Semenov and Rubinstein [97]’s work that hasn’t been explored in much depth is, if one assumes that all sites are fully associated (i.e. $X_i = 1$) and that intra-crosslinks are only formed between nearest neighbours, then one can calculate the fraction of sites inter- and intra-crosslinked. In making these assumptions, we can assume that the entropic penalty for forming an intra-crosslink is [97]:

$$\Delta S_{\text{intra.}} = m_{\text{intra.}} k_B \ln \ell^{3/2}, \quad (\text{C.50})$$

where $m_{\text{intra.}}$ is the number of intra-crosslinked pairs. If we assume our reference system is the fully associated system ($Z_{\text{assoc.}}$), then the partition function for the intra-crosslinked system is:

$$Z_{\text{intra.}} = Z_{\text{assoc.}} P_{\text{comb.}} W \exp(\Delta S_{\text{intra.}}/k_B), \quad (\text{C.51})$$

where $P_{\text{comb.}}$ and W are defined the same way as the dimer combinatorial term, only with $m_{\text{intra.}}$ being selected from m_t trimers. If we minimize equation C.51 with respect to $m_{\text{intra.}}$ and define $f_{\text{intra.}} = m_{\text{intra.}}/m_p$, then we obtain the following expression:

$$f_{\text{intra.}} = \frac{-1 + \sqrt{1 + 4\ell^{1/2}\rho_p\sigma_p^3}}{2\ell^{1/2}\rho_p\sigma_p^3}. \quad (\text{C.52})$$

The above equation is technically only valid for the divalent system as, for the trivalent system, there are a few more ways one could form inter-chain crosslinks. This is shown in Figure C.5. As we can see, in the case of the trivalent system, the fraction of sites which have formed an intra-crosslink is given by:

$$f_{\text{intra.,tri}} = \left(f_{\text{intra.}} X_m^2 + f_{\text{intra.}}^2 X_m^3 \right). \quad (\text{C.53})$$

Furthermore, in terms of forming inter-chain crosslinks, the trivalent system has three ways of doing so, rather than just one in the case of the divalent system:

$$\begin{aligned} f_{\text{inter.,tri}} = & (1 - f_{\text{intra.}})(1 - X_m)^2 X_m \\ & + (2f_{\text{intra.}}(1 - f_{\text{intra.}}) + (1 - f_{\text{intra.}})^2)(1 - X_m)^3. \end{aligned} \quad (\text{C.54})$$

